The Dynamics of Magma Intrusion:

Using magnetic anisotropy to understand magma emplacement in intrusions

Thesis submitted in accordance with the requirements of the University of Liverpool for the degree of Doctor of Philosophy

By

Simon A. Martin

April 2020

Declaration of Authorship

I declare that this thesis titled 'The Dynamics of Magma Intrusion: Using magnetic anisotropy to understand magma emplacement in intrusions' and the work therein are my own work. The material contained within this thesis has not been presented, nor is currently been presented, wholly or in part, for any other degree or qualification.

Signed:

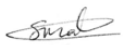

Simon A. Martin

April 2020

Abstract

Sheet intrusions provide key pathways for magma transport and storage as it flows through the Earth's crust. Many studies focus on the relationship between the intruding magma and the host rock through which it propagates, however the flow and emplacement processes occurring within the magma are often poorly constrained. Understanding this is vital for understanding the behaviour of active volcanic systems and the development of bodies of economic interest. To address this, I study how magnetic fabrics are preserved in a natural sill and dyke in combination with laboratory experiments using analogue materials to investigate the evolution of intrusion propagation and solidification.

The geochemistry and petrology of sills of the Little Minch Sill Complex, Isle of Skye, are well documented, however the physical processes of emplacement, i.e. magma flow and solidification, are relatively understudied. The studied sill was 6 m thick, of crinanite composition and a sheet with evidence of magma fingers. Anisotropy of magnetic susceptibility (AMS) and anisotropy of anhysteretic remanent magnetization (AARM) techniques were combined with petrology, to understand how magnetic fabrics vary across the sill length and thickness. AMS fabrics identified two groupings: Group A at the sill margins showed an initial magma flow aligned with the long-axis of the magma fingers, whereas Group B in the sill interior showed flow reorientation which was inferred to have occurred due to magma finger coalescence. AARM fabrics identified a post-emplacement flow regime, associated with migration of interstitial melt through the solidifying crystal mush. The contrasting fabrics demonstrate that multiple flow regimes were operational within the sill, and that these can be identified using multiple rock magnetism techniques.

Within a basaltic dyke from the Skye Dyke Swarm, multiple magnetic fabrics are recorded and originate from contrasting processes. Within the dyke core, magnetic fabrics originate from titanomagnetite, however in margin regions pyrrhotite becomes the dominant source of the fabrics. I identified that within the dyke core a record of lateral magma flow was preserved, however closer to the margins the fabrics were more indicative of magnetite breakdown and growth of pyrrhotite from a sulphide rich hydrothermal fluid which had overprinted any primary flow indicator. There was also variation in fabrics along strike of the dyke, with alteration of the dyke core also evident nearer to branching in dyke strike. This study shows the complexity and variation in magnetic fabrics, how this can vary over short (~13 m) distances and can be affected by post-emplacement alteration.

To understand how magnetic fabrics, develop during the propagation of sheet intrusions, a series of laboratory experiments were conducted. In these experiments plaster of Paris (magma analogue) seeded with magnetite particles, a pseudoplastic fluid, was injected into a box filled with flour (host rock analogue), a cohesive granular material. These materials were used to identify the evolution of AMS fabrics across multiple slices of model intrusions. The experimental intrusions formed a range of magma bodies including plutons, dykes, laccoliths and fingers, which indicate a range of processes occurring during initial emplacement and subsequent intrusion growth. AMS analyses of three parallel slices cut perpendicular to the flow axis, identified compressional and shear fabrics closer to the intrusion margins and towards the intrusion leading tips. Magnetic fabrics indicative of flow in the propagation direction were formed closer to the intrusion core and are like those observed in nature, thus demonstrating the potential of laboratory modelling for studying emplacement processes.

In combination, these studies of natural intrusions and laboratory experiments investigate the development and evolution of magnetic fabrics across the length and thickness of intrusions. This is important as understanding the evolution of flow during dyke and sill emplacement is vital for determining and improving current emplacement models.

Acknowledgements

Firstly, I would like to thank Janine Kavanagh for the great supervision you have given me over the last several years. Your support, encouragement and guidance are greatly appreciated, and thank you for having faith in me when I thought I wasn't progressing. You don't have to worry about me injuring myself in the field anymore.

I would also like to thank Andy Biggin for the support and guidance on rock magnetism you gave. On multiple occasions when I was having difficulty with understanding my data, you gave me ideas of pathways to explore.

I would like to thank Lis Rushworth, you are a great manager, your reliability in supporting me through my teaching and as a friend is greatly appreciated. I will miss the annual trip to Thurstaston. To the rest of the people in the School who I taught with thank you for the opportunity.

To Prokop and your colleagues at the Institute of Geophysics, thank you for your hospitality and accepting me during my time in your lab. It was a great experience and I hope to return in the future.

Thanks to Greig Paterson and Will McCarty for examining my thesis, and the advice with improving different sections. I really enjoyed my viva, despite the length.

To the many office mates and friends, thank you for being sounding boards for ideas or when I just needed a bit of a laugh or a moan. Elliot, Suraya and Louise, it's been fun chatting with you all, both in Liverpool and the field. Oliver, Cécile and Pam, you have been awesome friends, and I really miss our Sunday game nights.

Fiona, my geography partner in crime, I don't think I would have got through these years without you there. Being the only person who truly understood our position, it was good knowing I wasn't alone, and the support we have provided each other these last few months of isolation have been invaluable. You are great friend, however I'm not a fan of Casper being more loyal to you than me.

To my family, thank you for all the support over my academic career, the studying should be done for a while…now back to the Lego.

Finally, to Caroline, through the highs and lows, you have been brilliant over these last few years. I am glad you persisted in begging for a dog, as Casper, you truly are a man's best friend, and you filled a hole I didn't realise existed.

Table of Contents

Chapter 1: Introduction

This chapter forms a brief outline of the why studying magmatic intrusions is important, before outlining the key research questions. There is a brief description of each of the chapters which have been written in paper format and have either been published or prepared for submission.

1.1 Why study magmatic intrusions?

Understanding how magma is transported and emplaced within the crust is important for understanding the behaviour of active volcanic regions, on Earth (Chadwick et al., 2011; Bagnardi et al., 2013) and other bodies across the solar system, i.e. Io (Wilson and Head, 1983). Volcanic and igneous plumbing systems form the pathways that magma flows through within the crust, with the magma transported through a range of structures, including but not limited to dykes, sills and laccoliths. Some of which propagate to the surface and erupt whilst the majority arrest in the crust (e.g. Crisp, 1984; Gudmundsson, 2002) (Figure 1.1). Being able to monitor the propagation of magma intrusions in real time allows for more accurate forecasting of impending eruptions (Fee et al., 2011), as magma can be transported for many kilometres (both vertically and laterally) from its source prior to eruption; e.g. up to 40 km for the 2014 Bardarbunga eruption, Iceland (Sigmundsson et al., 2015) to >2100 km for the MacKenzie Dyke Swarm, Canada (Ernst and Baragar, 1992). This can increase the risk to populations not local to volcanic edifices, such as during the 2018 eruption of Kilauea, Hawai'i, where magma was erupted from the Lower East Rift Zone in the Pahoa district (~40 km form the volcano summit), destroying over 600 homes (County of Hawai'i, 2020). Magmatic intrusions are also of economic importance for mining and geothermal industries, as they can be host to a range of economically significant deposits such as copper-porphyry (Sun et al., 2013) and diamonds (Russell et al., 2019), or provide pathways for the transport of post-emplacement hydrothermal fluids through the crust (Stimac et al., 2015).

Further studies into magmatic intrusions are needed to unravel the dynamics of magma intrusion both syn- and post-emplacement, as most previous studies have focused on only the initial magma flow trajectory and our current understanding often assumes unidirectional magma flow. However, backflow into the volcanic vents when magma flux wanes has also been identified in observations of eruptions at Hawai'i (Wallace and Anderson, 1998), thus indicating highly variable magma flow directions can occur through time, and potentially at depth. Volcanic and igneous plumbing systems also provide pathways for the flow of post-emplacement hydrothermal fluids which may alter pre-existing mineral

fabrics or deposit new minerals. More detailed studies into magma flow dynamics across the breadth of intrusions, can be used as proxies for time intervals associated with magma transport and solidification, which could have large impact on our current understandings of intrusion emplacement.

1.2 Research questions

From the background covered here a series of research questions have been developed which I will try to address within this thesis.

1. *How does magma flow vary across the length and breadth of an intrusion? This is the main underlying question that underpins all chapters of this thesis.*
2. *How do magnetic fabrics vary across the length and breadth of solidified magma intrusions in nature? This question is addressed in chapters 3 and 4.*
3. *What are the processes that produce different magnetic fabrics and what can they tell us about the syn- and post-emplacement processes in ancient, solidified intrusions? This question is addressed in chapters 3 and 4.*
4. *How is flow preserved within laboratory models that use analogue materials and what can these models tell us about magma flow in nature? This question is addressed in chapter 5.*

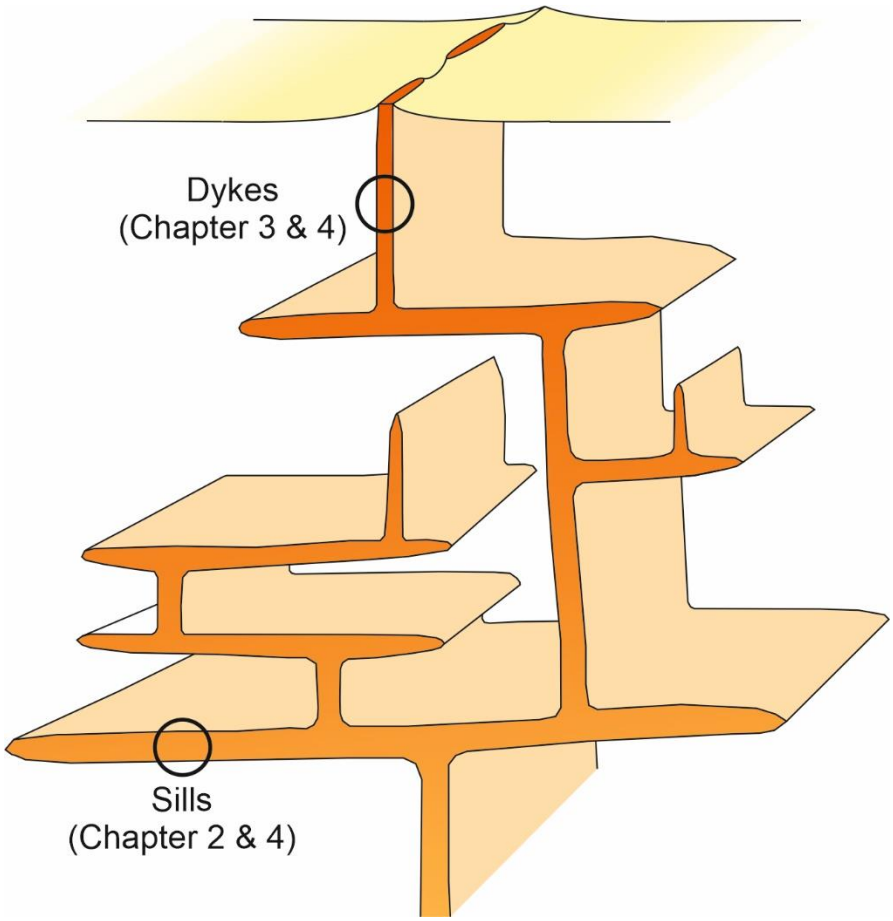

Figure 1.1 *Diagram showing a volcanic plumbing system with a series of interconnected sills and dykes. The intrusions identified will be covered in the respective chapters identified.*

1.3 Outline of the thesis

Chapter 2 forms a review of multiple aspects of dyke and sill emplacement. It covers a range of topics from dyke and sill emplacement models to how flow is recorded in the macro- and microscale fabrics of ancient, solidified sheet intrusions, including rock magnetism and magnetic anisotropy. There is also a detailed review of laboratory modelling and how sheet intrusions are studied using these techniques.

Chapter 3 focusses on how magnetic fabrics vary across the breadth of a sill and what the differences in fabrics mean in terms of the emplacement and solidification of the sill (Figure 1.1). The section of studied sill is situated in an abandoned quarry near Inver Tote, Isle of Skye Scotland. Samples were collected at 50 cm spacings across the thickness of the sill, from four sites due to restrictions with access. These samples were studied by Anisotropy of Magnetic Susceptibility (AMS), Anisotropy of Anhysteretic Remanent Magnetization (AARM) and rock magnetism with some optical and scanning electron petrology. The data are then discussed and used to identify the emplacement and solidification history of the sill. This

chapter is published as “The origin and evolution of magnetic fabrics in mafic sills” by Martin et al. (2019) in the journal Frontiers in Earth Science.

Chapter 4 is a detailed study of how magnetic fabrics vary across the length and breadth of a dyke from the same location as the sill. Here AMS and AARM fabrics are measured and analysed to identify the processes occurring both syn- and post-emplacement. For the dyke, two complete transects of 2 and 1.7 m breadth, were sampled at two sites separated by 13 metres along strike (Figure 1.1).

Chapter 5 is a study on how magnetic fabrics vary across the length and breadth of analogue intrusions created in the laboratory. In this study, a box was filled with fine grained wheat flour (host analogue) and intruded by plaster of Paris (magma analogue) seeded with magnetite particles which give rise to the magnetic fabrics being studied. After injection and solidification of the plaster, the intrusions were excavated to study their external morphologies. After which they were cut into thin slices to study their internal morphologies and subsequently drilled for core samples to study the magnetic fabrics (AMS) in the different sections of the intrusions.

Chapter 2: Review of dyke and sill emplacement

Magmatic intrusions have been studied in a variety of ways and using a variety of techniques. This chapter forms a review of the different types of magmatic intrusions, intrusion dynamics and how magma flow is preserved in the rock record within macro-scale structures, and micro-scale and magnetic fabrics, as understanding intrusion propagation and emplacement is important for a range of settings. I also include a review of analogue modelling techniques and how they have been utilized for understanding a range of magma rheologies and the processes occurring during the emplacement of sheet intrusions.

2.1 Intrusion types

Magmatic intrusions come in a range of shapes and sizes, from the sheet-like bodies of dykes and sills, to dome-shaped laccoliths or larger plutons. Dykes are vertical to sub-vertical sheets with dips of 80-90°, which generally have two walls and are usually discordant to bedding planes (Kavanagh, 2018). The length to thickness ratio of dykes is generally quite large, at 10^{2-4} (Gudmundsson, 2002; Barnett and Gudmundsson, 2014). Dykes are common structure for magma storage as only ~10% propagate to the surface and erupt (Gudmundsson et al., 1999).

Sills are emplaced as horizontal to sub-horizontal sheet intrusions with dips of 0-10°. They have a floor and roof and are generally emplaced concordant to bedding planes (Galland et al., 2018) e.g. in the Little Minch Sill Complex, Isle of Skye (Chapter 2). However, there are some exceptions to this rule where sills have been emplaced horizontally, but discordant to bedding planes, e.g. Loch Scridain Sill Complex, Isle of Mull, Scotland (Holness and Humphries, 2003). Whilst some sills have sheet like morphologies (e.g. Ferrar Large Igneous Province, Antarctica; Airoldi et al., 2012) some others have geometries more akin to fingers (e.g. Shonkin Sag Sill Complex; Pollard et al., 1975). Laccoliths are similar to sills in that they are horizontally oriented bodies, however they have a domed upper surface, e.g. Sandfell laccolith, Iceland (Mattsson et al., 2018) and tend to be more evolved compositions.

2.2 Dyke and sill emplacement models

Dyke and sill emplacement is controlled by a number of factors associated both in the host rock and the intruding magma, these include host rock strength (Gudmundsson, 2002; Kavanagh et al., 2006), magma overpressure (McLeod and Tait, 1999), magma rheology (Magee et al., 2013b) and magma flux (Castro et al., 2016). From these properties, two main

contrasting models of intrusion propagation have been developed: the hydraulic fracture model and the viscous indenter model.

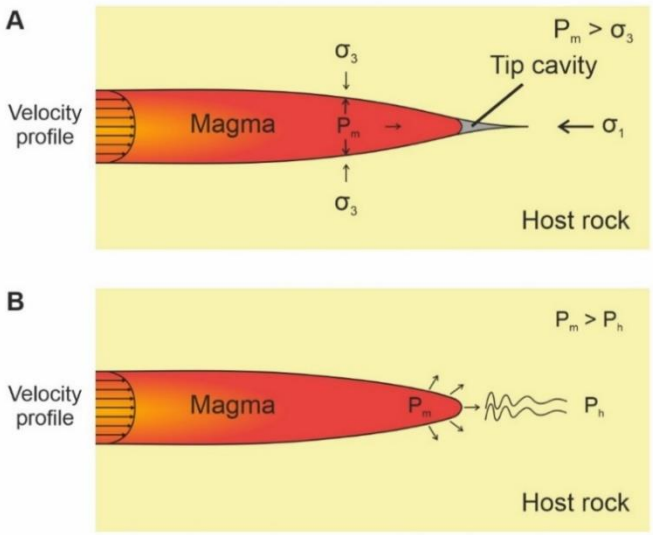

Figure 2.1 *Emplacement models for magma emplacement as sheet intrusions within the Earth's crust. A) The hydraulic fracture model where magma overpressure is greater than the pressure in the host rock keeping the fracture closed, as such causes fracture propagation (Lister, 1990). B) The viscous indenter model where magma forces its way into the host rock causing it to deform by ductile deformation, pushing the soft host rock out of its path (Donnadieu and Merle, 1998; Mathieu et al., 2008).*

The hydraulic fracture model is associated with a stronger crustal body, inferring an elastic crust that deforms by brittle fracturing at the intrusion tip from pressure applied to the tip from the propagating magma (Figure 2.1A). Fracturing and opening of the tip region creates space into which the magma can flow, resulting in tip propagation. Stresses within the crust determine the intrusion orientation with maximum stress (σ_1) being the propagation direction and the minimum stress (σ_3) being the opening direction (Anderson, 1951). Fracture propagation arrests when either a stiffer rock layer is reached (Kavanagh et al., 2006; Gudmundsson, 2011), the magma finds an alternative pathway (e.g. Acocella et al., 2009; Magee et al., 2013a) or there is a drop in overpressure (Taisne and Jaupart, 2009).

The viscous indenter model infers that the crust deforms in a ductile manner and is forced out of the way of the intruding magma (Figure 2.1B) (Galland et al., 2006). This style of emplacement is more common where sills are emplaced into sedimentary environments where the host rock is less consolidated and can be pushed aside or where hot magma can vaporise pore fluids which subsequently fluidise the rock (Kokelaar, 1982; Schofield et al., 2012a). It is also more common with higher viscosity magmas, which force their way through

poorly consolidated material (Mathieu et al., 2008). It is common at a range of viscosities, however the intrusion morphology with higher viscosity magmas often evolves to form laccoliths (Merle and Vendeville, 1995). Schofield et al. (2012a) identified a relationship between the emplacement depth and style of emplacement of horizontal sheet intrusions, with a boundary occurring at around 2km depth. Above this depth, structures more commonly associated with non-brittle processes occur, whereas between 2 and 5 km depth, structures associated with brittle deformation occurred.

2.3 Indicators of magma flow

Understanding intrusion emplacement mechanisms is important for identifying how magma behaves in active volcanic settings, however, the processes occurring within the flowing magma are often overlooked. By studying the structures exposed within ancient solidified sheet intrusions, from macro- to micro-scale, the processes forming them can be identified (Kavanagh, 2018). These processes may have both syn- and post emplacement origins e.g. magma flow and solidification, respectively. Field scale structures of magma flow, include magma fingers (e.g. Pollard et al., 1975; Schofield et al., 2010, 2012a), ropey flow structures (e.g. Liss et al., 2002; Kavanagh et al., 2018a) and flow lineations (e.g. Smith, 1987; Varga et al., 1998), whereas micro-scale structures include vesicle shapes (e.g. Coward, 1980; Liss et al., 2002), crystal alignment (e.g. Shelley, 1985; Geoffroy et al., 2002) and magnetic fabrics (e.g. Knight and Walker, 1988; Staudigel et al., 1992; Herrero-Bervera et al., 2001; Poland et al., 2004).

Magma fingers form where the host is soft enough for the magma to force its way through in a conduit morphology, thus creating rounded finger-like bodies (Pollard et al., 1975; Schofield et al., 2012a). These fingers have been found both in a range of exposed intrusion complexes e.g. Shonkin Sag sill, USA (Pollard et al., 1975), Golden Valley sill complex, South Africa (Figure 2.2a; also see Figure 1c in Schofield et al., 2012a), but have also been identified offshore using 3D seismic surveys (e.g. Miles and Cartwright, 2010; Magee et al., 2016). Where there is sufficient exposure to identify the presence of these structures, the finger axis is inferred to be the major flow axis, which if the source is known can give a flow vector (Schofield et al., 2010). Geophysical surveys have led to the identification of a series of meandering anomalies along the axis of intrusions located within the Møre Basin, offshore Norway, which were inferred to be a series of magma tubes (Miles and Cartwright, 2010). These tubes are suggested to be the location of prolonged magma transport from the feeder system to the terminating lobes forming along the front of the intrusion. Flow directions in small areas of sill intrusions can also be determined by the branching of secondary magma

tubes from a primary tube, with propagation occurring laterally at ~45° from the orientation of the feeder tube (Thomson and Hutton, 2004). If the propagation is unsuccessful in creating a new tube or propagation is small, horn-like structures can be formed.

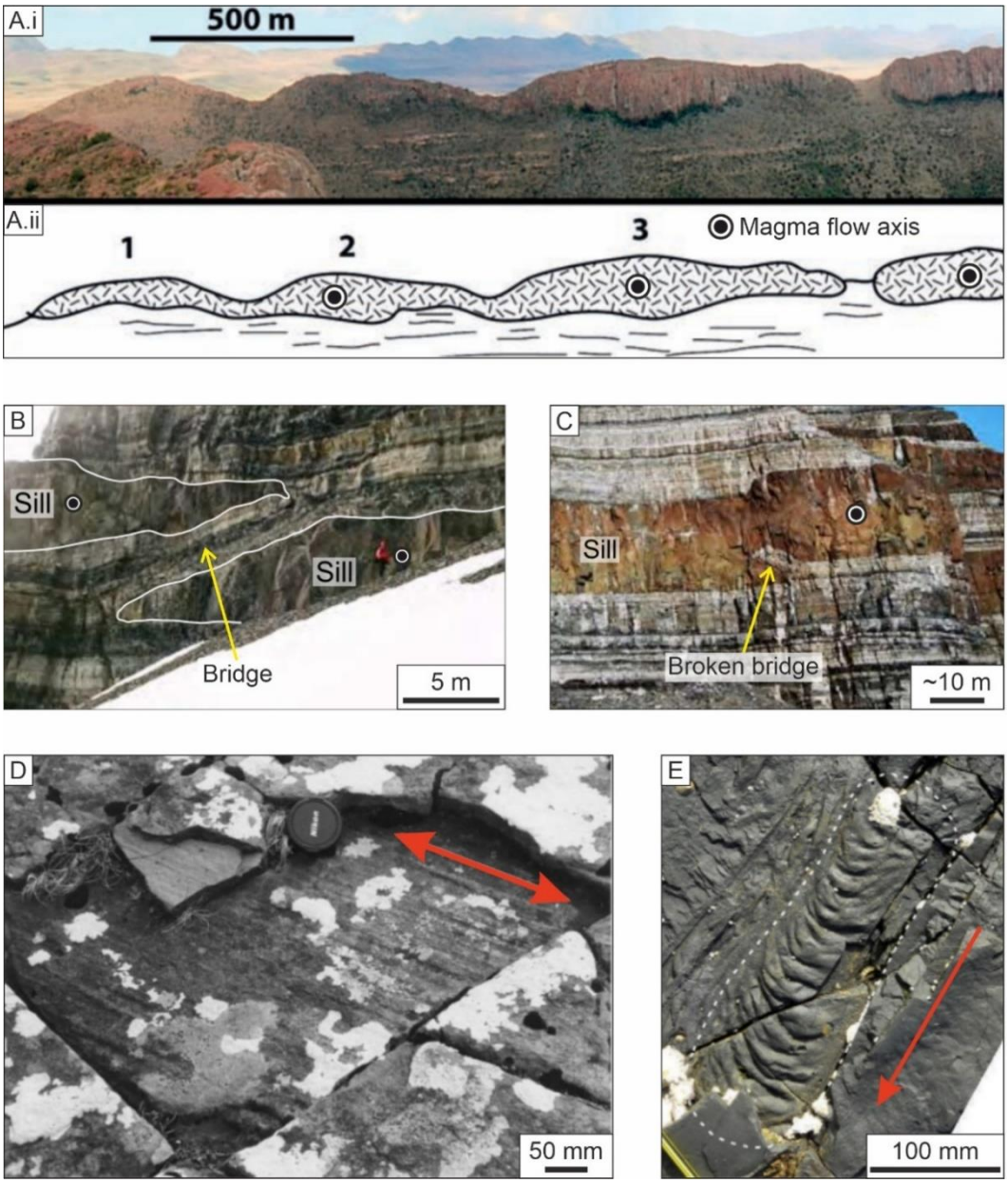

Figure 2.2 *Macroscale magma flow structures with black dots or red arrows indicating the magma flow axes; A.i) magma fingers in the Golden Valley Sill, South Africa, a part of the Karoo Igneous Province, with A.ii) a diagram of the outcrop with inferred magma flow axes (edited from Scofield et al. 2012). B) bridge structure between two sill segments with inferred flow axis of each sill, and C) a broken bridge (B and C edited from Magee et al., 2016). D) raised lineations or scour marks within the Traigh Bhàn na Sgùrra sill complex, Isle of Mull (edited from Holness and Humphries, 2003) and E) ropey flow structures preserved within elongated vesicles of a coastal part of the Karoo Igneous Province, South Africa (edited form Hoyer and Watkeys, 2017).*

At the field scale, en echelon fracturing can be used to infer the initial propagation direction (e.g. Rickwood, 1990; Magee et al., 2016), with the lineation of the bridge structure indicating the flow axis (Figure 2.2B; Figure 4 in Rickwood, 1990). This is due to the intrusion opening parallel to σ_3, which if this rotates from its initial orientation, causes the opening direction to change which results in segmentation of the intrusion (Anderson, 1951). Bridge structures are also referred to as relays (e.g. Stephens et al., 2017). In some cases, magma breaches these structures, rejoining the segments to create a single magma body (e.g. Rickwood, 1990; Magee et al., 2016, 2019), commonly referred to as broken bridges (Figure 2.2C; Figure 4Aiv in Magee et al., 2016).

Smaller scale structures that have been interpreted as indicators of magma flow include scour marks, magma ropes, and stretched vesicles. Scour marks appear as parallel raised lineations of rock within the solidified magma body and have been identified in both dykes (e.g. Smith, 1987; Varga et al., 1998) and sills (e.g. Holness and Humphreys, 2003). They are believed to form by molten magma flowing alongside more viscous to solid magma in the solidifying magma fronts (Smith, 1987) and can be evidence for laminar flow (Holness and Humphreys, 2003). Magma ropes have also been identified in both dykes (Kavanagh et al., 2018a) and sills (Liss et al., 2002; Hoyer and Watkeys, 2017). In the dyke example from the Isle of Skye, Scotland (Kavanagh et al., 2018a), the magma ropes appear as part of the chilled margins of a basaltic dyke, in direct contact with the host rock, a dolerite sill. Liss et al. (2002) found magma ropes in solidified strained vesicles in the upper margin of the Whin Sill exposed at Harkess Rock, Bamburgh, N. England. In both scenarios there was space for the semi-solid ductile magma to be deformed by shear from the surrounding flowing magma and thus be dragged in the direction of flow. These processes are like those forming ropey pahoehoe lava flows on the earth's surface (Fink and Fletcher, 1978).

In contrast to the macro-structures, micro-structures and fabrics can help to identify finer scale emplacement and solidification processes. Microstructures include crystal preferred orientations, vesicle shapes and orientations and magnetic anisotropy.

The statistical orientation of crystal orientation in rocks can be indicators of a range of processes, and is done by either studying the orientation of the grain shape (SPO), or the orientation of crystal lattices (LPO) or a combination of both (Figure 2.3A; Benn and Allard, 1989; Higgins, 2006; Roni et al., 2014; Burchardt et al., 2019). In magmas, these processes may be related to magma flow (e.g. Shelley, 1985) or compaction of a crystal pile (e.g. Holness et al., 2017b). For magma flow, shear within the magma reorients the crystals with

the long axis becoming sub-parallel to the flow axis, however this is dependent on both magma rheology and the amount and direction of strain within the magma. Many studies have used SPO and LPO to understand magma flow, in dykes (e.g. Shelley, 1985; Hastie et al., 2011), sills (Hoyer and Watkeys, 2017), and laccoliths (Burchardt et al., 2019).

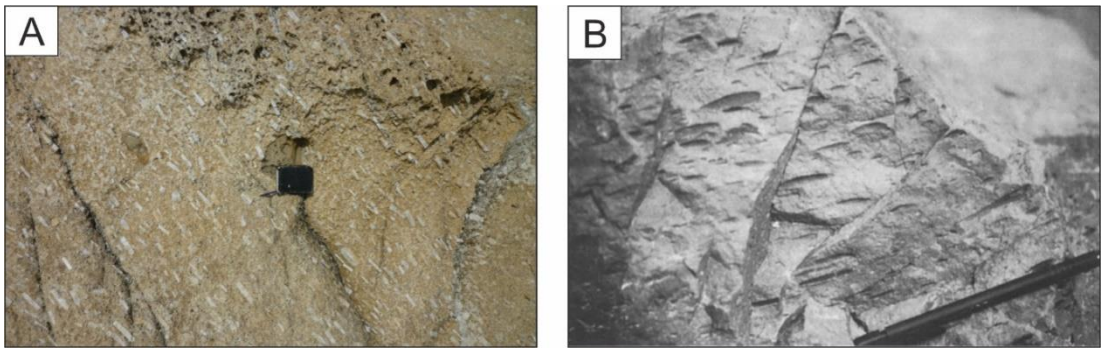

Figure 2.3 *Micro-scale magma flow indicators which aid in identification of magma flow directions; A) alignment of sanidine megacrysts in a porphyry in the San Martino, laccolith, Elba Island, Italy (Roni et al., 2014) (notebook for scale), and B) subhorizontal stretched vesicles within a dyke from the Troodos Ophiolite, Cyprus (Varga et al., 1998) (pen for scale).*

Crystal orientations have not only been used to infer flow directions, but they can also be used to determine the style of flow, e.g. laminar or turbulent. In sills of the Loch Scridain Sill Complex, Isle of Mull, Holness and Humphries (2003) characterised different flow regimes to have different orientations of crystal fabrics. In regions <3.5 m, where chilled margins were still present, aligned tabular crystals suggest areas of a more laminar flow regime, whereas in thicker sections, >3.5 m, where chilled margins had been eroded away, randomly oriented tabular crystals possibly suggest more of a turbulent flow regime. Knight and Walker (1988) note that flow becomes less turbulent with increased distance from the source, supporting the findings of Holness and Humphries (2003) for thinner parts of the intrusion. However, Holness and Humphries (2003) also identified that flow becomes localized and focussed through conduits which erode the chilled margins and surrounding host rock, as such cause evolution of the flow regime and potentially the development of more turbulent flow.

Vesicles are bubbles within crystalline rock that are formed by the exsolution of volatiles during cooling and decompression of a magma. Vesiculation occurs as the magma reaches shallow depths within the crust (Lejeune et al., 1999) and can play a key role in magma ascent and subsequently volcanic eruptions. When bubbles are small they remain rigid due to the capillary number and increase magma viscosity (discussed further in section 2.5.1) (Llewellin et al., 2002b). However, as the bubbles grow they reach a size where they can be deformed

by shear in the magma and act to lower viscosity (Manga et al., 1998). As magma cools, bubbles (particularly larger ones, perhaps formed by coalescence) may become stretched and elongated by shear (Coward, 1980), generally parallel or slightly oblique to the flow direction (Figure 2.3B; Varga et al., 1998; Liss et al., 2002). As the surrounding magma solidifies the final vesicle morphologies are preserved and, in some circumstances, can be used as flow indicators.

2.4 Rock magnetism and magnetic anisotropy

Magnetic fabrics are also commonly used for studying magma emplacement and magma flow using a range of techniques, the most common of which is anisotropy of magnetic susceptibility (AMS) (e.g. Knight and Walker, 1988).

Rock magnetism and magnetic anisotropy is the study of minerals and mineral orientations preserved within rocks, with applications in sedimentology, palaeontology, tectonics and volcanology to understand rock ages, palaeo-flow directions or formational processes that have produced the observed fabrics (e.g. Blundell, 1957; Tauxe, 2010). Within intrusive systems, rock magnetic techniques are often used to develop emplacement models for dykes, sills and laccoliths, determine magma flow trajectories and infer magma source locations (e.g. Knight and Walker, 1988; Staudigel et al., 1992; Varga et al., 1998; Herrero-Bervera et al., 2001; Poland et al., 2004; Roni et al., 2014), along with post-emplacement processes such as cooling contraction, alteration and or tectonic overprinting (e.g. Borradaile and Henry, 1997; Hrouda et al., 2015; Martin et al., 2019).

In this thesis, two magnetic fabrics are investigated, to understand syn- and post-emplacement processes associated with the emplacement of sheet intrusions. These fabrics are anisotropy of magnetic susceptibility (AMS) and anisotropy of anhysteretic remanent magnetisation (AARM), with both fabrics regularly applied to understanding intrusion processes (e.g. Raposo et al., 2007; Chadima et al., 2009; Selkin et al., 2014).

2.4.1. Rock magnetic properties and magnetic mineralogy

2.4.1.1 *Magnetic mineralogy*

A key step in any rock magnetism study is accurate identification of the magnetic carriers that contribute to the observed magnetic fabrics. All minerals exhibit some form of magnetic behaviour when under the influence of a magnetic field, either: diamagnetic, paramagnetic or ferromagnetic (Butler, 1992).

Diamagnetism is the response of an atom with a full outer shell of electrons to an induced magnetic field. The field causes the electrons in the outermost shell to align in the opposite direction to the field, giving rise to a relatively small negative magnetic susceptibility that is not dependant on temperature (Butler, 1992). When the induced field is removed, the magnetization of the material reverts to zero. Some examples of diamagnetic materials include quartz and calcite (Tauxe, 2010).

Materials that exhibit a paramagnetic behaviour have an odd number of electrons in the outer most shell that spin in random orientations in the absence of a magnetic field (Tauxe, 2010). When all the atomic magnetic moments of a material are combined, the resulting magnetisation is zero. If a magnetic field is induced on the material, the spin direction of the electrons in the outer shells align with the induced field (Butler, 1992). Removing the field allows the electrons in the outer shell to randomly orbit the atom again, thus returning the magnetisation to zero. The magnetic susceptibility of paramagnetic materials is positive and small but at least an order of magnitude greater than diamagnetic minerals (Butler, 1992), and is dependent on the strength of the field and the temperature. Examples of paramagnetic minerals include: biotite and fayalite (Butler, 1992; Tauxe, 2010).

Some materials possess a magnetic field when there is no external field present; this is known as remanent magnetisation or ferromagnetism (Tauxe, 2010). The remanent field is caused by strong coupling between dipoles of adjacent atoms and results in magnetisation orders of magnitude greater than paramagnetic materials (Butler, 1992). Like paramagnetism, ferromagnetism is temperature dependant in that a material exhibiting ferromagnetism only behaves in such a way below the Curie temperature (T_C). Above the Curie temperature, the material exhibits a paramagnetic behaviour due to expansion of the crystal lattice which results in decoupling of electrons between adjacent atoms (Tauxe, 2010). Each ferromagnetic phase has a maximum possible magnetisation relating to its temperature, known as the saturation magnetisation (Ms). This decreases as temperature increases reaching zero at the Curie temperature (Butler, 1992). The most common ferromagnetic minerals are magnetite, titanomagnetite and haematite (Table 2.1).

2.4.1.2 *Identifying the properties of magnetic minerals*

To identify the magnetic phases giving rise to observed magnetic fabrics, several properties are investigated, including but not limited to: coercivity, saturation magnetisation and Curie temperature. Coercivity is the ability of a magnetic mineral to resist an external magnetic field being applied to it (Tauxe, 2010). It is equivalent to the field strength needed to fully

demagnetise it or change the direction of its magnetisation, e.g. up to 50 mT for magnetite. Saturation magnetisation is the point at which a magnetic particle can no longer take an external field as all atomic moments have been aligned parallel to the field. To return the magnetisation to zero a field equal to the coercivity needs to be applied to the sample in the opposite direction. The values for coercivity and saturation magnetisation are easily identified for a sample using hysteresis experiments, using equipment such as a variable field translation balance (VFTB). See Table 2.1 for properties of common ferromagnetic minerals present in rocks.

Table 2.1: *Magnetic properties of a range of minerals often providing magnetic signals. *TM stands for titanomagnetite and the number (10 or 60) represents the percentage of iron replaced by titanium in the lattice. Adapted and expanded from Tauxe (2010).*

Magnetic Mineral	**Curie Temperature (˚C)**	**Coercivity**	**Saturation magnetisation ($Am^2 kg^{-1}$)**	**Reference**
Magnetite	[1] 580	[1] 20-50 mT	[2] 92	[1]Dunlop and Özdemir (1997), [2]O'Reilly (1984)
TM10*	500	-	-	Akimoto (1962)
TM60*	150	8 mT	24	Dunlop and Özdemir (1997)
Haematite	[1] 675	[2] Variable to 10's T	[1] 0.4	[1]O'Reilly (1984), [2]Banerjee (1971)
Maghemite	590-675	-	74	Dunlop and Özdemir (1997)
Pyrrhotite	[1] 270-325	[2] Variable to 100's mT	[3] 0.4-20	[1]Dekkers (1988), [2]O'Reilly (1984), [3]Worm et al. (1993)
Goethite	[1] 70-125	[2] Variable to 10's T	[1] Up to 1	[1]O'Reilly (1984), [2]Tauxe (2010)
Greigite	[1] 330	[1] 60-100 mT	[2] 25	[1]Roberts (1995), [2]Spender et al. (1972)

A VFTB measures the isothermal remanent magnetisation (IRM) acquisition, backfield curve, hysteresis loops, and thermomagnetic curves of a sample to characterise the properties of its magnetic carriers and help identify the mineral populations giving rise to the observed fabrics. It does this using masses of 150 mg of finely crushed rock powder loaded into a sample holder and covered with quartz wool. Isothermal remanent magnetization is where a field greater than the coercivity of a magnetic mineral is applied and the magnetic moments of the particles present flip to align more closely with the field direction, giving the sample a

remanence. This is undertaken by applying a magnetic field, removing the field and then measuring to see how well the sample takes the applied field, in steps of increasing field strength to +800 mT. Backfield measurements are made in a similar way to IRM acquisition but with an oppositely directed field in steps of up to -800 mT.

Hysteresis is where the field is swept from positive saturation to negative saturation and back again. It is measured during the application of a positively increasing field in one direction, then whilst it is being inverted and then again in the initial direction. Hysteresis curves are useful to help identify the saturation magnetization and coercivities of magnetic particles present in a sample.

The final experiment conducted using a VFTB is the measurement of the magnetic response of the minerals present during heating of the sample. During this experiment, a sample undergoes cyclic heating and cooling in a constant field of 240 mT. Measurement starts from 50 ˚C and continues whilst the temperature increases to 200 ˚C before cooling back to 50 ˚C. The heating and cooling cycle is then repeated multiple times, with increasing maximum temperature up to 700 ˚C (in 100 ˚C intervals) (see chapter 3 for example). These experiments allow the Curie temperatures of each of the magnetic carriers to be determined, which are specific to mineral composition. Data is then analysed using the RockMagAnalyzer 1.0 software (Leonhardt, 2006).

Two other contrasting, yet supporting, methods for determining Curie Temperatures are high temperature susceptibility and three component thermal demagnetization. High temperature susceptibility experiments aid in the identification of minerals that contribute to AMS fabrics (see section 2.4.2). In these experiments, the magnetic susceptibility of a sample is measured during the heating and cooling of the sample, up to a pre-specified temperature. In this thesis, these experiments are performed using an MFK-1A Kappabridge from AGICO (Advanced Geoscience Instruments Company), on crushed rock powder samples. The data is analysed using AGICO's Cureval8 software (Chadima and Hrouda, 2012).

Three-component thermal demagnetisation experiments use a modified version of the Lowrie (1990) method and are used to identify the unblocking temperatures of ferromagnetic minerals that give rise to AARM fabrics. Unblocking temperatures are the temperature at which the coercive force of a grain is overcome by thermal fluctuations resulting in its demagnetisation. In these experiments, three different strength fields are applied to a specimen in orthogonal directions, after AMS and AARM analyses are performed on the specimen, in decreasing magnitudes and orientations. The field strengths used in this

thesis are: x-axis of 1.5 T, y-axis of 0.4 T and z-axis of 0.02 T. These were chosen to target specific phases with coercivities within the ranges of each axis, i.e. pyrrhotite for the y-axis and titanomagnetites for the z-axis (see Table 2.1 for coercivities). Each specimen is then heated and cooled in steps of between 20 and 50 ˚C, to a maximum of 620 ˚C, which correspond with temperatures where it is believed that the magnetic remanence changes the fastest, i.e. just below the Curie temperatures of target minerals. Between each heating and cooling cycle, the magnetization of the sample is measured using an AGICO JR-6A spinner magnetometer with the output data separated by axis to determine the strength of each phase remaining at that temperature step. When the signal for an axis reduces to a magnetisation of 0 T, the remanence carrying phases in that field strength range have been demagnetised. The temperature at which this occurred is the unblocking temperature, which provides an indicator of the remanence carrying phases present. For example, if the y-axis with a strength of 0.4 T fully demagnetises by 350 ˚C, this indicates that the remanence carrying phases with coercivities between 0.02 and 0.4 T had unblocking temperatures below this temperature, e.g. pyrrhotite (see chapter 4).

2.4.2. Anisotropy of magnetic susceptibility

Magnetic susceptibility (MS) is the study of how susceptible a sample is to gaining an induced magnetic field (Knight and Walker, 1988; Raposo and Ernesto, 1995), which when the field is removed the sample returns to its original state. AMS is then the directional dependant response of the sample to the induced field. MS and AMS are affected by the strength, size, domain state and orientation of all magnetic minerals (dia-, para-, and ferro-magnetic) present within the sample (Khan, 1962). When present, ferromagnetic phases often dominate the AMS signals (Hargraves et al., 1991), however, in some situations paramagnetic phases may dominate the signal, when they occur in greater proportions than ferromagnetic phases. Magnetite is a common ferromagnetic mineral present in igneous rocks and is often the primary constituent giving rise to AMS fabrics (e.g. Hargraves et al., 1991).

Magnetic susceptibility (*K*) is defined as:

$$K = \frac{M_i}{H} \tag{2.1}$$

where M_i is the degree of induced magnetization and *H* is the strength of the magnetic field (Tauxe, 2010). AMS is measured using a Kappabridge (AGICO's MFK1-A for chapters 3 and 4, or KLY-4S for chapter 5), whereby a core or cube shaped sample is loaded into a sample holder and a magnetic field is induced in multiple orientations. Sample holders can either be fixed orientation, which means the sample needs manually rotating in up to 6 orientations,

or it can be an automatically rotated using either a single axis rotator, or a 3D rotator. In this thesis, an applied field of 200 A m^{-1} and a frequency of 967 Hz are the settings used for the MFK1-A Kappabridge and 200 A m^{-1} and a frequency of 875 Hz for the KLY-4S Kappabridge. After measuring multiple sub-specimens (>5), a normalized six rank ellipsoid tensor can be calculated.

The AMS ellipsoid is characterised by a second order ellipsoid tensor (Khan, 1962), with three principle eigenvectors: K_1, K_2 *and* K_3, where K_1 is the longest axis, K_2 is the intermediate axis and K_3 is the shortest axis (Knight and Walker, 1988). The ratio between the magnitudes of the tensor axes produces a range of ellipsoid properties: mean susceptibility (K_m), lineation (L), foliation (F), degree of anisotropy (P_j) and shape parameter (T). Magnetic lineation is the ratio between the magnitudes of K_1 and K_2 (Table 2.2). Magnetic foliation is ratio between the K_2 and K_3 axes. The degree of anisotropy is ratio between all 3 axes and with the shape parameter being the shape of the ellipsoid calculated from the natural logarithms of the ellipsoid axes (Table 2.2; and Jelínek, 1981). Four ellipsoid shapes exist which are exhibited by the AMS ellipsoid tensor; spherical ($K_1 = K_2 = K_3$), prolate ($K_1 > K_2 = K_3$), oblate ($K_1 = K_2 > K_3$) and triaxial ($K_1 > K_2 > K_3$) (Tauxe, 2010). The shapes of ellipsoid tensors are regularly used to interpret magmatic fabrics (e.g. Knight and Walker, 1988; Tauxe et al., 1998; Poland et al., 2004; Soriano et al., 2008). Prolate ellipsoids are commonly referred to as magnetic lineation, with the long axis of the ellipsoid being a similar orientation to the long axis of elongate crystals in magmatic rocks (Geoffroy et al., 2002). Comparably, oblate ellipsoids give rise to magnetic foliation which is like the planar arrangement of tabular phenocrysts. It should be noted that both magnetic lineation and magnetic foliation can be determined from the same AMS ellipsoid tensor.

Table 2.2: *Anisotropy parameters used by Anisoft software and can be found in Jelínek (1981). K_1, K_2 and K_3 are principal susceptibility axes, with η_1, η_2 and η_3 being their natural logarithms with $\eta = (\eta_1 + \eta_2 + \eta_3)/3$.*

Parameter		Solution
Mean Susceptibility	K_m	$(K_1+K_2+K_3)/3$
Lineation	L	K_1/K_2
Foliation	F	K_2/K_3
Corrected degree of anisotropy	P_j	$exp\sqrt{2[(\eta_1-\eta)^2+(\eta_2-\eta)^2+(\eta_3-\eta)^2]}$
Shape parameter	T	$(2\eta_2-\eta_1-\eta_3) / (\eta_1-\eta_3)$

2.4.3. Anisotropy for anhysteretic remanent magnetisation

Whilst AMS is a study of all minerals within a sample, AARM focusses on the statistical orientation of remanence bearing minerals, (i.e. single-domain and vortex-state sized grains) and the ability of these minerals to retain an imparted anhysteretic remanent magnetization in specific directions (McCabe et al., 1985; Jackson, 1991). The minerals that give rise to the AARM signals commonly occur as silicate mineral hosted inclusions of magnetite that are aligned along crystal lattices (Cheadle and Gee, 2017). Like AMS, AARM utilizes a second order ellipsoid tensor, with the same ellipsoid descriptions and orientations, however mean remanence is defined as K_{rem} and is calculated by averaging the axis magnitudes of the AARM ellipsoid.

An anhysteretic remanent magnetisation (ARM) is imparted in multiple stages, using a combination of an alternating field demagnetizer and a pulse magnetizer with subsequent measurement of the sample's magnetisation. In this thesis, an LDA5/PAM1 alternating-field demagnetizer and pulse magnetizer from AGICO impart the field, whilst a JR6-A spinner magnetometer measures the magnetisation. Initially, the natural remanent magnetisation is measured before the sample is demagnetised in a tumbling alternating current (AC) field, and subsequently remagnetised to find the saturation magnetisation using an applied direct current (DC) bias field. Once the saturation magnetisation has been reached, a DC bias field below the saturation magnetisation is chosen and an ARM is imparted in multiple directions (3, 6, 12 or 15) with measurement of the sample's magnetisation using AGICO's Rema6W software (Chadima et al., 2018b), occurring between each step. After all measurements have been made for a sample, the AARM ellipsoid is calculated using AGICO's Anisoft software (Chadima et al., 2018a).

2.4.4. Magnetic anisotropy for understanding magma intrusion processes

When the magnitudes, shapes and orientations of measured ellipsoid tenors are combined with field and petrological observations, the processes that have occurred both syn- and post emplacement of solidified magma bodies can be inferred (e.g. Varga et al., 1998; Liss et al., 2002; Chadima et al., 2009; Hrouda et al., 2015). AMS has commonly been used to understand the emplacement processes of dykes (e.g. Knight and Walker, 1988; Staudigel et al., 1992; Tauxe et al., 1998; Roni et al., 2014; Porreca et al., 2015), sills (e.g. Gil et al., 2002; Hrouda et al., 2015; Airoldi et al., 2016; Martin et al., 2019) and laccoliths (Mattsson et al., 2018), with the majority of the fabrics interpreted to indicate flow directions and in some circumstances even the sense of flow. AARM has been used multiple times to understand the processes occurring during dyke emplacement (e.g. Chadima et al., 2009; Silva et al., 2010;

Soriano et al., 2016), however the technique has only been used on a handful of occasions to study other types of intrusions, i.e. sills (Hrouda et al., 2015; Martin et al., 2019) or larger bodies such as the Stillwater Igneous Complex, MT, USA (Selkin et al., 2014). AARM is often less frequently used due to a combination of availability and access to the equipment needed and the long-time frame of data collection (~10 sub-specimens per day).

When the AMS K_1 axis is aligned with the long axis of the magnetic crystals (and phenocrysts when present) or with the AARM K_1 axis, and these are parallel to the margins of an intrusion (Figure 2.4A), this is referred to as a normal fabric (Figure 2.4B) (Rochette et al., 1992; Ferré, 2002; Chadima et al., 2009). In this case, the K_3 axis is also parallel to the crystal short axis and perpendicular to the intrusion plane, as such the resultant fabric can be used to infer the direction of magma flow (Figure 2.4B); i.e. the magnetic lineation and foliation are parallel to the dyke plane. Inverse fabrics occur when the AMS K_1 and K_3 axes are inverted with respect to crystal long axes, or AARM K_1 axis and K_3 axes and intrusion margins (Figure 2.4C). Here, the origin of the inverse fabrics are often inferred to originate from SD crystals dominating the magnetic fabrics (Potter and Stephenson, 1988; Rochette et al., 1992; Ferré, 2002). Anomalous fabrics are characterised by AMS and AARM ellipsoids which are oblique to each other, i.e. ellipsoid axes exhibit neither normal or inverse type fabrics (Soriano et al., 2016). Multiple origins exist for these types of fabrics, which stem from two different phenomena, either grain-scale variations or processes which resulted in the rotation of magnetic particles. Examples of grain-scale variations that lead to anomalous fabrics, include, combinations of SD and MD particles the give rise to the fabrics (Potter and Stephenson, 1988; Rochette et al., 1991) or alteration and growth of new magnetic phases (Rochette et al., 1991). Examples of processes which resulted in the rotation of magnetic particles, include; syn- or post-emplacement shear along the fracture (Dragoni et al., 1997; Clemente et al., 2007), cooling contraction and the formation of columnar jointing (Hrouda et al., 2015) or evolution of multiple flow regimes occurring within the same unit (Martin et al., 2019).

Textural anisotropy can also influence the orientation and shape of magnetic fabrics, as the distribution of adjacent magnetic minerals within a sample can result in a range of observed ellipsoid orientations (Stephenson, 1994; Cañón-Tapia et al., 1996). This is due to a phenomenon called magnetic interaction which occurs at the inter-grain scale and is where the adjacent particles within a sample interact with each other depending on their proximity. Homogenously distributed particles in planes display oblate fabrics with minimum susceptibility axes perpendicular the textural plane. Whereas particles in adjacent planes

that are closer together than those in the same plane exhibit AMS fabrics with long axis perpendicular to the textural anisotropy.

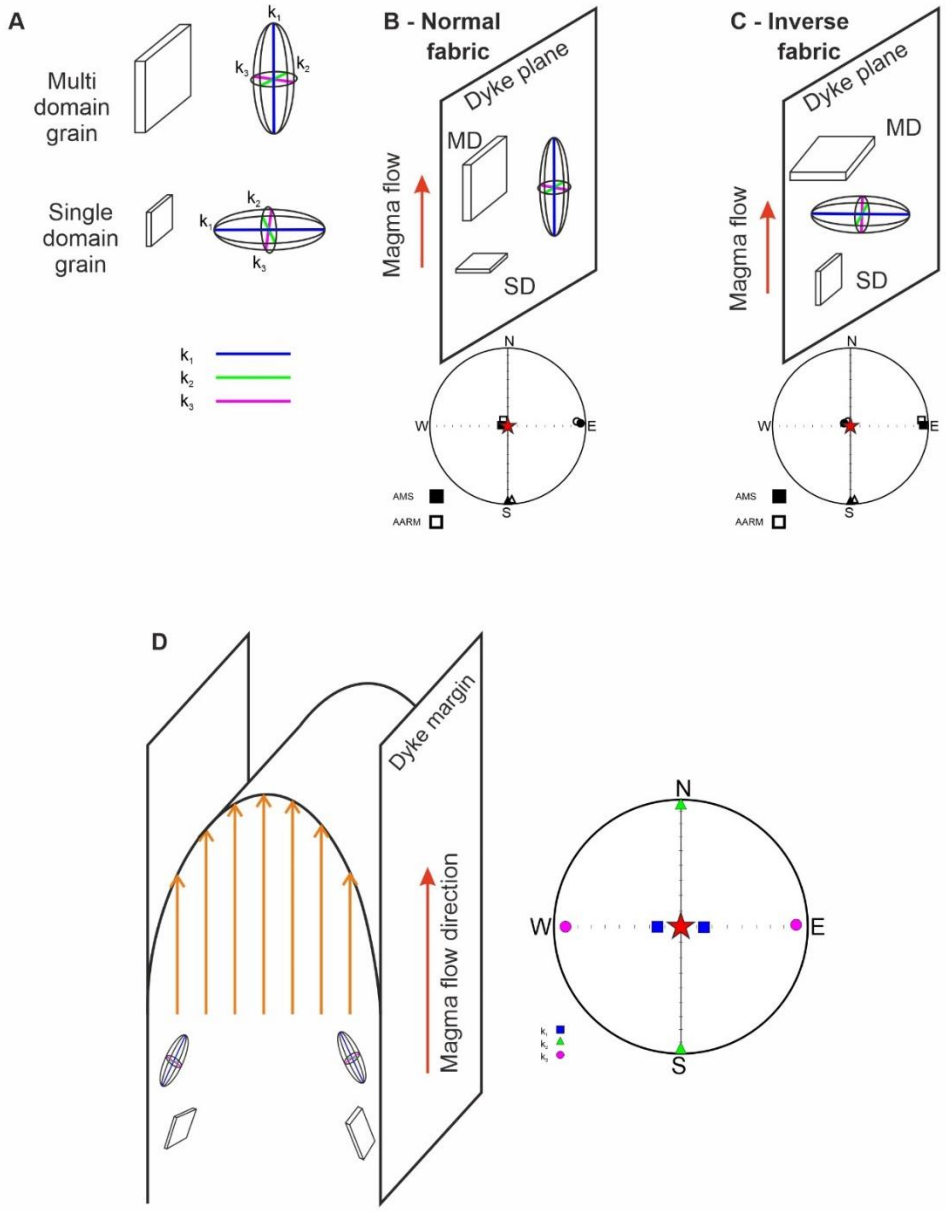

Figure 2.4 *Anisotropy of magnetic susceptibility (AMS) and anisotropy of anhysteretic remanent magnetisation (AARM) fabrics relative to crystal axes and intrusion orientations. A) AMS ellipsoid axis orientations and their relationship to the orientation of multidomain (MD) and single-domain crystals (SD). B) An example of a normal fabric where AMS K_1 and K_2 axes are in the plane of the dyke parallel to the long axes of MD crystals and K_3 is perpendicular to the dyke plane. C) An example of inverse fabrics where the K_1 and K_3 ellipsoid axes orientations are inverted, i.e. K_1 is perpendicular to the dyke plane. D) Using AMS fabrics to understand flow direction where the ellipsoids are imbricated with respect to the dyke plane, shown by the blue squares on the equal area plot being slightly offset from the dyke plane.*

When AMS fabrics are inclined with respect to intrusion margins, it suggests that the minerals that give rise to the magnetic fabrics have been inclined or reoriented by variations in simple shear conditions imparted by the static intrusion margin (Figure 2.4D) (e.g. Knight and Walker, 1988; Rochette et al., 1992). When this occurs, the orientation of magnetic lineation and foliation can be inferred not only as the flow direction but also the sense of flow during the initial magma emplacement (Geoffroy et al., 2002; Chadima et al., 2009).

2.5 Laboratory modelling

This section provides an outline of the properties of magmas, the importance of scaling and different types of laboratory models that have been designed to study intrusion emplacement and magma flow. There is a sub-section on the importance of understanding material properties and scaling laboratory models to nature. Next are sub-sections on laboratory models that investigate magma emplacement under either the hydraulic fracture or viscous indenter styles of intrusion. Subsequently there is a sub-section on how lava domes and flows have been studied through laboratory modelling, as they behave in similar ways to horizontal magma intrusions, then there is a section on how magma flow fabrics have been studied. The backgrounds on magma rheology (section 2.5.1), and lava domes and flows (section 2.5.6) are taken from Kavanagh et al. (2018b) and were written by myself, the full published version can be found in Appendix A.

2.5.1 Magma rheology

Magma is one of the principal components of all volcanic systems, and how it behaves as it flows and fragments is key to tackling perhaps all processes in volcanology. Therefore, this section begins with a detailed account of modelling magma rheology.

Magma is a multiphase fluid, comprising a melt phase with variable proportions of bubbles and crystals. The viscosity (η) of pure melt is considered Newtonian (Figure 2.5), with a linear relationship between shear stress (σ) and strain rate ($\dot{\gamma}$) (Lejeune and Richet, 1995; Ishibashi, 2009):

$$\eta = \frac{\sigma}{\dot{\gamma}}. \tag{2.2}$$

Due to its multiphase nature, magma is considered non-Newtonian. Several types of non-Newtonian rheology have been applied to model the behaviour of magmas and lavas based on field observations (Figure 2.5). A Bingham fluid has to overcome a yield stress before it can begin to flow (Hulme, 1974):

$$\eta = \frac{\sigma - \sigma_0}{\dot{\gamma}} \quad (2.3)$$

where σ_0 is the initial shear stress required to cause the onset of flow when $\dot{\gamma}$ = 0. Once the yield stress has been over- come, the fluid has a constant viscosity. More recently, the Herschel–Bulkley model (Herschel and Bulkley, 1926) has been applied to the behaviour of magmas due to its versatility in allowing for the modelling of a spectrum of magma behaviours (Llewellin et al., 2002b; Mueller et al., 2011):

$$\sigma = \sigma_0 + K\dot{\gamma}n \quad (2.4)$$

where σ_0 is yield stress when there is no flow, K is the consistency (η when $\dot{\gamma}$ = 1), and n is the degree of non-Newtonian behaviour (where n = 1 is Newtonian, n < 1 is shear thinning, and n > 1 is shear thickening). Viscosity is a key parameter that is considered in several of the important dimensionless numbers used in scaling experiments in volcanology, such as the Reynolds number, Rayleigh number, and Peclet number.

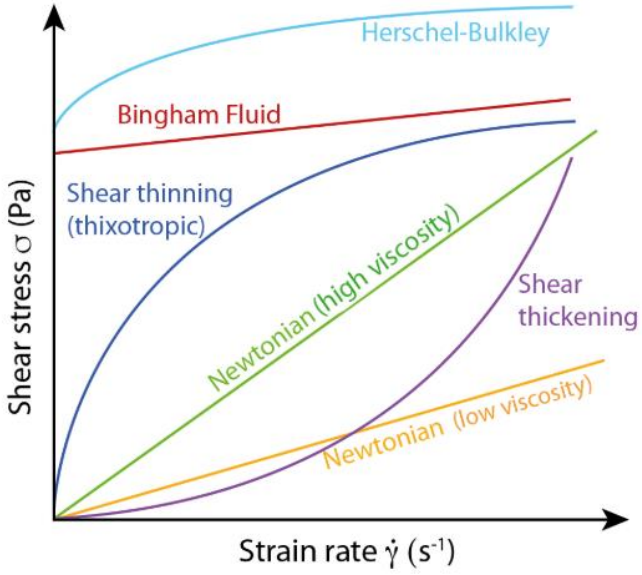

Figure 2.5 *Flow curves of different fluid rheologies, depending on shear stress and strain rate (Taken from Kavanagh et al., 2018b).*

Depending on the application and level of complexity, a variety of analogue materials have been used to model magma (see Table 2.3 for a summary). An important online resource administered by Alison Rust (University of Bristol) catalogues a range of analogue materials that have been used in volcanology, describing their material properties, applications, and limitations (https://sites.google.com/ site/volcanologyanalogues/home). Many models use a melt-only magma analogue for simplicity, or in more complex models two-phase suspensions

(bubbles in liquid, or crystals in liquid) and rarely three-phase (bubbles and crystals in a liquid). As such, the spectrum of rheology that has been considered in magma analogue models is broad and includes the use of Newtonian fluids, Bingham fluids, or Herschel–Bulkley.

Table 2.3: *Properties of analogue materials used to model magmas and lavas for rheology and processes. *Material not currently used in analogue modelling of volcanic processes however displays properties that may lead to its future use.*

System Component	Material	Key Properties		Example reference
		Rheology or Mechanical Behaviour	e.g. Viscosity, density, strength	
Magma or Lava analogues				
Syrups	Corn syrup	Newtonian	Density[a] of 1427-1431 kg m^{-3}, viscosity[ab] of 180-515 Pa s at 22 °C	[a]Schellart (2011) [b]Rust and Manga (2002b)
	Glucose syrup	T-dependant Newtonian	Density of 1427-1431 kg m^{-3}, viscosity of 454.7 Pa s at 20 °C	Schellart (2011)
	Golden Syrup	Newtonian	Density of 1386 kg m^{-3}, viscosity of 50-78 Pa s at 20 °C	Castruccio et al. (2010)
	Honey	Newtonian	Density[a] of 1429-1431 kg m^{-3}, viscosity[b] of 200 Pa s at 22 °C	[a]Schellart (2011) [b]Mathieu et al. (2008)
Oils	Glycerine	Newtonian	Density of 1260 kg m^{-3}, viscosity of 0.77 Pa s	Huppert and Hallworth (2007)
	Silicon oil	Newtonian	Density[a] of 1870 kg m^{-3}, viscosity[b] of 41.32 Pa s at 25 °C	[a]Del Gaudio (2014) [b]Mueller et al. (2010)
	Vegetable oil (Vegetaline)	Newtonian	Density of 890 kg m^{-3}, viscosity of 2 x 10^{-2} Pa s at 50 °C	Galland et al. (2006)
Waxes	Paraffin	T-dependant Newtonian	Density[a] of 600 kg m^{-3}, viscosity[b] of 10 Pa s at 52 °C	[a]Karlstrom and Manga (2006), [b]Rossetti et al. (1999)
	Polyethylene glycol (PEG)	T-dependant Newtonian	Density of 1126 kg m^{-3}, viscosity of 0.18 Pa s at 21 °C	Griffiths and Fink (1997)
Other	Air	Gas		
	Water	Newtonian	Density of 998.2 kg m^{-3}, viscosity of 0.01 cm s^{-1} at 20 °C	Huppert and Hallworth (2007)
	RTV silicone	Newtonian	When freshly exposed to air 25 Pa s solidifying after c. 5 hours	Gressier et al. (2010)

	Silicone putty	Viscoelastic/ Newtonian	Density of 1120-1140 kg m^{-3}. viscosities of 2-2.57 x 10^4 Pa s at 24 °C	Ramberg (1970)
	Gum rosin with 21.8% acetone	Newtonian	Density of 1000 kg m^{-3}, viscosity of 1.07 Pa s at room temperature	Lane et al. (2001)
	Hair gel	Shear thinning	27 Pa s at room temperature	Castruccio et al. (2014)
	Shaving foam	Viscoelastic	172 Pa s at room temperature	Bagdassarov and Pinkerton (2004)
	Collophony and ethyl phthalate mixtures	Viscoelastic	Densities of 1000 kg m^{-3}, viscosity of 5.73 x 10^6 Pa s at 22 °C. Collophony mixtures are almost Newtonian at low stress	Ramberg (1970)
	Plaster of Paris and water suspensions (2.2 to 2.6 ratio)	Shear thinning	Viscosity of 0.8 - 6.2 Pa s shear rate dependant	Závada et al. (2009)
Host rock analogues				
Gels	Gelatine (pig-skin type)	Viscoelastic	For 2.5 wt% at 10 °C: viscoelastic at strain rates <0.147 s^{-1}; however highly variable with different concentrations and temperatures. At strain rate of 10^{-2} s^{-1} viscosity is ~50 Pa s.	Di Giuseppe et al. (2009)
	Laponite powder (synthetic clay)*	Viscoelastic	Commonly used as a rheology-modifier with variable behaviour depending on concentration.	Ruzicka and Zaccarelli (2011)
	Carbopol*	Visco-elasto-plastic	Highly variable depending on concentration, shear stress and strain rate	Di Guiseppe et al. (2015)
Granular	Silica flour (spheres and crystals)	Brittle	When compacted: *crystals* have density of 1.33 g cm^{-3} ± 0.2%, cohesion of 288 Pa ± 26 with angle of internal friction 40°. *spheres* have density of 1.56 g cm^{-3} ± 0.18%, cohesion of 288 Pa ± 26 with angle of internal friction ~24°.	Galland et al. (2006)
	Diatomite powder	Frictional	When compacted: density of 400 kg m^{-3}, cohesion of 300 Pa at normal stresses 50-300 Pa.	Gressier et al. (2010)
	Sand	Shear	Cohesion of 0 - 10 Pa, angle of internal friction of 30°	Mathieu et al. (2008)
	Ignimbrite powder (Grande Nape Ignimbrite, Mont Dore volcano, France)	Shear	Cohesion of 100 - 230 Pa, angle of internal friction of 38°	Mathieu et al. (2008)

Other	Modelling clay	Plastic	At density of 1710 kg m^{-3}, yield strength 4.1 x 10^4 Pa s. Above yield strength viscosities range from 0.5-7.4 x 10^7 Pa s	Ramberg (1970)
	Painter's putty	Plastic	Densities of 1800-1900 kg m^{-3}, yield strength of 3 x 10^3 Pa s. Above yield stress viscosities from 1 x 10^4 to 10^7 Pa s	Ramberg (1970)
Particle analogues				
	Sand and gravel		Without mud – bulk density of 1710 ± 119 kg m^{-3} and internal angle of friction 39° With mud – bulk density of 1650 ± 107 kg m^{-3} and internal angle of friction 39°	Iverson et al. (2010)
	Spherical glass beads		Density of 2500 kg m^{-3}	Mueller et al. (2016)

2.5.1.1 *Two-phase suspensions: particle suspensions*

Particulate suspensions are ubiquitous across the volcanic system; from crystals in magma, where variations in crystal content mostly originate from changes in temperature, to ash particles within an eruptive plume, where the particle size and concentration within a volcanic plume or pyroclastic density current is related to the type of eruption. For the purposes of numerical and laboratory modelling, particle distributions are simplified by a single well-defined particle size or a small number of particles sizes used to replicate natural systems (e.g. Figure 2.6A-C). However, both numerical and laboratory studies have shown that particulate concentration has a first-order control on eruptive behaviour. The Einstein–Roscoe equation has been used in magma modelling to describe how the increase in crystal content affects the bulk viscosity, where an increase in the particle volume fraction (φ_p) causes an increase in bulk magma viscosity. Low φ_p magmas behave as Newtonian fluids whereas high φ_p mag- mas (φ_p = >30−40 %) behave as non-Newtonian fluids (e.g. Lejeune and Richet, 1995; Mueller et al., 2011). Bimodal crystal size populations act to reduce melt viscosity, with higher viscosities observed in unimodal crystal size suspensions compared with lower viscosities in bimodal crystal size suspensions (Castruccio et al., 2010).

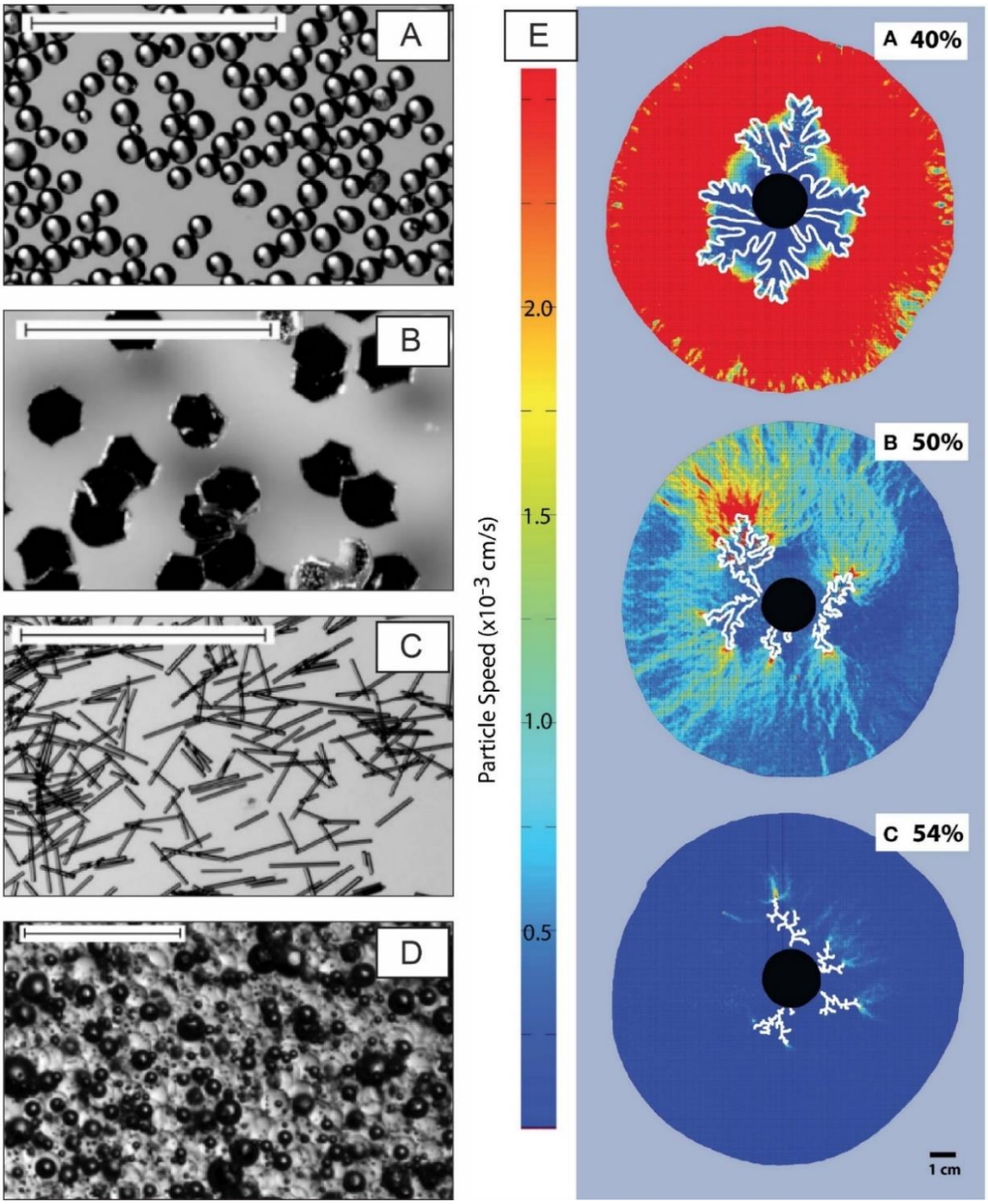

Figure 2.6 *Examples of experiments investigating magma rheology using analogue materials in laboratory experiments. (A) Spherical glass beads, (B) oblate art glitter, and (C) prolate glass fibres in silicone oil (scale bars 1 mm; Mueller et al., 2011); (D) three-phase fluid in which bubbles (black spheres) and spherical glass beads (light translucent particles) are suspended in golden syrup (scale bar 500 µm; Truby et al., 2015). These multi-phase fluids are measured using viscometers or rheometers with the aim of understanding the behaviour of natural magmas that have different crystal and bubble populations. Fluids with lower crystal and bubble populations behave as more Newtonian fluids, whereas higher crystal populations lead to non-Newtonian behaviour fluids. (E) Bubble injection experiments using a small-gap parallel-plate geometry to study the development of permeable pathways in a particle-rich suspension. Particle image velocimetry has been used to measure particle speed in three experiments with different crystal fraction (Oppenheimer et al., 2015).*

2.5.1.2 *Two-phase suspensions: bubble suspensions*

The effect that bubbles have on magma viscosity depends on bubble shape, size, and ability to deform under stress. In steady flow regimes, where stress and shear are constant, the bubbles reach an equilibrium deformation that can be measured by the dimensionless capillary number *Ca*, which describes the relative effects of viscous forces and surface tension acting between a liquid and a gas (Manga and Loewenberg, 2001; Llewellin et al., 2002b):

$$Ca = \frac{\eta_0 r \dot{\gamma}}{\Gamma} \tag{2.5}$$

where η_0 is the fluid viscosity without bubbles, r is the undeformed bubble radius, $\dot{\gamma}$ is strain rate, and Γ is interface surface tension between the liquid and gas. Small capillary numbers are dominated by surface tension, meaning that bubbles reach their equilibrium deformation soon after there is a change in shear rate (Llewellin et al., 2002b, 2002a). This produces spherical bubbles that act to increase the viscosity of the suspension by creating an obstacle to flow. Large capillary numbers give rise to easily deformable and often elongate bubbles, acting as sites where shear localisation can occur due to a reduction in friction, and therefore the presence of large bubbles will have a reduced impact on bulk viscosity (Manga et al., 1998; Mader et al., 2013). In unsteady flow regimes, when there is a variable strain rate, the forces causing deformation and restoration of the bubble shape are not in equilibrium (Llewellin et al., 2002b). As such, the *Ca* number (Eq. 2.5) does not adequately describe the behaviour of the bubble, and so a dynamic capillary number *Cd* is defined:

$$Cd = \lambda \frac{\ddot{\gamma}}{\dot{\gamma}} \tag{2.6}$$

where $\ddot{\gamma}$ is the rate of change of the imposed deforming force and λ is the relaxation time, which is the time taken for the bubble to return to spherical under the action of surface tension (Mader et al., 2013):

$$\lambda = \frac{\eta_0 r}{\Gamma} \tag{2.7}$$

2.5.1.3 *Three-phase suspensions*

Three-phase suspensions are well suited to explaining the behaviour of magmas and bring us closer to understanding volcanic systems, but they also present several challenges associated with the additional complexity modelled. A three-phase suspension can be modelled assuming a bubble suspension base fluid with the particles suspended within (see Figure 2.6D; Truby et al., 2015):

$$\frac{\eta^*}{\eta_b} = 1 - \frac{\varphi_p}{\varphi_m} \tag{2.8}$$

where $\eta*$ is relative viscosity, η_b is bubble suspension viscosity, φ_p is particle volume fraction and φ_m is the maximum packing fraction. This simplifies the calculation of the three-phase rheology and assumes a low *Ca* (see Truby et al., 2015); however, if this is not appropriate then η_b may need to be substituted by either the high *Ca* or *Cd* viscosity equation. This new model can account for a crystal-bearing magma that has no bubble content at depth but vesiculates during ascent. It therefore marks a significant advancement in our understanding of magma behaviour through time and space and will be an important tool in future models to better constrain the impact of three-phase magma rheology on volcanic eruptions. Laboratory experiments of degassing crystal-rich magmas have shown using analogue materials that gas escape and the development of permeable pathways in particle-rich suspensions can be fracture-like or due to bubble formation, and that the migration pathways are controlled by particle fraction and the degree of particle packing (see Figure 2.6E; Oppenheimer et al., 2015).

2.5.2 Material properties

When undertaking the modelling of volcanic systems using analogue materials, there is a need to understand the properties of the systems being studied, so that better comparisons with natural systems can be made (Merle, 2015), which helps to improve the validity of the models being run. In laboratory modelling of volcanic plumbing systems this means that the properties of the materials being used as analogues to represent both the host rock and the intruding magma need to be classified so that they can be appropriately scaled and tailored to the natural system.

For host rocks, the analogue materials that have been used vary greatly from gels that represent elastic host rocks (e.g. pig-skin gelatine; Kavanagh et al., 2013), to granular materials that represent brittle host rocks (e.g. sand or flour; Galland et al., 2006). To model the intruding magma, both air and water have been used to study the emplacement of Newtonian fluids (e.g. Muller et al., 2001; Kavanagh et al., 2006). Other materials that have been used include syrups, vegetable oils and waxes which behave as temperature-dependant Newtonian or non-Newtonian fluids, allowing for solidification and rheological evolution to occur during emplacement (e.g. Galland et al., 2006; Kervyn et al., 2009; Taisne and Tait, 2011; Chanceaux and Menand, 2016). For a larger list see Table 2.4 taken from Kavanagh et al. (2018b).

Table 2.4: *Examples of different analogue materials and their combinations used to model different parts of the volcanic and magmatic system.*

Processes considered	Analogue Material Combinations			Example studies
	Magma or Lava	Host	Particulates	
Magma				
Two phase: melt + bubbles	Golden syrup with nitrogen	-	-	Llewellin et al. (2002b)
	Aerated golden syrup	-	-	Bagdassarov and Pinkerton (2004)
	Corn syrup with air	-	-	Rust and Manga (2002b, 2002a)
Two phase: melt + crystals	Silicone oil with silica-glass beads	-	-	Mueller et al. (2010), Cimarelli et al. (2011)
	Silicone oil with art glitter	-	-	Mueller et al. (2010)
	Silicone oil with silicon carbide grit	-	-	Mueller et al. (2010), Cimarelli et al. (2011)
	Silicone oil with wollastonite particles	-	-	Mueller et al. (2010), Cimarelli et al. (2011)
	Golden syrup with glass beads	-	-	Mueller et al. (2011)
	Golden syrup with art glitter	-	-	Mueller et al. (2011)
	Golden syrup with glass fibres	-	-	Mueller et al. (2011)
	Shell Motor oil with paraplex plastic	-	-	Bhattacharji and Smith (1964)
	Epoxy resin with glass beads/carbon fibres	-	-	Cimarelli et al. (2011)
Three phase: melt + bubbles + crystals	Golden syrup, with air and glass beads	-	-	Truby et al. (2015)
Intrusions				
Dykes	Air	Gelatine	-	Muller et al. (2001), Rivalta et al. (2005), Le Corvec et al. (2013)
	Water	Gelatine	-	Fiske and Jackson (1972), McLeod and Tait (1999), Taisne et al. (2011)
	Air and water	Gelatine	-	Menand and Tait (2001)
	Hydroxyethyl cellulose	Gelatine	-	McLeod and Tait (1999)
	Silicone oil	Gelatine	-	McLeod and Tait (1999),

				Watanabe et al. (2002)
	Golden syrup	Sand and plaster powder mix	-	Kervyn et al. (2009)
	Golden syrup	Gelatine with a sand and plaster mix load	-	Kervyn et al. (2009)
	Golden syrup	Silica flour	-	Abdelmalak et al. (2012)
	Honey	Sand	-	Mathieu et al. (2008)
	Golden syrup	Ignimbrite powder	-	Mathieu et al. (2008)
Sills	Water	Gelatine	-	Kavanagh et al. (2006, 2015)
	Vegetable oil (Vegetaline)	Silica flour	-	Galland et al. (2006; 2012)
	Vegetable oil (Vegetaline)	Gelatine	-	Daniels and Menand (2015), Chanceaux and Menand (2014, 2016)
	RTV silicone	Diatomite powder	-	Gressier et al. (2010)
Larger igneous bodies	Hot salty water injected into cold fresh water	-	-	Huppert et al. (1986)
	KNO_3, $NaNO_3$ and K_2CO_3	-	-	Huppert and Turner (1981), Turner et al. (1983)
	Glycerine-ethanol mix injected into molten PEG 600 wax	-	-	Weinberg and Leitch (1998)
	Hydroxethylcelluloase polymer and silicone oil	-	-	De Bremond d-Ars et al. (2001)
	Diluted glucose syrup and bubbles	-	-	Namiki et al. (2016)
	Water or hydroxyethyl cellulose or silicone oil	Gelatine	-	McLeod and Tait (1999)
	Sunflower oil/silicone oil and natrosol solution/glucose solution/ Na polytungstate	-	-	Saumur et al. (2016)
	Glycerine	Gelatine	-	Koyaguchi and Takada (1994)
	Grease	Gelatine	-	Pollard and Johnson (1973)
	Silicone putty	Sand layers	-	Roman-Berdiel et al. (1995)
	Silicone putty/$KMnO_4$ solutions	Modelling clay/painter's putty/Concrete	-	Ramberg (1970)

Lavas				
Lava lakes and hot conduit	Golden syrup mixed with water	-	-	Beckett et al. (2011)
	Water and air	-	-	Witham et al. (2006)
	Paraffin wax	-	-	Karlstrom and Manga (2006)
Lava domes	PEG wax into sucrose solution	-	-	Griffiths and Fink (1993), Fink and Bridges (1995)
	PEG wax with kaolin powder	-	-	Griffiths and Fink (1997), Lyman et al. (2004)
	Plaster of Paris seeded with magnetite particles	Sand	-	Závada et al. (2009)
Lava flows	PEG wax into sucrose solution	-	-	Hallworth et al. (1987), Fink and Griffiths (1990)
	Glucose syrup into sucrose solution	-	-	Stasiuk et al. (1993)
	PEG 600 wax	Peg 600 wax surface	-	Kerr (2001)
	Paraffin wax	-	-	Miyamoto et al. (2001), Nolan (2014)
	Golden syrup and sugar crystals	-	-	Castruccio et al. (2010)
	Hot water	PEG 1000 wax surface	-	Huppert and Sparks (1985)
	KNO_3, $NaNO_3$ and K_2CO_3	-	-	Turner et al. (1983)
	Viscous silicone	-	-	Gilbert and Merle (1987)
	Corn starch and water slurry	-	-	Goehring and Morris (2005), Goehring et al. (2006)
Granular flows				
Pyroclastic density currents	-	-	Particle bearing freshwater injected into saline water	Carey et al. (1988)
	-	-	Methanol-ethylene glycol injected into water	Woods and Bursik (1994)
Lahars	-	-	Sand and gravel with and without mud	Iverson et al. (2010)

Plumes				
Plumes	-	-	Particle bearing freshwater into saline water	Carey et al. (1988)
	-	-	Cold or warm water into cold flowing water	Ernst et al. (1994)
	-	-	Methanol-ethylene glycol injected into fresh water	Woods and Caulfield (1992)
Ash dispersal	-	-	Spherical glass beads in water with various additives	Koyaguchi et al. (2009)
Air fall	-	-	Spherical glass beads in water with various additives	Koyaguchi et al. (2009)
	-	-	Soda-lime glass beads suspended in hot air	Mueller et al. (2016)

The properties of these different materials have measured using a range of equipment from viscometers and rheometers that measure the viscosity of fluids and visco-elasticity of gels (e.g. Rossetti et al., 1999; Llewellin et al., 2002b; Mueller et al., 2011; Kavanagh et al., 2013), to shear boxes that measure the cohesion and strength granular materials (e.g. Galland et al., 2006). Viscometry has been conducted since the nineteenth century, as described in a review by Dontula et al. (2005). In this method, a sample of material is tested in a viscometer by applying a known shear stress (σ) to a sample to determine the strain rate ($\dot{\gamma}$) (Weijermars, 1986), and from this the viscosity (η) can be calculated (Eq. 2.2). Several types of viscometer have been used; rotary, concentric cylinder, falling ball, tube and parallel plate, with each method able to quantify the behaviour at different ranges of shear rates (e.g. Lane et al., 2001; Rust and Manga, 2002a; Bagdassarov and Pinkerton, 2004). Rheometers work in similar ways to viscometers, however they are more advanced as they can be used to measure the properties at a range of temperatures using Peltier plates (e.g. Kavanagh et al., 2013). Several studies have used rheometers to characterise the properties of both magma and host rock analogues; e.g Llewellin (2002b) and Schellert (2011) for golden syrup magmas, and

Kavanagh et al. (2013) for gelatine hosts. Over recent years, rheometers have been used more regularly than viscometers due to the greater range of properties they can measure.

2.5.3 Scaling

The selection of materials to use in laboratory experiments has a large impact on the applicability and reproducibility of a model to natural systems. For the selection of appropriate materials, scaling of experimental parameters to nature is required with respect to universal laws that govern the physical systems being studied (Merle, 2015). The scaling of experiments was first described by Ampferer (1906; cited in Kavanagh et al., 2018b) who identified that as length scales are decreased from the natural-scale to a laboratory-scale model, the same needs to occur for all other "constants". Some of the most common fundamental units that are used are length (m), mass (kg), time (s) and temperature (˚K). From these fundamental units many other properties of natural and model materials can be identified, including velocity (ms^{-1}), stress (kg m^{-1} s^{-2} or Pa) and viscosity (kg m^{-1} s^{-1} or Pa s). Scaling is undertaken using two main methods, either by using 'scale factors' or by using Buckingham's (1914) 'Pi theorem' (also known as dimensional analysis). If scale factors and dimensionless numbers in laboratory models can be maintained, then the use of laboratory models to understand natural systems can be highly effective. In contrast, when these parameters are not calculated, or do not remain constant, then direct comparisons cannot be made. However, lessons can still be learnt, and processes can still be identified that occurred during the timescale of the experiment, although the link to nature needs to be made cautiously. Brief descriptions of the scaling methods are now presented, however the reader is directed to reviews on these topics by Galland et al. (2015) and Merle (2015) for more detail.

2.5.3.1 *Scale factors*

Scale factors underpin the scalability of laboratory experiments to natural systems. They represent the ratios between the natural system and models, determining aspects such as the length (h^*), density (ρ^*) and timescales (t^*) of experiments. These ratios are defined as:

$$h^* = \frac{h_m}{h_n}, \tag{2.9}$$

$$\rho^* = \frac{\rho_m}{\rho_n}, \tag{2.10}$$

$$t^* = \frac{t_m}{t_n}, \tag{2.11}$$

where *m* and *n* represent the model and nature respectively (Kavanagh et al., 2018b). From these simpler ratios, more complex ratios for parameters like viscosity can be determined, enabling the density and stress differences between host rock and magma to remain constant in the model. When modelling using granular materials, scaling ratios for the properties of the host material, such as cohesion (*C**) and the angle of internal friction (*φ*), and of the magma analogue, such as viscosity (*η**), need to be determined:

$$C^* = \frac{C_m}{C_n}, \tag{2.12}$$

$$\eta^* = \frac{\eta_m}{\eta_n}, \tag{2.13}$$

Galland et al. (2006) state that the angle of internal friction is dimensionless, as such should remain the same (or similar) between nature and the model. See Galland et al. (2006) for a more detailed description of the scaling parameters used in their granular type models.

2.5.3.2 *Buckingham's Pi theorem*

Buckingham's Pi theorem, also known as 'dimensional analysis', enables the determination of similarities between the natural and model systems using a series of dimensionless numbers (Buckingham, 1914). It works by assessing the key physical variables of the natural system to identify dimensionless parameter combinations and 'regimes' that can then be applied to the model to express the physics of the investigated processes. Common dimensionless numbers used in studying magmatic intrusions include the Reynolds number (*Re*), the Rayleigh number (*Ra*) or the Hubbert number (Merle, 2015; Kavanagh et al., 2018b).

Re is used to describe style of flow, with low *Re* indicating laminar flow and high *Re* indicating turbulent flow. It is defined as:

$$Re = \frac{\rho u h}{\eta}, \tag{2.14}$$

where *ρ* is fluid density, *u* is flow velocity, *L* is distance, and *η* is viscosity. This flow style will affect the trajectories of passive-tracer elongate crystals which align with the flow velocity vector in a flowing magma.

Ra is used to determine the presence of convective flow due to heat transfer, and is defined as:

$$Ra = \frac{g\alpha\Delta T h^3}{\eta\kappa}, \tag{2.15}$$

where, g is gravity, α is the coefficient of thermal expansion, ΔT is the temperature difference, and κ is thermal diffusivity. Low Ra indicate cooling by convection, whereas higher Ra indicate cooling via convection.

The Hubbert number is used to determine the ratio between gravity and cohesion, and is defined as:

$$Hu = \frac{\rho g h}{\tau_0}, \tag{2.16}$$

where ρ is the density and τ_0 is cohesion. Hu is implemented to accurately scale the cohesion of analogue materials to that of rocks found in nature (Merle, 2015).

2.5.4 Laboratory models with elastic host materials

The hydraulic fracture model of intrusion emplacement, where the crust is modelled as an elastic host, has been studied using a range of techniques to understand the processes and mechanisms involved in the propagation and emplacement of dykes (Figure 2.7A-B; e.g. Fiske and Jackson, 1972; Rivalta et al., 2005; Kervyn et al., 2009; Taisne et al., 2011; Kavanagh et al., 2018a), sills (Figure 2.7C; e.g. Rivalta et al., 2005; Kavanagh et al., 2006, 2017; Chanceaux and Menand, 2014, 2016), laccoliths (e.g. Pollard, 1973; Pollard and Johnson, 1973; Hyndman and Alt, 1987) and diapirs (e.g. Dietl and Koyi, 2011). These models predominantly use gelatine as a host material, as it behaves as a viscoelastic solid that can undergo elastic deformation prior to brittle fracture at low temperature and 2-5 wt% concentraion (Acocella and Tibaldi, 2005; Kavanagh et al., 2013). Gelatine is versatile in that its properties are directly linked to its mixing ratio with water during preparation, enabling different strength gelatine hosts to be prepared so that different strength host rocks in nature can be modelled (Rivalta et al., 2005). Other viscoelastic materials that have also been used as host the material when studying the propagation of brittle fractures or magmatic intrusions, include agar (Sumita and Ota, 2011) and laponite gel (Bertelsen et al., 2018).

Into the gelatine, a range of fluids have been injected as magma analogues, spanning Newtonian fluids such as air (e.g. Rivalta et al., 2005; Menand et al., 2010) and water (e.g. McLeod and Tait, 1999; Kavanagh et al., 2006) to temperature-dependant Newtonian fluids such as paraffin wax (Figure 2.7D; e.g. Taisne and Tait, 2011), vegetable oil (Vegetaline brand) (Figure 2.7E; e.g. Chanceaux and Menand, 2014, 2016) or molten gelatine (e.g. Hyndman and Alt, 1987; Pansino et al., 2019). Other viscous fluids, such as plaster of Paris, have also been intruded which solidify and can subsequently be excavated (Hubbert and Willis, 1957).

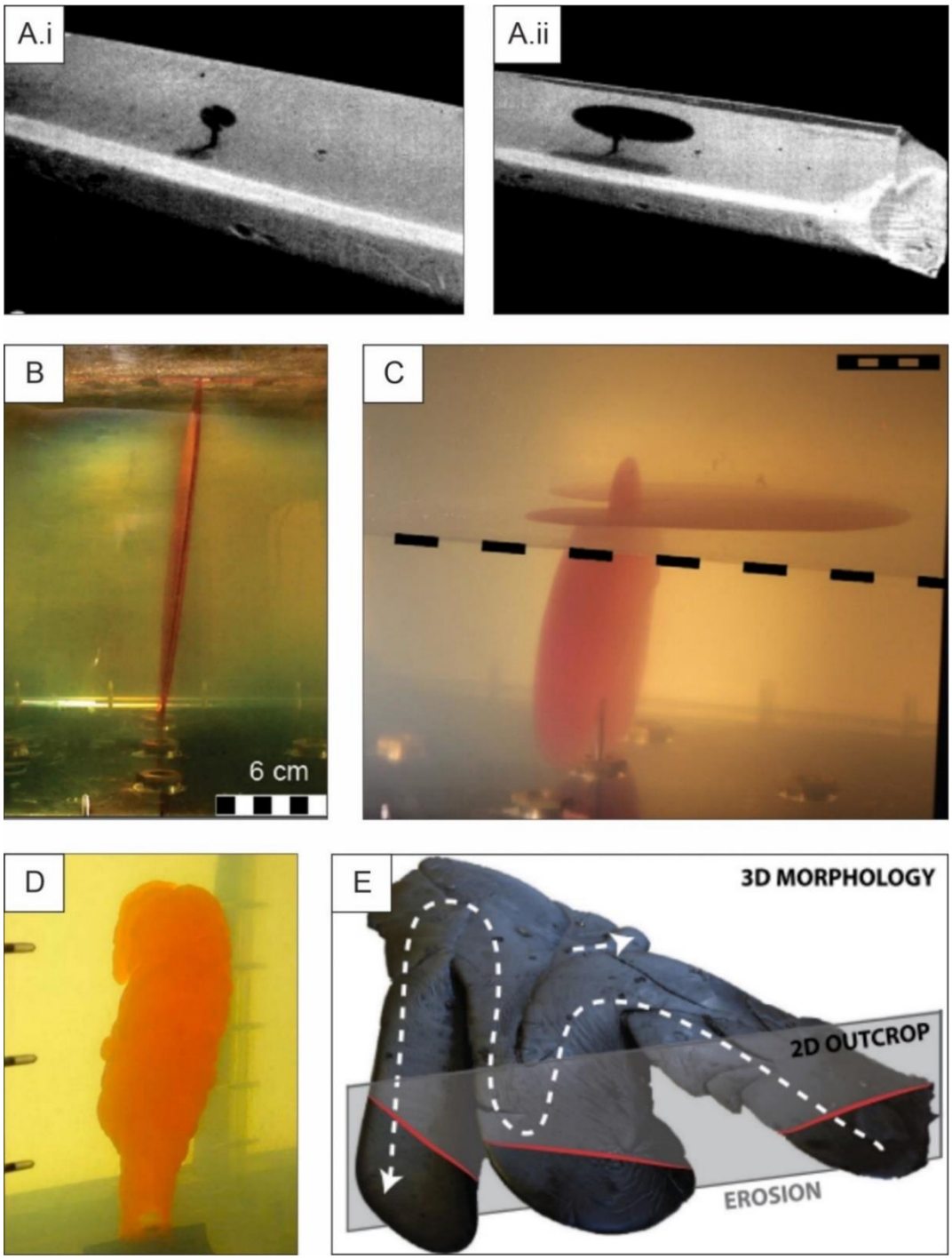

Figure 2.7 *Analogue models of dykes and sills that use viscoelastic gelatine to represent the host rock, however, use a range of intruding fluids. A) Injection of coloured water into a "ridge" shaped morphology with (i) at the onset of injection and (ii) during injection (Fiske and Jackson, 1972), B) coloured water dyke propagation into gelatine* (Kavanagh et al., 2018a)*, C) water injected into multi-layered gelatine block forming a sill at the interface (Kavanagh et al., 2017), D) injection of wax into gelatine to investigate the impact of cooling and solidification on intrusion morphology (Taisne and Tait, 2011), E) excavated complex sill structure created during injection of molten vegetable oil into gelatine block that was subsequently allowed to solidify (Chanceaux and Menand, 2016). Ropey structures can be seen in the sill surface.*

The experimental setup generally involve an acrylic or perpex tank that have different heights but either a square (e.g. Kavanagh et al., 2006; Taisne and Tait, 2009) or round base (e.g. McLeod and Tait, 1999; Rivalta et al., 2005; Kavanagh et al., 2017). Into the tank, hot molten gelatine is prepared and then loaded into the tank before being placed into a refrigeration unit to solidify, usually for over 24 hours (but over 100 hours for layered experiments). In multi-layer experiments, smaller volumes of gelatine are sequentially emplaced with solidification occurring between the addition of each subsequent layer to produce a bonded interface (Kavanagh et al., 2006). The strength of the interface depends on the temperature at which the second layer of gelatine is added to the first, with lower temperatures producing weak a weak interface or higher temperatures producing a stronger more diffuse boundary (Sili et al., 2019). The intruded fluid is then injected either from below (e.g. Watanabe et al., 2002; Rivalta et al., 2005; Kavanagh et al., 2006; Sili et al., 2019), above (e.g. Taisne and Tait, 2009) or from the side (e.g. Chanceaux and Menand, 2016; Urbani et al., 2018) into the solidified gel.

Single layer gelatine experiments generally study dyke propagation (e.g. McLeod and Tait, 1999; Taisne and Tait, 2011). Some models have studied the effect that the ambient stress field has upon intrusion morphology, by either compressing the gelatine by inserting sheets between the tank and the solidified gelatine block (Menand et al., 2010) or causing extension by replacing some gelatine with water at the edges of the tank and loading the surface from above (Daniels and Menand, 2015). Dyke propagation within volcanic edifices has been studied by either intruding directly into gelatine with an edifice-like conical or triangular-prism morphology (e.g. Fiske and Jackson, 1972; Acocella and Tibaldi, 2005; Tibaldi et al., 2014) or by injecting into a gelatine block with an overlying load to represent a volcanic edifice (e.g. Watanabe et al., 2002; Walter and Troll, 2003; Kervyn et al., 2009). Fiske and Jackson (1972) found that experimental dykes emplace radially around a conical edifice, however when the edifice was elongate (triangular prism) the dyke would propagate along the long-axis of the edifice before it would erupt. Intrusion propagation and morphology has also been studied in caldera settings by partially submerging a cup into the gelatine during preparation that was then removed after solidification thus creating an unloaded topography (Gaete et al., 2019).

Multi-layer experiments with different strength layers, have been prepared to study the effect of different strength host rocks on dyke, sill and laccolith emplacement (e.g. Hubbert and Willis, 1957; Rivalta et al., 2005; Kavanagh et al., 2006, 2017). The morphologies of the intrusions (Figure 2.7E; Chanceaux and Menand, 2016) and the effects they have on the

stress field in the surrounding host material has also been investigated using the photoelastic properties of gelatine (Kavanagh et al., 2017).

Many of the gelatine models have focussed on emplacement dynamics and effects the host-rock properties have on the intrusion type created, and the processes occurring within the intruding magma have been relatively understudied. A recent study by Kavanagh et al. (2018a) begins to address this gap, and is discussed in detail in section 2.5.7.

2.5.5 Laboratory models with granular hosts

In laboratory modelling, the viscous indenter style of intrusion emplacement where the crust is modelled as an inelastic deformable body, has been investigated to understand a range of processes and mechanisms that effect the morphology of dykes (Figure 2.8A-Ci; e.g. Mathieu et al., 2008; Abdelmalak et al., 2012; Wyrick et al., 2015; Guldstrand et al., 2017; Poppe et al., 2019), cryptodomes (Figure 2.8Cii; e.g. Schmiedel et al., 2017; Poppe et al., 2019), cone sheets (e.g. Galland et al., 2014; Poppe et al., 2019), sills (Figure 2.8Ciii-D; e.g. Galland et al., 2006; Galland and Scheibert, 2013; Schmiedel et al., 2017; Poppe et al., 2019) and laccoliths (Roman-Berdiel et al., 1995; Galland and Scheibert, 2013; Schmiedel et al., 2017). All of these models commonly use granular materials, such as sand, silica flour or mixes thereof, as analogues for an inelastic plastic crust (Table 2.4; Galland et al., 2006; Wyrick et al., 2015; Schmiedel et al., 2017; Poppe et al., 2019). These materials are used because they mimic natural rock material well, in that they fail both in tension and in shear.

The experimental setup for these experiments using a granular host-rock analogue is a square-based box filled with compacted granular material. Some models use multiple layers of granular materials, with differentiation either in the layer colour or material properties so that any sub-surface deformation of the host material by the intruding fluid can be observed post-emplacement (Figure 2.8B; Wyrick et al., 2015). The fluid is then injected into the base of the box using a volumetric pump (e.g. Galland et al., 2014; Guldstrand et al., 2017) or a hydraulic squeezer (Závada et al., 2011).

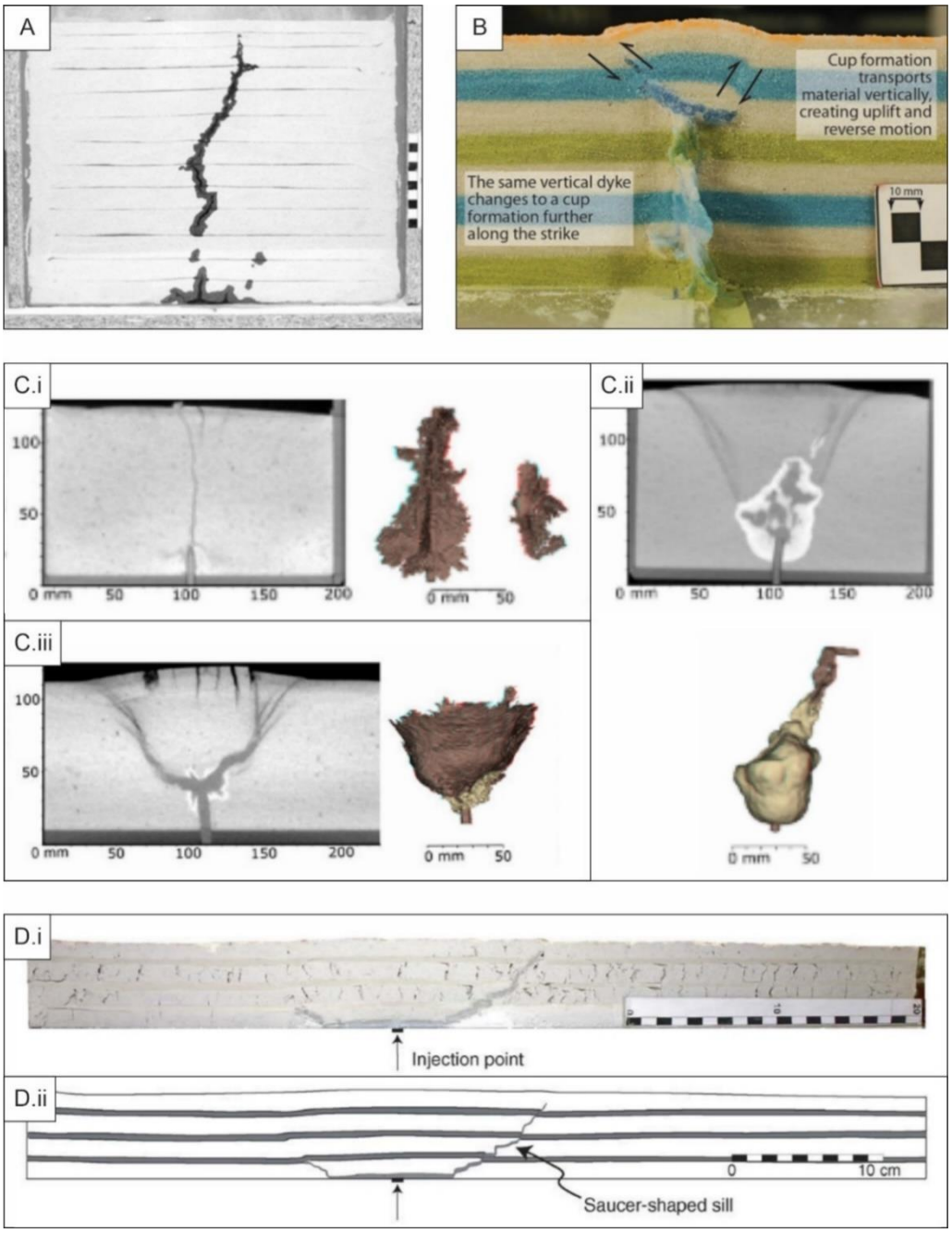

Figure 2.8 *Analogue models that focus on the viscous indenter model of intrusion propagation where intrusion occurs into inelastic granular host materials. A) Dyke propagation and formation in using golden syrup magma injected into ignimbrite powder (Mathieu et al., 2008). B) Propagation of a solidifying paraffin wax dyke into sand which can then be excavated to analyse the intrusion morphology (Wyrick et al., 2015). C) Golden syrup injected into mixtures of silica sand and gypsum powder whilst being monitored by x-ray computed tomography to analyse evolution of the 3D structure during emplacement of (i) a dyke, (ii) a cryptodome and (iii) a saucer shaped sill (Poppe et al., 2019). D) Intrusion of vegetable oil as a series of sills and cone sheets as it propagated through layers of silica crystals and silica spheres respectively. (i) Photograph of excavated model, (ii) diagram of (i) showing location of silica crystals (white) and silica spheres (dark grey) and saucer-shaped sill (Galland et al., 2006).*

One problem associated with using granular materials in analogue experiments that study magma intrusion is the lack of transparency of the medium. As such, solidifying fluids need to be used to observe the structures formed which are then excavated after the experiment has ended. The fluids used behave in a Newtonian manner at higher temperatures, however are solid at lower temperatures or closer to room temperature, e.g. golden syrup (e.g. Mathieu et al., 2008), vegetable oil (e.g. Galland et al., 2006, 2009) and paraffin wax (e.g. Wyrick et al., 2015). Even then however, the evolution of the intrusion over time is not possible to reconstruct other than qualitatively and based on assumptions about flow direction. The models of Kratinova et al. (2006) and Závada et al. (2011) begin to address this gap in the literature by studying the AMS fabrics preserved during the emplacement and solidification of plaster of Paris intrusion that have been seeded with fine grained magnetite particles. After solidification, the plaster bodies were excavated, sliced up and their internal fabrics studied, with different flow regimes identified, such as flow, shear and compression.

Multiple studies have recorded the surface deformation during experiments, either using photogrammetry (Tortini et al., 2014; Galland et al., 2016; Schmiedel et al., 2017) or x-ray computed tomography (CT) (Poppe et al., 2019). With photogrammetry, 3D changes in the surface topography can be calculated and determined using software such as MicMac (Galland et al., 2016). The recent use of x-ray CT in analogue modelling is a useful tool in determining evolution of the entire 3-dimensional structure of the model over short time-steps, which means that the different processes that occur during emplacement can be understood. By recording the deformation during intrusion emplacement and combining with the intrusion structure, a better understanding of the morphology of intrusions being formed during emplacement in nature (Poppe et al., 2019).

2.5.6 Laboratory modelling of lava flows and domes

The emplacement of lava domes and lava flows can be used as proxies for studying the processes occurring within actively propagating intrusions. This is due to similarities existing between these intrusive and extrusive sections of the volcanic system, for example, basaltic lava flows behave in similar ways to sill like bodies as they are both horizontally oriented sheet-like bodies that transport magma, with the main difference being the presence or lack of a lithostatic load. Sills have an upper contact with host rock with the overlying lithostatic load causing the magma to spread out laterally , which results in structures with high aspect ratios of ~1:200-2000 (Bunger and Cruden, 2011). In contrast, lava flows have an upper contact with either air or water which rapidly cool or quench flow margins and acts to channelize and increase the flow thicknesses due to solidification around edges. When this

is combined with a lack of an overlying lithostatic load, this results in low aspect ratios ranging from 1:>50 for mafic rheologies to 1:<8 for felsic rheologies (Walker, 1973). Due to lava flows and domes being key structures for the transport and storage of magma above the surface, I include here a background into analogue modelling of lava domes and flows, and how these can be a basis for analogue modelling of sheet intrusions. This section is an adapted version of sections 8 and 9 of Kavanagh et al. (2018b).

2.5.6.1 *Lava domes*

Lava domes are effusions of degassed, highly viscous, silica-rich magma that accumulate at volcanic vents. Their emplacement can cause the build-up of gas and pressure in the conduit, increasing the potential for explosive eruptions or the formation of pyroclastic density currents. Modelling lava dome emplacement and stability is key for identifying thresholds for collapse and therefore for assessing the potential risk of such events. Aspects of lava dome emplacement that have been studied in laboratory experiments include morphological variations due to topography (e.g. Lyman et al., 2004), magma rheology (e.g. Griffiths and Fink, 1993; Fink and Bridges, 1995), and the preservation of flow fabrics using magnetic fabrics (Závada et al., 2009). Lava dome models have been scaled by considering the Reynolds number (Re) ensuring laminar flow and the Bingham number (B), which quantifies stresses within the dome (Balmforth et al., 2000).

Dome morphology

Laboratory models of lava domes have largely focussed on the influence of lava rheology on dome morphology. Griffiths and Fink (1993) investigated the progressive spreading of lava domes by effusing liquid PEG 600 wax into a tank of cold sugar solution with a horizontal base. The temperature gradient between the wax and solution caused the onset of solidification, and the lava viscosity had a large influence on the morphology of the dome that was formed. Fink and Bridges (1995) found that pulsating the wax effusion and decreasing its temperature resulted in predominantly vertical growth of the dome rather than flow away from the vent, and so the length of lava domes could be explained primarily by variations in effusion rate. Several lines of evidence suggest that lava dome rheology in nature is more complex than a simple temperature-dependent Newtonian fluid. Balmforth et al. (2000) carried out numerical simulations of lava dome growth and evolution using a Herschel–Bulkley rheology, which were compared with kaolin–water slurry models. They found that the yield stress acting in the dome is important in determining dome morphology; however, the combined effects of shear thinning and yield stresses were difficult to distinguish. Experimentally, Blake (1990) used kaolin–water slurries to model dome

morphology in a Bingham fluid to identify yield stresses occurring within domes effused onto horizontal planes. Their domes were parabolic in nature with surface lineations that spiral out from the centre and are inferred to be areas of shear localisation, which allows for stable dome growth. Griffiths and Fink (1997) used a PEG–kaolin mixture to study lava dome morphology with the kaolin powder converting the fluid from a temperature-dependent Newtonian fluid to a Bingham fluid. These analogue lava domes produced spines and irregular breakouts of wax (Figure 2.9A) due to the yield strength of the magma analogue. Lyman et al. (2004) used a similar mixture to investigate the impact of slope and effusion rate on dome morphology. They found that contrasting dome morphologies (e.g. platy, spines, lobes) were associated with extrusion onto a surface at different slope angles, but that effusion rate had the greatest impact on dome morphology. These results can be compared to lava dome morphologies in nature, such as Wilson Butte in California (Lyman et al., 2004), to calculate the effusion rate of prehistoric domes.

Internal deformation of lava domes

Internal flow patterns within lava domes in nature have been inferred from crystalline and bubble fabrics within the crystalline lava, thus providing insight into the processes occurring within a dome during formation. Závada et al. (2009) studied magnetic fabric development within lava domes by effusing plaster of Paris seeded with magnetite particles from a point source, injecting with increasing pressure onto a deformable surface of sand (Figure 2.9B). The plaster of Paris and magnetite mixture behaves as a shear thinning fluid and was allowed to solidify once extruded. The solidified dome was then cut into slices and oriented samples drilled for analysis by applying anisotropy of magnetic susceptibility (AMS) to quantify the direction and intensity of any fabric that was developed by the magnetite particles during the extrusion of the lava dome. They found more concentrated suspensions with higher viscosity created complex dome structures that had relatively steep sides, akin to lava domes commonly observed in nature. Post emplacement cooling and alteration of the dome from hydrothermal fluids was modelled by Ball et al. (2015), who simulated the effect of heat and water flow though cooled lava domes over prolonged timescales (100 years). They determined that alteration is most likely to occur at boundaries between different parts of the dome, and that temperature greatly affects the potential for alteration with faster cooling rates reducing the likelihood of deep alteration within the dome.

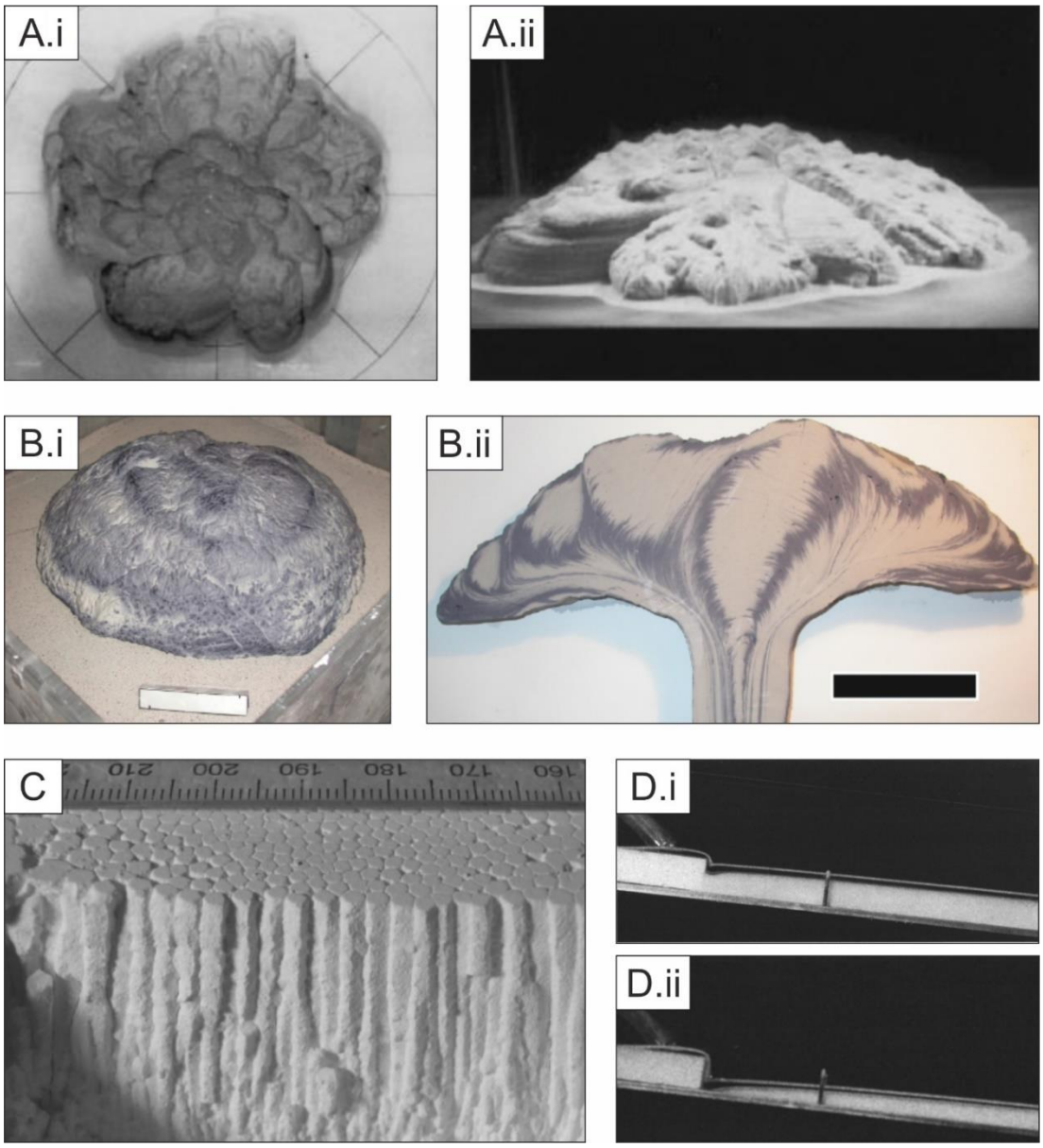

Figure 2.9 *Analogue models that study lava domes (A and B) and lava flows (C and D): (A) experiment by Griffiths and Fink (1997) of polyethylene glycol extruded from a point source imaged in (i) plan view and (ii) side view. (B) Photograph showing (i) external morphology and (ii) cross section through plaster of Paris analogue model of lava dome emplacement seeded with magnetic particles for AMS analysis (scale bars are 10 cm long, photos courtesy of Prokop Zavada. See also Zavada et al., 2009). (C) Dehydration of corn starch–water slurry to study the formation of columnar jointing structures in lava flows (modified from Goehring et al., 2006). (D) Effusion of molten wax onto bed of solid wax to study thermal erosion of lava flow into underlying material after (i) 4 and (ii) 14 min (Kerr, 2001).*

2.5.6.2 *Lava flows*

Laboratory and numerical modelling has been extensively applied to investigate lava flow emplacement. Scaling of lava flow models considers several aspects, such as the mechanism

of heat loss via the Peclet number (Pe) and dimensionless timescales (Ψ) for solidification (e.g. Fink and Griffiths, 1990, 1998). In the laboratory, the emplacement dynamics and morphology of lava flows has been investigated using Newtonian fluids (e.g. glucose syrup; Stasiuk et al., 1993) and more complex fluids that account for cooling and crystallisation and develop a solidified crust during flow (e.g. PEG wax; Hallworth et al., 1987; Fink and Griffiths, 1990; Gregg and Fink, 1995). These experiments model variations in heat flux, thermal gradients, and cooling on the temporal and spatial variation of lava flow viscosity, then extrapolating the impact these factors have on run-out length and flow morphology. Lavas have also been modelled in the laboratory as a particle suspension, with experiments showing that increasing particle volume fraction (Soule and Cashman, 2005; Castruccio et al., 2014) and particle size (Del Gaudio et al., 2013) increases lava viscosity and can affect lava flow morphology. High-concentration particle suspensions produce low flow velocities, shear localisation, and subsequent break-up of the flow surface, causing transition from pahoehoe-like to aa-like morphologies that are reminiscent of natural flows (Soule and Cashman, 2005).

Lava flow dynamics

The cooling mechanism of lava flows impacts the morphology and run-out length of the flow and therefore the hazards it may pose to surrounding populations. Recent work by Garel et al. (2012, 2014) has studied, in detail, the effects of cooling on the morphology of flows in the laboratory and numerically. They effused silicone oil (Garel et al., 2012) and PEG P3515 (Garel et al., 2012, 2014) onto a horizontal piece of polystyrene, which insulates the base of the flow, and developed a numerical model that considers both surface and basal cooling by scaling thermal boundary conditions and radiated power. They showed that cooling is primarily controlled by the effusion rate of the fluid, and that it is possible to estimate the effusion rate from observation of the surface thermal signal. Their results correlate with natural examples of effusion rates; however large amounts of uncertainty exist between these models and natural lava flows due to the complex nature of natural systems, i.e. variable flow dynamics and cooling profiles within the flow (Garel et al., 2012, 2014).

Lava flow levees and solidification

Critical in the cooling of lava fields is the development of lava levees, crust formation, and progressive breakout. This has been investigated in the laboratory using paraffin wax, where the progressive cooling of the hot, liquid wax causes levees to form and channelisation of the flow (Blake and Bruno, 2000; Miyamoto et al., 2001; Nolan, 2014). Crust formation over the cooling flow surface insulates the molten wax and creates tube-fed flows, and blockages or restrictions in the tube-fed flow of wax to the flow front lead to flow inflation and eventually

breakout from the crust. Blake and Bruno (2000) used PEG wax experiments to demonstrate the link between lava effusion rate, lava viscosity, and strength of the chilled crust, which impacts how and where breakouts from lobate structures occur. Karlstrom and Manga (2006) used spreading paraffin wax experiments to study the cooling and rifting associated with lava lakes, however their results can also be applied morphological transition from pahoehoe to aa flows due to fracturing and rifting of the cooling lava crust.

Solidification and development of columnar jointing in lava flows has been modelled using corn starch slurries that are placed under heat lamps to allow the water to evaporate away (Müller, 1998; Goehring and Morris, 2005). The loss of water was used as an analogue for heat loss within lavas; as the starch dries out it shrinks, resulting in cracks forming and propagating through the material (Figure 2.9C). The morphology of the vertical columns formed within the analogue lava correlates well with the morphology of columns in natural lava lakes and ponded lava flows such as in Hawaii (Müller, 1998; Goehring et al., 2006) or the Giant's Causeway in Northern Ireland (Goehring and Morris, 2005). However, further rheological studies to better understand the material properties are needed to improve scaling these experiments to nature.

Substrate erosion

Field observations of erosion channels within lava tubes suggest that assimilation of the lava substrate can occur when lava flows are emplaced with high heat flux or flow over substrate with a low melting temperature. Huppert and Sparks (1985) investigated the development of thermal erosion channels in komatiite lava flows by pouring hot water onto a slab of PEG 1000 wax; Komatiite lavas are thought to have had unusually high heat flux, and so thermal erosion of their substrate is expected to have been an important process in the development of these ancient flows. Kerr (2001) used theoretical models alongside molten PEG 600 effused onto an inclined sheet of solid PEG 600 (Figure 2.9D) to investigate how the thermal profile of lava flows evolves both spatially and temporally. His experimental results agreed with the theoretical models, which showed that there is a critical thickness range at which chilled margin formation at the base of the flow ceases and erosion begins, depending on the initial temperature of the lava; for basaltic lavas on Hawai'i, this range is 7.3 to 34 cm after a period of 0.21 to 4.6 days.

Flow indicators in lavas

When studying ancient solidified flows in nature, crystal distribution and stretched bubbles have been used to infer flow direction. The preservation of flow indicators in solidified lavas

was investigated in analogue experiments using layered viscous silicone to model internal strain within extruding and spreading fluids (Gilbert and Merle, 1987). The experiments showed that in channelised flows, or at the base of a lobe, the lava flow trajectory indicators could be both parallel and perpendicular to each other in the upper portion of lobes. When applied to lava flows in nature, such observations can explain emplacement mechanisms and possibly account for variations in deformed bubble and crystal shape-preferred orientations compared to AMS fabrics in different parts of the flow (e.g. Caballero-Miranda et al., 2016).

2.5.7 Laboratory modelling of flow structures

The use of laboratory modelling using analogue materials to understand the internal magma flow process is limited as the majority of studies only interpret the external morphology of an experimental intrusion (e.g. Taisne and Tait, 2011; Chanceaux and Menand, 2016) or lava flow (e.g. Gregg and Fink, 1995; Cashman et al., 2006). Studies of finer-scale flow fabrics or flow dynamics where individual particles or regions are tracked are a lot less common (e.g. Bhattacharji and Smith, 1964; Gilbert and Merle, 1987; Kavanagh et al., 2018a). Here, the analogue models that have been used to understand the flow dynamics in both intrusive and extrusive systems are reviewed (but with experimental setups described in previous sections).

Flow structures like ropes have been identified in several models and linked to the folding of the contact surface (exposed surface). These structures formed due to shear created by faster flowing magma analogue below a slower moving surface which then drags the surface, and as such folds it (Gregg and Fink, 1995). This has been found when producing both sill type morphologies (Figure 2.7E; Chanceaux and Menand, 2016) and during the formation of lava flows (Gregg and Fink, 1995; Cashman et al., 2006). The formation of these structures is linked to the rheology of the magma analogue, which tends to be temperature-dependant Newtonian, such as waxes or vegetable oils. These fluids are injected at temperatures above their melting points, however, during the experiment they cool and solidify from the surface inwards. Gregg and Fink (1995) also identified flow-parallel lineations in their wax models which they linked to the breakup of a lava flow surface. These lineations formed parallel to the opening direction of the breakup surface of the lava flow and are inferred to be in the direction of flow in submarine flows with rifted surfaces.

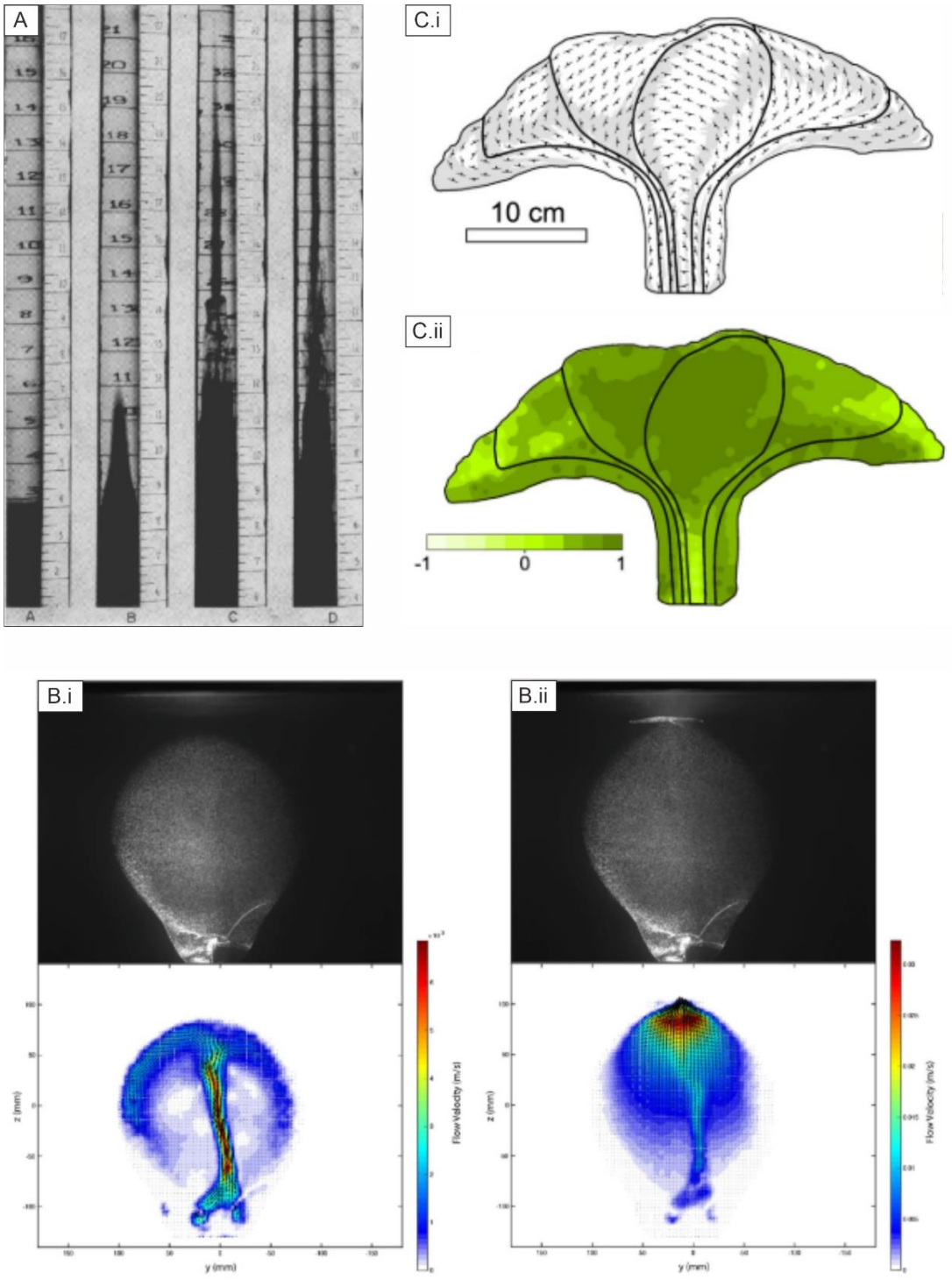

Figure 2.10 *Analogue models that study magma flow. A) Particles in oil during flow showing the localisation of crystals away from the margins of dykes (Bhattacharji and Smith, 1964); B) gelatine water models of Kavanagh et al.* (2018a) *where particles in the flow are illuminated by a laser sheet, from which flow trajectories were identified during (i) dyke growth and (ii) at eruption. C) AMS fabrics preserved within plaster model of Zavada et al. (2009) from Figure 2.10B.ii, (i) shows the magnetic foliation orientation and (ii) shows the shape parameter (1 is oblate and -1 is prolate).*

Analogue modelling studies on smaller-scale fabrics associated with crystals and vesicles within crystalline magma are also rare. The localisation of crystals away from dyke walls was investigated by Bhattacharji and Smith (1964), who used a range of oils (motor, coconut, turpentine) with added irregular-shaped particles (leucite, paraplex plastic, wood, charcoal or Bakelite) to model the dispersion of particles during analogue magma flow through a dyke (Figure 2.10A). The oils undergo laminar flow through the conduit with the particles suspended within. They found that the particles rotated away from the intrusion walls during flow due to the 'Magnus effect', which localised the particles into the dyke core. When flow ceased, the particles descended through the conduit and spread out closer to the margin again, however they re-localised toward the centre when flow resumed (Bhattacharji and Smith, 1964). This rotation away of larger particles away from dyke walls can help to understand crystal distributions during laminar flow in Newtonian fluids.

Larger scale flow dynamics have been studied by Kavanagh et al. (2018a) used water seeded with tracer particles illuminated by a laser sheet to track the fluid flow in a growing and then erupting dyke using particle image velocimetry (PIV) (Figure 2.10B). The experiments were videoed and the illuminated particles were tracked across multiple timesteps to map the flow trajectories. Four different stages of dyke growth were identified based on the fluid flow: from initial inception, to dyke propagation, the development of a centralised fluid jet and downflow at the dyke margin, and eventual eruption. These models are amongst the first to identify flow evolution during dyke emplacement.

The preservation of magnetic fabrics within analogue models have been investigated by a few studies where plaster of Paris (viscous magma analogue) is seeded with fine-grained magnetite particles (see Figure 5.2A in chapter 5 for particle shapes), which is subsequently squeezed or injected into vents of known geometries or through sand (Kratinová et al., 2006; Závada et al., 2009, 2011). These models are used to understand the flow fabrics and associated flow processes occurring within diapirs, diatremes, and lava domes (described above). These models use plaster of Paris as it behaves as a pseudoplastic fluid which solidifies, enabling it to be excavated and sampled to understand the preserved fabrics (Figure 2.10C). These models are unique, in that the method to analyse magnetic crystal fabric in the model is a direct equivalent of their measurement in nature, and so can be utilized to improve our understanding of the emplacement processes involved in the formation of magnetic fabrics in viscous magmatic structures in nature.

In summary, analogue models have been applied to understand a variety of different structures both at the macroscale, e.g. dyke and sill propagation, and microscale e.g. crystal and magnetic fabrics. However, there are still large gaps in applying laboratory modelling using analogue materials to understanding flow fabrics within sheet intrusions. The majority of the current studies of intrusion emplacement using laboratory modelling primarily focusses on the behaviour of the host material and the impact it has on intrusion morphology, however large gaps remain in relation to the behaviour of the intruding fluid during emplacement. The style of emplacement and associated flow fabrics occurring during magma intrusion, along with how these fabrics are then preserved in the solidified body is also poorly constrained. This is supported by a lack of understanding into how analogue intrusions grow and evolve through time. More specific to this thesis is the lack of understanding of the formation and distribution of magnetic fabrics associated with the emplacement and evolution of dykes and sills.

Chapter 3: The origin and evolution of magnetic fabrics in mafic sills

This paper has been published in Frontiers in Earth Science as Martin et al. (2019). Data collection, analysis and writing of the paper was done by myself, with the support from Janine Kavanagh and Andy Biggin. James Utley performed the QEMSCAN data collection, analysis and read the manuscript. Elliot Wood provided field support. See Appendix B for published version.

3.1 Abstract

Studying extinct volcanoes where erosion has exposed dykes and sills provides direct access to the fossil remnants of magma movement, however linking crystallised magma to emplacement dynamics is challenging. This study investigates how magma flow varies across the thickness of a thin (6 metres thick) mafic sill. We use a high-resolution sampling regime to measure micro-scale variations in magnetic anisotropy, which is associated with the orientation of the magnetic particles present within the crystalline rock. Fieldwork was conducted on exposed sills of the British and Irish Palaeogene Igneous Province, Isle of Skye, Scotland. Here Jurassic sedimentary rocks have been intruded by a series of sills, of picrite to crinanite composition, from the Little Minch Sill Complex (c.60 Ma). Anisotropy of magnetic susceptibility (AMS) and anisotropy of anhysteretic remanent magnetisation (AARM) signals have been used to separate a crinanite sill into distinct magnetic groupings. We identified two AMS groups (the upper and lower sill margins, and the central region) and four AARM groups (the lower margin, the middle region, a region just below the upper margin, and the upper margin). Both AMS and AARM signals originate from titanomagnetite of multi-domain or vortex-state to single-domain sized grains, respectively. The AMS and AARM fabrics are aligned with each other in the margin regions preserving a history of magma flow towards the North during initial emplacement. However, in the sill interior the AMS and AARM fabrics are oblique to each other, thus reflecting multiple origins. We suggest the AMS fabrics have recorded magma flow during sill growth, and AARM fabrics have recorded melt percolation flow as the interstitial melt migrated upwards through a solidifying crystal mush. We demonstrate that when AMS and AARM are used in combination they enable a detailed understanding of magma flow and solidification dynamics to be

obtained, from initial emplacement to solidification. Overall, our detailed sampling and analysis indicates that magnetic fabrics can be highly variable over small distances, supporting the suggestion of horizontal flow restriction and propagation path migration within growing sills, and that previous reports of magma flow and solidification dynamics based on under-sampled bodies may require reconsideration.

3.2 Introduction

Determining the physical, chemical and thermal processes that occur during the propagation, transport and emplacement of magma within magmatic intrusions is necessary for understanding how volcanic systems develop (e.g. Magee et al., 2018). Magma is transported through the crust in a series of sheet intrusions called dykes, inclined sheets, and sills (e.g. Mathieu et al., 2008). These sheet intrusions are an important structure for the transport and storage of magma in the crust, helping to build large magma reservoirs at depth, and are a key contributor to crustal growth (see review by Putirka, 2017; and references therein). The importance of dykes as feeders of magma to the surface is well known (e.g. Geshi et al., 2010; Gudmundsson et al., 2014), with sills also providing pathways for magma to travel many kilometres from their source regions (e.g. Airoldi et al., 2016). Understanding magma intrusion dynamics that occurred in the past is therefore important for mitigating volcanic hazards in the future through monitoring of active volcanoes (e.g. Sparks and Cashman, 2017). Sills are also of economic importance as they can be associated with maturing petroleum source rocks or creating traps (e.g. Monreal et al., 2009; Magee et al., 2018). Some kimberlitic sills are also hosts to diamonds (e.g. Sparks, 2013).

Traditionally the factors that influence the propagation of sheet intrusions through the crust, and their tendency to arrest or erupt, primarily consider deformation of the host rock, with intrusion propagation linked to: mode of fracture propagation (i.e. tensile, shear or mixed mode; Rubin, 1995), strength and rheology of the host rock (e.g. Geshi et al., 2012; Galland et al., 2014), mechanical layering of crustal strata (e.g. Kavanagh et al., 2006), interface strength between rock layers (e.g. Baer, 1991; Kavanagh and Pavier, 2014), and tectonic stresses (e.g. Paquet et al., 2007; Menand et al., 2010; Stephens et al., 2017). However, the physical properties of the magma can also affect the ability of a magma to intrude rather than erupt. These include magma overpressure (e.g. Lister and Kerr, 1991), flux (e.g. Fujita et al., 2004), rheology (including melt composition and the relative proportions of melt, bubbles and crystals, e.g. Castro et al., 2016), heat transfer (e.g. Annen and Sparks, 2002), and the coupling of magma and host-rock through magma buoyancy (e.g. Lister, 1991). How magmas flow, and how flow is preserved in the rock record during the emplacement and evolution of

sheet intrusions, is not often considered when investigating their formation. This contrasts with the study of larger igneous bodies, such as plutons, where the focus has been on magmatic processes and less with the interaction with the host-rock (e.g. Bons et al., 2015; Holness et al., 2017a; Kavanagh et al., 2018b).

There are two dominant models that explain the solidification of sheet intrusions, which has primary influence on how evidence of flow is preserved. The first model is typically applied to thin sills (<10 m) comprising a single pulse of magma which intrudes a colder host-rock and solidifies as a single unit via conductive cooling from the contact regions (e.g. Huppert and Sparks, 1989; Wartho et al., 2001; Petcovic and Dufek, 2005). This is often inferred from the presence of chilled margins at the contacts, and from symmetrical patterns of magma composition and mineral proportions across the interior of the solidified magma (e.g. Holness and Humphreys, 2003; Féménias et al., 2004). The second model is typically applied to thick intrusions (>10 m) where large volumes of magma are emplaced by multiple pulses which intrude in rapid succession into the same intrusion and homogenise (e.g. Annen, 2011; Menand, 2011; Holness et al., 2017a). There is good evidence that these relatively large volumes of magma can cool by convection (e.g. Holness et al., 2017a). Evidence of convection includes asymmetrical changes in chemistry, mineralogy, crystal preferred orientation and grain size distribution across the breadth of an intrusion (e.g. Holness and Humphreys, 2003; Holness et al., 2017a; Nicoli et al., 2018).

Rock structures such as macroscopic ropey surface textures (e.g. Liss et al., 2002; Schofield, 2009; Hoyer and Watkeys, 2017), strained and elongated vesicles (e.g. Coward, 1980; Varga et al., 1998; Hoyer and Watkeys, 2017), surface grooves, scour marks and striations (e.g. Smith, 1987; Varga et al., 1998) and steps, bridges and broken bridges (Thomson, 2007; Schofield, 2009; Magee et al., 2019) have been used to interpret local magma flow direction in ancient eroded magmatic intrusions. Microscale fabrics that potentially record magma flow include crystal preferred orientations (e.g. Geoffroy et al., 2002; Holness and Humphreys, 2003) and rock magnetic fabrics (e.g. Knight and Walker, 1988; Staudigel et al., 1992; Chadima et al., 2009; Magee et al., 2012). These microscopic fabrics are useful as they can record processes such as simple shear (e.g. Correa-Gomes et al., 2001), which can occur within both stationary and moving material (e.g. Holness et al., 2017a; Kendrick et al., 2017). When macroscale and microscale observations are used in combination (e.g. Mattsson et al., 2018), more complex emplacement histories can be unravelled. Studying two or (pseudo) three dimensional sections through crystallised bodies exposed by erosion (e.g. Summer Coon volcano, Colorado; Poland et al., 2004), can help to reconcile intrusion geometries and

flow patterns inferred from geophysical surveys (e.g. Thomson and Hutton, 2004; Thomson, 2007; Chadwick et al., 2011; Magee et al., 2018) and scaled analogue models (e.g. Kavanagh et al., 2006, 2015; Závada et al., 2009; Abdelmalak et al., 2012; Arbaret et al., 2013). An example of variable flow has recently been characterised in the analogue models of Kavanagh et al. (2018a) who identified flow circulation and channel development in a growing model dyke using particle image velocimetry.

Rock magnetic techniques, such as Anisotropy of Magnetic Susceptibility (AMS) or Anisotropy of Anhysteretic Remanent Magnetization (AARM), are commonly used to determine magma flow trajectories, with many studies applying one or both techniques to rock samples collected from dykes (e.g. Knight and Walker, 1988; Staudigel et al., 1992; Poland et al., 2004; Chadima et al., 2009; Silva et al., 2010) and sills (e.g. Liss et al., 2002; Polteau et al., 2008; Hrouda et al., 2015; Hoyer and Watkeys, 2017) of a wide range of magma composition and from various tectonic settings. However, these studies predominantly focus on measuring the initial magma flow direction by sampling near the intrusion contacts, resulting in a simplification and a potentially limited understanding of the overall emplacement history and how this changes through time. Problems can also arise deciphering the origin of the fabrics if other processes, such as shear along the fracture during emplacement (e.g. Correa-Gomes et al., 2001) or post emplacement alteration (e.g. Trindade et al., 2001; Archanjo and Launeau, 2004), have occurred.

This paper investigates how magnetic fabrics vary across the thickness of a relatively thin sill (6 m thick) from the Isle of Skye, Scotland. Rock magnetic analyses of closely-spaced rock samples of crystalline magma collected along the length and thickness of the sill provides a detailed account of how magnetic fabrics can vary spatially. We also present what we believe is one of the first applications of the AARM technique to understand sill emplacement histories. The AARM signals are compared with AMS fabrics and interpreted based on some basic petrographic analysis and simple thermal modelling to better our understanding of how syn- and post emplacement processes are recorded in magmatic intrusions, from sill propagation to solidification. We also make recommendations on how these techniques should be used to study magma flow in fossilised magma intrusions in the future.

3.3 Geological setting

To investigate how magnetic fabrics vary across the thickness of a sill we required a field location which provided a well exposed sill, with basal and upper contacts exposed, and a site that was easily accessible. As our study aims to collect rock samples at very high density, we also required an intrusion that was relatively thin (<10 m thick). To aid our interpretation

of our magnetic results we also required a site that had detailed petrographic work already available in the literature. Sills from the Trotternish Penninsula in the Isle of Skye fulfil all these criteria, and was therefore the ideal site where to conduct our study.

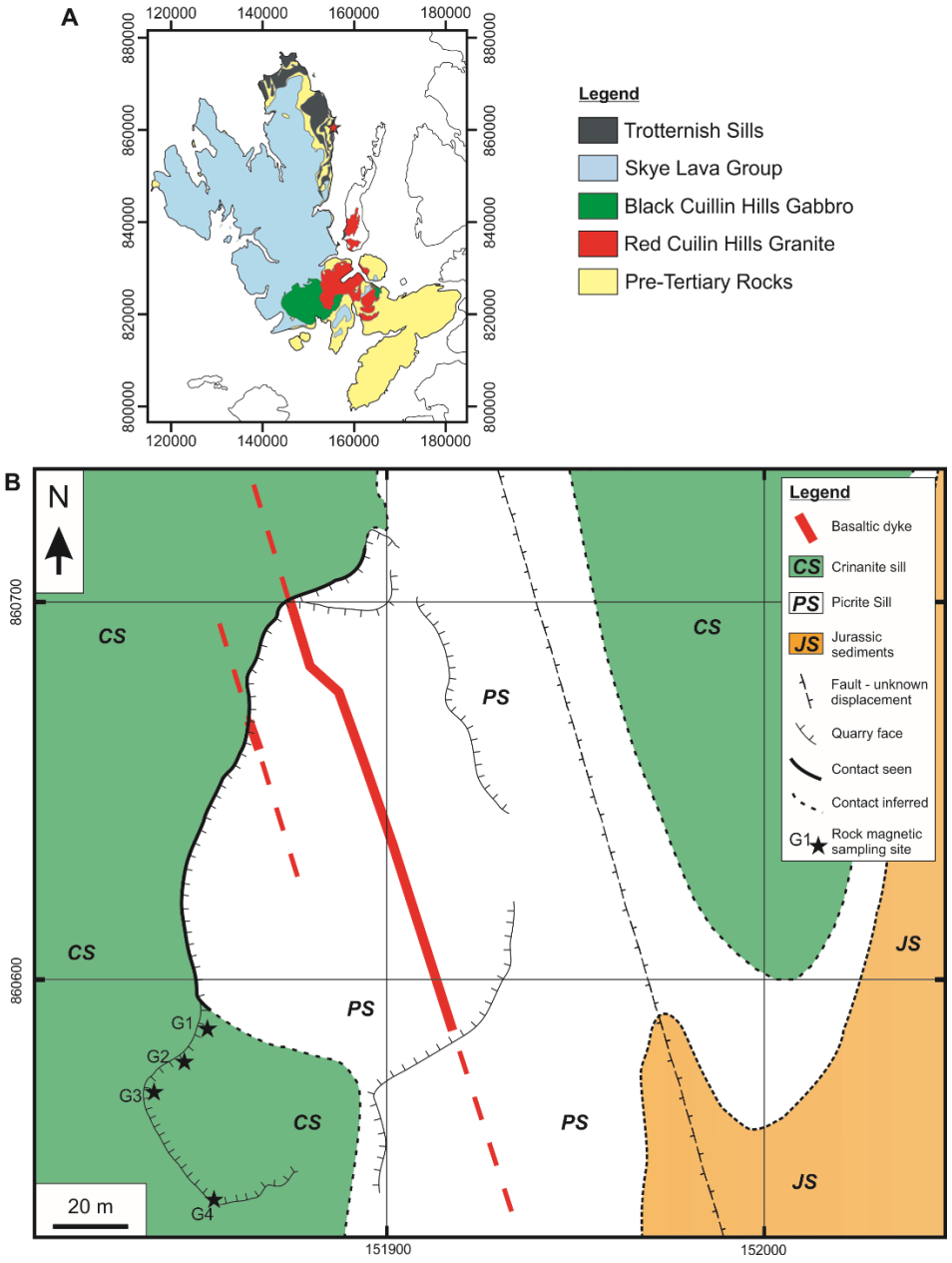

Figure 3.1 *Simplified geological map of the Isle of Skye (modified after EDINA Geology Digimap Service, 2008) showing location of Inver Tote (Red Star). (B) Geological map of disused quarry near Inver Tote, Isle of Skye, Scotland. Palaeogene age crinanite (CS) and picrite sills (PS) (green and white respectively) of the Little Minch Sill Complex, British and Irish Palaeogene Igneous Province, have intruded Jurassic sedimentary rocks (JS, orange). Cross cutting the area are two basaltic dykes (red). Locations of magnetic sampling sites are marked G1-4 in the SW end of the quarry.*

The Trotternish Peninsula is located in the north of the Isle of Skye, Northwest Scotland (Figure 3.1A). It is a 33 km long peninsula comprising a succession of Middle Jurassic sandstones and mudstones (~168 Ma) (Hudson and Trewin, 2002) capped by basaltic lava flows of the Skye Lava Group (~60 Ma) (Harris and Hudson, 1980; Gibb and Gibson, 1989; Emeleus and Bell, 2005). The sediments were intruded by a series of sills which comprise the Little Minch Sill Complex (LMSC), and are part of the British and Irish Palaeogene Igneous Province. The LMSC is considered to post-date the Skye Lava Group (Schofield, 2009; Hughes et al., 2015). The sills vary in composition from picrite (>40% olivine) to picrodolerite (15-40% olivine) to crinanite (analcime bearing olivine dolerite with <15% olivine) (Gibb and Henderson, 1984; Gibson and Jones, 1991; British Geological Survey, 2007). At a later stage, the region was crosscut by a series of NW-SE trending mafic dykes from the Skye Dyke Swarm (Hughes et al., 2015), a part of the North Britain Palaeogene Dyke Suite (Emeleus and Bell, 2005).

Structural mapping and rock sampling were conducted in an easily accessible quarry near Inver Tote (NG 51863 60609) (Figure 3.1) where a crinanite sill and a picrite sill (Figures 3.2A-B) have intruded sandstones and mudstones of the Elgol Sandstone Formation (Harris and Hudson, 1980). A combination of partially evolved olivine-bearing alkali-basalt parental magma and assimilated Lewisian Gneiss basement rocks have produced the crinanite composition (Gibson, 1990). At the site, and in the surrounding area, there are a series of NNW-SSE trending faults that cross-cut the sills (British Geological Survey, 2007). Within the quarry, two dykes from the Skye Dyke Swarm crop out parallel to the NNW-SSE striking faults.

The crinanite sill overlies the picrite sill and underlies Jurassic sedimentary rocks (Figure 3.2A). Its upper contact was not directly observed as the Jurassic host rocks have since been eroded, however following Gibson and Jones (1991) we infer that the resistant and exposed upper flat-lying surface of the quarry is the top of the sill. In the quarry, the crinanite sill has a thickness varying between 5 and 6 metres, with the upper surface being undulatory Schofield (2009). Schofield (2009) also suggested that the sill propagated as a series of fingers from a NNW to SSE direction, and that these fingers then merged during sill inflation. The lower contact of the crinanite sill has an overall strike of approximately 000/05º W, however it is undulose and trends 143/13° SW in the southern part of the quarry and 039/10° NW in the northern part. The underlying picrite sill is >15 and up to 42 metres thick (Gibson and Jones, 1991). There is a chilled margin at the base of the crinanite sill, however columnar jointing is continuous across the margin (Figure 3.2B).

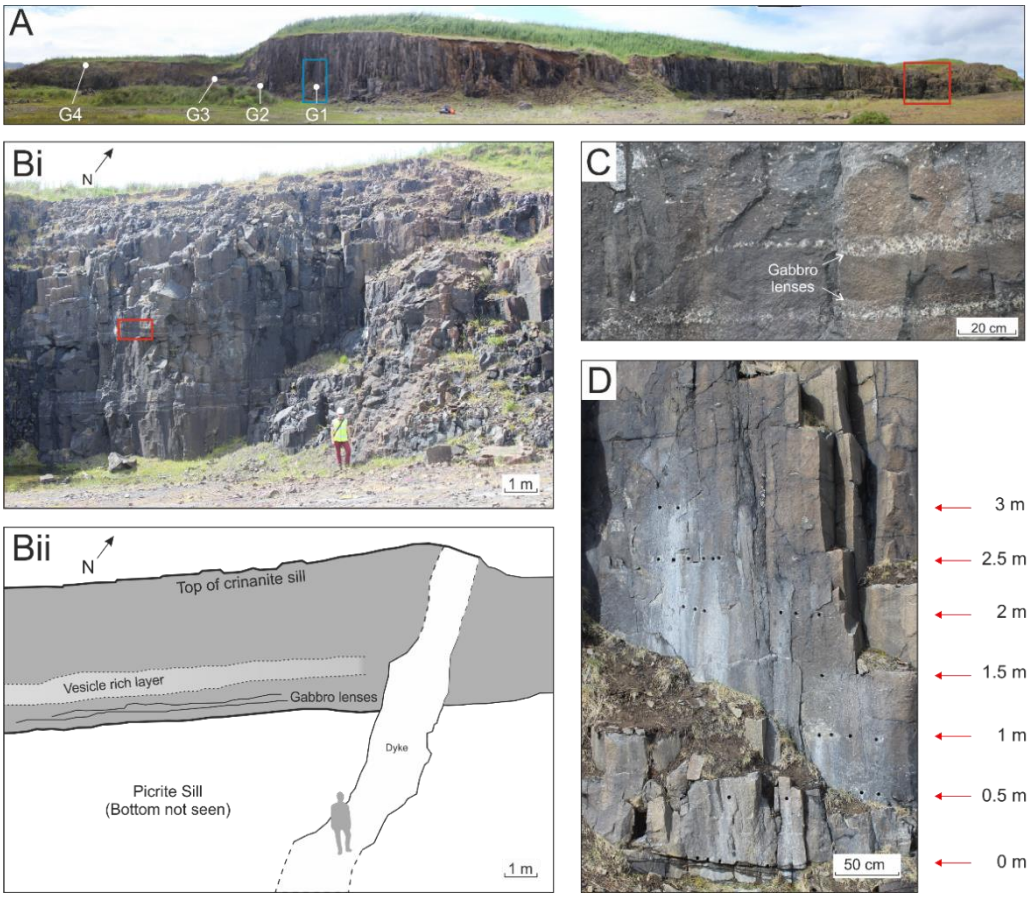

Figure 3.2 *Field photographs of crinanite and picrite sills that crop out in a quarry at Inver Tote. (A) Overview panoramic photograph showing magnetic sampling sites (G1-4), and the blue and red boxes are the locations of photos (B and D). (Bi) Photograph showing a crinanite sill, a picrite sill and a basaltic dyke. The red box is the location of photograph (C), and (Bii) is an interpretive drawing of (Bi) which shows the location of the units present. (C) Photograph of the lower portion of the crinanite sill showing the gabbro lenses. (D) Photograph of drill holes across the lowest 3 m of sampling heights in the crinanite sill (location G1).*

Within the crinanite, there are a series of horizontally elongate and laterally extensive gabbro lenses up to a 10 cm in thickness (Figure 3.2B-C). These are similar in composition to pegmatitic gabbro lenses mentioned by other authors who have published on the area (e.g. Gibson and Jones, 1991; Nicoli et al., 2018). There are also occasional amygdale rich bands throughout the thickness of the sill (Figure 3.2Bii). Vesicles are up to several centimetres in size; the smaller ones are spherical, but larger ones are flatter and elongate, with their short axes perpendicular to the sill plane. The largest vesicle observed was 20 cm long and 8 cm wide, and had a long axis oriented approximately ENE. Analcime is present as vesicle infill. Previous work in the area does not mention a crystal cargo within the crinanite at Inver Tote (e.g. Gibson and Jones, 1991), however it is present in other sills in the region such as the Shiant Isles picrodoleritie/crinanite unit (Holness et al., 2017a) and the Dun Raisburgh

crinanite (Nicoli et al., 2018) which have an approximant 3% crystal cargo consisting of olivine and plagioclase.

3.4 Rock magnetism and its application to volcanic rocks

Rock magnetism and magnetic anisotropy are commonly used in sedimentology, palaeontology, tectonics and volcanology to understand formational processes, determine rock ages, and palaeocurrent or flow trajectories (e.g. Blundell, 1957; Tauxe, 2010). Rock magnetism is often used to determine models of emplacement of dykes and sills, magma flow trajectories, and to infer intrusion source locations (e.g. Olazabal et al., 1999; Poland et al., 2004; O'Driscoll et al., 2006; Magee et al., 2018). In this study, we use anisotropy of magnetic susceptibility (AMS) and anisotropy of anhysteretic magnetisation (AARM) to understand variations in magma flow trajectories, and to decipher magma flow and solidification processes across the breadth of the crinanite sill.

Magnetic susceptibility is the study of how susceptible a sample is to gaining an induced magnetic field (Knight and Walker, 1988; Raposo and Ernesto, 1995) and is affected by the domain state, shape, size and orientation of all magnetic minerals (dia-, para- and ferro-magnetic) present in the sample (Khan, 1962). AMS is then the directional-dependent response of the magnetic minerals within the sample to the applied field (Knight and Walker, 1988; Raposo and Ernesto, 1995). Some phases, such as magnetite, often dominate the magnetic signal when present (e.g. Hargraves et al., 1991), however, this is dependant on the proportion of other magnetic minerals present. AARM differs from AMS in that it is used to study the fabric originating from magnetic remanence carrying grains, which tend to be single-domain (SD) or vortex-state (VS) in nature (McCabe et al., 1985; Jackson, 1991). The AARM fabric that the ferromagnetic minerals exhibit is linked to their ability to obtain an anhysteretic remanence (laboratory magnetisation). The ferromagnetic minerals that give rise to the AARM signal often occur as silicate mineral-hosted magnetites (Cheadle and Gee, 2017).

Magnetic susceptibility (K) is defined as;

$$K = \frac{M_i}{H} \tag{3.1}$$

where M_i is the degree of induced magnetization and H is the strength of the magnetic field. The magnetic susceptibility of a sample is characterised by a second order ellipsoid tensor (Khan, 1962), which has three principle eigenvectors: K_1, K_2 and K_3, where K_1 is the longest axis, K_2 is the intermediate axis and K_3 is the shortest axis (Knight and Walker, 1988). The ratio between the magnitudes of the different tensor axes gives rise to a range of ellipsoid

properties: lineation (*L*), foliation (*F*), degree of anisotropy (*Pj*) and shape parameter (*T*). There are four different shapes exhibited by an AMS ellipsoid: spheroidal ($K_1 = K_2 = K_3$), oblate ($K_1 > K_2 = K_3$), prolate ($K_1 = K_2 > K_3$) and tri-axial ($K_1 > K_2 > K_3$) (Tauxe, 2010). Ellipsoid tensor shapes can be used to interpret magmatic fabrics (e.g. Knight and Walker, 1988). Prolate shaped ellipsoids are commonly known as magnetic lineation (Table 3.1), being similar to the long axis of elongate crystals in magmatic rocks (Geoffroy et al., 2002). In comparison, oblate shaped ellipsoids give rise to magnetic foliation (Table 3.1), similar to the planar arrangement of tabular phenocrysts. AARM also utilizes a second order ellipsoid tensor, with the same ellipsoid descriptions, and is defined as $K_{(rem)}$ which is calculated by averaging different directions of imparted anhysteretic remanent magnetisations.

Table 3.1: *Anisotropy parameters used by Anisoft software and can be found in Jelínek (1981). K_1, K_2 and K_3 are principal susceptibility axes, with η_1, η_2 and η_3 being their natural logarithms with $\eta = (\eta_1 + \eta_2 + \eta_3)/3$.*

Parameter		Solution
Mean Susceptibility	K_m	$(K_1+K_2+K_3)/3$
Lineation	L	K_1/K_2
Foliation	F	K_2/K_3
Corrected degree of anisotropy	P_j	$exp\sqrt{2[(\eta_1-\eta)^2+(\eta_2-\eta)^2+(\eta_3-\eta)^2]}$
Shape parameter	T	$(2\eta_2-\eta_1-\eta_3)\ /\ (\eta_1-\eta_3)$

Combining the measured magnitude and orientation of ellipsoid tensors with field and petrological observations is used to infer magma flow that built now static, solidified magma bodies (e.g. Chadima et al., 2009; Liss et al., 2002; Varga et al., 1998). AMS has commonly been used to understand intrusive processes with many studies implementing the technique to interpret the observed fabrics (e.g. Knight and Walker, 1988; Staudigel et al., 1992; Roni et al., 2014). AARM has been used in many studies to infer the emplacement processes of dykes (e.g. Chadima et al., 2009; Silva et al., 2010; Soriano et al., 2016) and the Stillwater Igneous Complex, Montana, USA (Selkin et al., 2014), with only one study applying the technique to study sill emplacement (Hrouda et al., 2015).

When the AMS K_1 axis is aligned with the long axis of the magnetic crystals (and phenocrysts when present) or with AARM K_1 axis, and these are parallel to intrusion margins, this is known as a normal fabric (Rochette et al., 1992; Ferré, 2002; Chadima et al., 2009). In this case the K_3 axis are also parallel to the short axis of a crystal or the AARM K_3 axis, i.e. magnetic lineation and magnetic foliation are both parallel, and can be used to infer the magma flow

direction. At the margin regions of mafic intrusions AMS fabrics can be imbricated, which suggests that the magnetic minerals have been reoriented by simple shear conditions imparted by the flowing magma experiencing variations in strain rate imparted at a no-slip boundary with the host-rock (e.g. Knight and Walker, 1988; Rochette et al., 1992). In these situations, the imbricated magnetic lineation and foliation can be used to interpret the sense of magma flow during initial emplacement (Chadima et al., 2009; Geoffroy et al., 2002). Inverse fabrics occur when the AMS K_1 and K_3 axes are inverted with respect to crystal long axes or AARM K_1 and K_3 axes and the intrusion margins. In these situations, the origin of inverse fabrics is often related to SD crystals dominating the magnetic fabric (Potter and Stephenson, 1988; Rochette et al., 1992; Ferré, 2002). Anomalous fabrics are characterised by AMS and AARM ellipsoids with axes in orientations that fit neither a normal or inverse fabric (Soriano et al., 2016), the origins of which have been widely debated. Examples include: combinations of SD and multi-domain (MD) particles that produce the fabrics (Potter and Stephenson, 1988; Rochette et al., 1991), and processes such as syn- or post emplacement shear along the crack (Dragoni et al., 1997; Clemente et al., 2007), alteration (Rochette et al., 1991), or cooling contraction (Hrouda et al., 2015).

3.5 Methodology

3.5.1 Sampling

The crinanite sill was chosen as the ideal candidate to sample for our magnetic analysis. The quarry outcrop provides excellent exposure and access to the entire sill thickness, spanning the top and bottom contacts (6 m in total) and extending over ~45 m of sill length due to sampling logistics and field safety. Sampling was also conducted along the inferred axis of a finger-like morphology described by Schofield (2009).

Seventy-eight 2 cm diameter cores, up to 10 cm long, were collected at 50 cm intervals spanning the 6-metre thickness of the crinanite sill and spread laterally across 4 sample sites (G1-4 in Figures 3.1 and 3.2A). The samples were collected using a chainsaw motor-driven Stihl BT45 core drill. Six cores were collected at each 50 cm height interval (Figure 3.2D, Table 3.2). There was overlap in the sampled heights at the sites to enable correlation between them to be assessed during subsequent data processing and analysis. Cores were drilled horizontally, approximately in-plane with the sill, and were oriented in situ using both sun and magnetic compasses. In the laboratory, the rock cores were sliced into 2.2 cm long specimens, with each core producing one to three specimens, yielding a total of 147 specimens which were used for magnetic anisotropy analyses. Additional hand-sized oriented and unoriented rock samples were taken for basic petrographic analysis (Table 3.2).

Table 3.2: *Table showing the location and heights of thin sections for petrology and the number of cores collected for magnetic anisotropy studies. The number of specimens cut from the cores is also shown; *represents heights where one less specimen was used for AARM analysis.*

Height (m)	Description	Thin sections from hand specimens	Samples for AMS/AARM analysis	
			Number of cores	Number of specimens obtained from cores for use in magnetic analysis
0	Crinanite, including chilled margin	LMS-6, LMS-19-0m	6	13
0.3	Gabbro lens	LMS-5b-h, LMS-5b-v	n/a	n/a
0.5	Crinanite	-	6	12*
1.0	Crinanite	LMS-19-1m	6	11
1.5	Crinanite	-	6	9
2.0	Crinanite	LMS-19-2m	6	10*
2.5	Crinanite	-	6	10
3.0	Crinanite	LMS-7, LMS-19-3m	6	11*
3.5	Crinanite	-	6	11*
4.0	Crinanite	LMS-19-4m	6	12*
4.5	Crinanite	-	6	12*
5.0	Crinanite	LMS-19-5m	6	12*
5.5	Crinanite	-	6	12
6.0	Crinanite	LMS-8, LMS-19-6m	6	12

3.5.2 Characterisation of magnetic carriers

A key step in any rock magnetism study is accurate identification of the magnetic carriers that produce the AMS or AARM fabrics. Identification of the magnetic carriers in the Invertote crinanite sill was undertaken using core offcuts at each sampling height and taking three approaches: 1) multi-technique analysis using a variable field translation balance (VFTB), 2) high temperature susceptibility, and 3) three-component thermal demagnetisation, known as the Lowrie method (Lowrie, 1990).

Our VFTB measures the isothermal remanent magnetisation (IRM) acquisition and backfield demagnetisation curves, hysteresis loops, and thermomagnetic curves of a sample to characterise the properties of its magnetic carriers and thus help identify the mineral populations giving rise to the observed fabrics. Masses of 150 mg of fine powdered rock from core offcuts were measured for their IRM by applying a magnetic field, removing the field and then measuring the magnetization to see how well the sample takes the applied field,

stepwise to +800 mT. Backfield measurements were then made in a similar way but with an oppositely directed field of up to -800 mT. Hysteresis was then measured during the application of a field in one direction, then when the field is inverted and then in the original direction again. Finally, each sample underwent cyclic heating and cooling in a constant high field of 240 mT from 50 °C to 200 °C then back to 50 °C, before repeating and increasing the maximum temperature in 100 °C intervals for each cycle, up to a maximum temperature of 700 °C.

This determined the Curie temperatures of each of the magnetic carriers, which are specific to mineral composition. Data was subsequently analysed using the RockMagAnalyzer 1.0 software (Leonhardt, 2006).

High temperature susceptibility measurements were performed on fresh crushed samples from the core offcuts using the MFK-1A Kappabridge from AGICO (Advanced Geoscience Instruments Company). The temperature was incrementally increased from 30 °C to 700 °C and then decreased back to 40 °C with the magnetic susceptibility measured incrementally. The data was then analysed using the Cureval8 software from AGICO (Chadima and Hrouda, 2012).

Three-component thermal demagnetisation experiments using a modified version of the Lowrie (1990) method were conducted to identify unblocking temperatures of magnetic carriers giving rise to the signal observed in the AARM analyses. Unblocking temperatures are the temperature at which the coercive force of a grain is overcome by thermal fluctuations resulting in its demagnetisation. In these experiments, the different strength fields are applied to a core specimen, after AMS and AARM analyses were performed on the specimen, in decreasing magnitudes along the X, Y and Z axes of a representative cylindrical sub-specimen. The field strengths used were: x-axis of 1.5 T, y-axis of 0.4 T and z-axis of 0.02 T, which are the limits of the pulse magnetisers used, and were also chosen to identify specific phases identified during other thermomagnetic characterisation experiments. Each specimen was then heated and cooled in steps of between 20 and 50 °C, up to a maximum of 620 °C. These temperatures were chosen as temperatures where we believe the magnetic remanence is predicted to change the fastest, i.e. just below the Curie temperatures of minerals that are believed to give rise to the magnetic signals.

3.5.3 Magnetic anisotropy

AMS analyses were undertaken using a MFK1-A Kappabridge from AGICO using an applied field of 200 A m^{-1} and a frequency of 967 Hz, where each specimen was rotated along three

axes whilst a magnetic field was induced and measured before being processed into a mean tensor and projected onto a stereonet using AGICO's Safyr7 software (Chadima et al., 2018c). The AMS tensor three-axis orientations were analysed in AGICO's Anisoft4.2 software (Chadima and Jelinek, 2009) for processing anisotropy data, utilising Jelinek statistics (Jelínek, 1977, 1981). Susceptibilities are accurate to within 1% error.

Measurement of AARM was undertaken using a JR-6A dual speed spinner magnetometer, LDA5 alternating field (AF) demagnetiser and PAM1 anhysteretic and pulse magnetiser from AGICO. Each specimen underwent a multi-stage manual measurement of the natural remanent magnetisation, demagnetisation and subsequent remagnetisation procedure. Initial measurement of the natural remanent magnetisation (NRM) was made using the JR-6A spinner magnetometer and Rema6 instrument control software (Chadima et al., 2018b), before demagnetisation in a 100 mT alternating current (AC) field using the LDA5 AF demagnetiser. An anhysteretic remanent magnetisation was then applied to each sample in incrementally increasing direct current (DC) fields up to 500 µT, with subsequent measurements using the JR-6A and Rema6 software to determine the saturation magnetisation for each specimen. As the peak capable field, but one still below the saturation values of the field, 500 mT was used as the DC field strength for AARM acquisition. A six-position bias field application and measurement sequence was used for each specimen, with the data subsequently analysed using the Anisoft42 software (Chadima and Jelinek, 2009) to determine AARM tensor orientations.

3.5.4 Petrographic characterisation

Basic characterisation of the petrological textures of the crinanite was undertaken by analysing thin sections from twelve samples (Table 3.2) using Meiji MT9000 and NIKON Eclipse LV100Pol polarising microscopes. Seven of these samples, collected at 1 m intervals across the sill thickness, were oriented during collection and their thin sections were made in a N-S orientation that was perpendicular to the sill plane. Three additional un-oriented samples were collected from the central region, upper and lower contacts of the sill, and two samples were analysed from the gabbro lenses. Micro-scale imaging was completed by scanning electron microscopy using a Meiji TM3000 with a 15 eV beam current, and images processed using the Bruker Quantax 70 software. Quantitative Element Mapping using Scanning Electron Microscopy (QEMSCAN) was conducted on a FEI WellSite QEMSCAN for analysis of geochemistry from energy dispersive X-ray spectrometry. The Wellsite QEMSCAN SEM used a W-filament, operating at 15 kV. Two different measurement resolutions of 2 and

20 µm were used for QEMSCAN elemental mapping of the entire thin sections (up to 2 mm from each side).

3.6 Results

3.6.1 Rock Magnetism

3.6.1.1 *Thermomagnetic Experiments*

Thermomagnetic curves of in-field magnetisation (Figures 3.3Ai-iv) show two significant changes in magnetisation during cyclic heating of the crinanite sill samples. The first change occurred between 400 and 500 °C, causing the cooling curve from 500 °C to not overly the heating curve, perhaps due to alteration associated with incomplete oxyexsolution and resulting in the production of a higher Ti-titanomagnetite during heating. A subsequent small drop in magnetisation occurred at approximately 580 °C, indicating the presence of a small portion of almost pure magnetite.

3.6.1.2 *High Temperature Susceptibility Experiments*

High temperature susceptibility measurements on one sample from each height through the crinanite sill show similar patterns in both heating and cooling curves (Figure 3.3Bi-iv). During heating, the large drop in magnetisation at around 480 °C signifies the Curie temperature has been met and corresponds with the presence of low Ti-titanomagnetite (~Ti_{10}, i.e. titanomagnetite with approximately 10% Ti-content) for all samples (Akimoto, 1962). In all cases, the cooling curves do not follow the same trend as the heating curves, indicating that heating-induced alteration occurred. We interpret these results to mean a small amount of magnetite and a large amount of a Ti-rich titanomagnetite (possibly around Ti_{50}) was produced during heating, however some of the original low Ti-titanomagnetite remained (Figure 3.3Bi-iv).

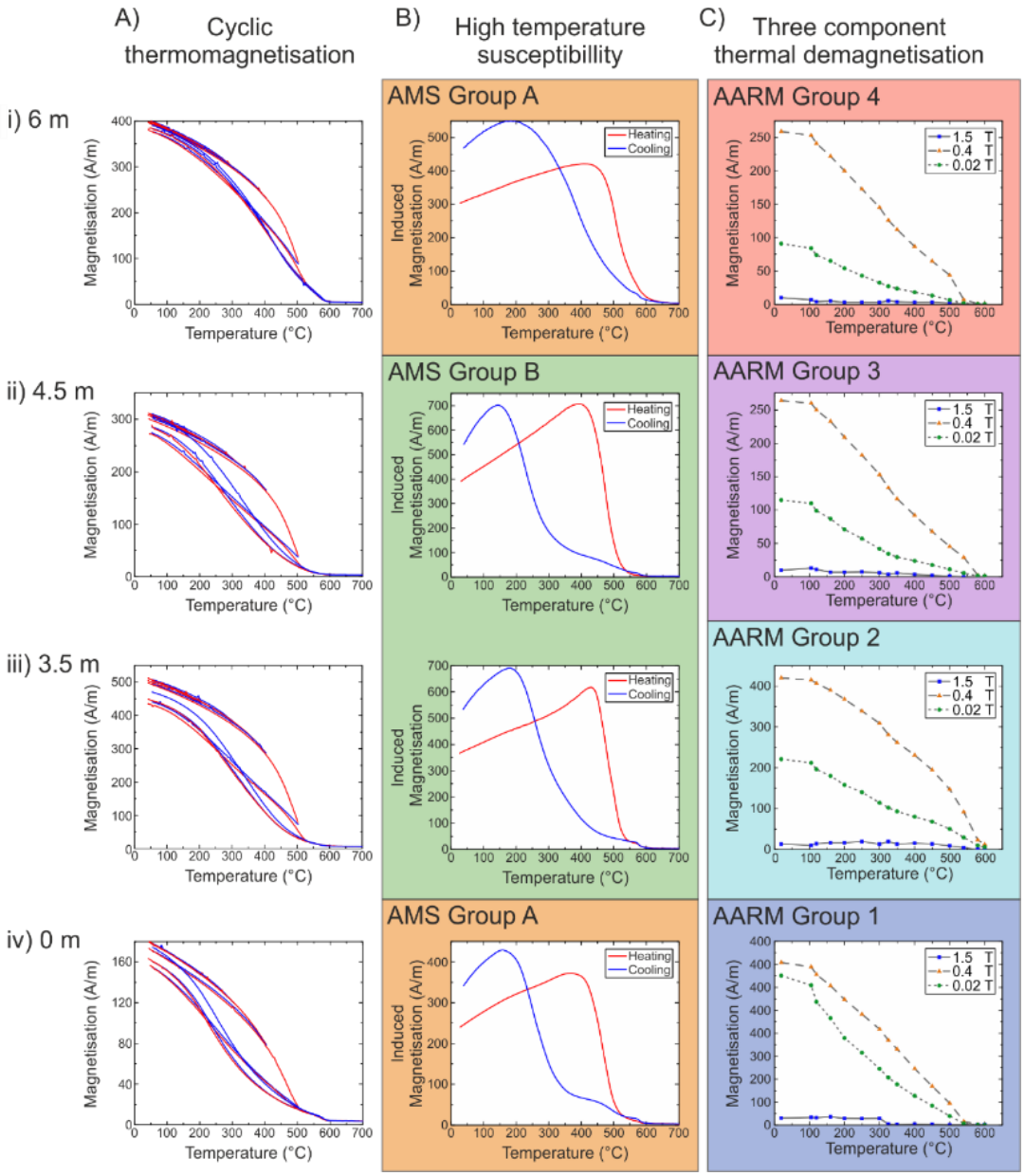

Figure 3.3 *Graphs showing data from (A) cyclic thermomagnetization, (B) high temperature susceptibility and (C) three component thermal demagnetization experiments for identification of magnetic carriers at select heights through the crinanite sill (see Table 2): (i) 6 m (the upper contact, sample 6.0b-G4), (ii) 4.5 m (sample 4.5a-G3), (iii) 3.5 m (sample 3.5a-G3), and (iv) 0 m (the lower contact, sample 0.0a-G1). In (A,B) the red curves are heating measurements and blue curves are cooling measurements. Background colours in (B,C) represent the two AMS and four AARM groups.*

3.6.1.3 *Lowrie Experiments*

Results from the modified Lowrie test show that the strongest components are in the 0.4 T range with gradually decreasing unblocking temperatures to a maximum of 580 °C (Figure 3.3Ci-iv), which is indicative of a range of Ti-titanomagnetite compositions. There is also a decrease in the relative proportion of the 0.02 T signal compared to the 0.4 T signal with

increasing height through the sill (Figures 3.3Ci-iv). This indicates a fining of the grain size due to a decrease in the amount of a softer, more multi-domain phase being detected by the 0.02 T strength signal. The unblocking temperature also increases from 560-570 °C at the margins of the sill to 580-600 °C towards the centre of the sill (Figure 3.4a), which possibly relates to the longer cooling time away from the margins allowing oxyexsolution to progress further. The fining of the grain size with increased height through the sill can also be seen in a Day plot (Day, Fuller, & Schmidt, 1977) where all samples fall within the VS region, but the samples at 0-50 cm heights plot closer to the MD region (Figure 3.4b) and the rest of the samples cluster towards lower Bcr/Bc values and slightly higher Mrs/Ms values (where Bcr is coercivity of remanence, Bc is bulk coercivity, Mrs is the remanent magnetic saturation and Ms is magnetic saturation). Overall, the thermomagnetic results and Lowie experiments produce a consistent signal of a mixture of MD to SD titanomagnetite that is the dominant source of the rock magnetic signals.

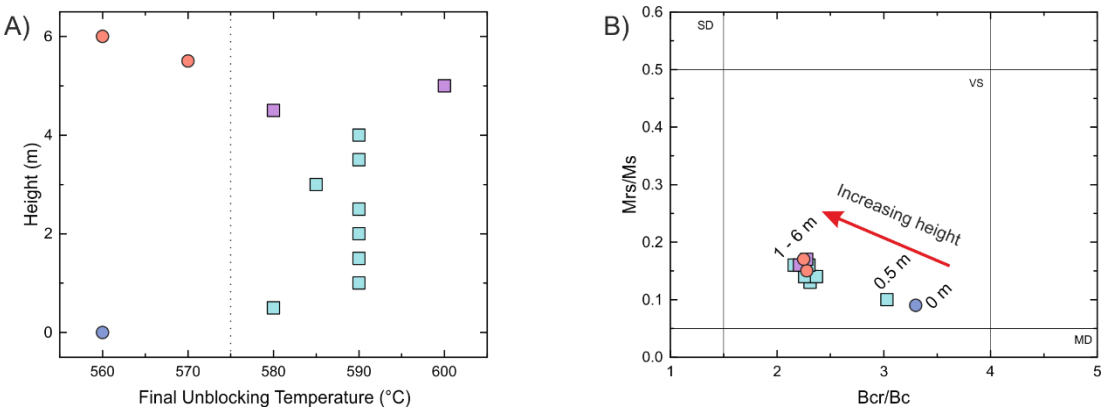

Figure 3.4 *Graphs showing results from experiments to identify the magnetic carriers and their domain states at each 0.5 m height across the crinanite sill thickness. (A) Unblocking temperatures against height, obtained from three component demagnetization experiments (modified Lowrie method), where the vertical dashed line separates the AMS groupings, and (B) Day plot showing single-domain (SD), vortex-state (VS) and multi-domain (MD) states, where Bcr/Bc is coercivity of remanence relative to bulk coercivity and Mrs/Ms is the remanent magnetic saturation relative to magnetic saturation calculated from hysteresis experiments. In both plots, circles indicate AMS group A and squares indicate AMS group B, and the colours indicate the 4 AARM groupings identified from ellipsoid orientations in Figure 3.6.*

3.6.2 Anisotropy of Magnetic Susceptibility

To visualise the AMS fabrics across the thickness of the crinanite sill a series of equal area diagrams are plotted, first presenting all of the measurements together to identify overall AMS patterns (Figure 3.5a). The combined measurements of all 147 specimens from the sill show an oblate AMS fabric, with the mean K_1 axis showing a shallow inclination to the north

east (Figure 3.5a). The overall mean K_3 axis is almost vertical. Combining all data together allows for a general fabric to be observed, however, there is a lot of scatter evident across the individual specimens, as observed in the wide 95% confidence angles for each axes of ellipsoid, e.g. mean K_1 orientation of 44.7° ± 46.5° declination with an inclination of 6.9° ± 21.5° (see Table 3.3).

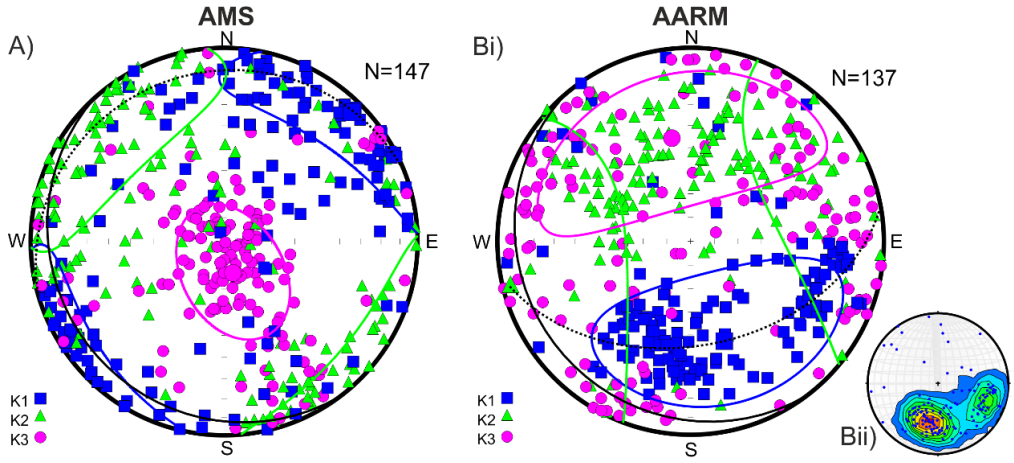

Figure 3.5 *Equal area plots of data from all specimens for both (A) AMS data (N = 147) and (B) AARM data (N = 137) with (Bi) representing data for all axes and (Bii) showing a contour plot of K1 axes. K1 axes are blue squares, K2 axes are green triangles and K3 axes are purple circles. Solid lines are the 95% confidence ellipses calculated by Anisoft 4.2. Solid black line represents the sill plane and the dashed black line represents the magnetic foliation plane.*

Equal area diagrams displaying the data separated into their respective heights shows distinct variations in AMS fabrics across the crinanite sill thickness (Figure 3.6a). The mean orientation of the tensors varies with height, with the K_1 axis in a broadly N-S orientation at the bottom contact, rotating to a NE-SW orientation between 0.5 and 5.0 metres in height, and rotating back to a N-S orientation at 5.5-6.0 metre heights (Figure 3.6a). The mean K_3 short axis is close to perpendicular to the sill plane, except between 3.0 and 4.5 m where they are inclined to either the south-east or south-west. At the 4.0-4.5 m heights, there is a large amount of scatter in the data, resulting in ellipsoids with wide ranging 95% confidence angles e.g. at 4.0 m the K_1 axis has a declination of 40.5° ± 40.9° and an inclination of 27.2° ± 34.3° (see Table 3.3). A small increase in K_m from 9.43 x 10^{-3} to 1.5 x 10^{-2} is observed from 0 to 1.0 m, after which K_m becomes more constant with a peak in mean susceptibility of 1.77 x 10^{-2} occurring at 3.5 m height (Figure 3.7Ai). Both magnetic lineation and magnetic foliation are characterised by mean variations in axis length of <1 and <1.25% respectively (Figures 3.7Aii-iii). The AMS foliations are consistently near parallel to the sill plane. However, at the lower margin the AMS foliation dips slightly towards the north (similarly to the K_1 axis). We

interpret this dip to be the result of an imbrication process that has developed during magma flow. This imbrication towards the south therefore reflect the flow direction being to the south at the time of solidification. Its location at the sill margin suggests this was the initial propagation direction of the growing sill. The other location where the AMS foliations are not aligned with the sill plane are between 3.0 and 4.5 heights, where the ellipsoids have rotated around either the K_1 (3-3.5 m) or K_2 (4-4.5 m) axes, by approximately 50° and 60° respectively. Low degrees of anisotropy (mean P_j values less than 2%) indicate that the ellipsoid shapes are close to spherical (Figure 3.7Aiv) suggesting a near uniform orientation of the larger MD magnetic minerals. The shape of the ellipsoid tensors (shown mostly by variations in the mean shape (Figure 3.7Av) varies across the sill thickness in an irregular and oscillatory manner.

Collectively the results suggest the AMS fabrics can be separated into two groups based only on the orientation of the ellipsoids, as the other parameters (L, F, P_j, T) show oscillatory trends throughout the sill thickness and as such cross the identified group boundaries. Group A fabrics (orange vertical bars in Figure 3.6A) are characterised by the mean K_1 axes that are trending in a N-S orientation with the mean k_3 axes perpendicular to the sill plane. It occurs at the lower sill margin (0 m) where it contacts the underlying picrite sill and the upper sill margin (5.5-6 m) where the sill it in contact with the overlying country rock. The thickness of the Group A fabrics is asymmetric, being <0.5 m thick at the lower contact (only evident in the 0 m height sample) and <1.5 m thick at the upper contact (evident in the 5.5 m and 6 m height samples). Group B fabrics (green vertical bar in Figure 3.6A) are characterised by the mean K_1 axis trending in a NE-SW orientation, with the mean K_3 axis still vertical but with variations of inclinations towards the SE and SW (e.g. at 3.5 and 4.0 m respectively). It occurs across the whole of the sill interior (0.5 – 5 m).

Table 3.3: *Table showing the location and heights of thin sections for petrology and the number of cores collected for magnetic anisotropy studies. The number of specimens cut from the cores is also shown; *represents heights where one less specimen was used for AARM analysis.*

AMS

Height	Number of Specimens	K_1			K_2			K_3		
		$k_1/1$	Declination	Inclination	$k_2/1$	Declination	Inclination	$k_3/1$	Declination	Inclination
Overall	147	1.003	44.7 ± 46.5	6.9 ± 21.5	1.001	313.2 ± 46.3	11.7 ± 30.2	0.996	164.4 ± 30.9	76.4 ± 21.2
0.0	13	1.007	355.7 ± 31.8	19.3 ± 7.6	1.002	86.6 ± 31.6	2.4 ± 13.8	0.991	183.3 ± 14.8	70.5 ± 8.7
0.5	12	1.004	234.8 ± 11.2	7.3 ± 5.9	0.999	324.9 ± 21.1	0.2 ± 8.5	0.996	56.8 ± 20.8	82.7 ± 8.5
1.0	11	1.003	235.2 ± 44.9	2.1 ± 12.3	1.002	145.0 ± 44.9	5.2 ± 13.2	0.995	347.5 ± 16.0	84.4 ± 8.4
1.5	9	1.008	240.7 ± 23.7	9.3 ± 12.8	1.001	332.1 ± 28.4	8.0 ± 7.5	0.990	102.1 ± 19.1	77.7 ± 12.7
2.0	10	1.004	238.8 ± 14.3	4.7 ± 4.8	0.999	148.0 ± 43.4	9.8 ± 9.4	0.997	354.1 ± 42.9	79.1 ± 4.9
2.5	10	1.004	230.6 ± 27.5	4.9 ± 7.5	1.001	321.3 ± 27.4	8.4 ± 12.0	0.995	110.7 ± 12.9	80.3 ± 6.1
3.0	11	1.004	51.3 ± 41.9	14.7 ± 7.7	1.002	308.7 ± 42.4	39.9 ± 22.7	0.994	157.3 ± 25.0	46.4 ± 5.6
3.5	11	1.004	57.5 ± 10.0	3.1 ± 8.9	0.999	323.8 ± 61.5	49.9 ± 9.5	0.997	159.1 ± 61.6	39.9 ± 9.4
4.0	12	1.003	40.5 ± 40.9	27.2 ± 34.3	0.999	309.2 ± 69.0	2.6 ± 39.7	0.998	214.2 ± 69.0	62.7 ± 32.4
4.5	12	1.002	83.4 ± 61.2	59.2 ± 43.7	1.000	336.0 ± 59.6	10.2 ± 36.9	0.998	240.3 ± 51.7	28.8 ± 29.1
5.0	12	1.003	58.7 ± 51.0	7.5 ± 20.0	1.001	327.4 ± 51.0	9.9 ± 25.6	0.996	185.3 ± 26.6	77.6 ± 18.9
5.5	12	1.003	342.8 ± 35.9	3.3 ± 11.9	0.999	77.3 ± 79.2	53.2 ± 18.9	0.998	250.3 ± 79.1	36.6 ± 11.6
6.0	12	1.005	21.5 ± 14.1	11.8 ± 13.0	0.999	111.7 ± 15.9	1.0 ± 8.5	0.995	206.6 ± 16.9	78.2 ± 8.1

AARM

Height	Number of Specimens	K_1			K_2			K_3		
		$k_1/1$	Declination	Inclination	$k_2/1$	Declination	Inclination	$k_3/1$	Declination	Inclination
Overall	137	1.014	161.4 ± 52.3	44.7 ± 30.5	0.995	255.5 ± 62.3	4.2 ± 51.8	0.991	349.7 ± 62.1	45.0 ± 30.5
0.0	13	1.021	348.4 ± 59.8	10.6 ± 17.6	1.005	80.2 ± 61.1	9.6 ± 21.6	0.974	211.4 ± 44.4	75.6 ± 19.8
0.5	10	1.021	209.8 ± 14.9	49.1 ± 11.3	0.991	315.7 ± 58.7	13.4 ± 8.8	0.988	56.3 ± 58.4	37.8 ± 11.6
1.0	10	1.014	190.2 ± 19.9	38.2 ± 11.2	0.996	329.7 ± 59.8	44.0 ± 12.1	0.990	82.1 ± 59.9	21.5 ± 17.1
1.5	9	1.030	193.7 ± 15.9	40.6 ± 8.4	0.990	291.9 ± 28.6	9.5 ± 14.4	0.980	32.6 ± 28.7	47.9 ± 8.9
2.0	9	1.012	223.9 ±40.7	65.4 ± 9.7	1.001	47.8 ± 41.7	24.5 ± 24.0	0.987	317.1 ± 26.7	1.5 ± 9.7
2.5	9	1.022	185.3 ± 14.1	39.5 ± 12.3	0.995	37.0. ± 27.1	45.9 ± 12.8	0.982	289.4 ± 26.7	16.4 ± 12.7
3.0	11	1.035	182.0 ± 13.0	47.9 ± 6.5	0.992	2.9 ± 20.4	42.1 ± 8.9	0.974	272.5 ± 20.4	0.4 ± 10.9
3.5	10	1.012	208.6 ± 53.5	49.6 ± 20.9	1.001	67.8 ± 56.4	33.4 ± 24.0	0.987	323.9 ± 42.0	20.0 ± 22.8
4.0	11	1.020	199.5 ± 28.3	47.7 ± 9.5	0.995	308.4 ± 56.9	16.4 ± 23.5	0.985	51.5 ± 56.8	37.6 ± 6.7
4.5	11	1.029	173.3 ± 22.3	46.2 ± 10.3	0.991	355.3 ± 36.6	43.8 ± 14.4	0.980	264.4 ± 35.8	1.0 ± 17.5
5.0	11	1.028	162.4 ± 25.2	35.4 ± 11.9	0.988	318.7 ± 66.7	52.2 ± 11.8	0.984	64.0 ± 66.7	11.6 ± 24.1
5.5	12	1.044	107.3 ± 11.3	33.9 ± 8.6	0.986	302.4 ± 19.7	55.1 ± 8.7	0.971	202.1 ± 20.2	7.1 ± 10.1
6.0	12	1.049	112.7 ± 16.1	28.1 ± 3.4	0.981	297.1 ± 26.3	61.8 ± 5.5	0.970	203.6 ± 26.3	1.9 ±15.3

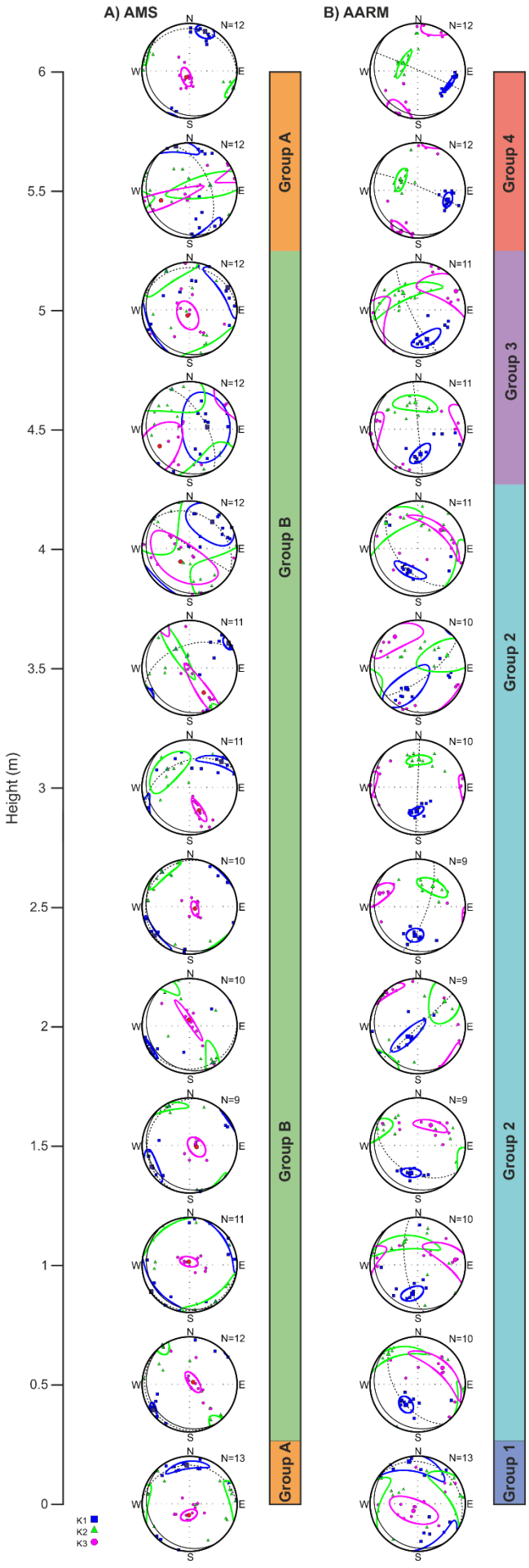

Figure 3.6 *Equal area plots showing (A) AMS measurements and the location of two AMS groups and (B) AARM measurements and the location of four AARM groups at different heights across the crinanite sill thickness. The number of specimens (N) used for each technique at each height is shown in the upper right of each plot. For all plots the K1 axes are blue squares, K2 axes are green triangles and K3 axes are purple circles, and the coloured solid lines are their respective 95% confidence ellipses. The solid black line represents the sill plane and the dashed black line represents the magnetic foliation plane.*

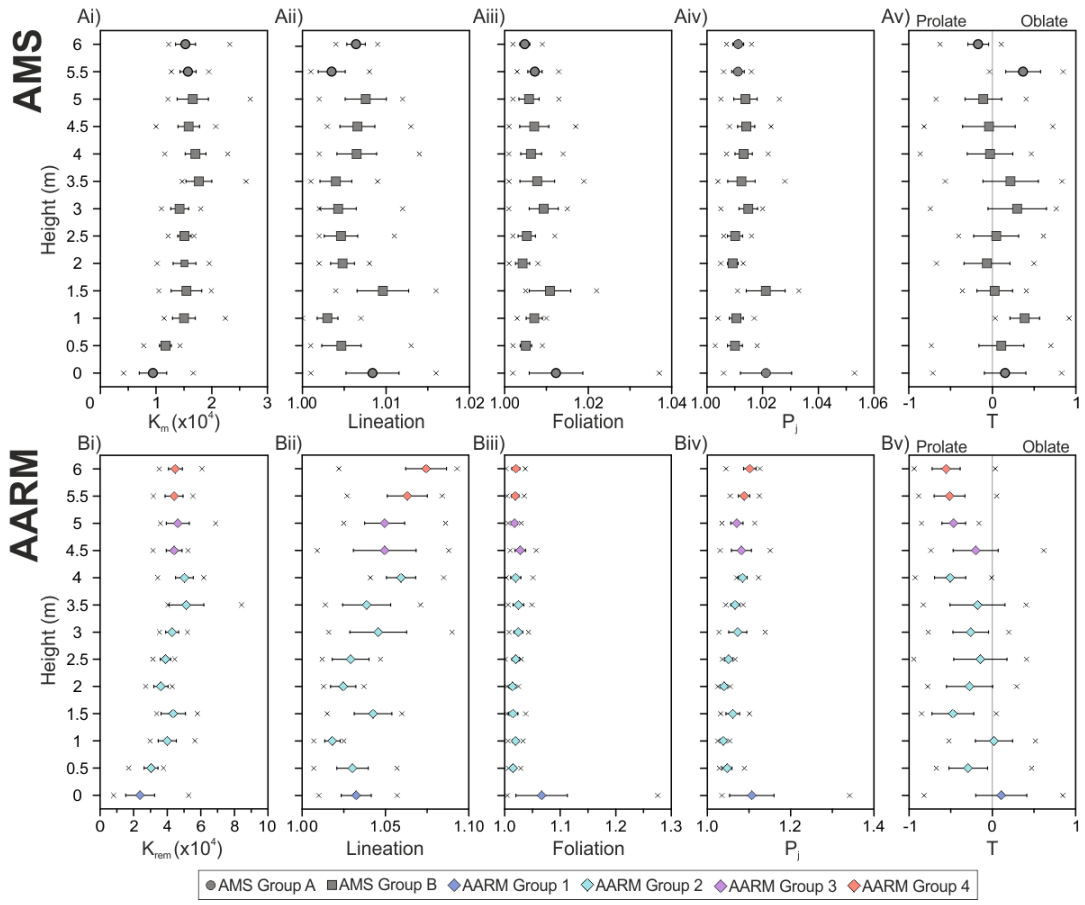

Figure 3.7 *Graphs showing (A) AMS and (B) AARM measurements at specific heights across the crinanite sill thickness: (i) mean susceptibility Km, (ii) lineation, (iii) foliation, (iv) degree of anisotropy Pj, and (v) shape parameter T. In all plots the symbol position (square, circle, or diamond) shows the mean measurement, the horizontal error bars show the 95% confidence intervals, and the crosses show the minimum and maximum values.*

3.6.3 Anisotropy of Anhysteretic Remanent Magnetisation

Similarly to the AMS data, to visualise the AARM fabrics across the thickness of the sill we have plotted a series of equal area diagrams, first grouping all the measurements to show overall patterns, and then plotting separate diagrams at individual heights through the sill to compare the AARM magnetic fabrics across the sill thickness. The overall orientation of all the AARM specimens show a mean K_1 axis dipping towards the south (blue squares, Figure 3.5Bi). However, within these data there are two distinct populations of ellipsoid long axis: the first and larger cluster is dipping towards S-SSW, and the second smaller population has a shallower dip towards the ESE (see contour plot of K1 axes, Figure 3.5Bii). The large amount of scatter associated with the K_2 and K_3 ellipsoids has given rise to wide ranging 95% confidence angles for which most of the populations for these do not reside, e.g. K_2 mean direction of 255.5° ± 62.3° declination and 4.2° ± 51.8° inclination (Table 3.3).

Similar to the AMS fabric analysis, when the AARM data are separated into their respective heights a wider range of fabric groups and trends are observed. Overall, we have identified four AARM fabric groups. AARM Group 1 is located at the lower margin (0 m), with a mean K_1 axis that shallowly dips 10.6° towards the north (Figure 3.6B, Table 3.3). The confidence angles are almost horizontal with K_1 and K_2 overlapping. The mean K_3 axis is almost vertical, 75.6° inclination with an overall oblate fabric. Group 2 is the thickest group, occurring between heights of 0.5-4.0 m and is characterised by the mean K_1 axes becoming more inclined towards the N-NE (dipping moderately to steeply towards the S-SW) and better-constrained confidence angles (see Table 3.3). Compared to AARM fabric Group 1, the ellipsoid shapes have become tri-axial to prolate with means of 0.1 to -0.5 (Figure 3.7Bv). AARM fabric Group 3 is found at the 4.5-5.0 m heights, where the mean ellipsoid long axes begin to rotate around the vertical towards the south-east (Figure 3.6B). Finally, AARM fabric Group 4 is associated with the upper margin region (5.5-6.0 m), where the mean ellipsoid k_1 axes shallowly dips to the ESE (Figure 3.8B), the mean K_3 fabric is horizontal and oriented in a NNE-SSW direction.

Across the thickness of the sill some gradual changes in the properties of the AARM fabrics were observed. The mean K_{rem} gradually increases from 2.3 x 10^4 to 5.1 x 10^4 with increased height from 0 to 3.5 m where it remains constant to the upper margin (Figure 3.7Bi). The degree of lineation also increases through the sill (Figure 3.7Bii). The foliation at the lower margin is considerably larger than the rest of the sill, up to 1.28 compared with <1.1 (Figure 3.7Biii). The orientation of the AARM foliations varies considerably across the breadth of the sill. At the lower margin it dips shallowly towards the north and elsewhere it is more steeply dipping (>40 °) and in a range of directions. It should be noted that the AARM fabrics are dominated by prolate ellipsoids (overall mean T of -0.26), which suggest that the magnetic lineation is better defined than magnetic foliation. Like the foliation, the degree of anisotropy shows an overall increasing trend with increasing distance from the lower contact. An exception to this occurs at the lower contact where P_j is significantly larger (Figure 3.7Biv). The ellipsoid shapes (T parameter) also become more prolate with increased height through the sill, with means of -0.51 and -0.56 at 5.5 m and 6 m, respectively (Figure 3.7Bv) which is similar to lineation (Figure 3.7Bii).

3.6.4 Composition and Petrographic Fabrics

The overall mineralogy of the crinanite sill consists of plagioclase (50%), olivine (3%), chlorite (12-13%), augite (15-19%), other pyroxenes (~1%), amphiboles (6-8%), oxides (~2%) and other minerals (up to 8%) of which ~1% consists zeolites (including analcime). The variations

observed occur at different heights across the sill (Figure 3.8). Post-solidification alteration caused chlorite to form from olivine and amphiboles to form from pyroxene. The original mineralogy and their proportions were therefore: olivine (15% bottom, 15% middle and 16% top), pyroxene (26% bottom, 28% middle and 24% top) plagioclase (50±1%) and oxide minerals (~2%) (Figure 3.8D). These proportions of olivine indicate that the sill lithology straddles the boundary between crinanite and picrodolerite compositions based on the classification of Gibb and Henderson (1984). However, in this paper we will refer to it as crinanite for ease of comparison with other studies in the area (e.g. Gibson and Jones, 1991; Nicoli et al., 2018).

Mineral textures across the crinanite sill reveal structures than enable the crystallisation sequence to be determined. The plagioclase is euhedral to subhedral and appears as two populations: the first group is present as stellate clusters (individual crystals to up 4 mm, e.g. Figure 3.9A) and the second group comprises small individual crystals (average 0.5 mm diameter). Olivine also occurs as two populations, both of which have been partially altered to chlorite; the first as rare euhedral phenocrysts (up to 2.5 mm, Figure 3.9B) and the second as subhedral to anhedral crystals (average of 1 mm diameter). The oxide phases (titanomagnetites and ilmenites) have grown both as isolated microcrystals from the crystallising interstitial melt and 0.1-1.3 mm crystal clusters, with the latter comprising ilmenite cores surrounded by titanomagnetite with exsolution laminae of ilmenite (Figure 3.9C). The larger crystals are located along the edges of pre-existing mineral phases, such as plagioclases (Figure 3.9A). Up to 5 mm sized anhedral pyroxene (augite) oikocrysts ophitically enclose all other mineral phases.

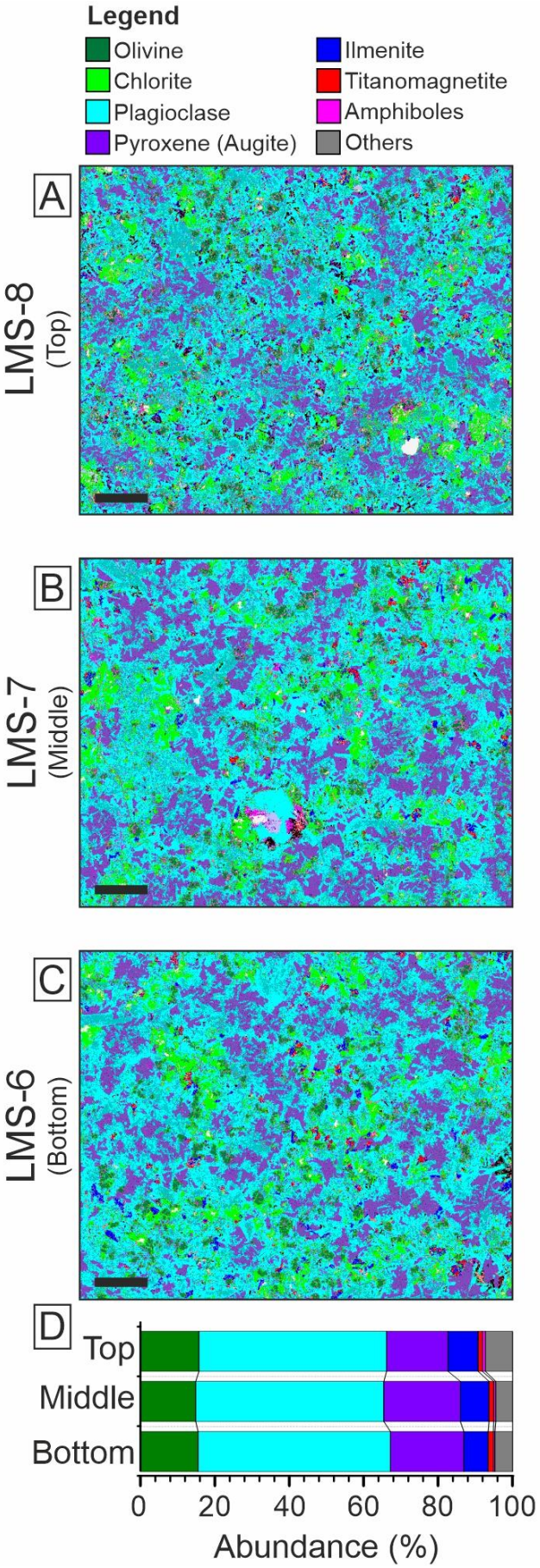

Figure 3.8 *Three QEMSCAN images and modal abundance estimates of crinanite thin sections from: (A) close to the top (LMS-8), (B) middle (LMS-7), and (C) close to the bottom (LMS-6) of the sill. Black scale bars represent 2 mm, and all scans were made at the same scale, note the variation in crystal size across the three thin sections. (D) The modal abundances of mineral phases in each sample estimated by QEMSCAN. Note that in (D) green represents the sum of olivine and chlorite, as chlorite is interpreted to be altered olivine. The "Other" classification includes the locations of analcime.*

The gabbro lenses within the crinanite sill consisted of similar constituents to the surrounding crinanite, except for a distinct lack of olivine, and have an irregular interface with the crinanite. The plagioclases and pyroxenes here were up to 8 mm in size (Figure 3.9D). Titanomagnetites and ilmenites were also present and were up to 3 mm in size.

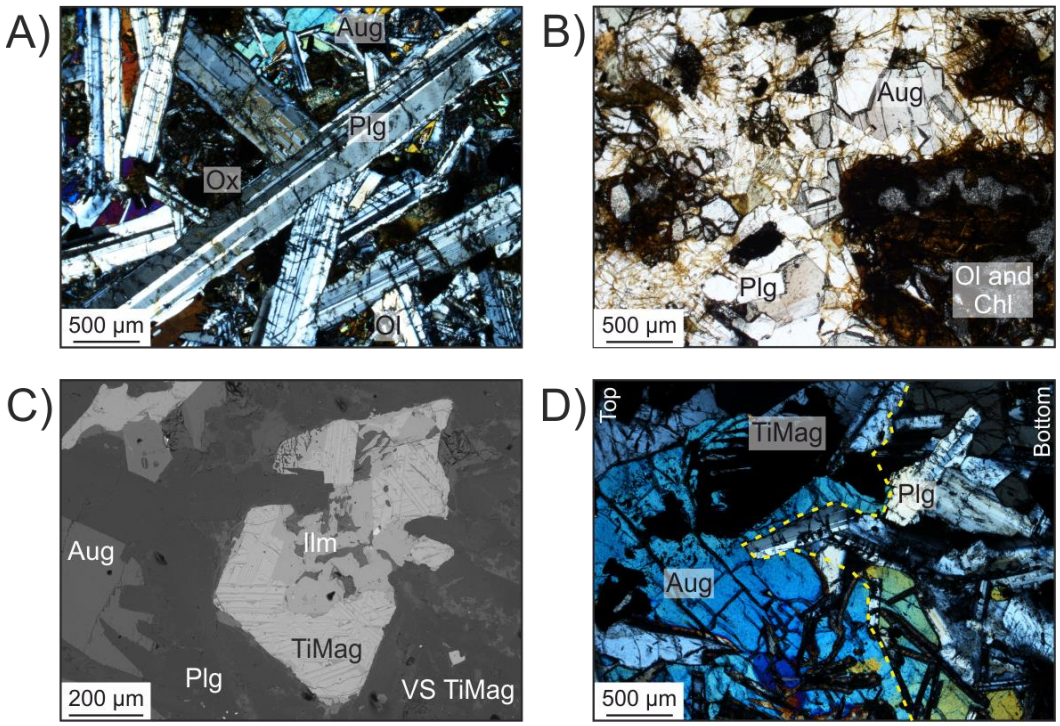

Figure 3.9 *Photomicrographs from optical microscopy viewed with crossed polarized light (A,B,D) and a backscattered electron SEM image (C). (A) A stellate plagioclase (Plg) crystal from near the top of the sill (sample LMS-19-6 m), with ophitic augite (Aug) and unclassified oxides (Ox). (B) An olivine phenocryst (Ol) partly altered to chlorite (Chl) from the lower margin of the sill (sample LMS-6). (C) An ilmenite grain (Ilm) surrounded by titanomagnetite (TiMag) with exsolution lamellae, sampled from near the base of the sill (sample LMS-6). In the lower right corner, a small VS-SD sized crystal of interstitial TiMag can be seen which has crystallized from the interstitial melt. (D) Boundary of the crinanite with a gabbro lens indicated by yellow dashed line, with the left part of the image showing the gabbro lens (top) and the crinanite in the right part of the image (bottom). The sample is located near to the base of the crinanite sill (sample LMS-5b). In all photomicrographs, the oxides are located within interstitial spaces often growing alongside pre-existing plagioclase crystals.*

3.7 Discussion

We now discuss our results to explore the origin and evolution of magnetic fabrics in sills. Bringing together our detailed magnetic analysis, we then use basic petrology and apply thermal modelling and constraints from the literature to synthesise an emplacement and

solidification model for the crinanite sill we studied. I propose that this model can be applied to mafic sills more generally.

3.7.1 Unravelling the magnetic anisotropy

Previous studies of magma flow in intrusions have found key indicators of recorded flow to manifest as AMS and AARM signals, with small confidence angles, and the alignment of phenocrysts, which can be associated with shear that aligns magnetic minerals and tabular crystals parallel to, or slightly imbricated to, the direction of flow (e.g. Knight and Walker, 1988; Chadima et al., 2009). In the Inver Tote sill, we identified two groups of AMS fabrics and four AARM groups (Figure 3.10A): AMS Group A at the sill's upper and lower contacts with the host rock, AMS Group B in the central region of the sill, and AARM Group 1 at the lower margin of the sill to Group 4 at the top margin. From these fabrics we can unravel the history of magma emplacement prior to and during solidification in different regions of the sill.

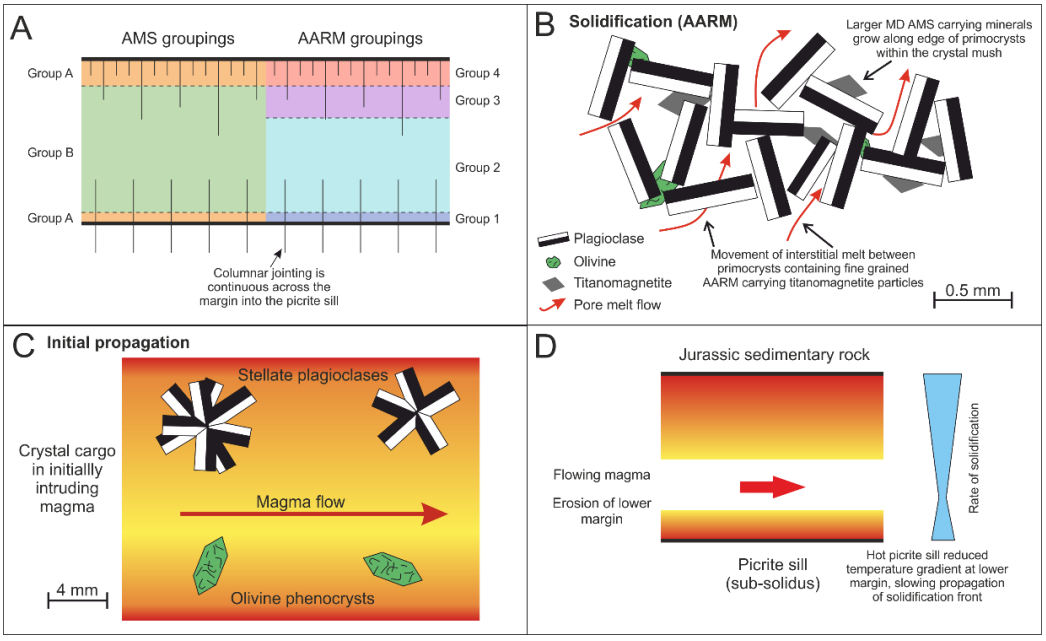

Figure 3.10 *Emplacement model for solidification of the sill inferred from magnetic and petrological fabrics. (A) Solidified crinanite sill showing AMS (Group A and B) and AARM groupings (Group 1 to 4). Dashed lines signify the approximate heights of the groupings. Columnar jointing (vertical solid lines) is continuous across the lower margin into the underlying picrite. (B) Micro-scale diagram showing both the larger MD sized particles growing on the edges of primocrysts that produce the AMS fabrics and pore-melt flow of interstitial fluid around plagioclase and olivine primocrysts to produce AARM fabrics. (C) Stellate plagioclase crystals and euhedral olivine phenocrysts present within the initially intruding magma. (D) Schematic diagram showing magma being emplaced between Jurassic sedimentary country rocks above and picrite sill below. Propagating solidification front from upper and lower margins is asymmetric due to varying host rock temperatures.*

The AMS fabrics predominantly originate from larger MD titanomagnetite crystals, with the orientation of these crystals providing the orientation of the magnetic susceptibility ellipsoids. These crystals are inferred to have grown along the edges of pre-existing phases (Figures 3.9 and 3.10B), some of which may have been oriented by flow of the magma under simple shear conditions (e.g. Correa-Gomes et al., 2001). In the margin regions, the location of AMS Group A fabrics (Figure 3.6A), the AMS foliations have their K_1 axes orientated in a NNW to SSE orientation. We interpret the dip in foliation to be an imbrication which has formed due to magma flow. We therefore infer that the orientation of initial magma flow was to the south (Figure 3.11A). This is consistent with the orientation of the long axis of finger-like structures described by Schofield (2009). With increased distance from the margin regions, ellipsoid orientations and magnetic foliations rotate around the vertical to a SW-NE orientation, which we infer to indicate reorientation of the magma flow direction during emplacement (Figure 3.11B), as the solidification fronts restricted the flow. The reason for this change in flow direction is unclear, but it may reflect the orientation of a more regional flow in a SW to NE direction (e.g. Liss et al., 2002). Its occurrence is broadly supported by the direction of stretched vesicles in the sill.

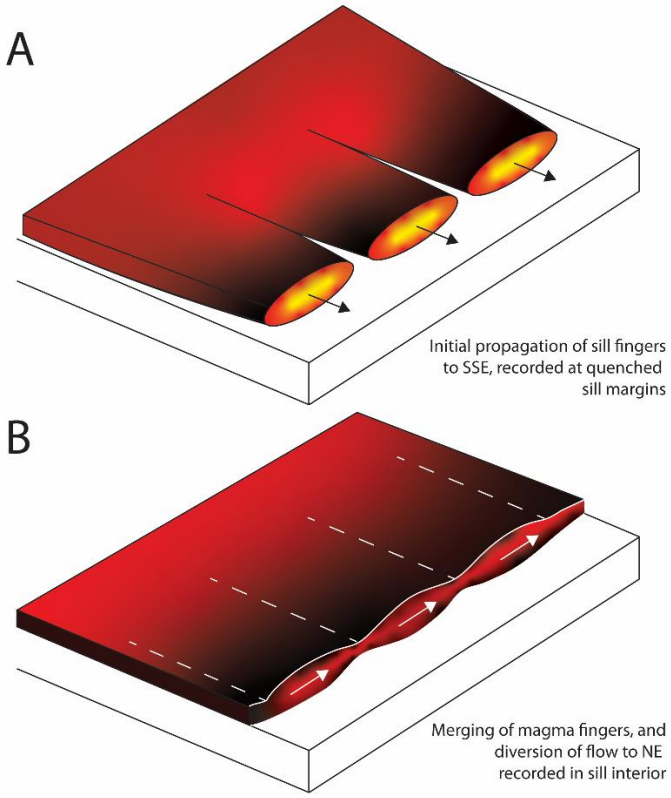

Figure 3.11 *Schematic diagram of initial sill emplacement as magma fingers which propagated to the SSE (A), which subsequently coalesced with diverted flow direction towards the NE (B).*

The AARM fabrics we measured originate from the orientation of SD to VS titanomagnetite crystals located along the edges of pre-existing mineral phases and as inclusions within the augite oikocrysts. I suggest the AARM magnetic lineation, created by the prolate nature of the ellipsoids, originates from in-situ melt-percolation flow and solidification of the interstitial melt through the interconnected pore spaces of a crystal mush after the sill had stopped growing (Figure 3.10B). At the lower margin the AARM signals are oriented in a N-S direction, representing AARM Group 1. However, in the upper margin region, the signals are reoriented in an E-W orientation (AARM Group 4) with the AARM fabrics in the interior of the sill separated into two groupings (2 and 3).

The only height where AMS and AARM signals agree is at the lower margin (0 m height) where both fabrics show a NNW to SSE orientation of the mean K_1 axes, which dips towards the NNE, a vertical orientation of the mean k_3 axes, and an oblate shape (Figure 3.8). These similarities in orientation of their ellipsoids is characteristic of a normal fabric and occur in the lower Group A and the Group 1 regions. The normal fabric observed supports the suggestion of flow towards the south, and we infer that the AMS and AARM fabrics in this region both originate from simple shear conditions during progressive solidification of a flowing magma causing alignment of the magnetic minerals. Both the AMS and AARM foliation planes and the magnetic lineation directions are imbricated towards the SSE with respect to the sill plane, indicating a sense of flow towards the south.

At the contrasting upper margin, the upper part of AMS group A K_1 signals are in a N-S orientation, however the AARM group 4 K_1 signals are oriented in an ESE-WNW direction and this offset is indicative of anomalous fabrics. The AMS signals represent the initial flow direction and orientation of MD crystals towards the south, however the contrasting AARM signals, where the K_1 axes are inclined to the WNW with respect to the sill plane and make up a larger proportion of the magnetic fabric (Figure 3.3C), suggest reorientation of flow during crystallisation of the interstitial melt as it flowed through pores in the crystal network, and so these fabrics likely formed once the sill had ceased propagating. Our interpretation of magma flow from NNW to SSE direction based on magnetic fabrics is supported by field observations by Schofield (2009) of similarly oriented finger-like sill morphologies in the area.

Throughout the interior of the sill (0.5-5.0 m) the magnetic signals varied quite substantially and have been separated into one group for the AMS but two for AARM. The AMS K_1 axes are shallowly dipping and orientated in NE-SW direction, however the AARM K_1 axes are inclined towards the N-NE (group 2) or are rotating towards the east (group 3). The shape fabrics also vary between the techniques with AMS being more oblate but AARM appearing

more tri-axial to prolate. These fabrics are anomalous and can also be interpreted as two different flow regimes associated with (i) initial emplacement of the sill (orientation of the AMS signals) and (ii) later crystallisation of the interstitial melt (orientation of the AARM signals), similar to those of inverse fabrics observed in the upper margin region. This indicates that the flow reoriented to a NE-SW direction, with imbrication in the AARM signal compared with the sill margins suggestive of flow of the interstitial melt to the N-NE whilst rising through the crystal mush. Some shear in the magma may still have been prevalent in order to cause the observed imbrication. The scatter associated with the AARM group 3 signals possibly shows the height at which the flow of the interstitial melt changed direction and rotated around towards the W (4.5-5.0 m).

Our samples were collected from 4 sites across the length of the sill (~45m) in a horizontal transect aligned approximately NE-SW and thus approximately parallel to our inferred initial sill propagation direction. This provide us an opportunity to assess continuity in fabrics along the sill length. Our results show good correlation between sites. For example, the magnetic fabrics from samples collected at 5.0 m height (sites 3 and 4, ~25 m separation) clustered together (Figure 3.6). In addition, the overall two populations in AARM ellipsoids (Figure 3.5Bii) contain samples from all sites. Overall this suggests we have not identified variations in flow fabric along the sill propagation direction.

3.7.2 Crystallisation history

The petrological results from light microscopy, SEM and QEMSCAN analyses suggest that crystallisation initiated with olivine and plagioclase. The presence of stellate plagioclase crystals (Figure 3.9A) and the larger euhedral olivine phenocrysts (Figure 3.9B) suggest these had space to grow unhindered, and so were likely surrounded by melt during crystallisation (Gibb and Henderson, 1996). The location of these phases in the upper and lower margins suggests that they were present as phenocrysts in the initially intruding magma (Figure 3.10C). This is similar to the Shiant Isles picrodolerite and crinanite sills (Gibb and Henderson, 1996; Holness et al., 2017a) and the Dun Raisburgh crinanite sill of the Isle of Skye (Nicoli et al., 2018).

The mineral textures suggest that small individual plagioclase crystals likely formed later and in situ once the sill propagation had ended (Gibb and Henderson, 1996; Holness, 2014). This large proportion of plagioclase present (50%) would have acted to create a rigid crystal network and prevent the flow of magma, as according to the Einstein-Roscoe equation a system becomes locked when up to 40% tabular crystals are present (Lejeune and Richet,

1995). The majority of the olivines then formed in situ from the solidifying interstitial melt. Nucleation of titanomagnetites and ilmenites within interstitial spaces demonstrates these also formed late, using olivine and plagioclase as nucleation sites. The remaining interstitial melt crystallized to form large augite crystals and complete the ophitic texture (Figure 3.9A and B). The lower proportion of augite observed in the upper margin may be the result of in situ differentiation and pore fluid flow of the crystallising interstitial melt away from the margin (Gibb and Henderson, 2006). These mineral proportion and relationships suggest an initial emplacement temperature of the intruding crinanite magma of approximately 1180-1200 °C (Nicoli et al., 2018).

The textural relationship between the magnetic carriers (titanomagnetites) and the other mineral phases present can help to infer the origin of the magnetic fabric and the time of its development. We suggest that the MD titanomagnetites (up to 1.3 mm), that likely provide the source of the AMS signal, used plagioclase and olivine as nucleation sites and grew from them into space which allowed them to grow larger becoming MD sized crystals (Figure 3.9C and 3.10B). In contrast, SD and VS titanomagnetites (<50 µm), that give rise to the AARM fabrics, have a more complex origin. Our observations that they appear within the interstitial spaces between plagioclases and olivines suggest that these smaller titanomagnetites are associated with crystallisation of the interstitial melt during melt-percolation flow through the permeable crystal network and were restricted by the available space (Figure 3.10B) (Oppenheimer et al., 2015). The relative decrease in proportion of the softer 0.02T strength MD phase compared with the stronger 0.4T SD/PSD phase is suggestive of a fining of the grain size with increased height through the sill, which in turn suggests faster crystallisation closer to the upper margin compared with the lower margin.

3.7.3 Thermal evolution

The crinanite sill has intruded between an overlying sedimentary rock and an underlying pre-existing picrite sill (Figure 3.10D). The thermal evolution of the crinanite sill is strongly associated with the temperatures of these contrasting host rock layers when the crinanite sill was initially emplaced and then solidified, and the pattern of columnar jointing can help to constrain the temperature of the country rock during intrusion. We observe that columnar jointing in the crinanite rock is closely spaced near the upper margin and widens towards the base. The columns are also continuous across the lower margin into the picrite below (see Figures 3.2B, 3.10A and Gibson and Jones 1991). Thermo-mechanical jointing experiments where cylinders of hot rock are cooled from their solidus temperatures to tensile failure, has shown that columnar jointing in mafic magmas forms during cooling through the

temperature range of 893-836 °C (Lamur et al., 2018). If we apply this to our study, it suggests that the columnar joints we observe to span the crinanite-picrite sill boundary, results in the interpretation that the two sills cooled as a single unit. Furthermore, the temperature of the picrite sill must have been above 836 ˚C. However, as the lower margin of the crinanite was chilled against the picrite this shows that there was still a large enough temperature gradient to quench the intruding magma. The mechanism of heat loss from the intruding basalt to its surrounding host rocks plays an important role in controlling the preservation of flow fabrics during sill growth and solidification.

By assuming that the sill cooled purely by conduction, we calculate that the timescale for solidification would have been 231 ± 40 days, using the equation:

$$t_{cd} = \frac{L^2}{k}. \quad (3.2)$$

where L is the half-thickness of the sill (3 m) and *k* is thermal diffusivity (4.5 x 10^{-7} (Hartlieb et al., 2016). Whereas, the 1D thermal model of Holness et al. (2012):

$$\tau = 0.1\frac{w^2}{k}\left(1 + cos\left(\frac{2\pi x}{w}\right)\right) \quad (3.3)$$

where *w* is the sill thickness (m) and *x* is the position within the sill, calculates a solidification time by conduction of 185 ± 32 days. Therefore, both conduction models broadly agree on the timescale of solidification. In both cases the error in solidification time is calculated assuming 0.5 m of variation in the sill thickness, but uncertainty in the thermal diffusivity of basaltic magma could potentially be a larger contributing factor.

To identify the possibility of cooling by convection, a key dimensionless parameter to consider is the Rayleigh number:

$$Ra = \frac{g\alpha\Delta T L^3}{\mu k} \quad (3.4)$$

where *g* is acceleration due to gravity (9.81 m/s^2), *α* is coefficient of thermal expansion, *ΔT* is the temperature difference between magma and host-rock (°C), *L* is the characteristic length (m), *μ* is magma viscosity (Pa s) and *k* is thermal diffusivity (m^2/s). For the crinanite sill we used; *α* of 4 x 10^{-5} (Murase and McBirney, 1973), *L* of 3 m (half the sill thickness as cooling occurs from both margins), *μ* of 30 Pa s (Lesher and Spera, 2015) and *k* of 4.5 x 10-7 (Hartlieb et al., 2016). For *ΔT* we use different values for the upper and lower margins: the temperature of the Jurassic sedimentary rock is assumed to have been 25 ˚C (assuming a standard continental geotherm, e.g. Furlong and Chapman, 2013), whereas 890 °C was used as the temperature of the underlying picrite sill, based on the upper temperature limit (Lamur et

al., 2018). The temperature of the intruding basaltic magma is assumed to have been 1200 °C. Therefore, ΔT of the upper and lower contacts was 1175 °C and 310 °C, respectively. Calculated Rayleigh numbers are therefore Ra = 2.35 x 10^5 for the lower margin and 9.22 x 10^5 for the upper margin. This suggests cooling by convection occurred during solidification of the sill, as these values are both larger than the critical value of 2772 (Fowler, 2004). Following this result, the time for the onset of convection is thus approximately 5 days, using the equation:

$$t_{cv} = \frac{l^2}{k} \tag{3.5}$$

where *l* is the thickness of the thermal boundary layer, calculated to be 0.43 m at the upper margin (based on the critical Ra of 2772). This indicates that initially the sill would have cooled by conduction at the margins, but then convection would have had time to develop, and therefore both conduction and convection were key process occurring during magma solidification.

These thermal models suggest that the margin regions where the magma was quenched against the host rock (i.e. the thermal boundary layer) are the only regions where the sill cooled by conduction, and that the central region of the sill experienced convective flow even after the sill had stopped its lateral growth. The conductively cooled regions are those which then produced the Group A AMS fabrics and the Group 1 and 4 AARM fabrics. At the lower margin, the rate of heat loss from the magma into the underlying picrite would have been lower than the upper margin into the country rock, due to smaller temperature differences with the host rocks. This would therefore produce an asymmetric cooling profile in the solidifying sill (Figure 3.10D). The warm floor of the sill would have acted to slow the inward propagation of the crystallisation front upwards from the lower margin of the sill (Figure 3.10C), with the faster cooling front from the upper margin preserving a thicker region where cooling occurred by conduction (Figure 3.6 and 3.10D). The presence of gabbro lenses in the lower portion of the sill, along with coarsening in the grain size of the magnetic carriers with increased distance from the upper margin (Figure 3.4C), supports this interpretation of an asymmetrical cooling history.

Huppert and Sparks (1989) developed three classifications for the types of chilled margins preserved in intrusions and how they form. They define the first type of contact to be dominated by conductive heat flux and the preservation of the chilled margin. The second margin type is defined as one where conductive heat flux is temporarily overtaken by outward heat flux causing melting of the margin region but returning to conductive heat flux

before the chilled contact is melted. This can occur as either convection at the upper margin or through flowing magma at the lower margin. The third type of margin is where the initial chilled contact becomes completely melted. Based on these definitions, we classify the upper margin of the crinanite sill to be a type one contact, where no melt back has occurred due to the thick region of the preserved magnetic fabrics. However, the lower contact represents a type two contact where some melting has occurred due to erosion by flowing magma during emplacement, however not enough to melt the quenched contact region. Quenching of the magma against the host during initial emplacement and cooling by conduction would have allowed the preservation of the direction of flow during initial emplacement. In this sill the initial flow has been inferred to be from NNW to SSE.

The variations in the temperatures of the host rock have resulted in the calculation of different thicknesses of the thermal boundary layer, with the upper layer being 0.43 m thick compared with the lower layer being thicker at 0.68 m. This has implications for the preservation of the magnetic fabrics and possibly also petrological (i.e. gravity settling) fabrics and suggests that there should be a thicker region of preservation of initial flow at the lower margin, however this is not the case and as such may be an indicator that erosion of the thermal boundary layer by flowing magma may have occurred during emplacement. Thermal erosion of boundary layers has been observed at other locations in the BPIP, i.e. in the Loch Scridain sill complex, Isle of Mull (Holness and Humphreys, 2003).

Within the sill interior, away from the margin regions and outside the calculated thermal boundary layers, are the areas of the sill that cooled by convection. The low degrees of anisotropy characterised by the AMS ellipsoids combined with large confidence angles (e.g. at the 4.5 m height, Figure 3.6 and Table 3.3) are indicative of magnetic carriers that display a near-uniform orientation. When this is combined with the knowledge that convection occurred, it suggests that the pre-existing phases present prior to crystallisation of the magnetic carriers may have been given a uniform orientation by melt flowing around them whilst growing within the magma, and hence the magnetic fabric is reflecting the uniform orientation of these phases and as such, could be used as an indicator of convection in other studies.

Studies on other intrusions (e.g. the Shiant Isles, Holness et al., 2017a) have identified the so-called ‘sandwich horizon’ (the final part of the sill to crystallise and the level that the upper and lower boundary solidification fronts meet) to be quite high within the intrusion (c.100-105 m within c.135 m thick sill). In contrast, in the Inver Tote sill, we infer this to be lower down within the intrusion based on the thermal modelling above, suspected asymmetry of

the thermal profile (Figure 3.10D), and potential thermal erosion of the lower margin solidification front.

3.7.4 Implications and Limitations of this study

Our study is focused on mafic sills, yet the flow and solidification processes we infer are also applicable to other magma types and other intrusion geometries, such as dykes or laccoliths. The intrusive nature of sills means that the physical, chemical and thermal processes occurring within the magma cannot be directly observed during emplacement. However, volcano observatories are reliant on interpreting the geophysical signals during emplacement, e.g. surface deformation and seismicity, that are associated with sill growth to forecast if, where and when an eruption may occur. We show that the rock record of sills contains key insights to help us interpret the nature of magma flow in active systems, and the dynamics of magma flow, from initial propagation to solidification, are important for controlling whether or not magma will erupt. We demonstrate how detailed studies of volcanic plumbing systems need to be an essential part of volcanic studies, and by modelling magma intrusion processes based on field, petrographic and magnetic observations collectively, we can inform the development of new and more robust understanding of magma flow dynamics.

Our study of flow and solidification preserved within the magnetic fabrics of a mafic sill is exceptionally detailed and demonstrates how a high sample density across the thickness of intrusions can provide insight to inform our understanding of magma intrusion. Our combination of petrographic analysis and two types of magnetic fabric analysis is not common; however we demonstrate how this combined and multidisciplinary approach enables the flow of magma during intrusion and the flow of interstitial melt during post-emplacement solidification can be unravelled. The use of AARM in the interpretation of magma emplacement processes is novel and has the potential to elucidate a different part of the magma intrusion and solidification process compared to other magnetic methods. AARM enables the interpretation of the signals associated with fine scale flow fabrics that may not be observed through other means. The only limitation to implementing AARM more widely to study magma intrusions is that it is a relatively time-consuming technique compared to AMS and requires equipment less commonly available.

Field studies of intrusions are limited due to the exposures being restricted to two-dimensional sections through the igneous body. Our high-resolution sampling strategy was possible due to both upper and lower margins of the sill being exposed in a quarry so that it

could be sampled relatively easily. It has allowed us to measure variations in magnetic fabrics and understand the emplacement and solidification of a relatively thin sill. This is a framework upon which to conduct studies on thicker sills and laccoliths, to investigate how magnetic and petrological fabrics vary across the breadth of intrusions which may have undergone a more complex emplacement history and may have been supplied by multiple pulses of magma. Additionally, we sampled along the axis of one suspected sill finger, however sampling perpendicular to the flow axis could potentially intersect multiple sill fingers. This would require a different field site as such sampling sections are not available at Inver Tote, but would provide the opportunity to potentially capture the sill's three-dimensional internal structure and further improve our model of sill flow and solidification processes.

3.8 Conclusions

Our analysis of how magnetic fabrics vary across the thickness of a sill from the Little Minch Sill Complex, Isle of Skye has given new insight into how magma flow and solidification evolves through time. Our study is one of the first to apply AARM to understand the emplacement of a relatively thin sill where the history of emplacement has the potential to be rather simple, as such emplacement models can be tested by studying small scale variations in the preserved fabrics across the sill thickness. However, the observations of both AMS and AARM signals in this study contrast dramatically and provide a new understanding of how flow through intrusions evolves through time. Variations in AMS and AARM signals across the breadth of the sill are indicative of complex emplacement processes and cooling history; AMS fabrics relate to the initial magma flow, and the AARM fabric relates to pore-melt flow of the interstitial liquid through the crystal mush. The underlying picrite sill may have slowed solidification at the lower margin of the crinanite sill, assisting in the development of asymmetry in the rate of solidification from the margins observed in both the AMS and AARM signals, and may have allowed channelization to develop. From this we interpret the initial flow direction in the sill at this location on the Isle of Skye, was from the NNW to SSE as fingers. During emplacement the main flow direction migrated to be from the SW to NE reflecting the regional flow regime. Calculations of thermal boundary layers and Rayleigh numbers suggest that both conduction and convection occurred during solidification. The complexities in magnetic fabrics recorded in this mafic sill demonstrate how magma flow can evolve through time across a thin relatively simple intrusion. Consequently, care needs to be taken when inferring magma flow from AMS as it may not be

reliable indicator of complex emplacement histories, as such reassessment of complex fabrics may be necessary to determine more accurate histories of magma flow.

Chapter 4: Multiple sources of magnetic fabrics in a dyke: Implications for syn- and post-emplacement processes

This manuscript has been prepared for submission to the Journal Studia Geophysica et Geodetica. Data collection, analysis and writing of the paper was done by myself, with support from Janine Kavanagh and Andy Biggin. Elliot Wood provided field support.

4.1 Abstract

Dykes are one part of volcanic plumbing systems, that form key pathways for the transport and emplacement of magma within the crust. This study investigates the syn- and post-emplacement processes associated with the emplacement of a mafic dyke. Fieldwork was undertaken on a basalt dyke, a part of the ~59 Ma Skye Dyke Swarm, British and Irish Palaeogene Igneous Province, which has intruded into Jurassic sedimentary rocks and Tertiary age mafic sills on the Isle of Skye, Scotland. Using a high-density sampling regime, I study the rock magnetic properties and associated anisotropy of magnetic susceptibility (AMS) and anisotropy of anhysteretic magnetization (AARM) fabrics spanning two profiles across the dyke-thickness separated by 13 m along the dyke strike. The magnetic fabrics originate from a mix of two predominant phases: a pseudo-single-domain pyrrhotite phase, which dominates the hydrothermally altered margin regions and a multi-domain titanomagnetite phase, which dominates the unaltered core region. The origin of the titanomagnetites within the dyke core represent fabrics associated with emplacement of the magma and suggest that magma locally flowed laterally along the dyke strike. By contrast, the pyrrhotites and their associated fabrics observed at the dyke margins originate from a sulphide rich fluid: the first of multiple post emplacement fluids that flowed through the area. Greater amounts of alteration were observed along strike, which can be associated with more damage of the host rock as the site is close to a branch in the dyke.

4.2 Introduction

Sheet intrusions are a series of magma hosted fractures that provide pathways through which magma can flow through the Earth's crust on its way to the surface. Dykes are one type of sheet intrusion and are subvertical (>80˚ dip) in orientation, providing key pathways for magma transport vertically through the crust. When dykes cluster together, it can lead to the formation of volcanic complexes or dyke swarms (Townsend et al., 2017). Only a small volume of magma (<10%) propagates to the surface and erupts (Crisp, 1984), as such, understanding the processes occurring during dyke propagation and emplacement is necessary for understanding the formation of these structures.

Dykes are generally associated with multiple environments, which include; volcanoes, in regions above mantle plumes or where rifting is occurring. Dyke emplacement in these regions can be separated into two contrasting styles, active and passive. Active emplacement is associated with magma overpressure causing fracturing of host rock into which the magma can flow, and the intrusion can propagate. This is common in volcanic settings where there is increased magma flux to the chamber and observed via inflation of the volcano with a chance of subsequent fissure eruption, e.g. during the 2004-2005 activity at Piton de la Fournaise volcano, La Reunion (Peltier et al., 2008). Passive dyke emplacement occurs where the crust is either being pulled apart resulting in tensile stresses fracturing crustal material and creating space into which magma can flow. This can be either in volcanic rift zones that are gravitationally unstable (e.g. the East Rift Zone, Kilauea, Hawai'i (Fiske and Jackson, 1972), or in areas of crustal extension which can be linked with mantle plumes (e.g. MacKenzie Dyke Swarm, Canada; Ernst and Baragar, 1992).

Many studies have focussed on dyke emplacement mechanisms that include observations of field relationships (e.g. Delaney and Pollard, 1982; Smith, 1987; Kavanagh and Sparks, 2011) and through geophysical surveys (e.g. Chadwick et al., 2011; Hjartardóttir et al., 2015). However, as dyke emplacement occurs in the subsurface, it is very difficult to monitor in real time, as only the signals observed at the surface such as ground deformation, and seismicity at depth can be measured during active intrusion, e.g. during the eruption of Bardarbunga, Iceland in 2014 (e.g. Hjartardóttir et al., 2015; Sigmundsson et al., 2015). Numerical modelling (e.g. Gudmundsson et al., 1999; Yamato et al., 2012) and analogue modelling techniques (Tibaldi et al., 2014; Kavanagh et al., 2018a) are based on conceptual dyke emplacement models which are grounded in field and geophysical observations. Most of these studies investigate the mechanics of dyke propagation, however understanding the processes occurring within the flowing magma is also vital.

Multiple structures associated with magma flow have been previously identified in multiple exposures. These structures include; en echelon segmentation (e.g. Schofield et al., 2012b), ropey flow structures (e.g. Liss et al., 2002; Kavanagh et al., 2018a), scour marks (e.g. Smith, 1987; Varga et al., 1998), stretched vesicles (e.g. Coward, 1980), crystal preferred orientations (e.g. Archanjo and Launeau, 2004) and magnetic fabrics (both anisotropy of magnetic susceptibility, AMS, and anisotropy of anhysteretic remanent magnetisation, AARM) (e.g. Knight and Walker, 1988; Callot et al., 2001; Chadima et al., 2009). Ropey flow structures and scour marks are only preserved in exceptional circumstances (e.g. Varga et al., 1998; Kavanagh et al., 2018a) as such there is the need to study the microscale crystal, vesicle

and magnetic fabrics. Dyke contact regions where chilled margins are present record a history of initial magma flow, whereas the central regions of intrusions may preserve records of later stage flow reorientation, reactivation or channelization (e.g. Platten and Watterson, 1987; Holness and Humphreys, 2003). A common assumption is that the predominant magma flow is vertical, however field evidence (e.g. Poland et al., 2004; Kavanagh et al., 2018a) and recent analogue modelling (e.g. Kavanagh et al., 2018a) suggest lateral flow is common not only in dykes but also other sub-vertical to inclined sheet intrusions (Magee, 2011). As such, understanding how magma flow fabrics vary across the breadth of intrusions is vital for determining more complete magma flow histories.

Rock magnetism and magnetic anisotropy are used across multiple fields of geology as records for understanding rock histories; from determining rock ages to identifying depositional, tectonic or syn- and post-emplacement processes, using the properties of the magnetic minerals present (Blundell, 1957; Raposo and Ernesto, 1995; Tauxe, 2010). In magmatic intrusions, rock magnetic techniques have been used to study models of emplacement and magma flow trajectories within plutons (e.g. Olazabal et al., 1999; Selkin et al., 2014), dykes (e.g. Knight and Walker, 1988; Staudigel et al., 1992; Varga et al., 1998; Clemente et al., 2007; Chadima et al., 2009) and sills (e.g. Hrouda et al., 2015; Závada et al., 2017; Martin et al., 2019), and to infer the intrusion source locations (e.g. Poland et al., 2004; O'Driscoll et al., 2006).

This study investigates how magnetic fabrics vary across basaltic dykes, by studying a ~2m thick basaltic dyke from the Isle of Skye, Scotland. Closely spaced samples, at 20-25cm separation across the dyke thickness, were collected from two transects (~13 m apart) for AMS and AARM analyses, to obtain a detailed understanding of the spatial variability of magnetic fabrics in dykes and their origins. The observed fabrics were interpreted in the context of field-based structural data and simple petrological analyses to understand how syn- and post-emplacement histories can be recorded in solidified mafic dykes.

4.3 Geological Setting: Dykes of the Skye Dyke Swarm

In order to investigate how magnetic fabrics vary across the length and breadth of a dyke and to understand the evolution of magma emplacement during the active lifetime of a dyke, a well exposed dyke where both margins were easily accessible was required. The chosen dyke would also benefit from having a well constrained tectonic history with no known tectonic overprinting events to simplify the analysis. The Isle of Skye has been intruded by the ~58 Ma Skye Dyke Swarm (SDS) (Figure 1A) and has been the focus of multiple studies for magnetic

(Herrero-Bervera et al., 2001), petrological and geochemical studies (e.g. Platten and Watterson, 1987; Hughes et al., 2015). As such it provides the exposure, background knowledge and opportunity for such a detailed study to be conducted and enhance the current understanding of the role of dyking in this region during the Palaeogene.

The Trotternish Peninsula is located in the North of the Isle of Skye (Figure 4.1A), and consists of a series of layered Middle Jurassic age (~168 Ma) sandstones and mudstones (Hudson and Trewin, 2002) overlain by the Skye Lava Group (~60 Ma) which is predominantly of basaltic composition (Hudson and Trewin, 2002; Emeleus and Bell, 2005). Postdating the emplacement of the lavas are a series of mafic sills of the Little Minch Sill Complex (LMSC), which intrude the Jurassic sedimentary rocks (Gibb and Gibson, 1989; Gibson and Jones, 1991; Schofield, 2009). Cutting through the sedimentary and igneous rocks are a series of basaltic dykes from the SDS and form part of the North Britain Palaeogene Dyke Suite (Emeleus and Bell, 2005; Hughes et al., 2015). The dykes have a general strike of NW-SE. Both the LMSC and the SDS form a part of the British and Irish Palaeogene Igneous Province.

Structural mapping and sampling for petrological and rock magnetic analyses were undertaken at Inver Tote quarry, Trotternish (NG 51863 60609), which is an abandoned quarry with easy access for sampling (Figure 4.1B). Here two stacked sills of picrite (lower) and crinanite (upper) composition (Figure 4.2A) from the LMSC, shallowly dip westwards, with a pegmatitic gabbro vein cutting through the picrite. Cross cutting the sills within the quarry are two NNW-SSE striking basaltic dykes from the SDS, following a similar orientation to faults in the surrounding area. In a gully to the east of the quarry a third dyke crops out (Figure 4.1B).

The western dyke had an average thickness of 0.4 m, with crystals up to 1 mm in size and no observed phenocrysts. On both margins, ropey structures appear on the contact surfaces with the sill host material. The ropes on the eastern margin of this dyke were curvate shaped and as such inferring an initial flow direction horizontally towards the north (see Figure 7a in Kavanagh et al., 2018).

The eastern dyke (Figure 4.1B) ranges in thickness between 1.7 and 2 m and its strike ranges from 120 – 170 ° in different exposed sections across the quarry floor (Figure 4.1B). Where the dyke is exposed in the quarry wall (Figure 4.2B), centimetre sized dykelets with calcite filled crack tips, are present within fractures in the sill host rock located to the eastern side of the dyke (Figure 4.2C). The origin of the fractures are related to both columnar jointing within the sill host material, and the damage zone surrounding the dyke. This study focusses

on 2 locations from this dyke which were located 13 m apart towards the north end of the outcrop in both the quarry wall (G5) and floor (G6) (Figures 4.1B and 4.2A). Alteration of the outer portions of the dyke is evident from the orange colouration of the face compared with the inner dyke core (Figure 4.2Ai and Bi), with alteration of the dyke at site G6 also evident as red discolouration (Figure 4.2Di). This dyke provided the most opportunity for study and sampling due to its thickness and exposure.

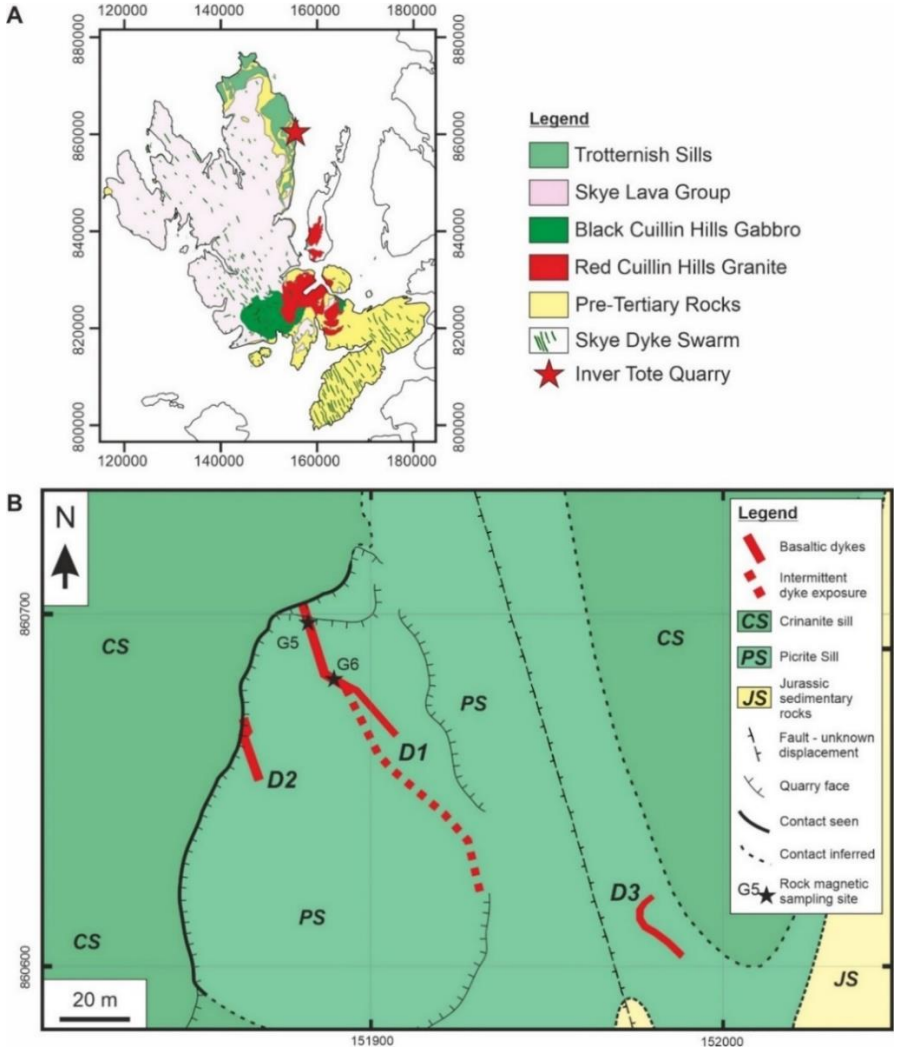

Figure 4.1 *A) Simplified geological map of the Isle of Skye showing main groups of rocks (simplified from BGS, 2008; adapted from Martin et al., 2019). The main portion of the Skye Dyke Swarm and its general orientation is defined by the green lines, and Inver Tote quarry is identified by red star. Co-ordinates refer to the British National Grid. B) Geological map of the dykes sampled at the disused quarry near Inver Tote, Isle of Skye, Scotland. Jurassic sedimentary rocks (JS, yellow) are intruded by Tertiary age mafic sills of crinanite (CS) and picrite (PS) composition (green). Cross cutting the area are three basaltic dykes (D1-3, red). The southern portion of D1 has infrequent exposure in the quarry floor as it is obscured by rubble (its approximate location is indicated by the red dashed line). Locations of magnetic sampling sites are marked G5 and G6 in the North end of the quarry.*

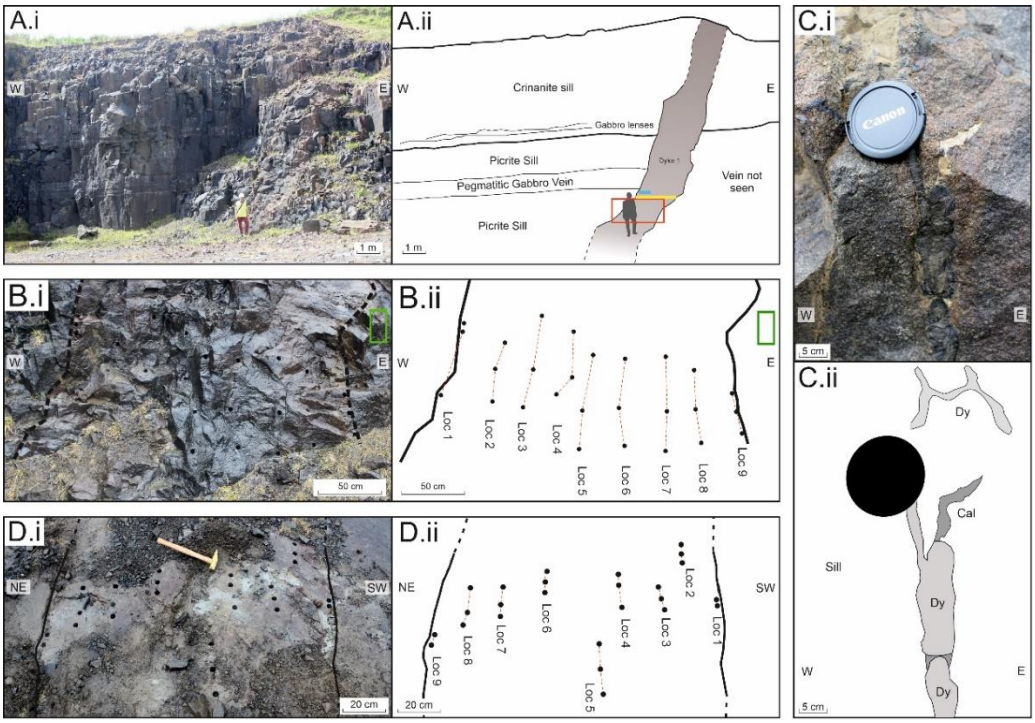

Figure 4.2: Field photographs (i) and diagrams (ii) of sills and a dyke that crop out in a quarry near Inver Tote, Isle of Skye. A) Photograph showing the intrusions that crop out in the quarry. These are a crinanite sill, picrite sill, basaltic dyke and a pegmatitic gabbro vein. Red box indicates the extent of B. The yellow line represents the location of Transect A, and the blue line above the sample for Transects B and C. B) Photograph showing a section of the whole thickness of the dyke at site G5. Photograph also shows the core locations of the sampling regime implemented for rock magnetic studies, with red dashed lines in (ii) connecting samples from the same locations. Green box in upper right shows the location of C. C) Photograph showing small dykelets (light grey) in picrite host rock (white) with associated crack tip filled with calcite (medium grey) to the east of the main dyke (green box in B). The dykelet has two sections with rounded tips above and below. In the upper part of the photo a complex dykelet can be observed in the upper surface of the block. D) Photograph showing a section of the dyke at site G6. Photograph also shows the core locations of the sampling regime implemented for rock magnetic studies, with red dashed lines in (ii) connecting samples from the same locations. Note the difference in orientation of this photograph.

4.4 Methodology

4.4.1 Sampling Regime

Fifty-two 2 cm diameter cores, up to 10 cm long, were collected at 25 cm intervals across the breadth of the dyke from 2 sample sites 13 m apart (G5-6 in Figure 4.1B). The cores were drilled using Stihl BT45 motor driven core drill with a diamond encrusted steel drill bit; six cores were collected from the internal parts of the dyke (locations 2-8) and five cores were collected from each margin (Figure 4.2B, Table 4.1). Cores from site G5 were oriented in situ

using both sun and magnetic compasses, however, the cores from G6 were oriented using a magnetic compass only due to the weather being overcast during extraction. A correction factor of +14˚, the mean difference between the magnetic and sun compass orientations of cores from site G5, was applied to the magnetic orientations of site G6. Additionally, oriented hand sized samples were collected at 50 cm intervals across the dyke thickness forming a thin section transect across the thickness (Transect A, yellow line in Figure 2Aii). A larger block was collected from the western margin for a series of 15 cm long continuous thin section transects (Transects B and C) to be made from the margin into the dyke interior (Table 4.1, blue line in Figure 2Aii). In the laboratory, cores were sliced into 2.2 cm long specimens with each core producing one to three specimens, yielding 96 specimens in total. Masses from the offcuts of one core from each location were crushed in a ceramic pestle and mortar and used for rock magnetic measurements to identify the magnetic carriers.

Table 4.1: *Table showing the location numbers and distances from the Western margin (see Figure 4.1B and D) of specimens and thin sections for magnetic anisotropy and petrology studies respectively. *The sample numbers for thin sections represent distances from the East margin for Transect A. **8 thin sections were made in total from block LMS-4a; h represents horizontally oriented transect (Transect B), v represents a vertically oriented transect (Transect C) and p is a thin section parallel to the dyke plane.*

Location number	G5			G6			Thin sections (collected at G5)
	Distance from west margin (m)	Specimens for AMS	Specimens for AARM	Distance from west margin (m)	Specimens for AMS	Specimens for AARM	
1	0	6	6	0	4	3	LMS-4a-(h1-4, v1-3, p)**
2	0.25	5	6	0.2	6	6	-
3	0.50	5	4	0.43	6	5	LMS-20-1.5m*
4	0.75	6	6	0.70	6	4	-
5	1.00	6	6	0.97	6	5	LMS-20-1m*
6	1.25	7	6	1.12	6	6	-
7	1.50	6	6	1.36	6	6	LMS-20-0.5m*
8	1.75	7	6	1.50	6	5	-
9	2.00	7	7	1.70	3	2	LMS-20-0m*

4.4.2 Petrological Analyses

Petrographic analyses were undertaken to aid in the identification and characterisation of the petrological constituents and textures of the dyke and to support the findings of the rock magnetic and magnetic anisotropy studies. Five samples from 50 cm distances across the

dyke thickness (Transect A) and 8 samples from near the Western margin (Transects B and C, Table 4.1). The five thin sections collected from Transect A were taken from oriented block samples separated by 50 cm intervals using multiple strike/dip measurements, whereas the Transect B and C thin sections were taken from a single block that was only oriented with up arrows providing four samples from a horizontally oriented transect (B), three samples from a vertically oriented transect (C) and one sample parallel to the dyke plane. Micro-scale imaging was undertaken using a Meiji TM3000 benchtop scanning electron microscope with a W-filament and a beam current of 15 kV.

4.4.3 Characterizing the Magnetic Carriers

Vital to magnetic studies is the characterization of the magnetic carriers that give rise to the observed AMS and AARM fabrics of the studied rock units. Identification of the magnetic carriers in the basaltic dyke at Inver Tote quarry was undertaken on samples collected at 25 cm intervals across the dyke width at site G5. Three sets of experiments were used to characterize the magnetic fabrics: (1) multi-technique analysis of isothermal remanent magnetisation (IRM), backfield demagnetisation, hysteresis, high temperature variation of spontaneous magnetisation using a variable field translation balance (VFTB), (2) high temperature susceptibility using an MFK1-A Kappabridge, and (3) three component thermal demagnetization using a method similar to that of Lowrie (1990) and a combination of a furnace and JR-6A spinner magnetometer. These three methods are described in detail in Martin et al. (2019).

The VFTB uses 150 mg of ground rock powder to measure the IRM and backfield curves, hysteresis loops, and high-temperature variation of spontaneous magnetisation. A rock chip is taken from the offcut section of the core, crushed using a pestle and mortar, and from this 150mg of the powder is then measured out and placed into the sample holder before being placed into the VFTB. These results help to identify specific properties of the magnetic carriers, which are an indicator of the mineralogies giving rise to the observed magnetic fabrics. The IRM was measured in zero field after applying a stepwise DC magnetic field, up to +800 mT. Backfield measurements were performed in the same fashion as the IRM in an opposing field of up to -800 mT. Hysteresis was measured during the application of an increasing positive field to 1000 mT, which was then removed and inverted before being returned to the original field. Finally, to determine the Curie temperature of the magnetic minerals present, the samples were placed in a 240 mT field and heated from 50°C to 700°C in 100°C steps, starting from 200°C. The data was analysed using RockMagAnalyzer 1.0 software (Leonhardt, 2006).

High temperature susceptibility measurements were made on a MFK1-A Kappabridge from AGICO (Advanced Geoscience Instruments Company). For these experiments, freshly crushed rock samples were heated in an Argon environment from 30°C to 700°C and then cooled back to 400°C whilst the bulk magnetic susceptibility was measured every 5-10 seconds. This data was analysed using AGICO's Cureval8 software (Chadima and Hrouda, 2012).

Three-component IRM thermal demagnetization experiments (Lowrie, 1990) were performed on one G5 specimen from each position across the thickness of D1. These samples underwent a complete AF demagnetization before having three different decreasing strength bias fields applied to them in three orthogonal directions. The fields used were: x-axis of 1.2 T, y-axis of 0.4 T and z-axis of 0.02 T. These field strengths are different to those set out by Lowrie (1990) as those used in this study were the limits of the pulse magnetisers available, however, they also coincide with the coercivities of minerals being targeted, i.e. titanomagnetite (10's mT; O'Reilly, 1984) and pyrrhotite (up to 100's mT; O'Reilly, 1984). Each specimen was then heated and cooled to a maximum of 620°C in steps of 20°C to 50°C, measuring in an AGICO JR-6A spinner magnetometer and the Rema6 software (Chadima et al., 2018b) after each heating step. This suite of experiments was performed after AMS and AARM analyses as the heating of the specimens caused alteration, changing the magnetic properties.

4.4.4 Magnetic Anisotropy Studies

The rock samples were studied both for their anisotropy of magnetic susceptibility (AMS) and anisotropy of anhysteretic remanent magnetisation (AARM) to understand the predominant crystal orientations of the magnetic minerals present.

Magnetic susceptibility is a measure of how easily a sample can take an induced magnetic field and is affected by the properties of all the magnetic minerals present within a sample, i.e. domain state, size, strength and their orientation (Khan, 1962). AMS is then the directional-dependent response of the constituents of the sample to the applied field (Knight and Walker, 1988; Raposo and Ernesto, 1995). Magnetic susceptibility (K) is defined as $K = M_i/H$ where M_i is the degree of induced magnetization and H is the strength of the magnetic field. It is characterised by a second order ellipsoid tensor with three principle eigenvectors: K_1, K_2 and K_3, where K_1 is the longest axis, K_2 is the intermediate axis and K_3 is the shortest axis (Knight and Walker, 1988) (Figure 4.3A). Stronger AMS signals result from more multi-domain sized crystals (> 50 µm), with certain ferromagnetic minerals (e.g. magnetite) tending to dominate susceptibility measurements (e.g. Hargraves et al., 1991). The ratios between

the tensor axis magnitudes result in a range of ellipsoid shapes: spheroidal, oblate, prolate and tri-axial (Tauxe, 2010). The spheroidal ellipsoid has little to no variation in the tensor axis magnitudes, as such $K_1 = K_2 = K_3$. The oblate ellipsoid describes samples where the K_3 axis is smaller than the similar sized K_1 and K_2 axes ($K_1 = K_2 > K_3$) and is known as magnetic foliation (Table 4.2). The prolate ellipsoid is where the K_1 axis is larger than the similar sized K_2 and K_3 axis ($K_1 > K_2 = K_3$), also known as magnetic lineation (Geoffroy et al., 2002). The tri-axial ellipsoid is where each axis has a different magnitude ($K_1 > K_2 > K_3$).

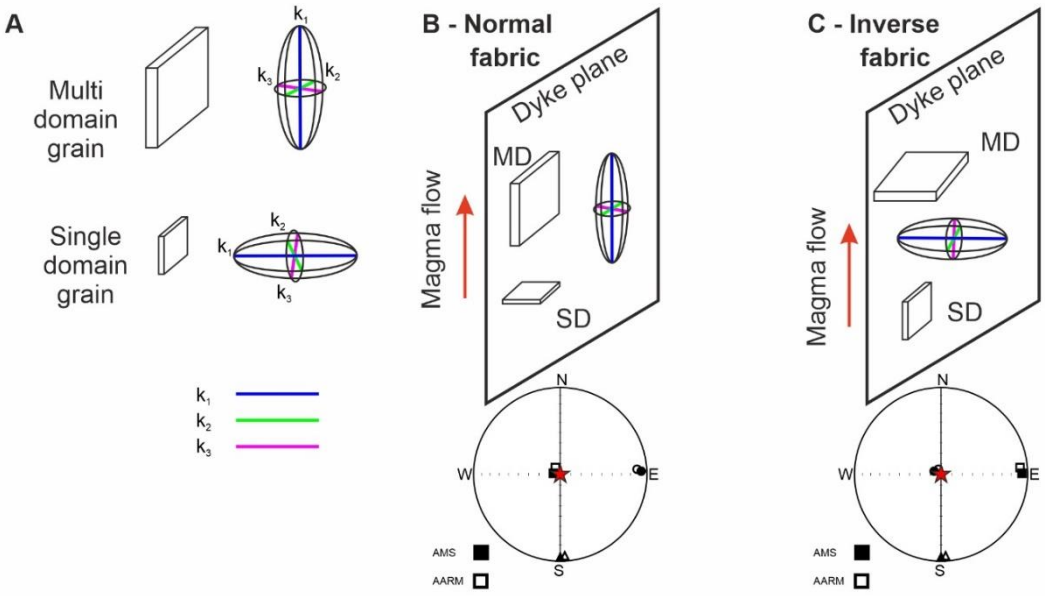

Figure 4.3 *Magnetic anisotropy tensors and the relationship to crystal fabrics and dyke planes. A) the relationship of the orientation of AMS ellipsoid tensor to multi-domain and single-domain crystals, B) an example of a normal fabric where the AMS ellipsoid orientation is parallel to the long axis of tabular crystals and the dyke plane, C) an example inverse fabrics where the AMS ellipsoid is perpendicular to the dyke plane. When MD crystals are dominant, AMS and AARM axes align, whereas when SD crystals are, AMS and AARM are inverted.*

Some studies have used AARM in addition to AMS to study the magnetic fabrics of intrusions (e.g. Chadima et al., 2009; Soriano et al., 2016; Martin et al., 2019). AARM identifies the fabrics that originate from magnetic remanence carrying minerals that are single domain (SD) to vortex-state (VS) in size (McCabe et al., 1985; Jackson, 1991). It also utilizes a second-order ellipsoid tensor, with similar properties to AMS (Table 4.2), however it is defined by K_{rem} instead of K, and is calculated by averaging the magnitudes of the AARM tensor axes.

Table 4.2: *Anisotropy parameters used by Anisoft software and can be found in Jelínek (1981). K_1, K_2 and K_3 are principal susceptibility axes, with η_1, η_2 and η_3 being their natural logarithms with $\eta = (\eta_1 + \eta_2 + \eta_3)/3$.*

Parameter		Solution
Mean Susceptibility	K_m	$(K_1+K_2+K_3)/3$
Lineation	L	K_1/K_2
Foliation	F	K_2/K_3
Corrected degree of anisotropy	P_j	$exp\sqrt{2[(\eta_1-\eta)^2+(\eta_2-\eta)^2+(\eta_3-\eta)^2]}$
Shape parameter	T	$(2\eta_2-\eta_1-\eta_3)\ /\ (\eta_1-\eta_3)$
Remanence	K_{rem}	$(K_1+K_2+K_3)/3$

When the magnitudes and orientations of the ellipsoids have been identified and compared with macroscale and microscale structures, the syn- and post emplacement processes that created the solidified magma bodies exposed through erosion can be determined (e.g. Varga et al., 1998; Liss et al., 2002; Clemente et al., 2007; Chadima et al., 2009; Hrouda et al., 2015). AMS is the most common of the magnetic fabrics utilized here to understand dyke emplacement processes (e.g. Knight and Walker, 1988; Staudigel et al., 1992; Poland et al., 2004; Roni et al., 2014), however AARM represents a powerful additional tool (e.g. Chadima et al., 2009; Silva et al., 2010; Soriano et al., 2016). When the AMS K_3 axis is perpendicular to the dyke plane, this is known as a normal magnetic fabric (Figure 4.3B; Rochette et al., 1992; Chadima et al., 2009) and can be used in collaboration with indicators of magmatic lineation (from macro and micro-scale structures), to infer the magma flow axis (Figure 4.3B). Near to intrusion margins, AMS fabrics are often imbricated with respect to the intrusion plane (Knight and Walker, 1988; Rochette et al., 1992) which can enable the true magma flow direction to be determined as the direction of imbrication. Inverse fabrics occur when the K_3 axis is aligned with crystal long axes and K_1 is perpendicular to the intrusion plane (Figure 4.3C) (Rochette et al., 1992; Chadima et al., 2009). Anomalous fabrics have been identified where the AMS and AARM ellipsoid axes are oblique to each other and have been attributed to a range of hybrid fabrics resulting from multiple mineral phases and domain states (Potter and Stephenson, 1988; Soriano et al., 2016). Other processes have also been attributed to the development of anomalous fabrics, including; syn- or post-emplacement shear along the crack (Dragoni et al., 1997; Clemente et al., 2007), alteration (Rochette et al., 1991; Just et al., 2004; Just and Kontny, 2012), cooling contraction (Hrouda et al., 2015) or different flow regimes occurring during the different process of magma emplacement and solidification (Martin et al., 2019).

AMS analyses were conducted on a MFK1-A Kappabridge from AGICO using an applied field of 200 A m^{-1} and a frequency of 967 Hz, where each specimen was sequentially rotated around 3 axes whilst an induced magnetic field was applied to the specimen. Measurement and processing of the susceptibility during induction of the field was performed by AGICO's Safyre7 software (Chadima et al., 2018c). Processing of the AMS tensor data was automatically completed by AGICO's Anisoft 4.2 software (Chadima and Jelinek, 2009). The software uses Jelinek statistics (Table 4.2) (Jelínek, 1977, 1981), with susceptibilities accurate to within 1% error.

Measurement of AARM was conducted using multiple pieces of equipment that include; a JR-6A dual speed spinner magnetometer, a LDA5 alternating field (AF) demagnetiser and a PAM1 anhysteretic pulse magnetiser from AGICO. The natural remanent magnetization (NRM) of each specimen was initially measured in the JR-6A spinner magnetometer, before undergoing demagnetization and subsequent remagnetization in 6 different orientations, using the LDA5 and PAM1 equipment respectively. The Rema6 software was used to control the JR-6A and measure the magnetisation of the specimens. The AARM ellipsoids were subsequently analysed using AGICO's Anisoft 4.2 software.

4.5 Results

4.5.1 Petrology

The dyke is a fine-grained basalt with a 1-2% population of plagioclase phenocrysts near to the margins that are up to 1 mm in size. Rare crystals of pyrite were also present. Vesicles increased in size from <0.1 mm close to the margins, to > 10 mm with greater distance away from the margins (Figure 4.4A). Small rounded blebs of fine grained mudrock xenoliths were found ~5 mm from the West margin, in thin section LMS-4a-par (Figure 4.4B). Under SEM-EDS, iron sulphides were found along and within 0.5 mm of fractures perpendicular to the dyke plane (Figure 4.4A and C). These sulphides were also present in some of the surrounding vesicles (Figure 4.4A and C), some of which show idiomorphic crystal shapes suggesting growth from the outside in. In some samples, cubic sulphide crystals were identified, however did not appear related to vesicles, suggesting basalt replacement. Calcite was present in any remaining voids, both within fractures in the host rock surrounding the dyke (Figure 4.3C) and also within vesicles (Figure 4.4). No oxides (i.e. titanomagnetites) were observed in the margin regions of the dyke.

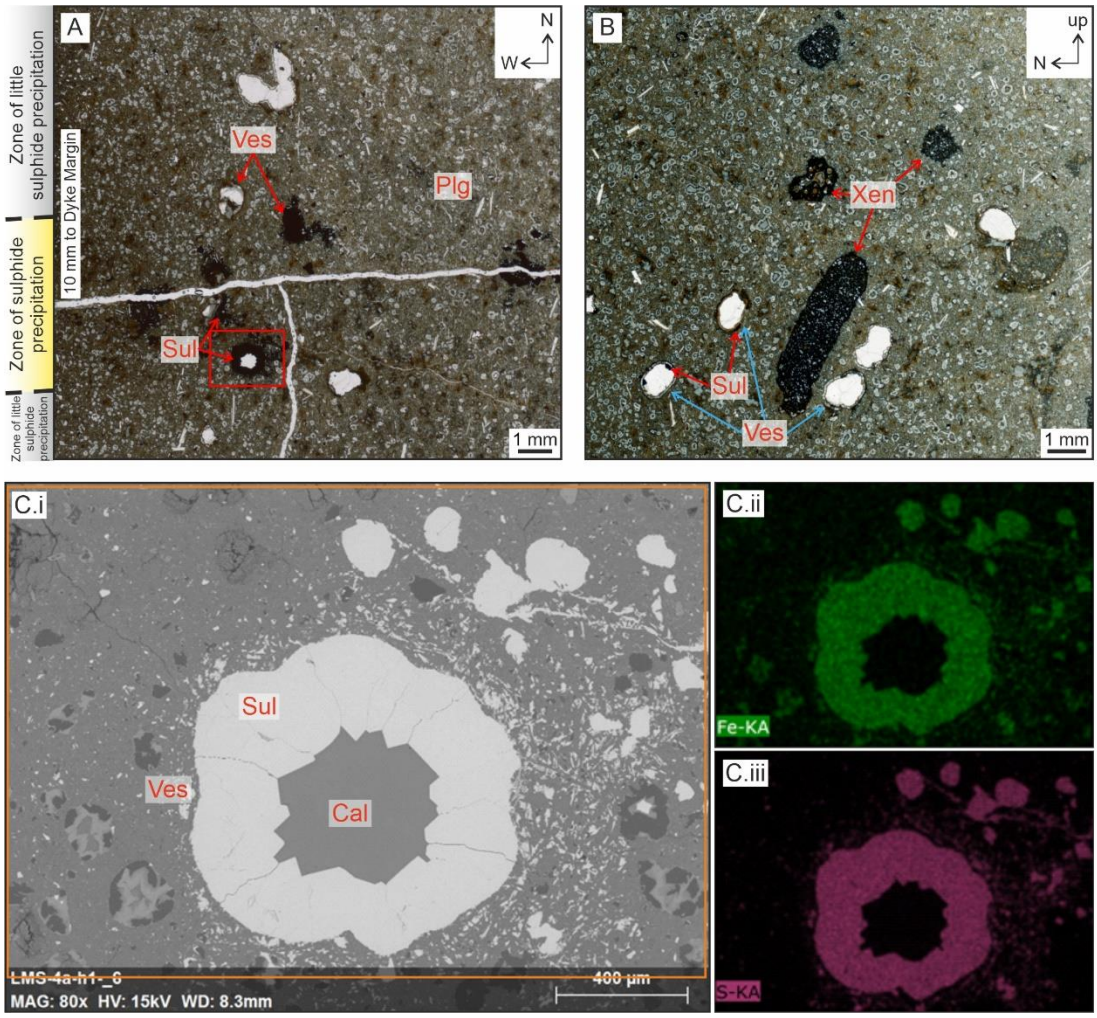

Figure 4.4 *Photomicrographs of samples from optical microscopy viewed in plane polarized light (A, B) and a backscattered electron SEM-EDS (C.i) with element maps for Fe (Cii) and S (Ciii) from thin sections collected from near the West margin of the basaltic dyke. A) Photomicrograph of thin section LMS-4a-h1. Left side of the image is 10 mm from the dyke margin, the dark spots within vesicles around the horizontal fracture are the location of iron sulphide minerals. Red box shows the location of (C). B) Photomicrograph of thin section LMS-4a-par collected parallel to the dyke plane, approximately 5 mm from the West margin. Many vesicles are present within the image from <0.2 mm to >10 mm in size. The dark rounded blebs are xenoliths of mudstones. C) High-magnification image of a single vesicle found in (A). Cii) and Ciii) are element maps for Fe (green) and S (purple), respectively. Iron sulphide has grown into the vesicle with the core later filled with calcite.*

4.5.2 Magnetic anisotropy

Here I describe how the observed magnetics vary across the breadth of the intrusion, by first looking at all the specimen data for site G5 AMS, before separating the data into the 9 sampling locations from across the dyke thickness. The same will follow for G6 AARM, before

moving onto a similar layout for site G5, firstly AMS then AARM. Locations 1 and 9 represent the West and East margins respectively, with locations 2 to 8 evenly spaced between.

4.5.2.1 *Magnetic anisotropy at site G5 (quarry wall)*

When all AMS specimen data for site G5 are combined (*n = 55*), the K_1 axis is oriented horizontally and, in a NW-SE orientation which is approximately 20° anticlockwise, with respect to the dyke plane (Figure 4.5A). The K_3 axis dips 39° towards 237°. The magnetic foliation dips 50° to the NE, oblique to the dyke plane.

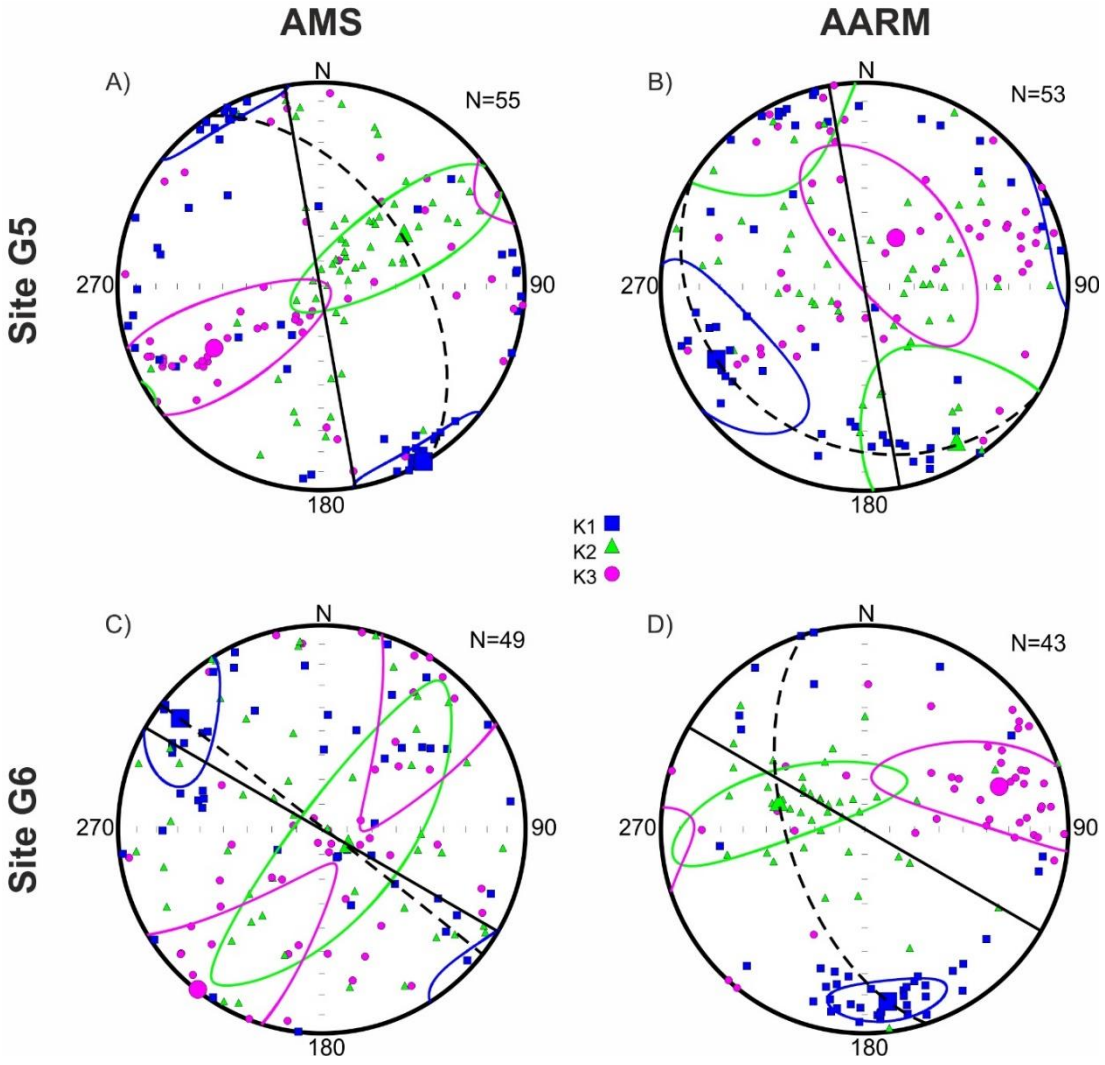

Figure 4.5 *Equal area plots showing data from all specimens for AMS (A, C) and AARM (B, D) with the data separated by sample site: G5 (A, B) and G6 (C, D) in Dyke 2. K_1 axes are blue squares, K_2 axes are green triangles and K_3 axes are purple circles. Solid ellipses are the 95% confidence ellipses calculated by Anisoft 4.2. The solid black line represents the dyke strike plane and the dashed line represents the magnetic foliation.*

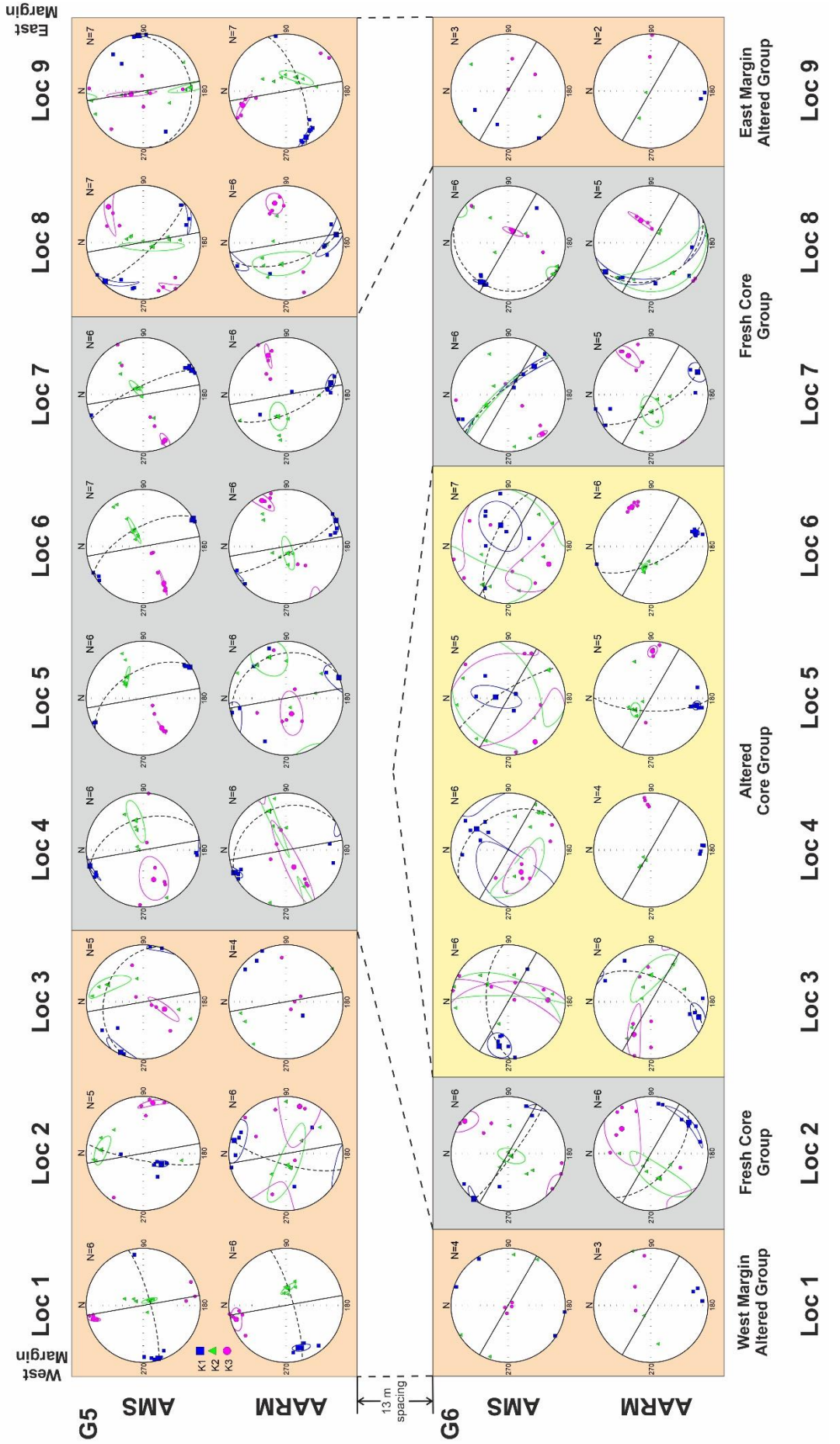
West Margin
East Margin
Loc 1
Loc 2
Loc 3
Loc 4
Loc 5
Loc 6
Loc 7
Loc 8
Loc 9
G5
AMS
AARM
G6
AMS
AARM
K1
K2
K3
13 m spacing
West Margin Altered Group
Fresh Core Group
Altered Core Group
Fresh Core Group
East Margin Altered Group

Figure 4.6 (previous page) Equal area plots showing AMS (A) and AARM (B) fabrics of specimens collected from the dyke, plotted against the location across the dyke breadth. The number of specimens for each position is shown to the upper right of each plot. K_1 axes are blue squares, K_2 axes are green triangles and K_3 axes are purple circles. Solid ellipses are the 95% confidence ellipses calculated by Anisoft 4.2. Solid black line represents the dyke plane and dashed line represents the magnetic foliation. The locations are separated into three groups based on the fabrics observed: East and West Margin Altered Groups (orange), the Fresh Core Group (grey) and the Altered Core Group (yellow).

When the specimens are separated into the different locations across the dyke thickness, a range of fabrics and fabric orientations were observed. In the margin regions, locations 1 and 9, the K_1 axes are subhorizontal and perpendicular to the dyke plane oriented in the ENE-WSW orientation (Figure 4.6A). The K_3 axes lie within the dyke plane for locations 1 and 9, however their orientations are perpendicular to each other, shallowly dipping to the N in the West margin (Location 1) compared with being subvertical in the East margin (Location 9). The magnetic foliation planes are perpendicular to the dyke plane in both margins, being subvertical and subhorizontal in the West and East margins respectively. Away from the margins (locations 2-8), the K_1 axes rotate away from being perpendicular to the dyke plane to being close to parallel with the dyke plane towards the dyke core (< 30°). The magnetic foliation planes in these locations are also less oblique with the dyke plane and can be considered imbricated.

Mean susceptibilities for G5 AMS increase towards the centre of the dyke, with the largest susceptibilities occurring in the core (K_m = 4-6 x 10^4, Figure 4.7Ai). Both magnetic lineation and foliation for AMS ellipsoids, and as such the degree of anisotropy, are stronger in the Eastern side and core of the dyke compared with the western side, however the western margin (loc 1) has ellipsoids that are larger than the adjacent location (loc 2) (Figures 4.7Aii-iv). It should be noted that for each of the K_m, L, F and P_j parameters, locations 2-3 are considerably smaller than the corresponding ellipsoid properties from the opposite side of the dyke (Locations 7-8). The ellipsoid shapes are prolate at the margins (locations 1 and 9), before appearing to be a mix of oblate and prolate at locations 2-3 and 7-8 (25-50 cm and 150-175 cm respectively), before becoming prolate again between locations 4 and 6 (Figure 4.7Av).

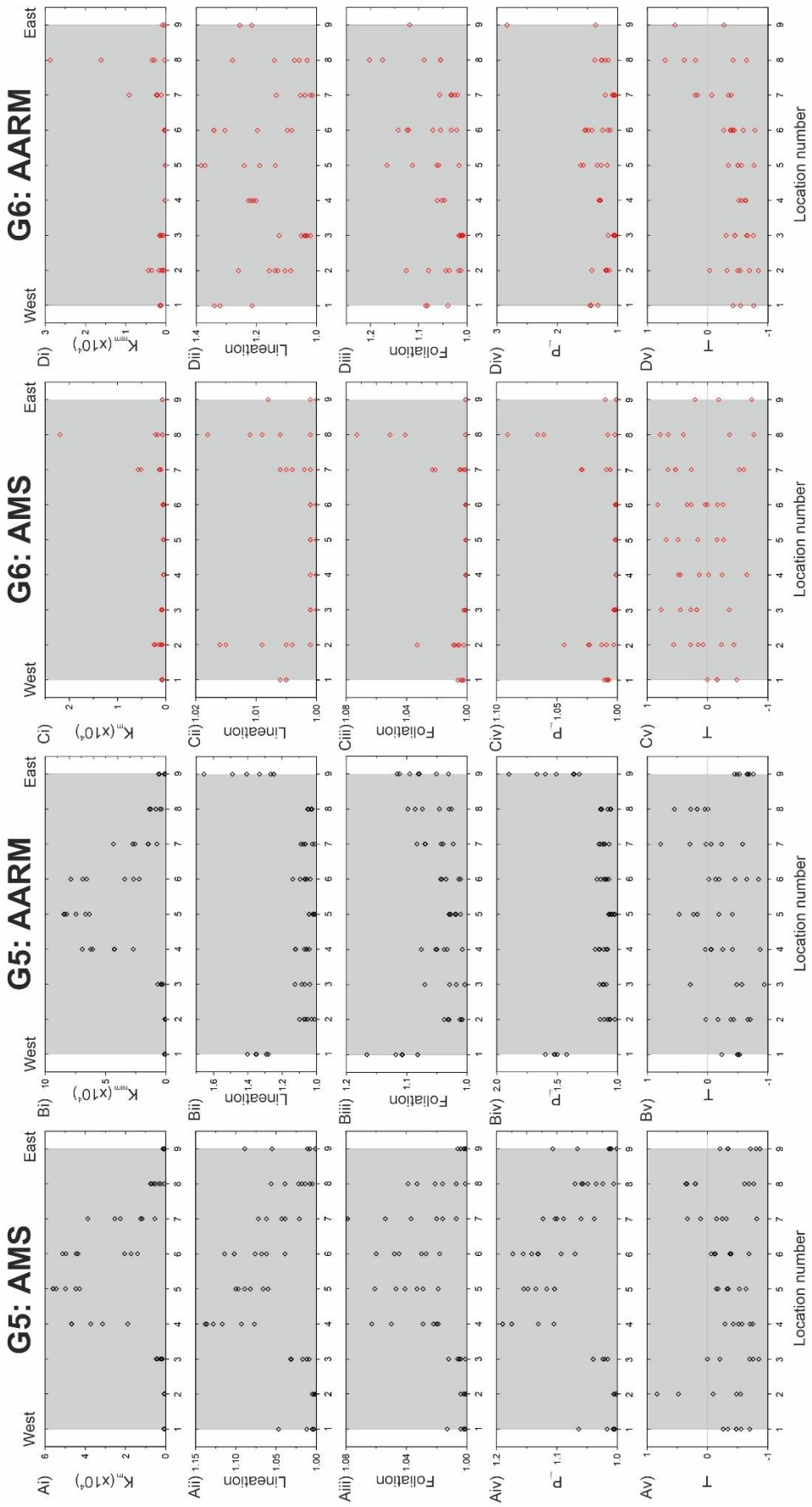

Figure 4.7 *Graphs showing (i) mean susceptibility, (ii) lineation, (iii) foliation, (iv) degree of anisotropy and (v) shape parameter characteristics for (A) G5 AMS, (B) G5 AARM, (C) G6 AMS and (D) G6 AARM ellipsoids of dyke D1, relative to the location across the dyke thickness. Data across the breadth of the dyke are shown by black diamonds for site G5 and red diamonds for site G6.*

The mean AARM K_1 ellipsoid for all specimens (n=53) dips shallowly to the WSW (20/224°) (Figure 4.5B). The mean K_3 axis dips more steeply to the NNE (33/69°), closer to less oblique with the dyke plane than the K_1 axis. There is a large amount of scatter associated with all 3 of the ellipsoid axes. The magnetic foliation plane is almost horizontal and nearly perpendicular to the dyke plane. The orientation of the AARM ellipsoid is considerably different to the orientation of the AMS ellipsoid, as the AMS K_1 axis is aligned with the AARM K_2 axis, whereas the AARM K_1 axis is in a similar orientation to the AMS K_3 axis.

At the margins, the K_1 axes are subhorizontal and perpendicular to the dyke plane (Figure 4.6B), the magnetic foliation planes are close to vertical. Away from the margins the K_1 orientations lie closer to the dyke plane and are subhorizontal, with magnetic foliation planes dipping between 70-85˚ to the West. In the dyke core regions (localities 4 and 5) the magnetic foliations appear shallower, dipping ~30˚ to the NE. AARM ellipsoid properties at G5 show a similar trend to that of the AMS with low K_{rem} at the margins, increasing towards the dyke core (Figure 4.7Bi). Magnetic lineation, foliation and degree of anisotropy are highest in the margins, with smaller values in the dyke core (location 5) (Figures 4.7Bii-iv). Ellipsoid shapes are wholly prolate at the margins, however become more mixed with more tri-axial fabrics present in the dyke interior (Figure 4.7v). This tendency is more prominent in the Eastern side (locations 7 and 8).

When these fabrics are compared, similarities and differences can be identified. In the margin regions (locations 1-3, 8-9; see Figure 4.6) the AMS and AARM fabric orientations are generally oblique to each other, with at least 2 axes not oriented in the same direction, as such are considered to be anomalous fabrics. The exception to this is location 1 where there is only a slight difference in the orientation of the ellipsoid tensors. In the dyke core (locations 4-7) the AMS and AARM ellipsoid orientations are more similar and can be considered normal fabrics.

4.5.2.2 *Magnetic anisotropy at site G6 (quarry floor)*

For site G6, 13 m to the south of site G5 in a section of the dyke striking 120˚ in the quarry floor. Fewer specimens were collected from this site (n = 49) resulting in some locations not having the minimum of 5 specimens required to perform Jelinek statistics.

The average ellipsoid for all specimens has a K_1 axis that is oriented towards the NW and sub-horizontal (13/308°) (Figure 4.5C), a deviation of 8° from the dyke plane (Figure 4.5C). The K_2 axis dips steeply and lies on the dyke plane, as such the magnetic foliation lies almost parallel

to the dyke plane. The K_3 axis is perpendicular to the dyke plane and is oriented towards the SW (1/218°).

At locations 1 and 9 there was insufficient data for Jelinek statistics to calculate 95% confidence ellipses. However, from the available data, the AMS k_1 axes are oriented perpendicular to the dyke plane at the western margin but are oblique at a range of angles at the Eastern margin (Figure 4.6). Location 2 has a magnetic foliation almost parallel to the dyke plane, however all other locations have magnetic foliations that are oblique by > 20˚. In the case of location 8, it is almost perpendicular. Reliable calculation of the mean ellipsoid for location 4 is prevented by scatter.

Mean susceptibility, lineation, foliation and degree of anisotropy all show similar trends in the ellipsoid properties with the margins being relatively low values, increasing at the adjacent locations (2 and 8) before decreasing again between locations 3 and 7 (Figure 4.7Ai-iv). The ellipsoid shapes are variable across each location, with specimens showing both oblate and prolate shapes (Figure 4.7Av).

For the AARM analysis, only 43 of the 49 specimens were used from the AMS due to them being too fragile for the spinner magnetometer. When the data for all specimens is combined (Figure 4.5D), the resulting K_1 axis dips shallowly to the south, and the K_3 axis to the East. The K_2 axis is almost in line with the dyke plane, however the orientation of the K_1 axis with respect to the dyke plane means that the magnetic foliation has a moderate dip of 59/211°, oblique to the dyke plane. In comparison with the AMS data, both ellipsoids show prolate shapes however their orientations are oblique to each other by ~35°.

The data for the AARM orientations are similar across the dyke breadth with a couple of exceptions (Figure 4.6D). This pattern is identified as sub-horizontal K_1 axes that dip to the S-SE (or NW for location 8) with the magnetic foliation planes dipping moderately to steeply towards the west. The main exception to this is location 3 where the K_1 axis is oriented to the SW and the foliation plane dips moderately towards the SE. The locations where there is insufficient data to perform Jelinek statistics in Anisoft 4.2 (locations 1, 4, 9) can still be discussed as the measured specimens have orientations that would be within or close to the confidence angles of adjacent locations (2, 5, 8 respectively).

K_{rem} and foliation for AARM has a similar fabric to the AMS K_m, whereby sites 2 and 8 are relatively higher compared to the surrounding locations (Figure 4.7Bi and Biii), however the central portion of the dyke (locations 5 and 6) also show higher foliations, similar to locations 2 and 8. Lineation and degree of anisotropy show slightly different trends in the ellipsoid

properties compared with the K_{rem} and foliation, with the margins and core being relatively higher than locations 3 and 7 (Figure 4.7Bii and Biv). The ellipsoid shapes are dominated by prolate fabrics in the Western portion of the dyke, from location 1 to 6, becoming more oblate towards the Eastern margin, across locations 7-9 (Figure 4.7Av). It should be noted here that the small number of useable specimens from some of the locations (1 and 9) may affect the interpretation in these places.

At site G6 across the entire breadth of the dyke, the AMS and AARM ellipsoid are not consistently aligned with each other, as such are characterised by anomalous fabrics. However, there are 2 exceptions to this, locations 3 and 8. At location 3, the AMS ellipsoid is prolate, with the K_1 axis slightly imbricated with respect to the dyke plane, however for the AARM ellipsoid, the K_1 and K_3 axes are switched, a characteristic of an inverse fabric. At location 8 the ellipsoid axes for both AMS and AARM are aligned with each other, as such are characteristic of a normal fabric. The fabrics for location 2 could also be considered normal as there is only a small variation in the K_2 and K_3 orientations when the AMS and AARM fabrics are compared.

In summary, at G5 the AMS and AARM fabrics at the margin locations (1 and 9) show contrasting fabrics compared to fabrics in the core, with foliations at the margins perpendicular to those in the dyke core. At site G6, the AMS and AARM analyses also show contrasting fabrics at different locations across the dyke thickness, with ellipsoid orientations being perpendicular then sup-parallel before becoming oblique to the dyke plane with increased distance from the margins towards the dyke core.

4.5.3 Rock Magnetic Properties

Thermoremanent magnetisation curves for site G5 show very weak magnetisations and susceptibility near to the margins (locations 1-3, 8-9 in Figure 4.8Ai and iii; see also Appendix C). During heating, these undergo large amounts of alteration, producing 1 or 2 phases with Curie temperatures between 580 and 350 °C on cooling from above 500°C (Figure 4.8A). High temperature susceptibility graphs also show large variations in heating and cooling curves for the same locations. In these experiments, alteration also occurs from 450 °C, forming one main phase with a Curie temperature of ~510 °C (Figures 4.8B). For site G6, thermomagnetisation data (Figure 4.9) follows a different trend in that the dyke core (loc 5, Figure 4.9C) shows similar properties to the dyke margins (locs 1 and 9, Figure 4.9A and E), whereas in between (locs 2 and 7, Figure 4.9B and D) show fabrics similar to the dyke core of site G5.

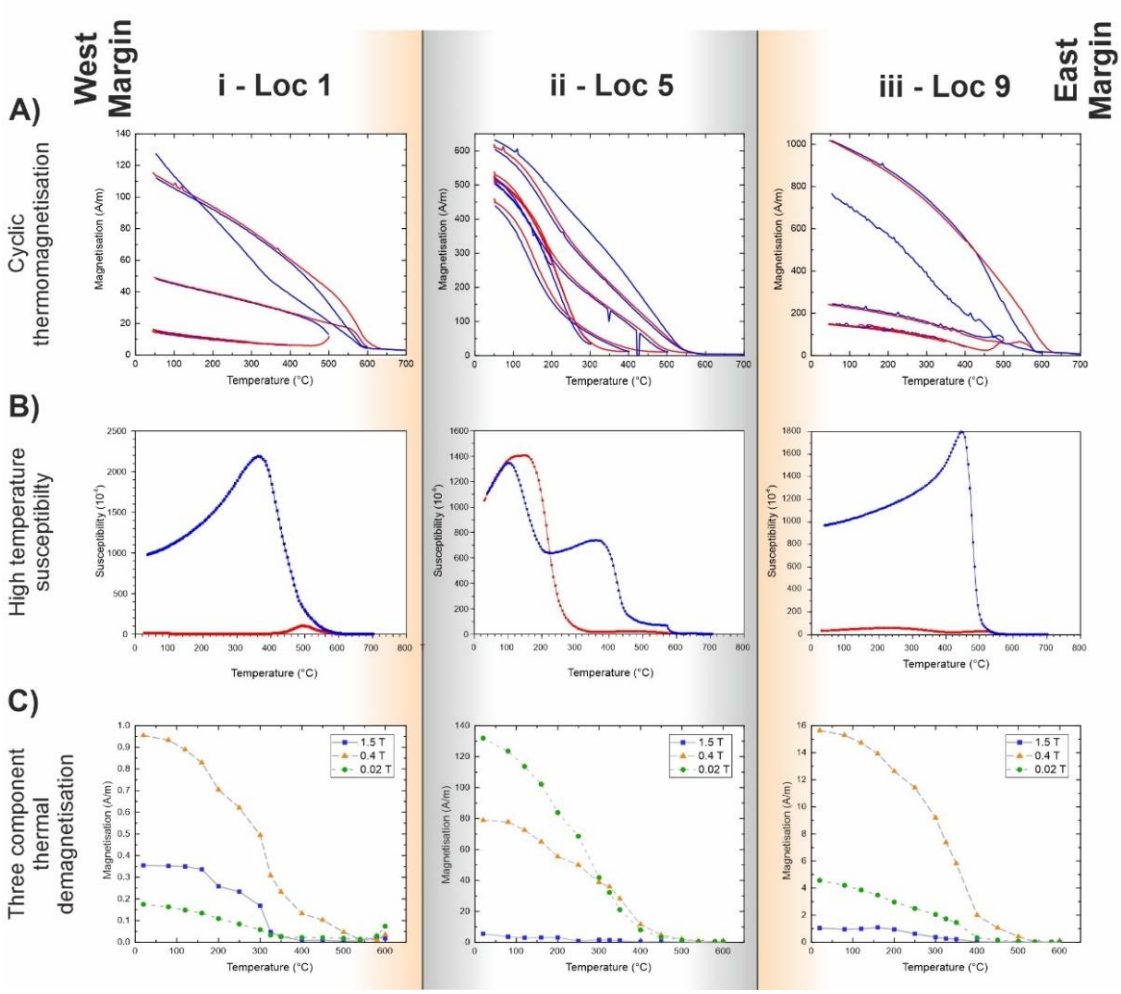

Figure 4.8 *Graphs showing representative data from thermomagnetic experiments for identification of magnetic carriers from site G5 across the D1 dyke thickness: A) Cyclic thermomagnetisation, B) High temperature susceptibility, and C) Three component thermal demagnetisation. The samples have been separated into 3 groupings: East and West Margin Altered Groups (grey; I and iii) and the Fresh Core Group (orange; ii).*

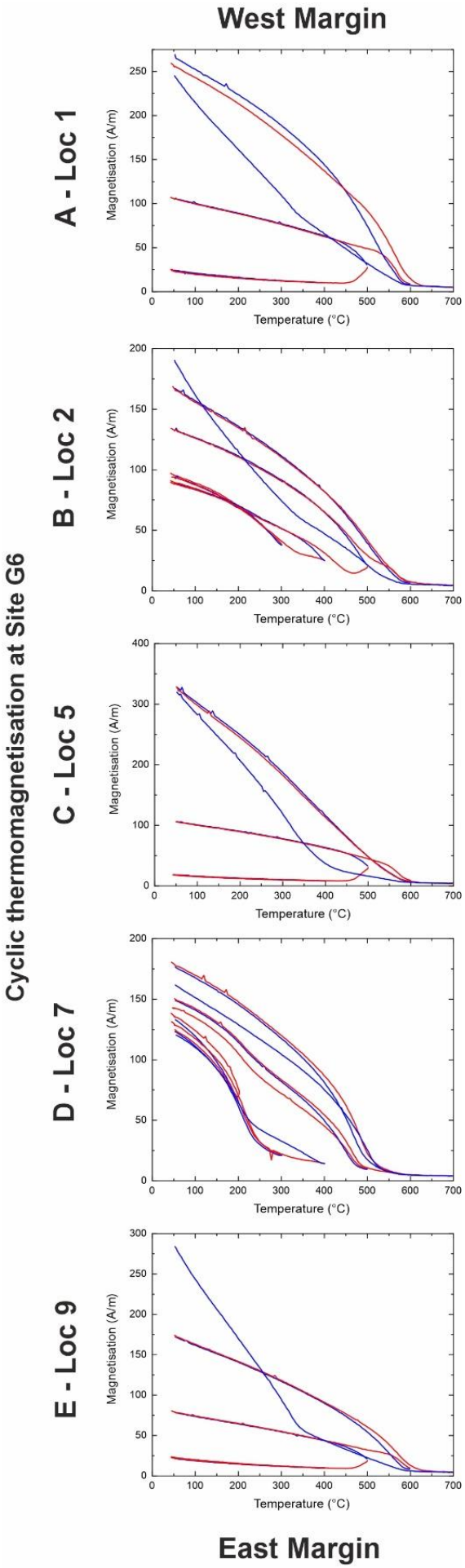

Figure 4.9 *Graphs showing representative data from cyclic thermomagnetisation data for identification of magnetic carriers from the dyke core to the eastern margin of D1 at site G6: A) Location 1 from the western margin, B) Location 2, C) Location 5 from the dyke core, D) Location 7 and E) Location 9 from the eastern margin.*

Experiments undertaken using the Lowrie (1990) protocol show multiple phases at each location. These phases occur predominantly as intermediate and soft phases, 0.4 and 0.02 T respectively (Figure 4.8C). The intermediate phase (between 0.02 and 0.4 T) is generally the most dominant phase apart from in locations 2, 4 and 5 (Appendix C), where the soft phase is the most common. For the intermediate phases, the greatest decrease in magnetization, and thus the unblocking temperature, occurs between 300 and 400 °C, which is suggestive of a pyrrhotite origin, supporting VFTB measurements. This is most evident in samples in the margin regions. At the locations where the soft phase is the most dominant (locations 2, 4 and 5), there are 2 apparent unblocking temperatures, the first larger decrease is between 160 and 200 °C with the second in a similar location to the intermediate phase. The first signal is indicative of a Ti-rich titanomagnetite (c. TM60, Tauxe, 2010), with the second also supporting the presence of pyrrhotite, which are believed to be pyrrhotite with coercivities straddling the boundary between the intermediate and hard phase field strengths. The hard phase (red) is generally very low to not present, except for locations 1 and 6 which it follows a similar trend to the intermediate phases. It should also be noted that the strengths of the magnetisations close to the margins was considerably lower than in the dyke core. The unblocking temperatures are summarised in Figure 4.10A.

Hysteresis measurements completed during the VFTB analyses enables calculation of the domain states of the magnetic carriers giving rise to the fabrics which are then summarised by using the saturation remanence/saturation magnetisation vs bulk coercivity plot of Tauxe et al. (2002). Figure 4.10B shows that with increased distance from the margins, the magnetic carriers increase in size from vortex to uniaxial single domain at locations 1 and 9 to MD in the dyke core (G5 locations 4-7). Experiments at G6 show contrasting behaviour of the magnetic carriers with locations 4-6 also showing vortex to cubic-SD behaviour, compared with locations 2, 3 and 7 showing MD behaviour (Figure 4.9 and 4.10B).

The patterns observed in rock magnetic characterization experiments, also suggest the presence of different magnetic carriers providing the signals observed in the magnetic anisotropy studies. At site G5, there appears to be two regions, one near the dyke margins which is dominated by pyrrhotite and the other towards the dyke core dominated by titanomagnetites. Whereas at site G6, there appear to be three regions of fabrics, the first two are similar to site G5, however are smaller in thickness, with a third in the dyke core with properties that also suggest pyrrhotite being the carrier of the magnetic signals.

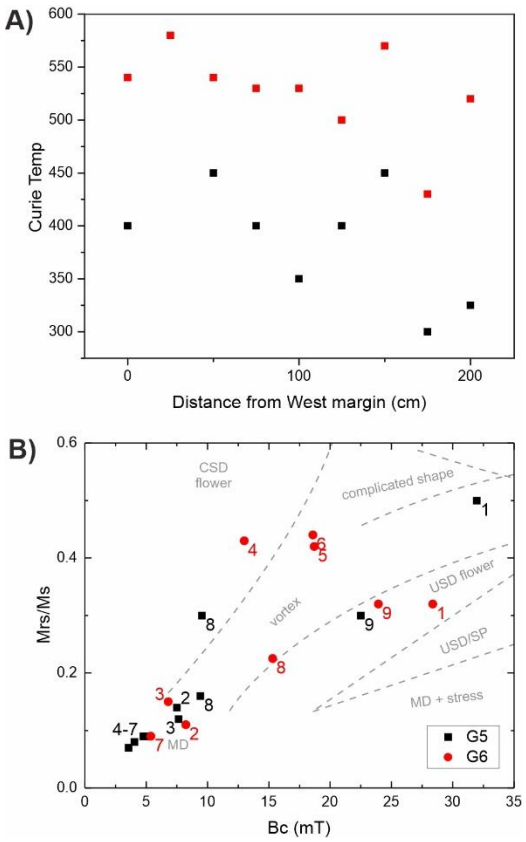

Figure 4.10 *Graphs showing identification of magnetic carriers. A) Unblocking temperatures against location across dyke breadth for site G5, obtained from three component demagnetization experiments (modified Lowrie method), black represents the lower unblocking temperature and red the final unblocking temperature. B) Squareness vs bulk coercivity plot (Tauxe et al., 2002) showing different shapes and sizes of magnetic carriers from flower or vortex state, to multi-domain (MD) state, where Bc is bulk coercivity and Mrs/Ms is the remanent magnetic saturation relative to magnetic saturation, also known as squareness. Black squares show data for site G5 and red circles show data for site G6.*

4.6 Discussion

From the combined AMS fabrics, AARM fabrics, rock magnetic carrier data and petrology, 3 groups of signals have been identified; the West Margin Altered Group (WMAG), the East Margin Altered Group (EMAG), the Fresh Core Group (FCG) and the Altered Core Group (ACG). These groupings provide insights of different parts of the dyke's history and are now discussed to explore the origin and evolution of the magnetic fabrics. By combining the results from each of the different methodologies, I attempt to produce a model for the syn- and post-emplacement processes that occurred.

4.6.1 Origin of the magnetic minerals

Previous studies into the origin of magnetic fabrics measured within exposed solidified intrusions have identified a range of potential origins for the signals, related to both syn- and post emplacement processes. Many of these studies have interpreted the observed magnetic fabrics to be indicators of magma flow direction when linked with other macroscale and microscale structures, in some cases even the sense of flow (e.g. Varga et al., 1998; Liss et al., 2002). However, some studies have also identified magnetic fabrics that have been changed by overprinting from tectonism (e.g. Burton-Johnson et al., 2019) or alteration of the magnetic carriers (Rochette et al., 1991; Just and Kontny, 2012).

In this study, multiple magnetic sources are giving rise to the magnetic fabrics which impact the ability to interpret some of the observed fabrics. The main fabrics that this refers to are those closest to the margins (grey zones in Figure 4.6 and 4.8). In these regions, rock magnetic characterisation experiments (Figure 4.8) determine the dominant phase to be pyrrhotite, a ferromagnetic iron sulphide with coercivities into the 100's of mT and a Curie temperature of ~ 325 ˚C (Tauxe, 2010). There is also a very small amount of Ti-rich titanomagnetites, with a Curie temperature around 150 ˚C (Tauxe, 2010), which is identified by the larger decreases in magnetisation of the soft phase in Lowrie method experiments such as at location 2 (Appendix C, Cii). During heating these phases undergo extensive alteration to the extent that there is growth of magnetite that dominates the signal of cooling curves in both thermomagnetisation and high temperature susceptibility experiments. Lower K_m values at the margins of G5 compared with the dyke core, 7.0×10^2 and 5.1×10^4, respectively, also support the hypothesis of different phases giving rise to the magnetic susceptibility at these locations.

Pyrrhotite was most commonly found in and around fractures (Figure 4.4A). Geochemical analyses by Hughes et al. (2015) suggested that the sulphur (i.e. pyrrhotites) originated from assimilation and melting of Jurassic sedimentary rocks, through which the dykes and sills intruded, which released allogenic S into the magma, rather than it originating from a post emplacement fluid source. They also reported a larger sulphur content in the proximity of mudrock xenoliths close to the dyke margins compared to the core of the dyke, which correlates with the strong pyrrhotite signal observed in unblocking temperatures (Figure 4.6C). Whilst these interpretations provide one possible origin for the sulphur-bearing minerals, I suggest an alternative process for the transport and precipitation.

The combination of the presence of a larger proportion of pyrrhotite in the margin regions combined with the presence of the pyrrhotite along with calcite and other minerals (Figures 4.3B and 4.4) within vesicles and fractures around both the dykes in the quarry, suggest that post-emplacement fluids flowed through the area. Alteration in the margin regions of the dyke (Figure 4.3Ci) suggest that these fluids were likely localised through permeable pathways that could be related to cooling related tensile fracturing associated with margin regions in contact with host rocks (Spry, 1962). These fluids may help to explain the lack of titanomagnetites within the margin regions, as the sulphide overgrowth could alter the iron bearing phases as they flowed though. Consequently, this would reduce the magnetisation of samples in these areas, as observed in the relatively low magnetization magnitudes (Figure 4.8A).

In the FCG, the magnetic fabrics are dominated by larger proportions of almost MD titanomagnetites (Figure 4.10B). These titanomagnetites have a range of concentrations of Ti which have undergone small amounts of deuteric oxidation due to Curie temperatures incrementally being pushed higher during cyclic thermomagnetisation experiments (Figure 4.8A). This lack of deuteric oxidation during cooling was likely due to a lack of free oxygen during emplacement as separation of the Ti-rich and Ti-poor phases did not occur until reheating. Variations in deuteric oxidation have been observed across the thickness of both a lava flow (Audunsson et al., 1992) and an ignimbrite (Çubukçu, 2015), where samples in contact with the pre-eruption topography have undergone little to no deuteric oxidation as there was no available oxygen post emplacement, combined with rapid cooling due to contact with the ground. This is in comparison to the upper regions of the deposits where the dissociation of water up through the flows combined with oxygen and water in the air enabled deuteric alteration to occur (Audunsson et al., 1992). Although these examples are extrusive in nature, they still support the dyke core having a lack of free oxygen for deuteric oxidation to occur.

In the FCG there is also a lower pyrrhotite signal. This switching of the dominant phase suggests that less alteration occurred within the dyke core compared with the margin regions. A slower cooling rate in the core would enable both larger titanomagnetite crystals to grow and reduce the amount of cooling related fracturing within the dyke core. Subsequently, this would reduce the number of pathways for post emplacement fluids to flow along and precipitate the sulphides and calcite that were observed closer to the margins. This also supports the lower sulphur proportions observed by Hughes et al. (2015), rather than the magma mixing that they suggest.

The ACG is the final group and is only present at site G6. It has properties that are like the EMAG and WMAG, in that they are dominated by pyrrhotite signals. This indicates that the core of site G6 has reverted to a similar alteration as that observed in the margins, suggesting that similar processes have occurred.

4.6.2 Variation along strike

Sites G5 and G6 are only 13 m apart along strike but nevertheless exhibit distinct properties as observed in the field data and apparent fabrics. In field evidence, the variations are seen in the thickness, orientation and proximity to the dyke branches. Within the observed magnetic fabrics, variations are associated with the location of the different magnetic carriers and their sizes, and the orientations, shapes and magnitudes of both AMS and AARM fabrics.

A major source of the variation could be attributed to differences in both the thickness and orientation of the dyke between the two sites. At site G5, the dyke is 2 m thick and strikes 170 ˚, whereas at site G6 the dyke is only 1.7 m thick and strikes 120 ˚. For the thickness this is a 30 cm difference and represents a 15% difference in the volume of the dyke between these points, which would impact the ratio of the altered to unaltered zones and as such may have affected the zone of the dyke being sampled.

The change in dyke strike from 120 ˚ to 170 ˚ and the proximity of the sites to the location of the bend would impact the flow processes occurring during emplacement. Site G5 was ~10 m from the bend, whereas site G6 was ~3 m from the bend, this difference in proximity could mean that site G5 preserved fabrics relating more to slower crystallization and a more uniform cooling history. Whereas site G6 was located not only closer to the bend between the two sites, but also close to a second bend and branching in the dyke further south (Figure 4.2B). Both the bend and branching would impact both the flow regimes present during emplacement but also the permeable pathway for the post emplacement fluids to flow through. This branching of the dyke would enable post emplacement fluids to access and subsequently alter the dyke core region giving rise to the fabrics seen in the ACG.

4.6.3 Emplacement model

The strongest direct evidence of initial propagation direction derives from field structures observed in the eastern edge of the dyke. Here the dykelets that intrude into the surrounding sill host rock, are parallel to the main dyke plane (Figure 4.3Cii) and have rounded dyke tips at the top and bottom. These morphologies are like lobate shaped magma bodies that have rounded margin regions, with flow through the middle. In the orientation that they are

observed this would suggest that this dykelet propagated towards the north. This northward propagation is supported by curved ropey flow structures on the eastern margin of the other dyke in the quarry (to the west of the studied dyke, Figure 4.2), which also indicates an initial propagation towards the north (Figure 4.11A). This is contrary to that described by Hughes et al., (2015) who described the magma rising from below as an explanation for the presence of mud rock xenoliths present within the margin regions of the dyke. This discrepancy can be accounted for by the magma initially rising through the crust, and thus the Jurassic strata, however due to the extensional setting the dyke was emplaced within, the fracture it passively filled may have propagated laterally northwards in this area, thus changing the flow direction to be more horizontal rather than vertical (Figure 4.11A). This location of the quarry towards the north-eastern edge of the Skye Dyke Swarm (Figure 4.2A), may also support the lateral propagation of the magma away from a source further towards the south. Walker (1993) also suggested that dykes found around the Cuillin Hills complex to the south of the Isle of Skye (Figure 4.2A), were emplaced due to crustal extension associated with horizontal minimum compressive stresses.

Where the magnetic fabrics are stronger and have not been altered (FCG), these fabrics can possibly be used as indicators of magma flow. In the core region here the AMS and AARM signals for site G5, have similar axes and magnetic foliation orientations as such show normal fabrics. The normal fabric which is imbricated with respect to the dyke plane also suggests flow direction towards the North (Figure 4.11A). The shallower dipping orientation of the foliation plane compared with the dyke plane may suggest a slight vertical component to the magma flow direction within the core of the dyke, however the AMS and AARM ellipsoid shapes are predominantly more tri-axial to prolate suggests the magnetic lineation is a reliable indicator for flow direction (Figures 4.7Av and 4.7Bv). The impact that this has on the overall history of flow within the dyke would be that the flow was initially horizontal, but then migrated to being more inclined in this section of the intrusion. This could be due to eruption of the dyke towards the North providing a path for magma evacuation or drain back into the fracture towards the South.

It is also believed that there were no obvious internal boundaries within the magma that would suggest multiple injections of magma, other than the difference in oxidation of the margin regions compared with the dyke core. We infer these apparent compositional differences to be related to post emplacement fluid flow through the weaker margin regions of the dyke (Figure 4.10B), where there is a permeable network associated with quenching of the magma against the host, and subsequent contraction and fracturing (Spry, 1962).

These fluids caused breakdown of the basalt and enables the growth of pyrrhotite and then subsequently calcite in the margin regions (yellow regions in Figure 4.11B). Along strike at site G6, this presence of pyrrhotite within the dyke core is attributed to the proximity of the site to the branched region, this enabled the hydrothermal fluid to access and subsequently alter the dyke core (Figure 11B).

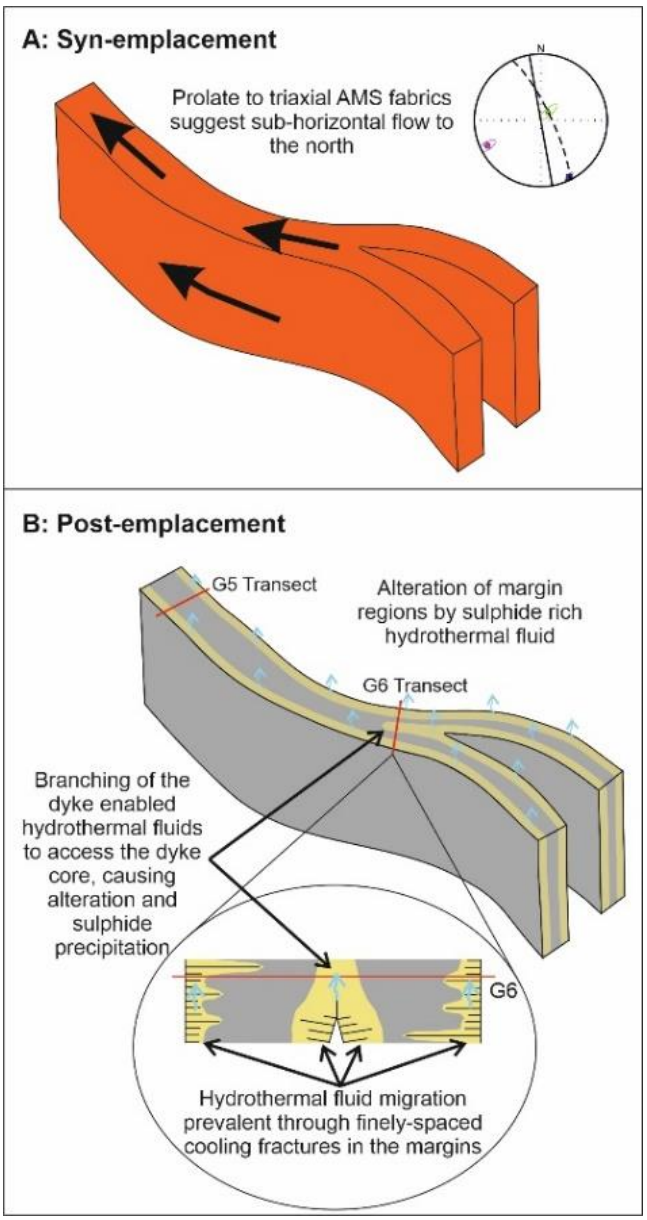

Figure 4.11 *Schematic diagrams of D1 dyke propagation and post-emplacement alteration. (A) Lateral magma flow during dyke propagation inferred from AMS normal fabrics in the dyke core. (B) Subsequent post emplacement hydrothermal fluids (blue) flowing through the small-spaced columnar jointing in the margin regions (yellow regions) resulting in growth of pyrrhotite crystals that dominate the magnetic fabrics. Alteration and precipitation of sulphides in the dyke core near G6 occurred due to proximity of the site to the branched section.*

4.6.4 Implications of the study

This study utilized a closely spaced sampling regime across the dyke thickness in order to understand the preserved fabrics and enabled the discovery of multiple fabrics originating from multiple sources. This shows the importance that sampling strategy, i.e. sampling of multiple regions of an intrusion, has for the identification of contrasting fabrics and the implications this has for understanding intrusion emplacement. Multiple studies focus on this the fabrics preserved only in the margin regions of intrusions (e.g. Knight and Walker, 1988; Poland et al., 2004; Clemente et al., 2007; Airoldi et al., 2012), which whilst useful for understanding initial propagation directions, can ignore large amounts of the emplacement history or be susceptible to alteration and as such unusable. This also means that in studies where anomalous or inverse fabrics are found close to intrusion margins, the fabrics preserved away from the margins could become important for understanding primary magma flow. Studying multiple regions of an intrusion also allows for the identification of more complete histories of intrusion emplacement, and aids in the development and re-evaluation of emplacement models. I propose a new mechanism of post-emplacement fluid migration within a dyke. The identification of post-emplacement fluids processes should be of great interest to both mining and geothermal industries, as this new model for the emplacement of multiple fluids could be of use when studying areas where more complex fabrics exist. Therefore, more detailed studies of dykes where evidence of post-emplacement fluid flow has been found could identify their emplacement direction and as such have the potential to act as trackers for the economic minerals they carry.

4.7 Conclusions

The analysis presented here on how magnetic anisotropy vary across both the thickness and length of a basaltic dyke provides new insight into the syn- and post-emplacement processes that occur during magma transport and storage. It also provides further insight into the effect that alteration has on pre-existing fabrics. This study uses a high-resolution sampling regime across the breadth of 2 sites separated along strike which have undergone contrasting amounts of alteration and as such have had syn-emplacement magnetic fabrics overprinted. Our observations of the AMS and AARM fabrics vary dramatically in terms of the orientation and shapes of ellipsoids, with the majority identified as anomalous magnetic fabrics both with respect to each other (i.e. ellipsoid orientations and properties) and with the dyke plane. These anomalous fabrics are linked to post-emplacement fluid flow associated with a sulphide rich body which allowed pyrrhotite to grow and titanomagnetites to break down. Where normal fabrics were observed, i.e. in the unaltered dyke core of site G5, horizontal

flow towards the North was inferred, which correlates with the orientation of macroscale ropey flow structures on an adjacent dyke within the quarry. These fabrics avoided alteration due to a lower amount of fracturing associated with slower cooling and insulation associated with increased distance from the intrusion margins. Along the dyke strike as site G6, more locations displayed anomalous fabrics and the presence of pyrrhotite. This is believed to be due to the site being near to a branched region in the dyke, which enabled post-emplacement fluids into the dyke core thus promoting greater amounts of alteration across the entire dyke thickness. The complexities observed in the magnetic and petrological fabrics of this mafic dyke demonstrate the complex nature not only of intrusions to be passages for magma flow through the crust, but also their ability to be sources of economic deposits. This study also highlights the complexities with understanding and interpreting both AMS and AARM fabrics, as there can be multiple histories that give rise to observed fabrics and as such implementing a sampling strategy, both density and distribution, that can understand these variations is essential.

Chapter 5: Plaster and Magnets: Tracking magma intrusion dynamics in the laboratory

This manuscript has been prepared for submission to the journal Earth and Planetary Science Letters. Data collection was undertaken at the Institute of Geophysics, Czech Academy of Sciences, Prague, in collaboration with Prokop Závada. Data analysis and preparation of the manuscript was done by myself with discussion and interpretation in collaboration with Janine Kavanagh and Prokop Závada.

5.1 Abstract

Understanding magma behaviour during emplacement within the crust is vital for determining the dynamic processes occurring in volcanic systems. Here I describe results from analogue laboratory experiments that study fluid flow during magma intrusion. Multi-coloured plaster of Paris (a pseudoplastic fluid and the magma analogue) seeded with magnetite particles was loaded sequentially or annularly into a piston, and injected through a central port in the base of a 1.2 x 1.2 x 0.5 m box filled with fine grained wheat flour (a cohesive granular material and the crust analogue). This created experimental plumbing systems which once solidified were excavated and photographed so the external morphology could be characterised in 3D. Cup structures, radial intrusions and arrested dykes were identified, which all had surface planar crenulations and lineations. Sequential colouring identified the external regions of the plumbing system which were active at a given time. Annular colouring enabled characterisation of the internal structures by slicing the intrusions into thin sheets.

Closely spaced sampling across the length, breadth and thickness of the intrusion slices enabled detailed three-dimensional mapping of magnetic fabrics using anisotropy of magnetic susceptibility. The observed fabrics, preserved by the orientation of the magnetite particles, indicate that a series of complex processes occurred during emplacement. These results suggest it is possible to successfully model the development of magnetic fabrics in analogue magma intrusions in the laboratory, providing a new method for direct comparison with field-based indicators of magma flow in solidified intrusions. This has important implications for the interpretation of flow fabrics in fossil and active intrusions in nature.

5.2 Introduction

Intrusions are important structures for transporting magma through the lithosphere, both on Earth and on other terrestrial planets (Ernst et al., 2001). Dykes in particular transport magma both vertically and laterally over great distances from source locations; up to 40 km for the

2014 Bardarbunga eruption, Iceland (Sigmundsson et al., 2015) whereas >2100 km for the MacKenzie Dyke Swarm, Canada (Ernst and Baragar, 1992), with the majority of dykes arresting prior to eruption (Gudmundsson, 2002). Monitoring dyke propagation in real time can only be done by measuring the signals created by active emplacement as magma moves and creates new pathways through the rock; e.g. seismicity and ground deformation (Sigmundsson et al., 2015), whereas understanding magma flow in exposed ancient intrusions only provides us with insight into the final flow processes prior to solidification (e.g. Smith, 1987). As such linking the dynamic emplacement of dykes with the processes that have occurred is problematic as the geological and geophysical observations we have are all indirect.

There is some debate over the direction of magma movement within dykes as they propagate through the crust, with a range of indictors from field-scale to micro-scale have previously been used to interpret dyke propagation and magma flow directions. However, these interpretations are restricted to 2D slices along the intrusion with limited locations were large exposure along strike is available, e.g. Colarado, USA (Smith, 1987; Poland et al., 2004). At the field scale, structures such as en echelon dyke segments, magma fingers, surface lineations and magma ropes (e.g. Pollard et al., 1975; Smith, 1987; Kavanagh et al., 2018a) have been identified, whereas, at the microscale, fabrics such as, crystal alignment, vesicle morphology and magnetic anisotropy have been used to interpret magma flow directions (e.g. Bhattacharji and Smith, 1964; Coward, 1980; Knight and Walker, 1988; Hastie et al., 2011). In standard dyke propagation models, early flow directions are preserved in margin regions, with later stage emplacement preserved internally. However, analogue experiments have shown that the migration of the magma flow trajectory within a growing dyke may be more common than initially thought, with a central vertical magma jet and downflow in the more distal dyke margins (Kavanagh et al., 2018a). Anisotropy of Magnetic Susceptibility (AMS) is commonly used to study magnetic fabrics preserved within crystallised intrusions (e.g. Knight and Walker, 1988; Raposo et al., 2004; Hastie et al., 2014) with a range of processes contributing to the observed fabrics; e.g. magma flow, post emplacement alteration and tectonic stresses (e.g. Rochette et al., 1991; Borradaile and Henry, 1997; Tauxe et al., 1998). However, the use of AMS can be restricted by sample size, sample density and sampling strategy meaning that it often shows a single localised view of a complex three-dimensional system.

Two leading theories exist for the emplacement of sheet intrusions in nature, with magma intruding as either a viscous indenter or by hydraulic fracturing (see reviews by Galland et al., 2015; Kavanagh et al., 2018b). In the viscous indenter model, a viscous magma pushes

through a brittle host rock causing inelastic deformation (Donnadieu and Merle, 1998) whereas in the hydraulic fracturing model the crust behaves elastically and fractures with fluid pressure within the fracture holding the fracture open (Lister, 1990). Both styles of emplacement have been widely studied through analogue laboratory modelling, and recent advances in imaging techniques have enabled these models to become more quantitative and representative of the natural environment, e.g. through the use of digital image correlation, particle image velocimetry, careful scaling and detailed measurement of material properties (e.g. Galland et al., 2006; Kavanagh et al., 2013, 2018a; Schmiedel et al., 2017; Poppe et al., 2019). These methodologies enable links to be drawn more strongly between real time observations of host rock deformation and intrusion morphologies, thus bridging the gap between active and extinct systems in nature and enabling dynamics to be inferred from now static observations.

In this study, I performed a series of novel laboratory models where plaster of Paris seeded with magnetite (magma analogue) was injected into fine grained wheat flour (host analogue) to investigate the flow processes linked with AMS development and evolution in analogue magma intrusions. I show for the first time how analogue experiments can aid in the interpretation of the dynamic processes creating the AMS fabrics observed in natural samples, as the AMS results collected here are compared with AMS results from fossilised dykes in nature. Comparing the results to natural examples also acts to validate the methodology for its application in the future.

5.3 Methodology

5.3.1 Model setup

For our method, we apply the viscous indenter model of intrusion propagation, to study the development of magnetic fabrics during magma emplacement. To do this, we fill a box with fine grained wheat flour (host analogue) a cohesive granular material that deforms brittlely (Walter and Troll, 2001), analogous to brittle crust, and inject it with plaster of Paris (magma analogue) from below (Figure 5.1A). The box was 1.2 x 1.2 x 0.5 m and had a 2 cm hole in the centre of the base onto which a 5 cm long rubber nozzle was attached and then held closed by compacting flour against either side, this prevented flour from entering the injector. This size of box was chosen to reduce edge effects that may occur due to using a lower viscosity plater mixture than previous experiments using the material (e.g. Kratinová et al., 2006; Závada et al., 2009), which used boxes with dimensions up to 0.6 x 0.6 x 0.5 m.

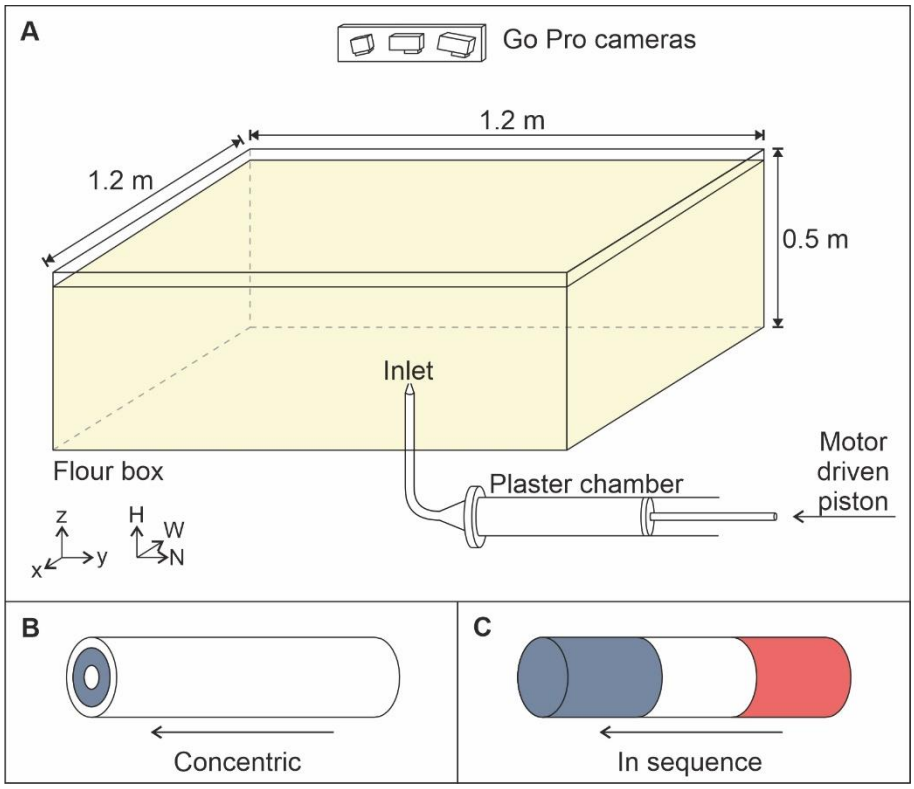

Figure 5.1 *Experimental setup showing the chamber holding in the plaster located below the box holding the flour and connected via an inlet in the centre of the base of the box. 3 GoPro cameras were suspended over the middle of the box. Coloured plaster was loaded into the chamber in either a (B) concentric pattern or (C) the sequential pattern.*

Fine grained wheat flour was chosen due to it being cost efficient in the required quantities and also due to it being non-carcinogenic when compared with other cohesive granular materials, e.g. silica flour (e.g. Galland et al., 2009). ~420 kg of fine-grained wheat flour was loaded into a 1.2 x 1.2 x 0.5 m box filled to a depth of 45 cm (Figure 5.1A). The mechanical properties of the flour were not measured directly, however Walter and Troll (2001) used direct shear tests to determine that it follows the Mohr-Coulomb failure criterion:

$$\tau = C + \mu \times \sigma_n \quad (5.1)$$

where σ_n and τ represent normal and shear stresses, C is material cohesion and μ represents tan ϕ where ϕ is the angle of internal friction (see Galland et al., 2006). Walter and Troll (2001) calculated that dry wheat flour had a cohesion of 35 Pa, a density of 0.57 kg/m^3 and an angle of internal friction (Φ) of 33°, which I assume are also appropriate for these experiments. Walter and Troll (2001) did not report errors, however based on work by Poppe (2019) errors could be up to 20%. Previous experiments that injected plaster of Paris into granular materials, used plexiglass boxes that had 46 to 60 cm square bases (e.g. Kratinová

et al., 2006; Závada et al., 2009), whilst these dimensions were sufficient for those models, would not be appropriate in this study. This is due to the nature of the intrusive morphologies that I aimed to model (dykes) combined with the lower viscosity plaster of Paris used, meant that a larger box was required to minimize edge effects. The upper surface of the flour was smoothed off using a blade set at 5 cm depth from the top of the box and coloured sand sprinkled over the top.

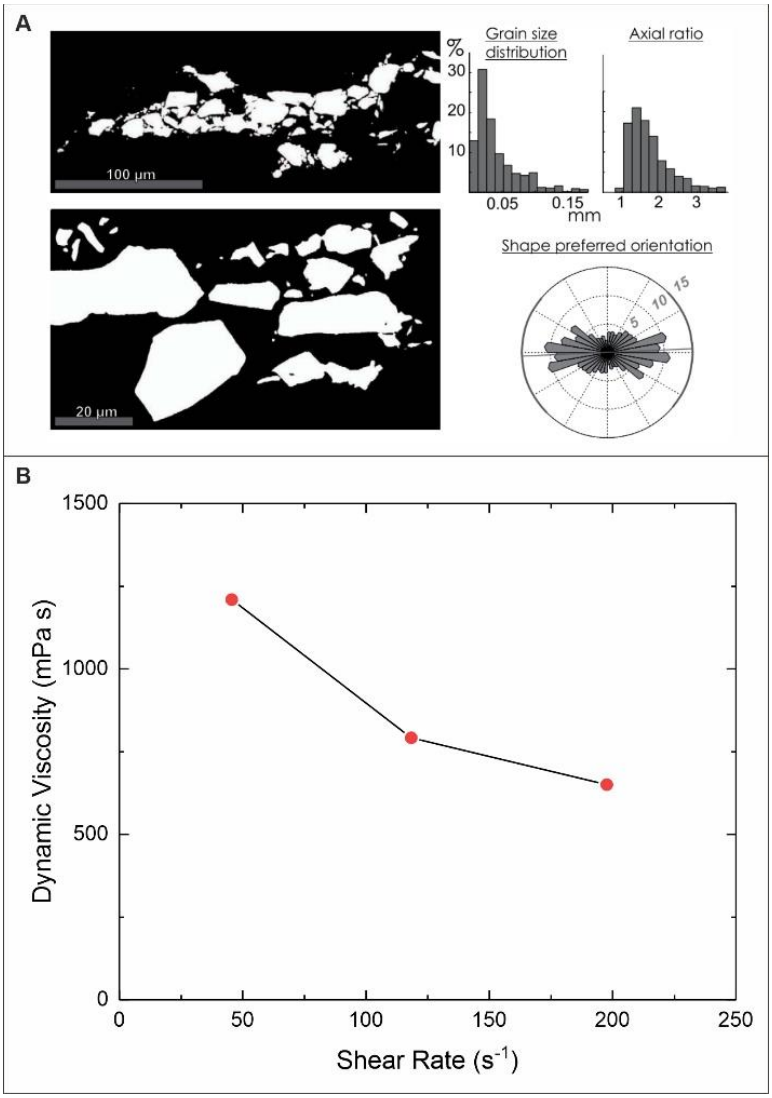

Figure 5.2 *Material properties. (A) Grain size and shape characteristics of magnetite particles suspended in plaster of Paris (taken from Kratinová et al., 2010). (B) Graph showing shear rate against dynamic viscosity for the plaster of Paris/water slurry using a mixing ratio of 2:1.*

To prepare the magma analogue, 14 kg of plaster of Paris was mixed with 7 kg of water forming a slurry that behaved as a pseudoplastic fluid with a yield strength solidifying through time (Závada et al., 2009). Plaster solidification would have occurred in < 30 minutes, which

is shorter than the timescale of an experiment (including preparation), so 150 g of a powder called "Retardan" was added which delayed this to several hours so that solidification affects were not considered during emplacement. The plaster was also seeded with 50 g of fine-grained magnetite powder (<0.2 mm, mode 0.02 mm; Kratinová et al., 2010; see Figure 5.2A). The magnetite was added as it is easily suspended in the slurry and it provides the particles necessary for magnetic analyses, as previous experiments by Kratinová et al. (2006) on the magnetic properties of the plaster of Paris have shown that it is diamagnetic with very low magnetic susceptibility, K = ~-5 x 10^{-6}. Dynamic viscosity was measured using a concentric cylinder setup on a Haake Rotovisco RV 20 viscometer, at shear rates of 45, 118 and 197.56 s^{-1} and calculated to be 1210, 792 and 650 mPa s respectively, for a 2:1 plaster to water mixture (Figure 5.2B). These values suggest the material is shear thinning, which agrees with Zavada et al. (2009) who measured similar plaster mixtures but at higher mixing ratios.

Once mixed the plaster was separated into 3 batches so that it would be dyed prior to loading into a cylindrical chamber depending on if the internal fabrics, or the order of emplacement was being studied. In experiments where the internal fabrics were to be studied post solidification, blue dye was added to a third of the plaster slurry and then loaded into the chamber using a series of nested pipes, each calculated to hold a similar volume of each batch, in a concentric coloured pattern of white-blue-white (Figure 5.1B). For experiments to identify the order of emplacement of the different parts of the intrusion, two of the plaster batches were dyed with blue and red before being loaded into the chamber sequentially (blue-white-red) so that injection could occur in sequence (Figure 5.1C). A piston was then inserted into the chamber and the complete injection system suspended below the box and connected to the nozzle which had been fixed into place prior to the flour being loaded into the tank.

Table 5.1: Experimental timings for each experiment in the series. Mixing ratio is the ratio of dry plaster to water. *Volume injected, injection velocity, injection rate and shear rate for experiment 1 were calculated using the values calculated for experiment 3 scaled by experiment duration. This is due to missing data for initial and final piston positions within the chamber. Experiment 3 was used for this as it used the same motor settings as experiment 1.

Experiment number	Mixing ratio	Motor start (s)	Motor stop (s)	Experiment duration (s)	Eruption (s)	Volume injected (m^3)	Injection velocity ($m\ s^{-1}$)	Plaster flux ($m^3\ s^{-1}$)	Shear rate (s^{-1})
1	2:1	48	1248	1200	1043	*3.8 x 10^{-3}	*6.62 x 10^{-3}	*2.08 x 10^{-6}	*0.66
2	2:1	15	1980	1965	270	8.7 x 10^{-3}	1.15 x 10^{-2}	3.60 x 10^{-6}	1.15
3	2:1	0	1820	1820	1820	3.2 x 10^{-3}	1.00 x 10^{-2}	3.16 x 10^{-6}	1.00
4	2:1	20	1635	1615	975	2.9 x 10^{-3}	1.04 x 10^{-2}	3.26 x 10^{-6}	1.04
5	1.8:1	20	835	815	815	1.5 x 10^{-3}	1.31 x 10^{-2}	4.12 x 10^{-6}	1.31

5.3.2 Experimental procedure

Experiments commenced by activating a computer-driven motor, running at a constant velocity, which gradually pushed the piston into the chamber and injected the plaster mixture into the box (see Table 5.1 for rates and timings). The force applied to the piston was digitally recorded at 5 second intervals. Once injection had stopped, the plaster was left for several hours to solidify.

The volume of plater (V) injected was calculated using:

$$V = \pi r^2 L \tag{5.2}$$

where, r is the radius of the chamber (0.075 m) and L is the difference between the start and end position of the piston within the chamber (m).

The mean injection velocity into the box from the conduit (υ_{con}) was calculated using:

$$\upsilon_{con} = \frac{\upsilon_p A_p}{A_{con}} \tag{5.3}$$

where, υ_p is the mean injection velocity of the piston in the chamber (m s^{-1}), A_p is the cross-sectional area of the piston (1.22 x 10^{-2} m^2) and A_{con} is the cross-sectional area of the conduit (3.14 x 10^{-4} m^2). Mean plaster flux, f (m^3 s^{-1}) was calculated using the equation:

$$f = Vt \tag{5.4}$$

where t is the experiment duration (s). The data for these parameters can be found in Table 1. The mean shear rate ($\dot{\gamma}$) of the plaster at injection can also be calculated using:

$$\dot{\gamma} = \frac{\upsilon_{con}}{0.5 W_{con}} \tag{5.5}$$

where W_{con} is the thickness of the conduit (0.02 m). Using the strain rate and the measured rheology of the plaster (Figure 5.2), the plaster viscosity at injection is estimated to be ~1.2-1.5 Pa s.

Once solidified, the intrusions were carefully excavated from the flour and photographed in situ to construct a 3D model using an open-source photogrammetry software. The outer intrusion morphology was studied in detail, and then the analogue volcanic plumbing system was sliced parallel and perpendicular to the flow axis to study the internal fabrics by observing the colour band distributions. 5 mm diameter by 4.5 mm long cores were drilled

from each of the slices in a grid pattern, for analysis of the AMS fabrics associated with the orientation of the magnetite particles.

5.3.3 AMS analysis

AMS fabrics can be reliable indicators of emplacement dynamics of igneous materials when studied in detail (e.g. Knight and Walker, 1988; Hargraves et al., 1991; Chadima et al., 2009). The fabrics observed correspond to the preferred orientation of magnetic particles within the magma, or in our case the magnetite suspended within the plaster slurry.

To analyse the AMS of the drilled experimental cores, each core was placed in a sample holder and placed in an AGICO KLY-4S Kappabridge fitted with a 3D rotator. The Kappabridge settings used were an applied field of 200 A m^{-1} and a frequency of 875 Hz. The AMS of each sample was measured using AGICO's Safyr7 software (Chadima et al., 2018c), with the measured ellipsoid axes orientations processed using AGICO's Anisoft 4.2 software (Chadima and Jelinek, 2009), utilising Jelinek statistics (Jelínek, 1977). AMS presents itself as a second order ellipsoid tensor with three principal axes; the longest K_1, intermediate K_2, and shortest K_3. The mean susceptibilities, K_m, are calculated by $(K_1 + K_2 + K_3)/3$ and were characterized by strengths of between 1-3 x 10^{-3}. The ellipsoid properties are important for understanding how magnetic fabrics develop, including: lineation (L, K_1/K_2), foliation (F, K_2/K_3), degree of anisotropy (Pj) and shape parameter (T) (Jelínek, 1981).

5.4 Results

In total 4 experiments were conducted, with the main variables being the colouring scheme and the injection rate. All experiments produced similar structures and so the description below is based on a representative example from experiment 2.1A.

5.4.1 Excavated intrusion: external morphology

For experiment 1, the total volume of the injected plaster was 2.1 x 10^{-3} m^3. The overall dimensions of the excavated analogue volcanic plumbing system were 44 cm long, 29.5 cm wide and 46.5 cm tall. The furthest sub-surface point of the intrusion from the injection point was 36 cm away, this was the tip of radial intrusion 2 (Figure 5.3A). For experiment 1, the overall morphology comprised structures at multiple scales. The macroscale structures were, a central magma body with a cup-shaped upper surface, three radial intrusions at ~120° strike separations emanating from the injector and central body, an arrested dyke, and a conduit to the surface (Figure 5.3A). Meso-scale structures observed in the sides of the intrusion were, parallel vertical lineations on the sub-vertical sides of central body (Figure 5.3), and symmetrical and asymmetrical surface ridges on radial intrusion walls (Figure 5.4).

Symmetrical ridges (Figure 4A) occur as broadly horizontal elongated ridges that are parallel to the intrusion strike and the known propagation direction. Asymmetrical ridges (Figure 4B) occur perpendicular to the flow direction and often have a curved shape. In total ~10 sets of asymmetrical ridges occur on the surface of radial intrusion 1 (Figure 4B).

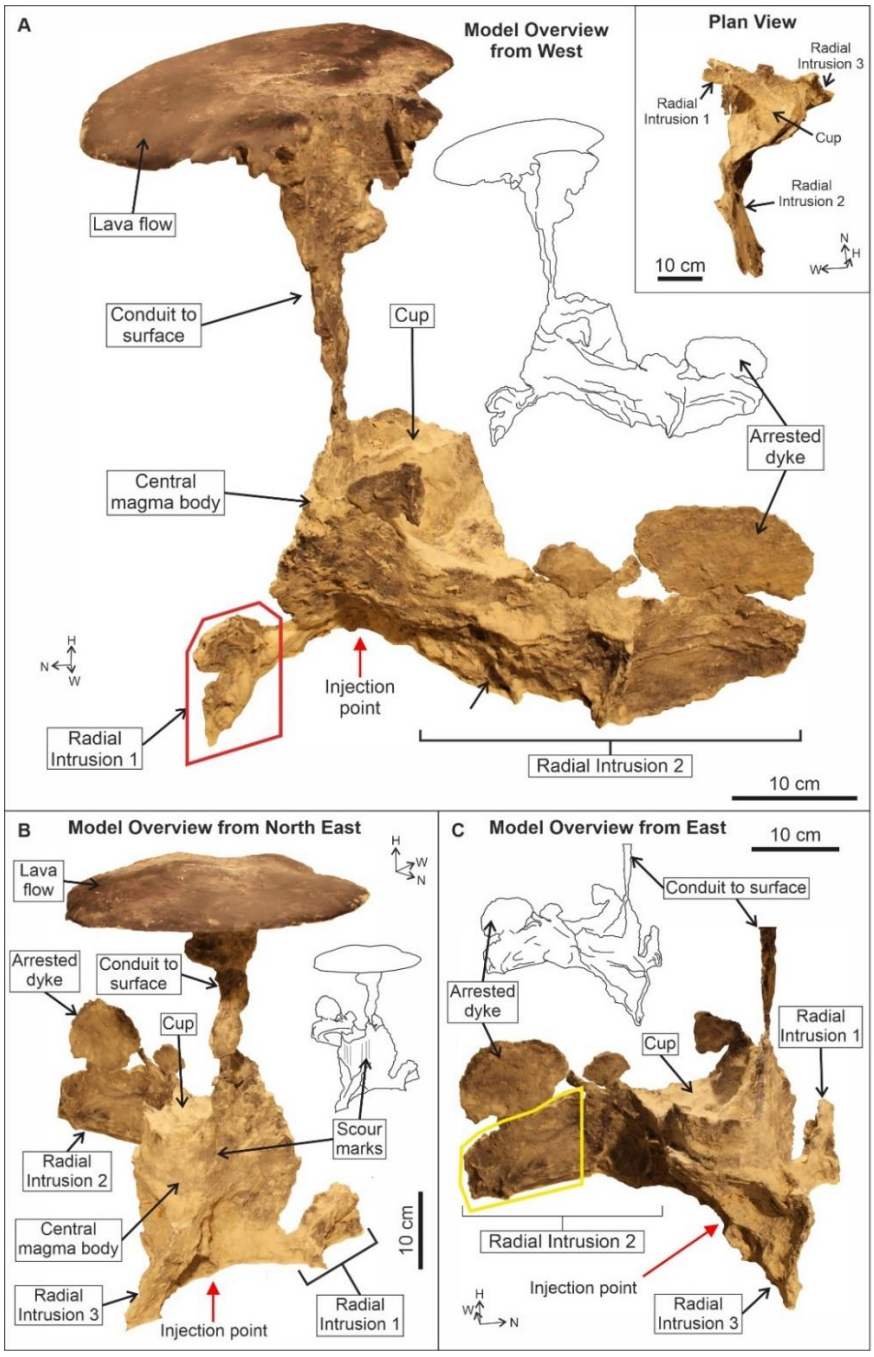

Figure 5.3 *Annotated photographs and diagrams of experiment 2-1A once excavated. (A) Photograph showing the overall intrusion morphology from west view with inset top-down view, red box indicates the section in Figure 5.4B. (B) Photograph of the intrusion morphology from north east. (C) Photograph of the intrusion morphology from east. Yellow box indicates the section shown in Figure 5.4A. Lava flow not shown due to being outside of photograph extent. Black bars represent 10 mm.*

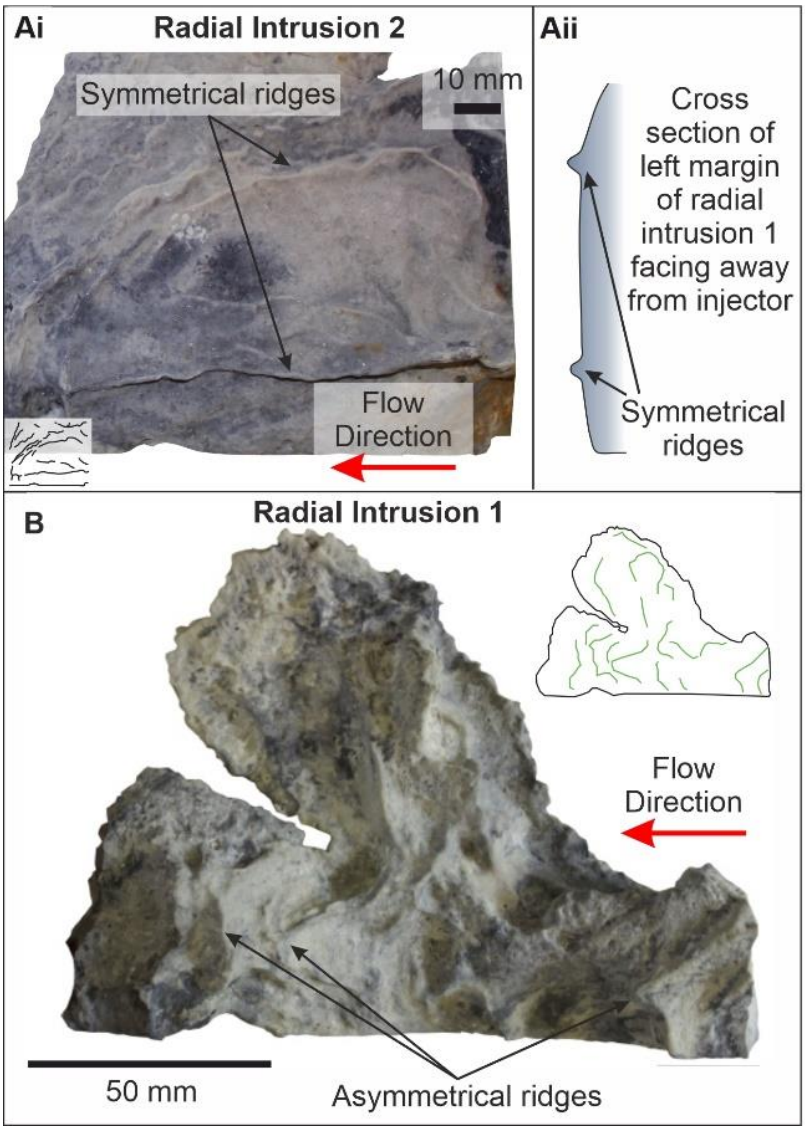

Figure 5.4 *Surface ridges in laboratory models. (A) Symmetrical ridges on the surface of radial intrusion 2 of the plaster model showing failed intrusion as sills into the flour, similar to sill- or dykelets, with (ii) showing a cross sectional schematic of the ridges. (B) Photograph of symmetrical ridges on the surface of radial intrusion 1. The contrasting colours on the intrusion surface represent dyed and undyed plaster. The ridge shapes are shown as green lines on the accompanying sketch.*

5.4.2 Excavated intrusion: internal morphology

The internal fabric of radial intrusion 1 (Figure 5.5) comprised between 10 and 15 concentric rings of the coloured and non-coloured plaster, observed in vertically cut faces perpendicular to the dyke axis (Figure 5.5Bi, Ci, Di). The number of coloured rings correlates with the number of asymmetrical ridges observed on the intrusion surface. This concentric pattern of multiple coloured bands suggests flow localisation through the intrusion core due to the colours building up in layers as new plaster progressively flowed through the section.

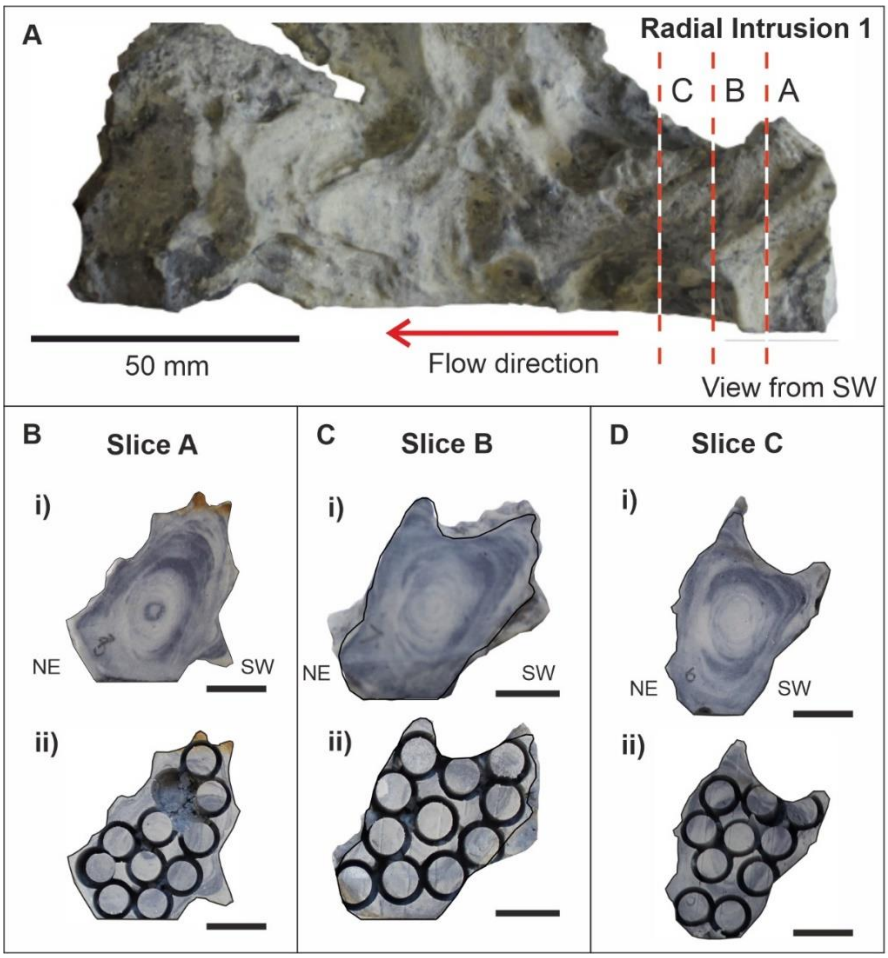

Figure 5.5: Photographs of radial intrusion 1. (A) Close-up photograph of the Radial Intrusion 1 (red box in Figure 5.3A), with the location of the three slices (A, B, and C) cut perpendicular to intrusion axis. Photographs of the internal morphology of slice A (B), slice B (C) and slice C (D), where (i) and (ii) represent the undrilled and drilled slices, respectively and all slices are oriented towards the source (flow towards the reader). Black bars represent 10 mm.

5.4.3 AMS analysis of experiment 2:1A

In total 835 cores were collected and measured for their AMS across 17 slices (A-Q), a sub-set from three slices A-C are presented here. The AMS data measured from radial intrusion 1 slices A, B and C (Figure 5.6A-C), show a range of K_1 orientations that group into two clusters that dip shallowly and are oriented up to 30° relative to the intrusion orientation (Figure 5.6). The ESE K_1 cluster on the stereonet corresponds to samples located near the right margin of the slices (green squares in Figure 5.6), whereas the NNW/SSE cluster on the stereonet corresponds to samples from the left margin of the slices (red squares in Figure 5.6). The K_3 axes orientations form 2 girdles across the plot, sub-perpendicular to the intrusion strike (red vertical line). All AMS ellipsoids exhibited oblate shapes (Figure 5.7), except for the central samples (blue) which are tri-axial to prolate. Samples at the margins show degrees of

anisotropy of P_j = 1.27-1.38 (crosses in Figure 5.7), which are greater than samples collected from the intrusion centre, P_j = 1.12-1.28 (diamonds in Figure 5.7). Ellipsoid errors did not exceed 1%.

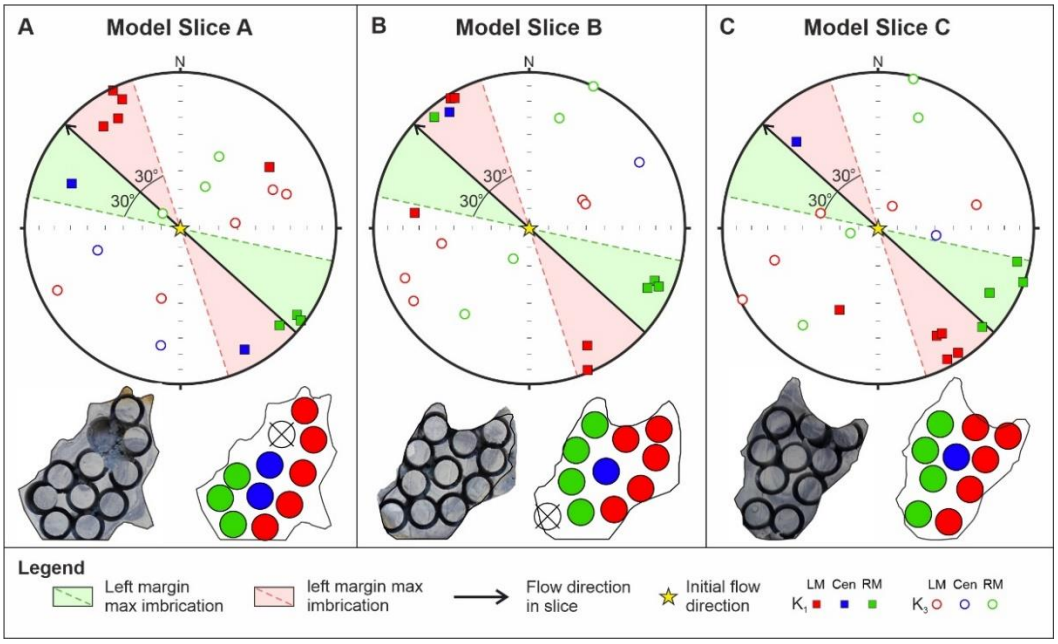

Figure 5.6 *Anisotropy of Magnetic Susceptibility (AMS) plots showing K_1 (solid squares) and K_3 (empty circles) for AMS data collected from three slices of Radial Intrusion 1 from experiment 2.1A: (A) slice A, (B) slice B and (C) slice C. Samples are colour-coded based on their position within the slice: right margin (Green), left margin (red) and centre (Blue). Dashed lines show maximum deviations of ± 30° declination from the intrusion strike direction preserving flow as AMS fabric imbrication, as identified by Varga et al. (1998) and modified from Geoffroy et al. (2002). Red and green zones represent left and right margins respectively. Yellow star shows initial vertical flow at conduit.*

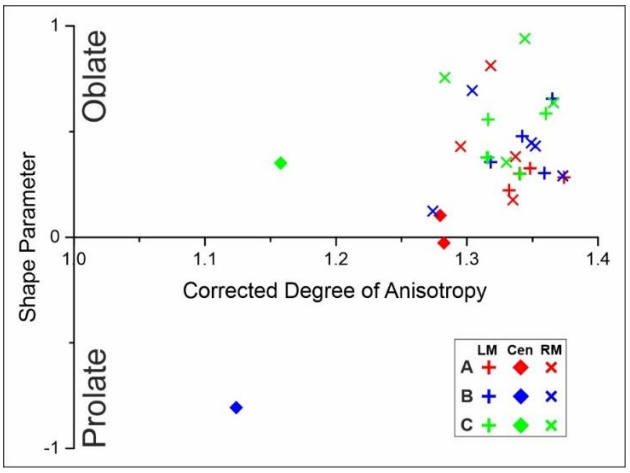

Figure 5.7 *Graph showing degree of anisotropy (Pj) against the shape parameter (T) for the samples from slices A-C. The positions of samples collected can be seen in Figure 5.5.*

5.4.4 Syn-emplacement host-rock deformation structures

During experiment 2.1A, time-lapse photography of the surface deformation was collected (Supplementary Video 1). After 435 seconds, a series of fractures had developed approximately 5 cm SW of the centre of the box. They were radial around a central ring fault system. Over time these fractures widened, with the central section inside the ring fault uplifted towards the camera. Initially the west portion of the uplifted section migrated westwards, however, after 925 seconds the south portion began migrating further southwards. Eruption occurred along the NE edge of the ring fault after 995 seconds. Injection was stopped at 1200 seconds. In total 2.12 x 10^{-3} m^3 of the plaster/water slurry was injected (Table 5.1).

5.5 Discussion

5.5.1 Controls on the large-scale intrusion morphology

Understanding the processes that give rise to the different structures observed in the laboratory model can help us to improve our understanding of the development of sheet intrusions in nature and how flow is recorded in solidified magma bodies. Both the model magma analogue and model host-rock analogue controlled the morphology of the analogue volcanic plumbing system that was formed.

The initial injection applied a radial maximum compressive pressure to the flour around the inlet, pushing the flour upwards and outwards. The pressure exceeded the tensile strength of the flour, causing it to fail under tension resulting in the crack opening in the direction of σ_3, perpendicular to σ_1 (Figure 5.8A), initially as mode I style fractures (Pollard, 1987). The relatively high injection rate meant that the plaster initially flowed as a low viscosity fluid into these fractures, with an estimated shear rate of 1.2-1.5 Pa s (Figure 5.2). These plaster-filled fractures propagated vertically and laterally from the injector, forming a ring-like fault structure which was then intruded by the plaster to form a cup-structure (Figure 5.8B). Contemporaneously, three radial dyke-like intrusions forming at ~120˚ separation around the injector, the initial orientations of which were random. Above one of these, the arrested dyke was also formed (above radial intrusion 2 in Figure 5.3A) and had a similar morphology to a penny-shaped crack, which can be attributed to propagation of a plaster-filled fracture from a point source (Pollard, 1973). This dyke may have stalled either during inflation of the main magma body or when a conduit to the surface developed, diverting the plaster to eruption.

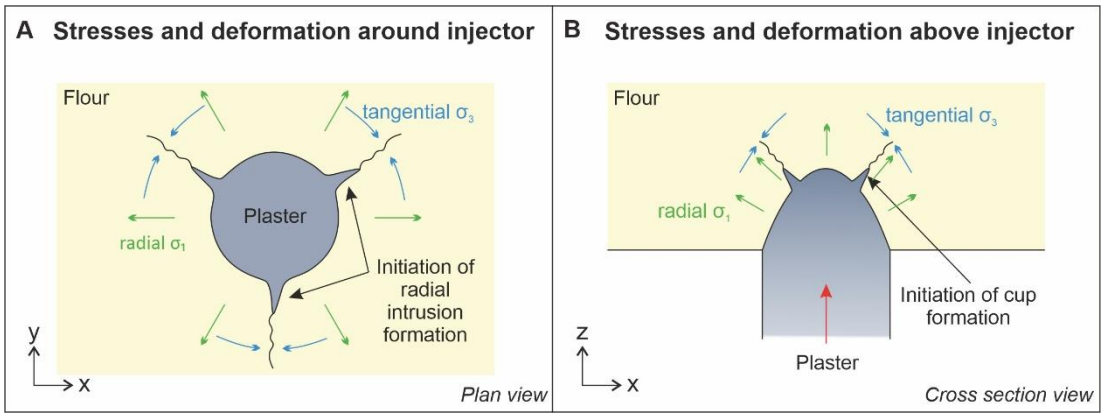

Figure 5.8 *Schematic diagrams showing stresses and deformation around the injector associated with initial emplacement of viscous plaster of Paris, in (A) plan view and (B) cross section. Plaster then flows into the fractures forming the radial intrusions and cup structure. The orientation of σ_1 is in green and σ_3 is in blue.*

A combination of prolonged plaster flow into the cup-structure and rotation of σ_3 to vertical, assisted inflation of the host material vertically along mode II type fracturing of the ring fault system (e.g. Pollard, 1987; Rubin, 1995). This uplifted the upper surface of the model and created space for plaster to accumulate, building the central body. This structure is similar to other cup-shaped analogue magma intrusions formed in wax models (Wyrick et al., 2015), with similar processes to those inferred for the formation of structures (dykes and cups) in the analogue models described by Mathieu et al., (2008) who injected golden syrup and honey into compacted sand and also by Galland et al., (2014) who injected solidifying vegetable oil into silica flour.

The uplifted flour surface and associated surface fracturing is linked to the intruding plaster pushing the flour up and out, resulting in the development of mode I tension fractures that propagated down from the flour surface towards the growing central body with opening directions parallel to σ_3 orientation (Walter and Troll, 2001; Poppe et al., 2019). Eruption occurred when the ring fault that propagated down from the flour surface, intersected with plaster contained within the cup structure, creating a conduit to the surface. The propagation of ring faults downward from the upper surface has also been observed in the analogue models of dyke propagation by Abdelmalak et al. (2012) who injected golden syrup into fine grained silica powder.

5.5.2 External and internal structures indicate flow dynamics

The structures identified on the external surfaces of the excavated model volcanic plumbing system reveal additional insight into its propagation dynamics. These include scour marks, symmetrical ridges and asymmetrical ridges, with each structure associated with different physical processes.

Associated with the inflation of the central body, were the development of a series of sub-vertical parallel striations on its outer surface (Figure 5.3). These originated from the plaster scraping against asperities in the flour wall during emplacement, which are reminiscent of inflation scarps in lava flows (Hon et al., 1994) or to scour marks identified in dykes at Spanish Peaks, Colorado, USA (Smith, 1987). In these natural examples, the solidified magma scratches grooves into the ductile magma that is flowing past.

The symmetrical ridges on the experimental radial intrusions (Figure 5.4A) are aligned parallel to the flow axis and so may be attributed to the formation of sill-lets (similar to dykelets). These may have formed due to overpressure in the analogue magma pushing small amounts of magma into a 'damage zone' of small fractures that propagate away from the main intrusion, parallel to the flow axis (e.g. Johnson and Pollard, 1973).

The asymmetrical surface ridges that were formed on the radial intrusion segments with the steeper side oriented towards the intrusion tip (Figure 5.3B and 5.4B), the formation of which could be attributed to a combination of 2 processes. Firstly, the strain rate decreased as the fluid propagated further from the injector, and this caused the relative viscosity of the plaster to increase (Figure 5.2). This caused a pressure build up in the fluid as the propagating tip slowed down but the fluid flow from the injector continued. This pressure was then subsequently released as a breakout at the intrusion tip (Figure 5.9). The breakout margins were then deformed by shear stresses between the outer surface of the intrusion and freely flowing plaster through the intrusion core, dragging forward the dyke margins and causing them to wrinkle and fold. This process is envisaged to be like a vertically-oriented counterpart to the formation of ropey structures on the surface of pahoehoe lavas. Such asymmetric ropey structures have been observed in the field on exceptional exposures of chilled dyke margins (Figure 5.10). The occurrence of breakout during dyke propagation is reminiscent of similar structures produced in gelatine experiments using a solidifying magma analogue (Taisne and Tait, 2011). Additionally, Chanceaux and Menand (2016) also identified ropey structures on the surface of sills produced in experiments where hot solidifying vegetable oil was intruded into gelatine.

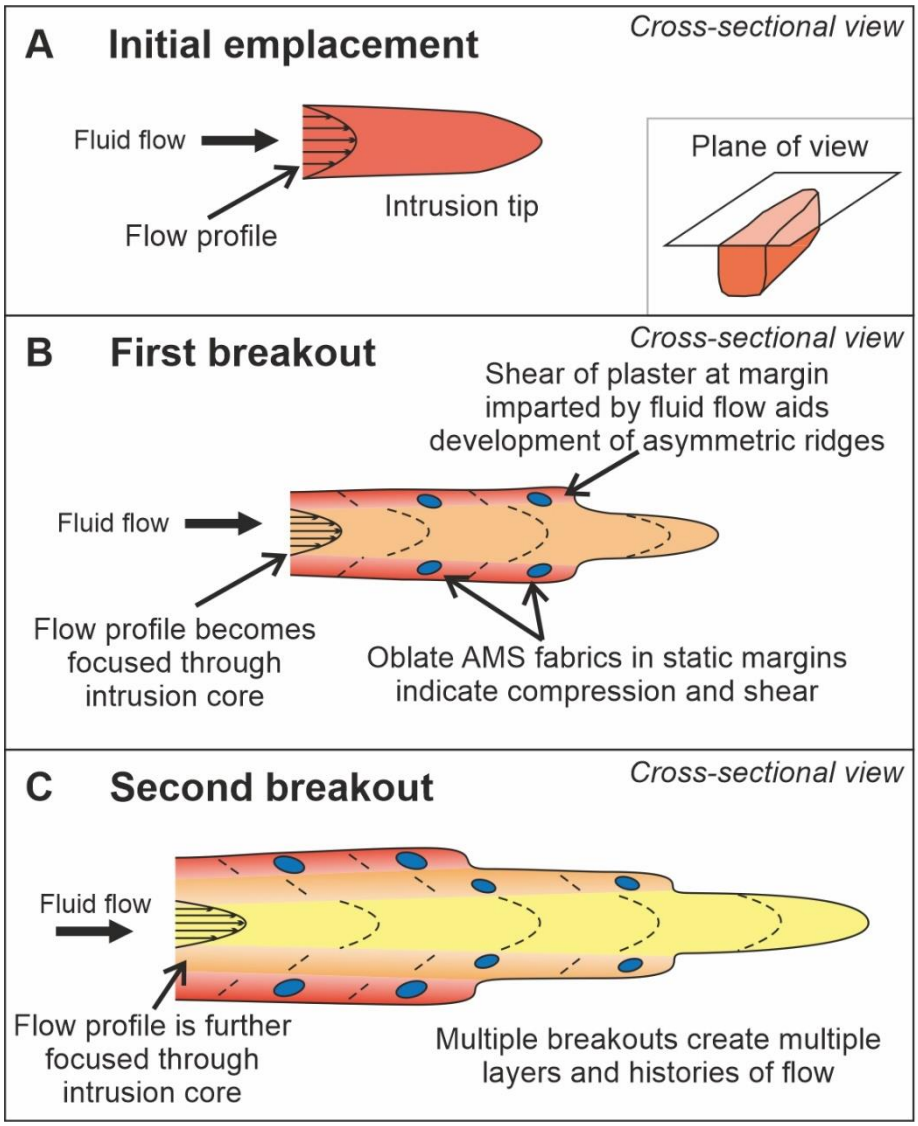

Figure 5.9 *Emplacement model showing the development of the flow fabrics from the analysed section of the intrusion. (A) Initial emplacement of fluid in fracture with inferred flow profile, inset shows the plane of the cross-section. (B) Breakout of plaster from the intrusion tip with compression of the plaster and magnetite in the margin regions producing oblate AMS fabrics (blue ellipses). Asymmetric ridges formed by a combination of plater breakout at the intrusion tip and shear of new plaster through the intrusion core. (C) Inflation of the intrusion outwards as more plaster flows through. Plaster flow becomes concentrated through the intrusion core with further*

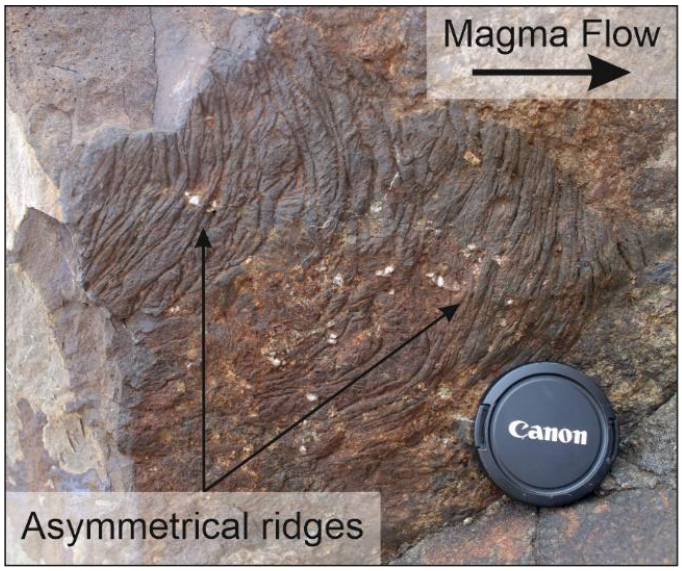

Figure 5.10 *Photograph or ropey flow structures preserved on the margin of dyke that outcrops within Inver Tote quarry, Isle of Skye, Scotland. The ropey fold structures that have been inferred to show the flow direction during initial emplacement.*

The concentric colouring pattern observed within the slices of the intrusion (Figure 5.5B-D) suggests flow localisation occurred within the intruding plaster as new plaster pulses flowed through the intrusion core. Flow localisation has been observed in cross-sections of fossilized natural intrusions, which have has their crystal fabrics analysed, such as in the sills of Mull (Holness and Humphreys, 2003). These intrusions showed wider coarser-grained regions of the intruding sheet and greater thermal alteration and erosion of the surrounding host rock, which was attributed to prolonged magma flow through those regions.

When the number of colour bands observed in intrusion slices (10-15), is compared with the number of asymmetric surface ridges (9-10), the numbers are similar. This supports the argument for multiple plaster pulses flowing through the intrusion and the progressive stress build-up and break-out in the tip region (Figure 5.9) with subsequent dragging of the external surface.

5.5.3 AMS analysis and comparison with nature

For AMS fabrics to be used to interpret the flow direction and sense of flow, magnetic lineation and foliation should be imbricated with respect to the intrusion plane with a maximum deviation of 30° from strike (Figure 5.10; Varga et al., 1998; Geoffroy et al., 2002). Within the studied slices from radial intrusion 1 (Figure 5.5A-C), the AMS results show two clusters of K_1 orientations that are imbricated with respect to the dyke plane, and therefore can be interpreted as showing the flow direction when compared with the "model" AMS fabric showing flow in sheet intrusion (Figure 5.10; Varga et al., 1998; Geoffroy et al., 2002). The Varga et al. (1998) model suggests that normal AMS fabrics with K_1 axes that lie within

30˚ of intrusion margins are imbricated, with the direction of imbrication pointing in the direction of magma flow. In the case of the radial intrusion 1, this imbrication shows flow from the inlet towards the intrusion tip, which is in agreement with the known location of the source (Figure 5.9). This correlation between these laboratory results and "model" fabrics shows promise for verification of the method used.

The oblate nature of the AMS fabrics in the margins of the experimental intrusion (Figure 5.7), are likely formed from compression of the plaster against the margin (Figure 5.9) orienting the K_3 axes to be sub-perpendicular to the dyke plane, with shear orienting the K_1 axes towards the intrusion tip. Mattsson et al. (2018) observed similar patterns in K_3 axis orientations in oblate ellipsoids, being perpendicular in the margins of the felsic Sandfell laccolith, E. Iceland. In their study, they attributed the oblate AMS fabrics with K_3 orientations perpendicular to the intrusion margins to compression and shear of the intruding magma against the host rock. Tri-axial to prolate ellipsoids, characteristic of the internal samples showed K_1 axes sub-parallel to both the intrusion plane and flow axis, as such can be used to infer flow (Figure 5.6). The slight misalignment of the K_1 axes with the intrusion plane in these samples may be a sampling artefact as the exact centre of intrusion may not have been collected due to the complex intrusion morphology, however they still lie within 30 ° of the intrusion plane (Varga et al., 1998).

In order to better validate these laboratory models, the obtained data need to be compared with AMS data from dykes in nature. A selection of examples of magnetic fabrics from solidified natural dykes that have been identified as having lateral magma flow (Poland et al., 2004; Aubourg et al., 2008; Hastie et al., 2011; Delcamp et al., 2014), have been collated and combined with the data from this study in Figure 5.11. Their dyke planes have been aligned in the same orientation as the studied model intrusion for ease of comparison. Strong similarities exist between the natural and studied analogue samples with imbricated ellipsoid orientations of up to ± 30° with respect to the dyke plane, as such supporting the interpretation of lateral magma flow both in the analogue models and the natural samples

A few samples from the left margin show differences of >30 ° with respect to the dyke plane (red squares in Figure 5.6). This may be caused by a range of processes, such as flow in the analogue intrusion not being completely horizontal, or other processes occurring within the model that were not expected, such as shear along the fracture during emplacement (e.g. Clemente et al., 2007).

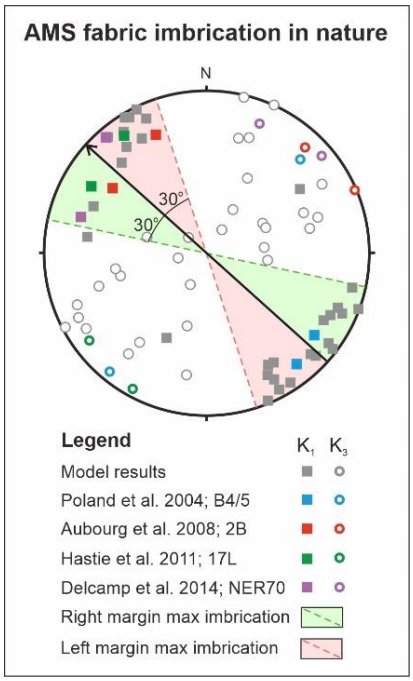

Figure 5.11 *Anisotropy of Magnetic Susceptibility (AMS) plots showing K_1 (solid squares) and K_3 (empty circles) for AMS data collected from natural samples by Poland et al. (2004), Aubourg et al. (2008), Hastie et al. (2011), and Delcamp et al. (2014) and the slices from this study (grey). Natural data has been rotated to show the flow in the same orientation as experiment 1. Shaded regions show theoretical model AMS orientations for a dyke showing lateral flow. Maximum deviations of ± 30° from the dyke strike direction for AMS fabric imbrication, as identified by Varga et al. (1998) and modified from Geoffroy et al. (2002); Blue and purple zones represent left and right margins, respectively.*

There is variation in the degree of anisotropy between the analogue models (P_j of 1.25-1.4) and natural samples, P_j of 1.0-1.2 for samples collected from a sill and dyke from the Isle of Skye, Scotland in chapters 3 and 4, and 1.0-1.1 for samples from a dyke in Tenerife, Spain by Delcamp et al. (2014). This is likely an artifact of contrasting sample dimensions between the two methods, with volumes of ~3.53 x 10^{-7} m^3 for analogue models and ~2.76 x 10^{-3} m^3 for natural samples, resulting in fewer magnetic particles present. This means that the applied field and subsequent calculated AMS ellipsoid would be averaged over a fewer number of particles across the sample, thus increasing the effect of grain shape and textural anisotropy on P_j (Cañón-Tapia et al., 1996).

5.5.4 Limitations

The main limitation with these experiments is the ability to control the properties of the host-rock analogue when using such large material quantities. The largest technical challenge was obtaining a uniform compaction of the flour to all areas of the box in order to reduce

heterogeneities and as such improve the experimental reproducibility and the scalability to the natural environment. When loading the box this was done with a hoist that ran over one side of the box, resulting in the flour being loaded into one side then manually moved around to fill the box, so possibly created a heterogeneous compaction in the lower portion of the box. This was mitigated as much as possibly when distributing the flour to the rest of the box and subsequent agitation once fully loaded, prior to smoothing off the upper surface. The agitation was done for a similar amount of time for each experiment with a similar amount of flour used for each time, to give as uniform an overburden compaction as possible. However, similarities in the overall intrusion morphology and structures formed across the experiments, i.e. radial dyke structure, central magma body with cup-shaped upper surfaces and lobate tips, suggests that the method for loading the flour into the box was sufficient. Any heterogeneity present may help with scaling to nature as the Earth's crust is not homogenous as such magma can encounter stronger and weaker rocks during its emplacement within the crust (e.g. Kavanagh et al., 2006).

Another limitation of these experiments, is the inability to directly record the growth of the analogue plumbing systems, requiring the use of sequentially coloured plaster and post-emplacement excavation to reconstruct this. This limitation encounters similar problems as studying active dyke propagation in nature and would need techniques such as 3D X-ray CT (Poppe et al., 2019) to monitor this in the laboratory. However, such techniques require smaller experiment tanks, ~20 x 20 x 16 cm (Poppe et al., 2019), which is not possible for this plaster-flour experimental setup or resolution the AMS sampling.

5.6 Conclusions

In this study, I have demonstrated the versatility of the experimental methodology, and its ability to model structures and magnetic fabrics that have been observed in solidified intrusions around the world. This allows a better understanding of emplacement processes to be developed. In the slices studied, imbrication of the AMS ellipsoids in the direction of the dyke tip, backs up both the model fabric arrangement and examples from solidified dykes. Understanding these processes enhances our understanding of how magma plumbing systems in active volcanic settings develop, both on Earth and across the solar system. This method can easily be adapted to study the emplacement mechanisms in other types of intrusive settings, such as sills, laccoliths and larger bodies like magma chambers.

Chapter 6: Summary and Conclusions

This thesis has investigated how magma flow is preserved within magmatic intrusions and the role in which magnetic fabrics can be used to understand both syn- and post-emplacement processes. A basaltic dyke and a crinanite sill from the Isle of Skye, Scotland, part of the British and Irish Palaeogene Igneous Province, were studied in combination with laboratory experiments using analogue materials to investigate the following aims:

1. How does magma flow vary across the length and breadth of an intrusion?
2. How do magnetic fabrics vary across the length and breadth of solidified magma intrusions in nature?
3. What are the processes that produce different magnetic fabrics and what can they tell us about the syn- and post-emplacement processes in ancient solidified intrusions?
4. How is flow preserved within laboratory models that use analogue materials and what can these models tell us about magma flow in nature?

Firstly, a crinanite sill was investigated to understand how magma flow evolved through time by identifying variations in fabrics across the intrusion breadth, to determine the implications this had on its emplacement and subsequent solidification. Secondly, a basaltic dyke from the same location was investigated in the same manner but at two locations separated over a relatively short distance along strike. Finally, laboratory experiments using analogue materials whereby plaster of Paris seeded with magnetite particles was injected into fine grained wheat flour to understand intrusion emplacement dynamics by linking intrusion morphology to magnetic fabrics.

6.1 Summary of papers

The first paper in this thesis (chapter 3) used a combination of rock magnetic analyses, petrology and thermal modelling to investigate the syn- and post-emplacement processes associated with emplacement of a sill from the Little Minch Sill Complex, Isle of Skye. Within this study, I used AMS and AARM to study how magnetic fabrics varied across the breadth of a sill exposed within Inver Tote quarry. Within the exposure, I identified multiple different fabrics which indicate different parts of the sill emplacement history. At the margins, AMS fabrics suggested that initial flow occurred in a NW-SE orientation, which correlated with the axis of magma fingers identified by Schofield (2009) (Figure 6.1Bi). During inflation of the sill, adjacent magma fingers coalesced creating a more sheet-like body, allowing magma to flow between the individual fingers in a NE-SW direction (Figure 6.1Bii). As the sill cooled,

crystallisation caused the magma to lock up, which led to flow becoming concentrated within the interstitial pore spaces (Figure 6.1Biii), rising obliquely through the sill away from the lower contact which experienced a slower cooling rate due to a pre-existing hot sill directly below. This asymmetric profile in the solidification rate also resulted in an asymmetric profile in the preserved magnetic fabrics.

The second paper of this thesis (chapter 4) focussed on a dyke from the Skye Dyke Swarm, Isle of Skye, and used a combination of rock magnetic analyses and petrology to investigate the syn- and post-emplacement evolution of the dyke from two locations separated along strike by a relatively short distance of ~13m. Within this study, AMS and AARM were used to study the evolution of the magnetic fabrics, identifying variations in the fabrics both across the dyke breadth and along strike. At site G5 the margin regions were shown to be dominated by pyrrhotite whereas in the dyke core titanomagnetites were identified as the magnetic carriers. This difference originated from a post-emplacement sulphide rich fluid (Figure 6.1Cii) that flowed through the permeable network associated with cooling related columnar jointing formed during rapid cooling of hot magma as it came into contact with cold host rock. This fluid altered the initial basalt, breaking down pre-existing magnetic phases and growing pyrrhotite within fractures and vesicles, with replacement of basalt also occurring. Within the fresh unaltered dyke core, AMS and AARM signals aligned and were indicators of normal fabrics and as such suggested that lateral magma flow along dyke strike occurred (Figure 6.1Ci). Site G6 exhibited contrasting magnetic fabrics to site G5, in that the dyke core region also appeared altered, whereas locations 2, 3 and 7 (closer to the dyke margins) were characterised by titanomagnetite bearing fabrics. This variation can be attributed to the site being close to branching of the dyke, which would enable the post emplacement fluids to access and subsequently alter the dyke core region. The larger amount of alteration at site G6 prevented identification of the magma flow fabrics within this region. This has large implications for understanding the magnetic fabrics preserved within intrusions and using the observed fabrics of one location and applying the results to the entire intrusion, as large variations in fabrics were identified over relatively small distances.

The third paper of this thesis (chapter 5) involved laboratory experiments using analogue materials to understand the processes preserved during the emplacement of analogue intrusions. In the study, plaster of Paris seeded with magnetite was injected into a box filled with fine grained wheat flour. GoPro cameras recorded the surface deformation during injection, identifying a series of radial fractures combined with ring faults, and eventually eruption of the plaster. Once solidified, the intrusion was excavated, and multiple structures

were identified at different scales. Macro-scale structures included, a central magma body with a cup-shaped upper surface, three radial ring dykes, lobate dyke tips, a conduit to the surface and a subsequent lava flow (when injection continued post eruption). Smaller scale structures were observed on intrusion surfaces, these included, scour marks, symmetrical and asymmetrical ridges. When the intrusions were sliced up and studied, the internal fabrics indicated lateral flow along the radial intrusions with flow localisation into conduits. AMS data suggested that compression of the plaster against the dyke wall occurred in the margin regions, whilst stretching associated with flow dominated fabrics in the dyke core. Imbrication of the AMS fabrics in the walls supported flow away from the known source, which correlates well with idealised fabrics identified by Varga et al. (1998), and also with a range of natural examples (Poland et al., 2004; Aubourg et al., 2008; Hastie et al., 2011; Delcamp et al., 2014), helping to validate the methodology.

The models performed in this thesis have a great potential to support and emphasise the processes occurring within natural plumbing systems, however the studied analogue intrusion is restricted in its application to the natural examples studied in chapters 3 and 4. In the case of the sill from chapter 3, the main AMS fabrics that can be compared with the analogue models, are those closest to the margins which exhibit an imbrication consistent with magma flow. These fabrics are like those observed adjacent to the margins of the analogue model, with both sets of fabrics lying within 30˚ of the intrusion planes (Varga et al., 1998). However, it should be noted that the intrusion planes are perpendicular to each other, i.e. the sill is horizontal and the analogue intrusion is vertical, which means that contrasting syn- and post-emplacement processes are occurring within the bodies, thus making the experiments not completely comparable.

A comparison of the AMS fabrics from the dyke in chapter 4 with those in the analogue intrusion is easier than the sill samples due to both intrusion planes being vertical. However, comparisons can only be for fabrics preserved within the intrusion cores, due to the natural dyke margins being altered by hydrothermal fluid flow. From the natural and model intrusion cores, similar AMS fabrics with both magnetic lineation and shape anisotropy are observed, with both properties showing sub-horizontal imbricated prolate fabrics indicative of magma flow along intrusion strike. Whilst only four samples were collected from the centre of the laboratory model slices (two from slice A and one each from slices B and C; Figure 5.6), the results of these data still demonstrate the potential of using a combination of AMS fabrics from the cores of both natural and analogue intrusions to identify magma flow.

Whilst there are some comparisons that can be made between the orientations of magnetic fabrics observed in nature and the experiments, there is one main caveat with the models which makes accurate comparisons difficult. This is the lack of scaling the model properties and dimensions to the natural system, as such what the models actually represent is difficult to determine. The parameters where the lack of scaling has the greatest impact is on the material properties, which subsequently effects other variables, including intrusion morphology. The missing properties of the flour mean that the strength relationship between the intruding plaster and the host can not be determined which subsequently impacts the behaviour and morphology of the intrusion, along with the flow fabrics created during emplacement. This is most evident in the aspect ratio (length-thickness) of the experiment compared to nature, i.e. 36:2 for Radial Intrusion 2 compared to ~1000:1 for natural dykes. Whilst these values for natural dykes refer to basaltic rheologies, more evolved magmas still have aspect ratios in the >100:1 (Bunger and Cruden, 2011). This means that direct comparisons cannot be done accurately, and any comparisons made should be done with care.

6.2 The dynamics of magma flow in intrusions using magnetic fabrics

Plumbing systems consist of multiple types of intrusions and intrusion morphologies (Figure 6.1A), with a range of factors influencing emplacement style, morphology, and how magma flows through them. These factors include host rock strength (e.g. Kavanagh et al., 2006; Vachon and Hieronymus, 2017), stress orientations (e.g. Stephens et al., 2017), magma overpressure (e.g. McLeod and Tait, 1999), flux (e.g. Castro et al., 2016), and rheology (Magee et al., 2013b; Mattsson et al., 2018). How magma flows through sheet intrusions cannot be measured directly, instead it relies on observations of solidified intrusions exposed through erosion or using laboratory experiments using analogue materials.

Several macro-scale flow indicators were identified in this thesis, which can be linked between the sill and dyke with the laboratory models. Firstly, the presence of magma fingers in the sill (Figure 6.1Bi) can be linked to the tip region of radial intrusion 1 (Figure 5.4B) of the laboratory model as fingers start as smaller lobes which continue to propagate. If propagation of intrusion 1 had continued the lobes may have coalesced, like the coalesced fingers of the sill. On one dyke in the quarry, magma ropes were observed on the exposed margins, with similar features observed on the margins of the analogue intrusions and are attributed to shear folding of viscous fluid at the intrusion margins. The presence of these features in both locations suggests that similar processes were occurring during the formation of both natural and laboratory intrusions.

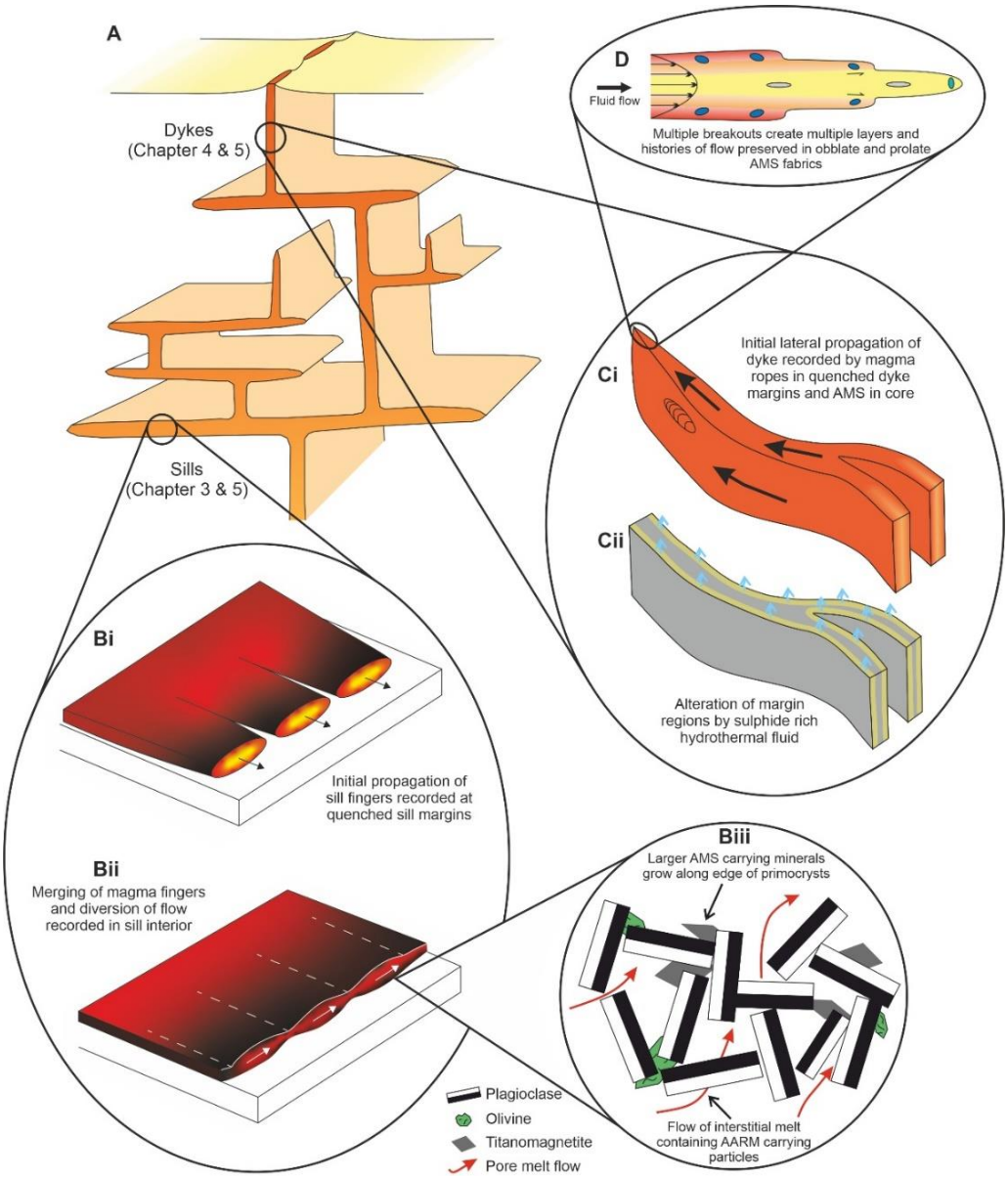

Figure 6.1 *Schematic diagram showing what has been learnt from these studies. A) Volcanic and igneous plumbing system showing a series of interconnected dykes and sills. B) Emplacement of sill as fingers (i) which inflated and coalesced (ii). During solidification, the crystal mush locked up and flow of interstitial melt occurred through interconnected pore spaces (iii). C) Lateral magma flow along the dyke (i), prior to solidification and subsequent flow of hydrothermal fluid through the margin regions (ii) which altered the magnetic fabrics. D) Prolate AMS fabrics within intrusion core, with imbricated fabrics near to intrusion margins showing flow direction, along with oblate fabrics (blue ellipses) suggesting compression and shear of the fluid near to the intrusion tip and margins.*

This thesis identified multiple flow regimes present in both natural and experimental intrusions that help to understand the dynamics of magma flow. In the sill initial flow was identified through AMS fabrics at intrusion margins and was aligned with the orientation of magma fingers, whereas after coalescence the flow direction changed to reflect a more

regional flow trajectory. An asymmetrical flow profile was observed across the sill thickness which was due to the sill intruding between host sedimentary rocks and a pre-existing hot but solid sill that was still above the temperature of formation of columnar jointing (~890 ˚C). Thermal modelling also identified that convection was likely to have played a key part during emplacement and solidification due to the sill thickness and estimated solidification time. Evidence of convection is believed to be present in AMS fabrics with low degrees of anisotropy and large confidence ellipses suggests a uniform distribution of magnetic fabric providing phases and may be an indicator of crystals tumbling during convection.

Variations in flow were also observed at multiple scales within the sill. The AMS fabrics recorded both the general flow directions (NNW-SSE rotating to SW-NE) as well as the presence of convection, which was identified to have occurred during solidification. In contrast, AARM fabrics suggested that pore-melt flow occurred during magma lock-up and subsequent solidification of the crystal pile (Figure 6.1Biii). The contrast in these fabrics has implications for using a combination of both techniques in the study of intrusive systems, as the techniques identify different parts of the emplacement and solidification history.

Commonly associated with magmatic activity are hydrothermal systems, which can flow through sheet intrusions after they have solidified. In these situations, the post-emplacement fluids can alter mineral fabrics, as such identifying flow from AMS can be problematic. However, macroscale fabrics located on dyke margins, i.e. ropey flow structures, can be used when present. This is the case in the margin regions of the dyke studied in this thesis, where a post-emplacement hydrothermal fluid altered the basalt and grew pyrrhotite (Figure 6.1Cii), however ropey surface structures observed on a nearby dyke were used to infer lateral magma flow (Figure 6.1Ci). AMS fabrics preserved in the unaltered dyke core also suggested lateral magma flow towards the north. Lateral flow was also observed in laboratory experiments as radial intrusions were observed that propagated away from a central point source. AMS fabrics suggested multiple flow regimes occurring, from compression and shear of the plaster in the margins producing oblate shaped fabrics, compared with prolate fabrics suggesting lateral flow along dyke strike in the intrusion core. AMS fabrics in the margins of laboratory experiments also showed imbricated fabrics which pointed towards the intrusion tip (Figure 6.1D), similar to what is observed in multiple studies of dykes in nature.

All three chapters of this thesis identified variations in magnetic fabrics with increased distance from intrusion margins. This identification has large implications for how magnetic

fabrics are used to study intrusive systems as variations in magnetic fabric can be identified over relatively short distances. These fabrics can suggest differences in flow regime (chapters 3 and 5) or alteration (chapter 4), and indicate that the processes occurring within intrusions are very complex and that current emplacement models may need revisiting.

6.3 Further questions

Several questions have arisen from this study which would further develop and improve our understanding of the processes occurring during the emplacement and solidification of sheet intrusions:

1. In chapter 3, I studied the variation in fabrics across sill breadth, however, this could be developed further by investigating variation of magnetic fabrics along sill length, as multiple sills have been identified to have lateral variations in macroscale structures, e.g. magma fingers (Schofield et al., 2010) or thickness variations (Holness and Humphreys, 2003). The Loch Scridain Sill Complex, Isle of Mull, would be a prime example for this, with some data collection already undertaken (field mapping and sample collection) at 3 locations across the complex. In this area there is large scale exposure across both the length and breadth of an individual sill which would enable a more complete evolution of magma flow to be identified.
2. Both the dyke and sill studied within this thesis were relatively thin in, as such it would be of interest to test the emplacement and solidification models on thicker intrusions, and at locations where there is greater exposure and access for sampling across the intrusion length and breadth, such as the Cedar Mountain region of Utah, USA. This would improve our understanding of development and evolution of large igneous plumbing systems.
3. The laboratory experiments used here were undertaken as part of a proof of concept study to investigate the usefulness of the method in understanding sheet intrusion emplacement dynamics. The methodology works well for this; however, fine tuning is required to ensure reproducibility of model results. This can be done in multiple ways:
    a. Expanding the data set both in the number of experiments run but also in the number analysed for their AMS fabrics would help to improve the validity of the models and enable similarities and differences to be better identified.
    b. Changing the viscosity of the plaster of Paris would mean that the method could be applied to the modelling of different viscosity magmas and could be used in the modelling of other structures, such as basaltic lava flows.

References

Abdelmalak, M.M., Mourgues, R., Galland, O., and Bureau, D., 2012, Fracture mode analysis and related surface deformation during dyke intrusion: Results from 2D experimental modelling: Earth and Planetary Science Letters, v. 359–360, p. 93–105, doi:10.1016/j.epsl.2012.10.008.

Acocella, V., Neri, M., and Sulpizio, R., 2009, Dike propagation within active central volcanic edifices: constraints from Somma-Vesuvius, Etna and analogue models: Bulletin of Volcanology, v. 71, p. 219–223, doi:10.1007/s00445-008-0258-2.

Acocella, V., and Tibaldi, A., 2005, Dike propagation driven by volcano collapse: A general model tested at Stromboli, Italy: Geophysical Research Letters, v. 32, p. 1–4, doi:10.1029/2004GL022248.

Airoldi, G.M., Muirhead, J.D., Long, S.M., Zanella, E., and White, J.D.L., 2016, Flow dynamics in mid-Jurassic dikes and sills of the Ferrar large igneous province and implications for long-distance magma transport: Tectonophysics, v. 683, p. 182–199, doi:10.1016/j.tecto.2016.06.029.

Airoldi, G., Muirhead, J.D., Zanella, E., and White, J.D.L., 2012, Emplacement process of Ferrar Dolerite sheets at Allan Hills (South Victoria Land, Antarctica) inferred from magnetic fabric: Geophysical Journal International, v. 188, p. 1046–1060, doi:10.1111/j.1365-246X.2011.05334.x.

Akimoto, S., 1962, Magnetic properties of FeO-Fe2O3-TiO2 system as a basis of rock magnetism: Journal of Physical Society of Japan, v. 17, p. 706–710.

Ampferer, O., 1906, Über das Bewegungsbild von Faltengebirgen: Jahrbuch der Geologischen Reichsanstalt, v. 56, p. 539–622.

Anderson, E.M., 1951, The dynamics of faulting and dyke formation with applications to Britain: Edinburgh, Oliver and Boyd, 206 p., https://books.google.co.uk/books?id=4M5OAQAAIAAJ.

Annen, C., 2011, Implications of incremental emplacement of magma bodies for magma differentiation, thermal aureole dimensions and plutonism–volcanism relationships: Tectonophysics, v. 500, p. 3–10, doi:10.1016/j.tecto.2009.04.010.

Annen, C., and Sparks, R.S.J., 2002, Effects of repetitive emplacement of basaltic intrusions on thermal evolution and melt generation in the crust: Earth and Planetary Science Letters, v. 203, p. 937–955, doi:10.1016/S0012-821X(02)00929-9.

Arbaret, L., Launeau, P., Diot, H., and Sizaret, S., 2013, Magnetic and shape fabrics of magnetite in simple shear flows: Journal of Volcanology and Geothermal Research, v. 249, p. 25–38, doi:10.1016/j.jvolgeores.2012.09.003.

Archanjo, C.J., and Launeau, P., 2004, Magma flow inferred from preferred orientations of

plagioclase of the Rio Ceara-Mirim dyke swarm (NE Brazil) and its AMS significance: Geological Society, London, Special Publications, v. 238, p. 285–298, doi:10.1144/GSL.SP.2004.238.01.17.

Aubourg, C., Tshoso, G., Le Gall, B., Bertrand, H., Tiercelin, J.-J., Kampunzu, A.B., Dyment, J., and Modisi, M., 2008, Magma flow revealed by magnetic fabric in the Okavango giant dyke swarm, Karoo igneous province, northern Botswana: Journal of Volcanology and Geothermal Research, v. 170, p. 247–261, doi:10.1016/j.jvolgeores.2007.10.013.

Audunsson, H., Levi, S., and Hodges, F., 1992, Magnetic property zonation in a thick lava flow: Journal of Geophysical Research, v. 97, p. 4349–4360, doi:10.1029/91JB01508.

Baer, G., 1991, Mechanisms of dike propagation in layered rocks and in massive, porous sedimentary rocks: Journal of Geophysical Research, v. 96, p. 11911, doi:10.1029/91JB00844.

Bagdassarov, N., and Pinkerton, H., 2004, Transient phenomena in vesicular lava flows based on laboratory experiments with analogue materials: Journal of Volcanology and Geothermal Research, v. 132, p. 115–136, doi:10.1016/S0377-0273(03)00341-X.

Bagnardi, M., Amelung, F., and Poland, M.P., 2013, A new model for the growth of basaltic shields based on deformation of Fernandina volcano, Galápagos Islands: Earth and Planetary Science Letters, v. 377–378, p. 358–366, doi:10.1016/j.epsl.2013.07.016.

Ball, J.L., Stauffer, P.H., Calder, E.S., and Valentine, G.A., 2015, The hydrothermal alteration of cooling lava domes: Bulletin of Volcanology, v. 77, p. 1–16, doi:10.1007/s00445-015-0986-z.

Balmforth, N.J., Burbudge, A.S., Craster, R. V., Salzig, J., and Shen, A., 2000, Viscoplastic models of isothermal lava domes: Journal of Fluid Mechanics, v. 403, p. 37–65, doi:10.1007/978-3-642-74379-5.

Banerjee, S.K., 1971, New Grain Size Limits for Palaeomagnetic Stability in Haematite: Nature Physical Science, v. 232, p. 15–16, doi:10.1038/physci232015a0.

Barnett, Z.A., and Gudmundsson, A., 2014, Numerical modelling of dykes deflected into sills to form a magma chamber: Journal of Volcanology and Geothermal Research, v. 281, p. 1–11, doi:10.1016/j.jvolgeores.2014.05.018.

Beckett, F.M., Mader, H.M., Phillips, J.C., Rust, A.C., and Witham, F., 2011, An experimental study of low-Reynolds-number exchange flow of two Newtonian fluids in a vertical pipe: Journal of Fluid Mechanics, v. 682, p. 652–670, doi:10.1017/jfm.2011.264.

Benn, K., and Allard, B., 1989, Preferred mineral orientations related to magmatic flow in ophiolite layered gabbros: Journal of Petrology, v. 30, p. 925–946.

Bertelsen, H.S., Rogers, B.D., Galland, O., Dumazer, G., and Benanni, A., 2018, Laboratory modeling of coeval brittle and ductile deformation during magma emplacement into viscoelastic rocks:

Frontiers in Earth Science, v. 6, doi:10.3389/feart.2018.00199.

BGS, 2008, 1:250000 British Geology, SHAPE geospatial data, scale 1:250000, Tile ng, BGS: EDINA Geology Digimap Service, http://digimap.edina.ac.uk (accessed March 2015).

Bhattacharji, S., and Smith, C.H., 1964, Flowage differentiation: Science, v. 145, p. 150–153, doi:10.1126/science.145.3628.150.

Blake, S., 1990, Viscoplastic models of lava domes, *in* Fink, J.H. ed., Lava flows and domes: emplacement mechanisms and hazard implications, p. 88–128.

Blake, S., and Bruno, B.C., 2000, Modelling the emplacement of compound lava flows: Earth and Planetary Science Letters, v. 184, p. 181–197, doi:10.1016/S0012-821X(00)00278-8.

Blundell, D., 1957, A palaeomagnetic investigation of the Lundy dyke swarm: Geological Magazine, v. 44, p. 187–193.

Bons, P.D., Baur, A., Elburg, M.A., Lindhuber, M.J., Marks, M.A.W., Soesoo, A., Van Milligen, B.P., and Walte, N.P., 2015, Layered intrusions and traffic jams: Geology, v. 43, p. 71–74, doi:10.1130/G36276.1.

Borradaile, G.J., and Henry, B., 1997, Tectonic applications of magnetic susceptibility and its anisotropy: Earth-Science Reviews, v. 42, p. 49–93, doi:10.1016/S0012-8252(96)00044-X.

de Bremond d'Ars, J., Arndt, N.T., and Hallot, E., 2001, Analog experimental insights into the formation of magmatic sulfide deposits: Earth and Planetary Science Letters, v. 186, p. 371–381, doi:10.1016/S0012-821X(01)00254-0.

British Geological Survey, 2007, Portree, Scotland Sheet 80E, Solid and Drift Geoloy, 1:50 000 Geology Series.:

Buckingham, E., 1914, On Physically Similar Systems; Illustrations of the Use of Dimensional Equations: Physical Review, v. 4, p. 345–376.

Bunger, A.P., and Cruden, A.R., 2011, Modeling the growth of laccoliths and large mafic sills: Role of magma body forces: Journal of Geophysical Research, v. 116, p. B02203, doi:10.1029/2010JB007648.

Burchardt, S., Mattsson, T., Palma, J.O., Galland, O., Almqvist, B., Mair, K., Jerram, D.A., Hammer, Ø., and Sun, Y., 2019, Progressive Growth of the Cerro Bayo Cryptodome, Chachahuén Volcano, Argentina—Implications for Viscous Magma Emplacement: Journal of Geophysical Research: Solid Earth, v. 124, p. 7934–7961, doi:10.1029/2019JB017543.

Burton-Johnson, A., Macpherson, C.G., Muraszko, J.R., Harrison, R.J., and Jordan, T.A., 2019, Tectonic strain recorded by magnetic fabrics (AMS) in plutons, including Mt Kinabalu, Borneo: A tool to

explore past tectonic regimes and syn-magmatic deformation: Journal of Structural Geology, v. 119, p. 50–60, doi:10.1016/j.jsg.2018.11.014.

Butler, R.F., 1992, Paleomagnetism: magnetic domains to geologic terranes: Boston, Blackwell Scientific Publications.

Caballero-Miranda, C.I., Alva-Valdivia, L.M., González-Rangel, J.A., Gogitchaishvili, A., Urrutia-Fucugauchi, J., and Kontny, A., 2016, Vertical AMS variation within basalt flow profiles from the Xitle volcano (Mexico) as indicator of heterogeneous strain in lava flows: Journal of Volcanology and Geothermal Research, v. 311, p. 9–28, doi:10.1016/j.jvolgeores.2016.01.003.

Callot, J., Geoffroy, L., Aubourg, C., Pozzi, J.P., and Mege, D., 2001, Magma flow directions of shallow dykes from the East Greenland volcanic margin inferred from magnetic fabric studies: Tectonophysics, v. 335, p. 313–329.

Cañón-Tapia, E., Walker, G.P.L., and Herrero-Bervera, E., 1996, The internal structure of lava flows - Insights from AMS measurements I: Near-vent a'a: Journal of Volcanology and Geothermal Research, v. 70, p. 21–36, doi:10.1016/0377-0273(95)00050-X.

Carey, S.N., Sigurdsson, H., and Sparks, R.S.J., 1988, Experimental studies of particle-laden plumes: Journal of Geophysical Research, v. 93, doi:10.1029/jb093ib12p15314.

Cashman, K. V, Kerr, R.C., and Griffiths, R.W., 2006, A laboratory model of surface crust formation and disruption on lava flows through non-uniform channels: Bulletin of Volcanology, v. 68, p. 753–770, doi:10.1007/s00445-005-0048-z.

Castro, J.M., Cordonnier, B., Schipper, C.I., Tuffen, H., Baumann, T.S., and Feisel, Y., 2016, Rapid laccolith intrusion driven by explosive volcanic eruption: Nature Communications, v. 7, p. 13585, doi:10.1038/ncomms13585.

Castruccio, A., Rust, A.C., and Sparks, R.S.J., 2014, Assessing lava flow evolution from post-eruption field data using Herschel-Bulkley rheology: Journal of Volcanology and Geothermal Research, v. 275, p. 71–84, doi:10.1016/j.jvolgeores.2014.02.004.

Castruccio, A., Rust, A.C., and Sparks, R.S.J., 2010, Rheology and flow of crystal-bearing lavas: Insights from analogue gravity currents: Earth and Planetary Science Letters, v. 297, p. 471–480, doi:10.1016/j.epsl.2010.06.051.

Chadima, M., Cajz, V., and Týcová, P., 2009, On the interpretation of normal and inverse magnetic fabric in dikes: Examples from the Eger Graben, NW Bohemian Massif: Tectonophysics, v. 466, p. 47–63, doi:10.1016/j.tecto.2008.09.005.

Chadima, M., and Hrouda, F., 2012, Cureval8:, http://www.agico.com/text/software/cureval/cureval.php.

Chadima, M., Hrouda, F., and Jelinek, V., 2018a, Anisoft5:, http://www.agico.com/text/software/anisoft/anisoft.php.

Chadima, M., and Jelinek, V., 2009, Anisoft42:, http://www.agico.com/text/software/anisoft/anisoft.php.

Chadima, M., Pokorny, J., Dusek, M., and Vyslouzil, J., 2018b, Rema6:, http://www.agico.com/text/software/rema6/rema6.php.

Chadima, M., Pokorny, J., and Studynka, J., 2018c, Safyr7:, http://www.agico.com/text/software/safyr/safyr.php.

Chadwick, W.W., Jónsson, S., Geist, D.J., Poland, M., Johnson, D.J., Batt, S., Harpp, K.S., and Ruiz, A., 2011, The May 2005 eruption of Fernandina volcano, Galápagos: The first circumferential dike intrusion observed by GPS and InSAR: Bulletin of Volcanology, v. 73, p. 679–697, doi:10.1007/s00445-010-0433-0.

Chanceaux, L., and Menand, T., 2014, Solidification effects on sill formation: An experimental approach: Earth and Planetary Science Letters, v. 403, p. 79–88, doi:10.1016/j.epsl.2014.06.018.

Chanceaux, L., and Menand, T., 2016, The effects of solidification on sill propagation dynamics and morphology: Earth and Planetary Science Letters, v. 442, p. 39–50, doi:10.1016/j.epsl.2016.02.044.

Cheadle, M.J., and Gee, J.S., 2017, Quantitative textural insights into the formation of gabbro in mafic Intrusions: Elements, v. 13, p. 409–414, doi:10.2138/gselements.13.6.409.

Cimarelli, C., Costa, A., Mueller, S., and Mader, H.M., 2011, Rheology of magmas with bimodal crystal size and shape distributions: Insights from analog experiments: Geochemistry, Geophysics, Geosystems, v. 12, p. 1–14, doi:10.1029/2011GC003606.

Clemente, C.S., Amorós, E.B., and Crespo, M.G., 2007, Dike intrusion under shear stress: Effects on magnetic and vesicle fabrics in dikes from rift zones of Tenerife (Canary Islands): Journal of Structural Geology, v. 29, p. 1931–1942, doi:10.1016/j.jsg.2007.08.005.

Correa-Gomes, L.C., Souza Filho, C.R., Martins, C.J.F.N., and Oliveira, E.P., 2001, Development of symmetrical and asymmetrical fabrics in sheet-like igneous bodies: The role of magma flow and wall-rock displacements in theoretical and natural cases: Journal of Structural Geology, v. 23, p. 1415–1428, doi:10.1016/S0191-8141(01)00007-4.

Le Corvec, N., Menand, T., and Lindsay, J., 2013, Interaction of ascending magma with pre-existing crustal fractures in monogenetic basaltic volcanism: an experimental approach: Journal of Geophysical Research: Solid Earth, v. 118, p. 968–984, doi:10.1002/jgrb.50142.

Coward, M.P., 1980, The analysis of flow profiles in a basaltic dyke using strained vesicles: Journal of the Geological Society, v. 137, p. 605–615, doi:10.1144/gsjgs.137.5.0605.

Crisp, J.A., 1984, Rates of magma emplacement and volcanic output: Journal of Volcanology and Geothermal Research, v. 20, p. 177–211, doi:10.1016/0377-0273(84)90039-8.

Çubukçu, H.E., 2015, Vertical variation in the deuteric oxidation of titanomagnetites in an ignimbrite deposit: Kizilkaya Ignimbrite (Cappadocia, Turkey): Journal of Volcanology and Geothermal Research, v. 308, p. 10–18, doi:10.1016/j.jvolgeores.2015.10.006.

Daniels, K.A., and Menand, T., 2015, An experimental investigation of dyke injection under regional extensional stress: Journal of Geophysical Research: Solid Earth, v. 120, p. 2014–2035, doi:10.1002/2014JB011627.

Dekkers, M.J., 1988, Magnetic properties of natural pyrrhotite Part I: Behaviour of initial susceptibility and saturation-magnetization-related rock-magnetic parameters in a grain-size dependent framework: Physics of the Earth and Planetary Interiors, v. 52, p. 376–393, doi:10.1016/0031-9201(88)90129-X.

Delaney, P.T., and Pollard, D.D., 1982, Solidification of basaltic magma during flow in a dike: American Journal of Science, v. 282, p. 856–885.

Delcamp, A., Petronis, M.S., and Troll, V.R., 2014, Discerning magmatic flow patterns in shallow-level basaltic dykes from the NE rift zone of Tenerife, Spain, using the Anisotropy of Magnetic Susceptibility (AMS) technique: Geological Society, London, Special Publications, v. 396, p. 87–106, doi:10.1144/SP396.2.

Dietl, C., and Koyi, H., 2011, Sheets within diapirs - Results of a centrifuge experiment: Journal of Structural Geology, v. 33, p. 32–37, doi:10.1016/j.jsg.2010.10.010.

Donnadieu, F., and Merle, O., 1998, Experiments on the identation process during cryptodome intrusions: New insights into Mount St. Helens deformation: Geology, v. 26, p. 79–82, doi:10.1130/0091-7613(1998)026<0079:EOTIPD>2.3.CO.

Dontula, P., Macosko, C.W., and Scriven, L.E., 2005, Origins of concentric cylinders viscometry *: v. 55455, p. 807–818, doi:10.1122/1.1940640.

Dragoni, M., Lanza, R., and Tallarico, A., 1997, Magnetic anisotropy produced by magma flow: Theoretical model and experimental data from Ferrar dolerite sills (Antarctica): Geophysical Journal International, v. 128, p. 230–240, doi:10.1111/j.1365-246X.1997.tb04083.x.

Dunlop, D.J., and Özdemir, Ö., 1997, Rock Magnetism: Fundamentals and Frontiers: 1–573 p.

Emeleus, C.H., and Bell, B.R., 2005, The Palaeogene volcanic districts of Scotland: British Geological Survey, Nottingham, 212 p.

Ernst, R., and Baragar, W., 1992, Evidence from magnetic fabric for the flow pattern of magma in the Mackenzie giant radiating dyke swarm: Nature, v. 356, p. 511–513, http://www.nature.com/nature/journal/v356/n6369/abs/356511a0.html (accessed December 2014).

Ernst, G.G.J., Davis, J.P., and Sparks, R.S.J., 1994, Bifurcation of volcanic plumes in a crosswind: Bulletin of Volcanology, v. 56, p. 159–169, doi:10.1007/BF00279601.

Ernst, R., Grosfils, E., and Mège, D., 2001, Giant Dike Swarms: Earth, Venus, and Mars: Annual Review of Earth and Planetary Sciences, v. 29, p. 489–534, doi:10.1146/annurev.earth.29.1.489.

Fee, D., Garces, M., Orr, T., and Poland, M., 2011, Infrasound from the 2007 fissure eruptions of Klauea Volcano, Hawai'i: Geophysical Research Letters, v. 38, p. 1–5, doi:10.1029/2010GL046422.

Féménias, O., Diot, H., Berza, T., Gauffriau, A., and Demaiffe, D., 2004, Asymmetrical to symmetrical magnetic fabric of dikes: Paleo-flow orientations and Paleo-stresses recorded on feeder-bodies from the Motru Dike Swarm (Romania): Journal of Structural Geology, v. 26, p. 1401–1418, doi:10.1016/j.jsg.2003.12.003.

Ferré, E.C., 2002, Theoretical models of intermediate and inverse AMS fabrics: Geophysical Research Letters, v. 29, p. 31–34, doi:10.1029/2001gl014367.

Fink, J.H., and Bridges, N.T., 1995, Effects of eruption history and cooling rate on lava dome growth: Bulletin of Volcanology, v. 57, p. 229–239, doi:10.1007/BF00265423.

Fink, J.H., and Fletcher, R.C., 1978, Ropy pahoehoe: Surface folding of a viscous fluid: Journal of Volcanology and Geothermal Research, v. 4, p. 151–170, doi:10.1016/0377-0273(78)90034-3.

Fink, J.H., and Griffiths, R.W., 1998, Morphology, eruption rates, and rheology of lava domes: Insights from laboratory models: Journal of Geophysical Research: Solid Earth, v. 103, p. 527–545, doi:10.1029/97JB02838.

Fink, J.H., and Griffiths, R.W., 1990, Radial Spreading of Viscous Gravity Currents With Solidifying Crust: Journal of Fluid Mechanics, v. 221, p. 485–509, doi:10.1017/S0022112090003640.

Fiske, R.S., and Jackson, E.D., 1972, Orientation and Growth of Hawaiian Volcanic Rifts: The Effect of Regional Structure and Gravitational Stresses: Proceedings of the Royal Society A: Mathematical, Physical and Engineering Sciences, v. 329, p. 299–326, doi:10.1098/rspa.1972.0115.

Fowler, C.M.R., 2004, The Solid Earth: An Introduction to Global Geophysics: Cambridge University Press.

Fujita, E., Ukawa, M., and Yamamoto, E., 2004, Subsurface cyclic magma sill expansions in the 2000

Miyakejima volcano eruption: Possibility of two-phase flow oscillation: Journal of Geophysical Research: Solid Earth, v. 109, p. 1–22, doi:10.1029/2003JB002556.

Furlong, K.P., and Chapman, D.S., 2013, Heat Flow, Heat Generation, and the Thermal State of the Lithosphere: Annual Review of Earth and Planetary Sciences, v. 41, p. 385–410, doi:10.1146/annurev.earth.031208.100051.

Gaete, A., Kavanagh, J.L., Rivalta, E., Hilmi Hazim, S., Walter, T.R., and Dennis, D.J.C., 2019, The impact of unloading stresses on post-caldera magma intrusions: Earth and Planetary Science Letters, v. 508, p. 109–121, doi:10.1016/j.epsl.2018.12.016.

Galland, O., 2012, Experimental modelling of ground deformation associated with shallow magma intrusions: Earth and Planetary Science Letters, v. 317–318, p. 145–156, doi:10.1016/j.epsl.2011.10.017.

Galland, O. et al., 2018, Storage and Transport of Magma in the Layered Crust—Formation of Sills and Related Flat-Lying Intrusions (S. Burchardt, Ed.): Elsevier Inc., 113–138 p., doi:10.1016/b978-0-12-809749-6.00005-4.

Galland, O., Bertelsen, H.S., Guldstrand, F., Girod, L., Johannessen, R.F., Bjugger, F., Burchardt, S., and Mair, K., 2016, Application of open-source photogrammetric software MicMac for monitoring surface deformation in laboratory models: Journal of Geophysical Research B: Solid Earth, v. 121, p. 2852–2872, doi:10.1002/2015JB012564.

Galland, O., Burchardt, S., Hallot, E., Mourgues, R., and Bulois, C., 2014, Dynamics of dikes versus cone sheets in volcanic systems: Journal of Geophysical Research: Solid Earth, v. 119, p. 6178–6192, doi:10.1002/2014JB011059.

Galland, O., Cobbold, P.R., Hallot, E., de Bremond d'Ars, J., and Delavaud, G., 2006, Use of vegetable oil and silica powder for scale modelling of magmatic intrusion in a deforming brittle crust: Earth and Planetary Science Letters, v. 243, p. 786–804, doi:10.1016/j.epsl.2006.01.014.

Galland, O., Holohan, E.P., Van Wyk de Vries, B., and Burchardt, S., 2015, Laboratory Modelling of Volcano Plumbing Systems: A Review, *in* Breitkreuz, C. and Rocchi, S. eds., Physical Geology of Shallow Magmatic Systems, Springer, Cham, p. 147–214, doi:10.1007/11157.

Galland, O., Planke, S., Neumann, E.-R., and Malthe-Sørenssen, A., 2009, Experimental modelling of shallow magma emplacement: Application to saucer-shaped intrusions: Earth and Planetary Science Letters, v. 277, p. 373–383, doi:10.1016/j.epsl.2008.11.003.

Galland, O., and Scheibert, J., 2013, Analytical model of surface uplift above axisymmetric flat-lying magma intrusions: Implications for sill emplacement and geodesy: Journal of Volcanology and Geothermal Research, v. 253, p. 114–130, doi:10.1016/j.jvolgeores.2012.12.006.

Garel, F., Kaminski, E., Tait, S., and Limare, A., 2014, An analogue study of the influence of solidification on the advance and surface thermal signature of lava flows: Earth and Planetary Science Letters, v. 396, p. 46–55, doi:10.1016/j.epsl.2014.03.061.

Garel, F., Kaminski, E., Tait, S., and Limare, A., 2012, An experimental study of the surface thermal signature of hot subaerial isoviscous gravity currents: Implications for thermal monitoring of lava flows and domes: Journal of Geophysical Research: Solid Earth, v. 117, p. 1–18, doi:10.1029/2011JB008698.

Del Gaudio, P., 2014, Rheology of bimodal crystals suspensions: Results from analogue experiments and implications for magma ascent: Geochemistry, Geophysics, Geosystems, v. 15, p. 284–291, doi:10.1002/2013GC005078.

Del Gaudio, P., Ventura, G., and Taddeucci, J., 2013, The effect of particle size on the rheology of liquid-solid mixtures with application to lava flows: Results from analogue experiments: Geochemistry, Geophysics, Geosystems, v. 14, p. 2661–2669, doi:10.1002/ggge.20172.

Geoffroy, L., Callot, J.P., Aubourg, C., and Moreira, M., 2002, Magnetic and plagioclase linear fabric discrepancy in dykes: a new way to define the flow vector using magnetic foliation: Terra Nova, v. 14, p. 183–190, doi:10.1046/j.1365-3121.2002.00412.x.

Geshi, N., Kusumoto, S., and Gudmundsson, A., 2012, Effects of mechanical layering of host rocks on dike growth and arrest: Journal of Volcanology and Geothermal Research, v. 223–224, p. 74–82, doi:10.1016/j.jvolgeores.2012.02.004.

Geshi, N., Kusumoto, S., and Gudmundsson, A., 2010, Geometric difference between non-feeder and feeder dikes: Geology, v. 38, p. 195–198, doi:10.1130/G30350.1.

Gibb, F.G.F., and Gibson, S.A., 1989, The Little Minch Sill Complex: Scottish Journal of Geology, v. 25, p. 367–370, doi:10.1144/sjg25030367.

Gibb, F.G.F., and Henderson, C.M.B., 2006, Chemistry of the Shiant Isles Main Sill, NW Scotland, and wider implications for the petrogenesis of Mafic Sills: Journal of Petrology, v. 47, p. 191–230, doi:10.1093/petrology/egi072.

Gibb, F., and Henderson, C., 1996, The Shiant Isles Main Sill: structure and mineral fractionation trends: Mineralogical Magazine, v. 60, p. 67–97.

Gibb, F.G.F., and Henderson, C.M.B., 1984, The structure of the Shiant Isles sill complex, Outer Hebrides: Scottish Journal of Geology, v. 20, p. 21–29, doi:10.1144/sjg20010021.

Gibson, S.A., 1990, The geochemistry of the Trotternish sills, Isle of Skye - crustal contamination in the British Tertiary Volcanic Province: Journal of the Geological Society, v. 147, p. 1071–1081, doi:10.1144/gsjgs.147.6.1071.

Gibson, S.A., and Jones, A., 1991, Igneous stratigraphy and internal structure of the Little Minch Sill Complex, Trotternish Peninsula, northern Skye, Scotland: Geological Magazine, v. 128, p. 51–66.

Gil, A., Lago, M., Galé, C., Pocoví, A., and Arranz, E., 2002, Magnetic fabric in folded sills and lava flows. A case study in the Permian basalts of the Anayet Massif (Pyrenean Axial Zone, Spain): Tectonophysics, v. 350, p. 1–15, doi:10.1016/S0040-1951(02)00078-1.

Gilbert, E., and Merle, O., 1987, Extrusion and radial spreading beyond a closing channel: Journal of Structural Geology, v. 9, p. 481–490.

Di Giuseppe, E., Corbi, F., Funiciello, F., Massmeyer, A., Santimano, T.N., Rosenau, M., and Davaille, A., 2015, Characterization of Carbopol hydrogel rheology for experimental tectonics and geodynamics: Tectonophysics, v. 642, p. 29–45, doi:10.1016/j.tecto.2014.12.005.

Di Giuseppe, E., Funiciello, F., Corbi, F., Ranalli, G., and Mojoli, G., 2009, Gelatins as rock analogs: A systematic study of their rheological and physical properties: Tectonophysics, v. 473, p. 391–403, doi:10.1016/j.tecto.2009.03.012.

Goehring, L., and Morris, S.W., 2005, Order and disorder in columnar joints: Europhysics Letters, v. 69, p. 739–745, doi:10.1209/epl/i2004-10408-x.

Goehring, L., Morris, S.W., and Lin, Z., 2006, Experimental investigation of the scaling of columnar joints: Physical Review E, v. 74, p. 036115.

Gregg, T.K.P., and Fink, J.H., 1995, Quantification of submarine lava-flow morphology through analog experiments: Geology, v. 23, p. 73–76, doi:10.1130/0091-7613(1995)023<0073:QOSLFM>2.3.CO.

Gressier, J.B., Mourgues, R., Bodet, L., Matthieu, J.Y., Galland, O., and Cobbold, P., 2010, Control of pore fluid pressure on depth of emplacement of magmatic sills: An experimental approach: Tectonophysics, v. 489, p. 1–13, doi:10.1016/j.tecto.2010.03.004.

Griffiths, R.W., and Fink, J.H., 1993, Effects of surface cooling on the spreading of lava flows and domes: Journal of Fluid Mechanics, v. 252, p. 667–702, doi:10.1017/S0022112093003933.

Griffiths, R.W., and Fink, J.H., 1997, Solidifying Bingham extrusions: a model for the growth of silicic lava domes: Journal of Fluid Mechanics, v. 347, p. 13–36, doi:10.1017/S0022112097006344.

Gudmundsson, A., 2011, Deflection of dykes into sills at discontinuities and magma-chamber formation: Tectonophysics, v. 500, p. 50–64, doi:10.1016/j.tecto.2009.10.015.

Gudmundsson, A., 2002, Emplacement and arrest of sheets and dykes in central volcanoes: Journal of Volcanology and Geothermal Research, v. 116, p. 279–298, doi:10.1016/S0377-0273(02)00226-3.

Gudmundsson, A., Lecoeur, N., Mohajeri, N., and Thordarson, T., 2014, Dike emplacement at Bardarbunga, Iceland, induces unusual stress changes, caldera deformation, and earthquakes: Bulletin of Volcanology, v. 76, p. 869, doi:10.1007/s00445-014-0869-8.

Gudmundsson, A., Marinoni, L.B., and Marti, J., 1999, Injection and arrest of dykes: Implications for volcanic hazards: Journal of Volcanology and Geothermal Research, v. 88, p. 1–13, doi:10.1016/S0377-0273(98)00107-3.

Guldstrand, F., Burchardt, S., Hallot, E., and Galland, O., 2017, Dynamics of Surface Deformation Induced by Dikes and Cone Sheets in a Cohesive Coulomb Brittle Crust: Journal of Geophysical Research: Solid Earth, v. 122, p. 8511–8524, doi:10.1002/2017JB014346.

Hallworth, M.., Huppert, H., and Sparks, S., 1987, A laboratory simulation of basaltic lava flows.: Modern Geology, v. 11, p. 93–107.

Hargraves, R.B., Johnson, D., and Chan, C.Y., 1991, Distribution anisotropy: The cause of AMS in igneous rocks? Geophysical Research Letters, v. 18, p. 2193–2196, doi:10.1029/91GL01777.

Harris, J.P., and Hudson, J.D., 1980, Lithostratigraphy of the Great Estuarine Group (Middle Jurassic), Inner Hebrides: Scottish Journal of Geology, v. 16, p. 231–250, doi:10.1144/sjg16020231.

Hartlieb, P., Toifl, M., Kuchar, F., Meisels, R., and Antretter, T., 2016, Thermo-physical properties of selected hard rocks and their relation to microwave-assisted comminution: Minerals Engineering, v. 91, p. 34–41, doi:10.1016/j.mineng.2015.11.008.

Hastie, W.W., Watkeys, M.K., and Aubourg, C., 2014, Magma flow in dyke swarms of the Karoo LIP: Implications for the mantle plume hypothesis: Gondwana Research, v. 25, p. 736–755, doi:10.1016/j.gr.2013.08.010.

Hastie, W.W., Watkeys, M.K., and Aubourg, C., 2011, Significance of magnetic and petrofabric in Karoo-feeder dykes, northern Lebombo: Tectonophysics, v. 513, p. 96–111, doi:10.1016/j.tecto.2011.10.008.

Hawai'i, C. of, 2020, Kilauea Eruption Recovery: Housing Resources:, https://recovery.hawaiicounty.gov/resources/housing-resources (accessed July 2020).

Herrero-Bervera, E., Walker, G.P.L., Cañon-Tapia, E., and Garcia, M.O., 2001, Magnetic fabric and inferred flow direction of dikes, conesheets and sill swarms, Isle of Skye, Scotland: Journal of Volcanology and Geothermal Research, v. 106, p. 195–210.

Herschel, W.H., and Bulkley, R., 1926, Konsistenzmessungen von Gummi-Benzollösungen: Kolloid-Zeitschrift, v. 39, p. 291–300.

Higgins, M.D., 2006, Quantitative textural measurements in igneaous and metamorphic petrology: Cambridge, Cambridge University Press.

Hjartardóttir, Á.R., Einarsson, P., Gudmundsson, M.T., and Högnadóttir, T., 2015, Fracture movements and graben subsidence during the 2014 Bárðarbunga dike intrusion in Iceland: Journal of Volcanology and Geothermal Research, v. 310, p. 242–252, doi:10.1016/j.jvolgeores.2015.12.002.

Holness, M., 2014, The effect of crystallization time on plagioclase grain shape: Contributions to Mineralogy and Petrology, v. 16, p. 1–19, doi:10.1007/s00410-014-1076-5.

Holness, M.B., Farr, R., and Neufeld, J.A., 2017a, Crystal settling and convection in the Shiant Isles Main Sill: Contributions to Mineralogy and Petrology, v. 172, p. 7, doi:10.1007/s00410-016-1325-x.

Holness, M.B., and Humphreys, M.C.S., 2003, The Traigh Bhan na Sgurra Sill, Isle of Mull: Flow Localization in a Major Magma Conduit: Journal of Petrology, v. 44, p. 1961–1976, doi:10.1093/petrology/egg066.

Holness, M.B., Richardson, C., and Helz, R.T., 2012, Disequilibrium dihedral angles in dolerite sills: A new proxy for cooling rate: Geology, v. 40, p. 795–798, doi:10.1130/G33119.1.

Holness, M.B., Vukmanovic, Z., and Mariani, E., 2017b, Assessing the Role of Compaction in the Formation of Adcumulates: a Microstructural Perspective: Journal of Petrology, v. 58, p. 643–674, doi:10.1093/petrology/egx037.

Hon, K., Kauahikaua, J., Denlinger, R., and Mackay, K., 1994, Emplacement and inflation of pahoehoe sheet flows: observations and measurements of active lava flows on Kilauea volcano, Hawaii: Geological Society of America Bulletin, v. 106, p. 351–370, doi:10.1130/0016-7606(1994)106<0351:EAIOPS>2.3.CO;2.

Hoyer, L., and Watkeys, M.K., 2017, Using magma flow indicators to infer flow dynamics in sills: Journal of Structural Geology, v. 96, p. 161–175, doi:10.1016/j.jsg.2017.02.005.

Hrouda, F., Buriánek, D., Krejčí, O., and Chadima, M., 2015, Magnetic fabric and petrology of Miocene sub-volcanic sills and dykes emplaced into the SW Flysch Belt of the West Carpathians (S Moravia, Czech Republic) and their volcanological and tectonic implications: Journal of Volcanology and Geothermal Research, v. 290, p. 23–38, doi:10.1016/j.jvolgeores.2014.12.001.

Hubbert, M.K., and Willis, D.G., 1957, Mechanics of hydraulic fracturing: Petroleum Transactions, AIME, v. 210, p. 153–166, doi:10.1016/c2013-0-12927-3.

Hudson, J.D., and Trewin, N.H., 2002, Jurassic, *in* Trewin, N.H. ed., The Geology of Scotland, London, The Geological Society, p. 323–350.

Hughes, H.S.R., Boyce, A.J., McDonald, I., Davidheiser-Kroll, B., Holwell, D.A., McDonald, A., and Oldroyd, A., 2015, Contrasting mechanisms for crustal sulphur contamination of mafic magma:

evidence from dyke and sill complexes from the British Palaeogene Igneous Province: Journal of the Geological Society, v. 172, p. 443–458, doi:10.1144/jgs2014-112.

Hulme, G., 1974, The interpretaion of lava flow morphology: Geophys. J. R. Astr. Soc., v. 39, p. 361–383.

Huppert, H.E., and Hallworth, M.A., 2007, Bi-directional flows in constrained systems: Journal of Fluid Mechanics, v. 578, p. 95–112, doi:10.1017/S0022112007004661.

Huppert, H.E., and Sparks, R.S.J., 1989, Chilled margins in igneous rocks: Earth and Planetary Science Letters, v. 92, p. 397–405, doi:10.1016/0012-821X(89)90063-0.

Huppert, H.E., and Sparks, R.S.J., 1985, Komatiites I: Eruption and flow: Journal of Petrology, v. 26, p. 694–725, doi:10.1093/petrology/26.3.694.

Huppert, H.E., Sparks, R.S.J., and Turner, J.S., 1983, Laboratory investigations of viscous effects in replenished magma chambers: Earth and Planetary Science Letters, v. 65, p. 377–381, doi:10.1016/0012-821X(83)90175-9.

Huppert, H.E., Sparks, R.S.J., Whitehead, J.A., and Hallworth, M.A., 1986, Replenishment of magma chambers by light inputs: Journal of Geophysical Research, v. v. 91, p. 6113–6122, doi:10.1029/JB091iB06p06113.

Huppert, H.E., and Turner, J.S., 1981, A laboratory model of a replenished magma chamber: Earth and Planetary Science Letters, v. 54, p. 144–152, doi:10.1016/0012-821X(81)90075-3.

Hyndman, D.W., and Alt, D., 1987, Radial Dikes, Laccoliths, and Gelatin Models: The Jounal of Geology, v. 95, p. 763–774.

Ishibashi, H., 2009, Non-Newtonian behavior of plagioclase-bearing basaltic magma: Subliquidus viscosity measurement of the 1707 basalt of Fuji volcano, Japan: Journal of Volcanology and Geothermal Research, v. 181, p. 78–88, doi:10.1016/j.jvolgeores.2009.01.004.

Iverson, R.M., Logan, M., LaHusen, R.G., and Berti, M., 2010, The perfect debris flow? Aggregated results from 28 large-scale experiments: Journal of Geophysical Research, v. 115, doi:10.1029/2009jf001514.

Jackson, M., 1991, Anisotropy of magnetic remanence: A brief review of mineralogical sources, physical origins, and geological applications, and comparison with susceptibility anisotropy: Pure and Applied Geophysics, v. 136, p. 1–28, doi:10.1007/BF00878885.

Jelínek, V., 1981, Characterization of the magnetic fabric of rocks: Tectonophysics, v. 79, p. T63–T67, doi:10.1016/0040-1951(81)90110-4.

Jelínek, V., 1977, The statistical theory of measuring anisotropy of magnetic susceptibility of rocks

and its application.: Brno, Czech Republic, Geofysika, 4 p.

Johnson, A.M., and Pollard, D.D., 1973, Mechanics of growth of some laccolithic intrusions in the Henry mountains, Utah, I. Field observations, Gilbert's model, physical properties and flow of the magma: Tectonophysics, v. 18, p. 261–309, doi:10.1016/0040-1951(73)90050-4.

Just, J., and Kontny, A., 2012, Thermally induced alterations of minerals during measurements of the temperature dependence of magnetic susceptibility: A case study from the hydrothermally altered Soultz-sous-Forêts granite, France: International Journal of Earth Sciences, v. 101, p. 819–839, doi:10.1007/s00531-011-0668-9.

Just, J., Kontny, A., De Wall, H., Hirt, A.M., and Martín-Hernández, F., 2004, Development of magnetic fabrics during hydrothermal alteration in the Soultz-sous-Forêts granite from the EPS-1 borehole, Upper Rhine Graben: Geological Society Special Publication, v. 238, p. 509–526, doi:10.1144/GSL.SP.2004.238.01.26.

Karlstrom, L., and Manga, M., 2006, Origins and implications of zigzag rift patterns on lava lakes: Journal of Volcanology and Geothermal Research, v. 154, p. 317–324, doi:10.1016/j.jvolgeores.2006.01.004.

Kavanagh, J.L., 2018, Mechanisms of Magma Transport in the Upper Crust—Dyking, *in* Burchardt, S. ed., Volcanic and Igneous Plumbing Systems, Elsevier, p. 55–88, doi:10.1016/b978-0-12-809749-6.00003-0.

Kavanagh, J.L., Boutelier, D., and Cruden, A.R., 2015, The mechanics of sill inception, propagation and growth: Experimental evidence for rapid reduction in magmatic overpressure: Earth and Planetary Science Letters, v. 421, p. 117–128, doi:10.1016/j.epsl.2015.03.038.

Kavanagh, J.L., Burns, A.J., Hazim, S.H., Wood, E., Martin, S.A., Hignett, S., and Dennis, D.J.C., 2018a, Challenging dyke ascent models using novel laboratory experiments: Implications for reinterpreting evidence of magma ascent and volcanism: Journal of Volcanology and Geothermal Research, v. 354, p. 87–101, doi:10.1016/J.JVOLGEORES.2018.01.002.

Kavanagh, J.L., Engwell, S., and Martin, S.A., 2018b, A review of laboratory and numerical modelling in volcanology: Solid Earth, v. 9, p. 531–571, doi:10.5194/se-9-531-2018.

Kavanagh, J.L., Menand, T., and Daniels, K.A., 2013, Gelatine as a crustal analogue: Determining elastic properties for modelling magmatic intrusions: Tectonophysics, v. 582, p. 101–111.

Kavanagh, J.L., Menand, T., and Sparks, R.S.J., 2006, An experimental investigation of sill formation and propagation in layered elastic media: Earth and Planetary Science Letters, v. 245, p. 799–813, doi:10.1016/j.epsl.2006.03.025.

Kavanagh, J.L., and Pavier, M.J., 2014, Rock interface strength influences fluid-filled fracture

propagation pathways in the crust: Journal of Structural Geology, v. 63, p. 68–75, doi:10.1016/j.jsg.2014.03.001.

Kavanagh, J.L., Rogers, B.D., Boutelier, D., and Cruden, A.R., 2017, Controls on sill and dyke-sill hybrid geometry and propagation in the crust: The role of fracture toughness: Tectonophysics, v. 698, p. 109–120, doi:10.1016/j.tecto.2016.12.027.

Kavanagh, J.L., and Sparks, R.S.J., 2011, Insights of dyke emplacement mechanics from detailed 3D dyke thickness datasets: Journal of the Geological Society, v. 168, p. 965–978, doi:10.1144/0016-76492010-137.

Kendrick, J.E., Lavallée, Y., Mariani, E., Dingwell, D.B., Wheeler, J., and Varley, N.R., 2017, Crystal plasticity as an indicator of the viscous-brittle transition in magmas: Nature Communications, v. 8, p. 1–12, doi:10.1038/s41467-017-01931-4.

Kerr, R.C., 2001, Thermal erosion by laminar lava flows: Journal of Geophysical Research B: Solid Earth, v. 106, p. 453–465, doi:10.1029/2001JB000227.

Kervyn, M., Ernst, G.G.J., Van Wyk De Vries, B., Mathieu, L., and Jacobs, P., 2009, Volcano load control on dyke propagation and vent distribution: Insights from analogue modeling: Journal of Geophysical Research, v. 114, p. 26, doi:10.1029/2008JB005653.

Khan, A., 1962, The anisotropy of magnetic susceptibility of some igneous and metamorphic rocks: Journal of Geophysical Research, v. 67, p. 2873–2885.

Knight, M., and Walker, G., 1988, Magma flow directions in dikes of the Koolau Complex, Oahu, determined from magnetic fabric studies: Journal of Geophysical Research, v. 93, p. 4301–4319.

Kokelaar, B.P., 1982, Fluidization of wet sediments during the emplacement and cooling of various igneous bodies: Journal of the Geological Society, v. 139, p. 21–33, doi:10.1144/gsjgs.139.1.0021.

Koyaguchi, T., Ochiai, K., and Suzuki, Y.J., 2009, The effect of intensity of turbulence in umbrella cloud on tephra dispersion during explosive volcanic eruptions: Experimental and numerical approaches: Journal of Volcanology and Geothermal Research, v. 186, p. 68–78, doi:10.1016/j.jvolgeores.2009.01.014.

Koyaguchi, T., and Takada, A., 1994, An experimental study on the formation of composite intrusions from zoned magma chambers: Journal of Volcanology and Geothermal Research, doi:10.1016/0377-0273(94)90081-7.

Kratinová, Z., Machek, M., and Kusbach, V., 2010, Fabric Transpositions in Granite Plutons – An Insight from Non-scaled Analogue Modelling: Journal Of The Geological Society Of India, v. 75,

p. 267–277.

Kratinová, Z., Závada, P., Hrouda, F., and Schulmann, K., 2006, Non-scaled analogue modelling of AMS development during viscous flow: A simulation on diapir-like structures: Tectonophysics, v. 418, p. 51–61, doi:10.1016/j.tecto.2005.12.013.

Lamur, A., Lavallée, Y., Iddon, F.E., Hornby, A.J., Kendrick, J.E., Von Aulock, F.W., and Wadsworth, F.B., 2018, Disclosing the temperature of columnar jointing in lavas: Nature Communications, v. 9, doi:10.1038/s41467-018-03842-4.

Lane, S.J., Chouet, B.A., Phillips, J.C., Dawson, P., Ryan, G.A., and Hurst, E., 2001, Experimental observations of pressure oscillations and flow regimes in an analogue volcanic system: Journal of Geophysical Research, v. 106, p. 6461–6476, doi:10.1029/2000jb900376.

Lejeune, A.M., Bottinga, Y., Trull, T.W., and Richet, P., 1999, Rheology of bubble-bearing magmas: Earth and Planetary Science Letters, v. 166, p. 71–84.

Lejeune, A.M., and Richet, P., 1995, Rheology of crystal-bearing silicate melts: An experimental study at high viscosities: Journal of Geophysical Research, v. 100, p. 4215, doi:10.1029/94JB02985.

Leonhardt, R., 2006, Analyzing rock magnetic measurements: The RockMagAnalyzer 1.0 software: Computers and Geosciences, v. 32, p. 1420–1431, doi:10.1016/j.cageo.2006.01.006.

Lesher, C.E., and Spera, F.J., 2015, Thermodynamic and Transport Properties of Silicate Melts and Magma: Elsevier Inc., 113–141 p., doi:10.1016/B978-0-12-385938-9.00005-5.

Liss, D., Hutton, D.H.W., and Owens, W.H., 2002, Ropy flow structures: A neglected indicator of magma-flow direction in sills and dikes: Geology, v. 30, p. 715–718, doi:10.1130/0091-7613(2002)030<0715:RFSANI>2.0.CO;2.

Lister, J.R., 1990, Buoyancy-driven fluid fracture: The effects of material toughness and of low-viscosity precursors: Journal of Fluid Mechanics, v. 210, p. 263–280, doi:10.1017/S0022112090001288.

Lister, J.R., 1991, Steady solutions for feeder dykes in a density-stratified lithosphere: Earth and Planetary Science Letters, v. 107, p. 233–242, doi:10.1016/0012-821X(91)90073-Q.

Lister, J., and Kerr, R., 1991, Fluid-Mechanical Models of Crack Propagation and Their Application to Magma Transport in Dykes: Journal of Geophysical Research: Solid …, v. 96, p. 49–77.

Llewellin, E.W., Mader, H.M., and Wilson, S.D.R., 2002a, The constitutive equation and flow dynamics of bubbly magmas: Geophysical research letters., v. 29, p. 2170, doi:10.1029/2002GL015697.

Llewellin, E.W., Mader, H.M., and Wilson, S.D.R., 2002b, The rheology of a bubbly liquid: Proceedings

of the Royal Society of London, v. 458, p. 987–1016, doi:10.1098/rspa.2001.0924.

Lowrie, W., 1990, Identification of Ferromagnetic Minerals in a rock by coercivity and unblocking temperture properties: Geophysical Research Letters, v. 17, p. 159–162.

Lyman, A.W., Koenig, E., and Fink, J.H., 2004, Predicting yield strengths and effusion rates of lava domes from morphology and underlying topography: Journal of Volcanology and Geothermal Research, v. 129, p. 125–138, doi:10.1016/S0377-0273(03)00236-1.

Mader, H.M., Llewellin, E.W., and Mueller, S.P., 2013, The rheology of two-phase magmas: A review and analysis: Journal of Volcanology and Geothermal Research, v. 257, p. 135–158, doi:10.1016/j.jvolgeores.2013.02.014.

Magee, C., 2011, Emplacement of sub-volcanic cone sheet intrusions: University of Birmingham, 352 p.

Magee, C. et al., 2016, Lateral magma flow in mafic sill complexes: Geosphere, v. 12, p. GES01256.1, doi:10.1130/GES01256.1.

Magee, C. et al., 2018, Magma Plumbing Systems: A Geophysical Perspective: Journal of Petrology, p. 1–35, doi:10.1093/petrology/egy064.

Magee, C., Jackson, C. a.-L., and Schofield, N., 2013a, The influence of normal fault geometry on igneous sill emplacement and morphology: Geology, v. 41, p. 407–410, doi:10.1130/G33824.1.

Magee, C., Muirhead, J., Schofield, N., Walker, R.J., Galland, O., Holford, S., Spacapan, J., Jackson, C.A.L., and McCarthy, W., 2019, Structural signatures of igneous sheet intrusion propagation: Journal of Structural Geology, v. 125, p. 148–154, doi:10.1016/j.jsg.2018.07.010.

Magee, C., O'Driscoll, B., Petronis, M.S., Stevenson, C.T.E., Clay, P.L., and Gertisser, R., 2013b, Magma rheology variations in sheet intrusions of the Ardnamurchan Central Complex (Scotland) inferred from gabbro inclusion characteristics: Journal of Petrology, v. 54, p. 75–102, doi:10.1093/petrology/egs064.

Magee, C., Stevenson, C., O'Driscoll, B., Schofield, N., and McDermott, K., 2012, An alternative emplacement model for the classic Ardnamurchan cone sheet swarm, NW Scotland, involving lateral magma supply via regional dykes: Journal of Structural Geology, v. 43, p. 73–91, doi:10.1016/j.jsg.2012.08.004.

Manga, M., Castro, J.M., Cashman, K. V., and Loewenberg, M., 1998, Rheology of bubble-bearing magmas: Journal of Volcanology and Geothermal Research, v. 87, p. 15–28, doi:10.1016/S0012-821X(98)00278-7.

Manga, M., and Loewenberg, M., 2001, Viscosity of magmas containing highly deformable bubbles: Journal of Volcanology and Geothermal Research, v. 105, p. 19–24, doi:10.1016/S0377-

0273(00)00239-0.

Martin, S.A., Kavanagh, J.L., Biggin, A.J., and Utley, J.E.P., 2019, The Origin and Evolution of Magnetic Fabrics in Mafic Sills: Frontiers in Earth Science, v. 7, p. 1–23, doi:10.3389/feart.2019.00064.

Mathieu, L., van Wyk de Vries, B., Holohan, E.P., and Troll, V.R., 2008, Dykes, cups, saucers and sills: Analogue experiments on magma intrusion into brittle rocks: Earth and Planetary Science Letters, v. 271, p. 1–13, doi:10.1016/j.epsl.2008.02.020.

Mattsson, T., Burchardt, S., Almqvist, B.S.G., and Ronchin, E., 2018, Syn-emplacement fracturing in the sandfell laccolith, eastern iceland—implications for rhyolite intrusion growth and volcanic hazards: Frontiers in Earth Science, v. 6, doi:10.3389/feart.2018.00005.

McCabe, C., Jackson, M., and Ellwood, B.B., 1985, Magnetic anisotropy in the Trenton Limestone: Results of a new technique, anisotropy of anhysteretic susceptibility: Geophysical Research Letters, v. 12, p. 333–336, doi:10.1029/GL012i006p00333.

McLeod, P., and Tait, S., 1999, The growth of dykes from magma chambers: Journal of Volcanology and Geothermal Research, v. 92, p. 231–245, doi:10.1016/S0377-0273(99)00053-0.

Menand, T., 2011, Physical controls and depth of emplacement of igneous bodies: A review: Tectonophysics, v. 500, p. 11–19, doi:10.1016/j.tecto.2009.10.016.

Menand, T., Daniels, K. a., and Benghiat, P., 2010, Dyke propagation and sill formation in a compressive tectonic environment: Journal of Geophysical Research, v. 115, doi:10.1029/2009JB006791.

Menand, T., and Tait, S.R., 2001, A phenomenological model for precursor volcanic eruptions:, www.nature.com (accessed April 2020).

Merle, O., 2015, The scaling of experiments on volcanic systems: Frontiers in Earth Science, v. 3, p. 1–15, doi:10.3389/feart.2015.00026.

Merle, O., and Vendeville, B., 1995, Experimental modelling of thin-skinned shortening around magmatic intrusions: Bulletin of Volcanology, v. 57, p. 33–43.

Miles, a., and Cartwright, J., 2010, Hybrid flow sills: A new mode of igneous sheet intrusion: Geology, v. 38, p. 343–346, doi:10.1130/G30414.1.

Miyamoto, H., Itoh, K., Kogure, J., Tosaka, H., Tokunaga, T., Fukui, K., and Mogi, K., 2001, Experimental studies on Non-Newtonian fluids flow as analogues of lava flows: Toward a numerical model with a cooling crust: Journal of Theoretical and Applied Mechanics, v. 50, p. 351–356.

Monreal, F.R., Villar, H.J., Baudino, R., Delpino, D., and Zencich, S., 2009, Modeling an atypical

petroleum system : A case study of hydrocarbon generation , migration and accumulation related to igneous intrusions in the Neuquen Basin , Argentina: Marine and Petroleum Geology, v. 26, p. 590–605, doi:10.1016/j.marpetgeo.2009.01.005.

Mueller, S.B., Kueppers, U., Ayris, P.M., Jacob, M., and Dingwell, D.B., 2016, Experimental volcanic ash aggregation: Internal structuring of accretionary lapilli and the role of liquid bonding: Earth and Planetary Science Letters, doi:10.1016/j.epsl.2015.11.007.

Mueller, S., Llewellin, E.W., and Mader, H.M., 2011, The effect of particle shape on suspension viscosity and implications for magmatic flows: Geophysical Research Letters, v. 38, p. 1–5, doi:10.1029/2011GL047167.

Mueller, S., Llewellin, E.W., and Mader, H.M., 2010, The rheology of suspensions of solid particles: Proceedings of the Royal Society A, v. 466, p. 1201–1228, doi:10.1007/BF01432034.

Müller, G., 1998, Starch columns: Analog model for basalt columns: Journal of Geophysical Research, v. 103, p. 15239, doi:10.1029/98JB00389.

Muller, J.R., Ito, G., and Martel, S.J., 2001, Effects of volcano loading on dike propagation in an elastic half-space: J Geophys Res, v. 106, p. 11101–11113, doi:10.1029/2000JB900461.

Murase, T., and McBirney, A.R., 1973, Properties of some common igneous rocks and their melt at high temperatures: Geological Society of America Bulletin, v. 84, p. 3563–3592, doi:10.1130/0016-7606(1973)84%3C3563:POSCIR%3E2.0.CO;2.

Namiki, A., Rivalta, E., Woith, H., and Walter, T.R., 2016, Sloshing of a bubbly magma reservoir as a mechanism of triggered eruptions: Journal of Volcanology and Geothermal Research, doi:10.1016/j.jvolgeores.2016.03.010.

Nicoli, G., Holness, M., Neuberg, J., and Farr, R., 2018, Microstructural evidence for crystallization regimes in mafic intrusions: a case study from the Little Minch Sill Complex, Scotland: Contributions to Mineralogy and Petrology, v. 173, doi:https://doi.org/10.1007/s00410-018-1525-7.

Nolan, M., 2014, Levee Stability and The Evolution of 'A'a Lava Flow-Fields: University of Portsmouth, 1–263 p.

O'Driscoll, B., Troll, V.R., Reavy, R.J., and Turner, P., 2006, The Great Eucrite intrusion of Ardnamurchan, Scotland: Reevaluating the ring-dike concept: Geology, v. 34, p. 189–192, doi:10.1130/G22294.1.

O'Reilly, W., 1984, Rock and Mineral Magnetism: Glasgow, Blackie and Son, 220 p.

Olazabal, A.A., Carracedo, M., and Aranguren, A., 1999, Petrology, magnetic fabric and emplacement in a strike-slip regime of a zoned peraluminous granite: the Campanario-La Haba pluton, Spain:

Geological Society, London, Special Publications, v. 168, p. 177–190, doi:10.1144/GSL.SP.1999.168.01.12.

Oppenheimer, J., Rust, A.C., Cashman, K. V., and Sandnes, B., 2015, Gas migration regimes and outgassing in particle-rich suspensions: Frontiers in Physics, v. 3, p. 1–13, doi:10.3389/fphy.2015.00060.

Pansino, S., Emadzadeh, A., and Taisne, B., 2019, Dike Channelization and Solidification: Time Scale Controls on the Geometry and Placement of Magma Migration Pathways: Journal of Geophysical Research: Solid Earth, v. 124, p. 1–20, doi:10.1029/2019JB018191.

Paquet, F., Dauteuil, O., Hallot, E., and Moreau, F., 2007, Tectonics and magma dynamics coupling in a dyke swarm of Iceland: Journal of Structural Geology, v. 29, p. 1477–1493, doi:10.1016/j.jsg.2007.06.001.

Peltier, A., Famin, V., Bachèlery, P., Cayol, V., Fukushima, Y., and Staudacher, T., 2008, Cyclic magma storages and transfers at Piton de La Fournaise volcano (La Réunion hotspot) inferred from deformation and geochemical data: Earth and Planetary Science Letters, doi:10.1016/j.epsl.2008.02.042.

Petcovic, H.L., and Dufek, J.D., 2005, Modeling magma flow and cooling in dikes: Implications for emplacement of Columbia River flood basalts: Journal of Geophysical Research, v. 110, p. B10201, doi:10.1029/2004JB003432.

Platten, I.M., and Watterson, J.S., 1987, Magma Flow and Crystallization in Dyke Fissures, *in* Halls, H.C. and Fahrig, W.F. eds., Mafic Dyke Swarms: Geological Association of Canada Special Paper 34, p. 65–73.

Poland, M.P., Fink, J.H., and Tauxe, L., 2004, Patterns of magma flow in segmented silicic dikes at Summer Coon volcano, Colorado: AMS and thin section analysis: Earth and Planetary Science Letters, v. 219, p. 155–169, doi:10.1016/S0012-821X(03)00706-4.

Pollard, D., 1973, Derivation and evaluation of a mechanical model for sheet intrusions: Tectonophysics, v. 19, p. 233–269.

Pollard, D.D., 1987, Elementary fracture mechanics applied to the structural interpretation of dykes, *in* Halls, H.C. and Fahrig, W.F. eds., Mafic Dyke Swarms, Geological Association of Canada Special Paper 34, p. 5–24.

Pollard, D.D., and Johnson, A.M., 1973, Mechanics of growth of some laccolithic intrusions in the Henry Mountains, Utah, II: Tectonophysics, v. 18, p. 311–354, doi:10.1016/0040-1951(73)90051-6.

Pollard, D.D., Muller, O.H., and Dockstader, D.R., 1975, The Form and Growth of Fingered Sheet

Intrusions: Geological Society of America Bulletin, v. 86, p. 351, doi:10.1130/0016-7606(1975)86<351:TFAGOF>2.0.CO;2.

Polteau, S., Mazzini, A., Galland, O., Planke, S., and Malthe-Sørenssen, A., 2008, Saucer-shaped intrusions: Occurrences, emplacement and implications: Earth and Planetary Science Letters, v. 266, p. 195–204, doi:10.1016/j.epsl.2007.11.015.

Poppe, S., 2019, Magma intrusion and related deformation of the Earth's upper crust in nature and analog experiments: 192 p.

Poppe, S., Holohan, E.P., Galland, O., Buls, N., Gompel, G. Van, Keelson, B., Tournigand, P., Brancart, J., Hollis, D., and Nila, A., 2019, An Inside Perspective on Magma Intrusion : Quantifying 3D Displacement and Strain in Laboratory Experiments by Dynamic X-ray Computed Tomography: Frontiers in Earth Science, v. 7, p. 1–20, doi:10.3389/feart.2019.00062.

Porreca, M., Cifelli, F., Soriano, C., Giordano, G., and Mattei, M., 2015, Magma flow within dykes in submarine hyaloclastite environments: an AMS study of the Miocene Cabo de Gata volcanic units: Geological Society, London, Special Publications, v. 396, p. 133–157, doi:10.1144/SP396.14.

Potter, D.K., and Stephenson, A., 1988, Single-domain particles in rocks and magnetic fabric analysis: Geophysical Research Letters, v. 15, p. 1097, doi:10.1029/GL015i010p01097.

Putirka, K.D., 2017, Down the crater: Where magmas are stored and why they erupt: Elements, v. 13, p. 11–16, doi:10.2113/gselements.13.1.11.

Ramberg, H., 1970, Model studies in relation to intrusion of plutonic bodies, *in* Newall, G. and Rast, N. eds., Mechanism of igneous intrusion: Proceedings of a Symposium of the Same Name Held in Liverpool University 9, 10, 11 January 1969 Under the Auspices of Liverpool Geological Society, Liverpool, Gallery Press, p. 261–288.

Raposo, M.I.B., Chaves, A.O., Lojkasek-Lima, P., D'Agrella-Filho, M.S., and Teixeira, W., 2004, Magnetic fabrics and rock magnetism of Proterozoic dike swarm from the southern São Francisco Craton, Minas Gerais State, Brazil: Tectonophysics, v. 378, p. 43–63, doi:10.1016/j.tecto.2003.10.017.

Raposo, M.I.B., D'Agrella-Filho, M.S., and Pinese, J.P.P., 2007, Magnetic fabrics and rock magnetism of Archaean and Proterozoic dike swarms in the southern São Francisco Craton, Brazil: Tectonophysics, v. 443, p. 53–71, doi:10.1016/j.tecto.2007.08.001.

Raposo, M.I.B., and Ernesto, M., 1995, Anisotropy of magnetic susceptibility in the Ponta Grossa dyke swarm (Brazil) and its relationship with magma flow direction: Physics of the Earth and Planetary Interiors, v. 87, p. 183–196, doi:10.1016/0031-9201(94)02970-M.

Rickwood, P.C., 1990, The anatomy of a dyke and the determination of propagation and magma flow directions, *in* Mafic dykes and emplacement mechanisms, v. 2;, p. 81–100.

Rivalta, E., Böttinger, M., and Dahm, T., 2005, Buoyancy-driven fracture ascent: Experiments in layered gelatine: Journal of Volcanology and Geothermal Research, v. 144, p. 273–285, doi:10.1016/j.jvolgeores.2004.11.030.

Roberts, A.P., 1995, Magnetic properties of sedimentary greigite (Fe3S4): Earth and Planetary Science Letters, v. 134, p. 227–236, doi:10.1016/0012-821X(95)00131-U.

Rochette, P., Jackson, M., and Aubourg, C., 1992, Rock Magnetism and the Interpretation of Anisotropy of Magnetic Susceptibility: Reviews of Geophysics, v. 30, p. 209–226.

Rochette, P., Jenatton, L., Dupuy, C., Boudier, F., and Reuber, I., 1991, Diabase dikes emplacement in the Oman Ophiolite: A magnetic fabric study with reference to geochemistry, *in* Peters, T., Nicolas, A., and Coleman, R.G. eds., Ophiolite genesis and evolution of the oceanic lithosphere, p. 55–82, doi:10.1007/978-94-011-3358-6.

Roman-Berdiel, T., Gapais, D., and Brun, J.P., 1995, Analogue models of laccolith formation: Journal of Structural Geology, v. 17, p. 1337–1346, doi:10.1016/0191-8141(95)00012-3.

Roni, E., Westerman, D.S., Dini, A., Stevenson, C., and Rocchi, S., 2014, Feeding and growth of a dyke-laccolith system (Elba Island, Italy) from AMS and mineral fabric data: Journal of the Geological Society, v. 171, p. 413–424, doi:10.1144/jgs2013-019.

Rossetti, F., Ranalli, G., and Faccenna, C., 1999, Rheological properties of paraffin as an analogue material for viscous crustal deformation: Journal of Structural Geology, v. 21, p. 413–417, doi:10.1016/S0191-8141(99)00040-1.

Rubin, A., 1995, Propagation of magma-filled cracks: Annual Review of Earth and Planetary Sciences, v. 23, p. 287–336.

Russell, J.K., Sparks, R.S.J., and Kavanagh, J.L., 2019, Kimberlite Volcanology: Transport, Ascent, and Eruption: Elements, v. 15, p. 405–410, doi:10.2138/gselements.15.6.405.

Rust, A.C., and Manga, M., 2002a, Bubble shapes and orientations in low Re simple shear flow: Journal of colloid and interface science, v. 249, p. 476–480, doi:10.1006/jcis.2002.8292.

Rust, A.C., and Manga, M., 2002b, Effects of bubble deformation on the viscosity of dilute suspensions: Journal of Non-Newtonian Fluid Mechanics, v. 104, p. 53–63, doi:10.1016/S0377-0257(02)00013-7.

Ruzicka, B., and Zaccarelli, E., 2011, A fresh look at the Laponite phase diagram: Soft Matter, v. 7, p. 1268, doi:10.1039/c0sm00590h.

Saumur, B.M., and Cruden, A.R., 2016, On the emplacement of the voisey's bay intrusion (Labrador, Canada): Bulletin of the Geological Society of America, v. 128, p. 147–168, doi:10.1130/B31240.1.

Schellart, W.P., 2011, Rheology and density of glucose syrup and honey: Determining their suitability for usage in analogue and fluid dynamic models of geological processes: Journal of Structural Geology, v. 33, p. 1079–1088, doi:10.1016/j.jsg.2011.03.013.

Schmiedel, T., Galland, O., and Breitkreuz, C., 2017, Dynamics of Sill and Laccolith Emplacement in the Brittle Crust: Role of Host Rock Strength and Deformation Mode: Journal of Geophysical Research: Solid Earth, v. 122, p. 8860–8871, doi:10.1002/2017JB014468.

Schofield, N., 2009, Linking sill morphology to emplacement mechanisms.

Schofield, N., Brown, D., Magee, C., and Stevenson, C., 2012a, Sill morphology and comparison of brittle and non-brittle emplacement mechanisms: Journal Of The Geological Society, v. 169, p. 127–141, doi:10.1144/0016-76492011-078.Sill.

Schofield, N., Heaton, L., Holford, S.P., Archer, S.G., Jackson, C. a.-L., and Jolley, D.W., 2012b, Seismic imaging of "broken bridges": linking seismic to outcrop-scale investigations of intrusive magma lobes: Journal of the Geological Society, v. 169, p. 421–426, doi:10.1144/0016-76492011-150.

Schofield, N., Stevenson, C., and Reston, T., 2010, Magma fingers and host rock fluidization in the emplacement of sills: Geology, v. 38, p. 63–66, doi:10.1130/G30142.1.

Selkin, P.A., Gee, J.S., and Meurer, W.P., 2014, Magnetic anisotropy as a tracer of crystal accumulation and transport, Middle Banded Series, Stillwater Complex, Montana: Tectonophysics, v. 629, p. 123–137, doi:10.1016/j.tecto.2014.03.028.

Shelley, D., 1985, Determining paleo-flow directions from groundmass fabrics in the Lyttelton radial dykes, New Zealand: Journal of Volcanology and Geothermal Research, v. 25, p. 69–79, doi:10.1016/0377-0273(85)90005-8.

Sigmundsson, F. et al., 2015, Segmented lateral dyke growth in a rifting event at Bárðarbunga volcanic system, Iceland: Nature, v. 517, p. 191–195, doi:10.1038/nature14111.

Sili, G., Urbani, S., and Acocella, V., 2019, What Controls Sill Formation: An Overview From Analogue Models: Journal of Geophysical Research: Solid Earth, v. 124, p. 8205–8222, doi:10.1029/2018JB017005.

Silva, P.F., Marques, F.O., Henry, B., Madureira, P., Hirt, A.M., Font, E., and Lourenço, N., 2010, Thick dyke emplacement and internal flow: A structural and magnetic fabric study of the deep-seated dolerite dyke of Foum Zguid (southern Morocco): Journal of Geophysical Research, v. 115, p. B12108, doi:10.1029/2010JB007638.

Smith, R.P., 1987, Dyke emplacement at Spanish Peaks, Colorado, *in* Halls, H.C. and Fahrig, W.F. eds., Mafic Dyke Swarms: Geological Association of Canada Special Paper 34, Geological Association of Canada, p. 47–54.

Soriano, C., Beamud, E., and Garcés, M., 2008, Magma flow in dikes from rift zones of the basaltic shield of Tenerife, Canary Islands: Implications for the emplacement of buoyant magma: Journal of Volcanology and Geothermal Research, v. 173, p. 55–68, doi:10.1016/j.jvolgeores.2008.01.007.

Soriano, C., Beamud, E., Garcés, M., and Ort, M.H., 2016, "Anomalous" magnetic fabrics of dikes in the stable single domain/superparamagnetic threshold: Geophysical Journal International, v. 204, p. 1040–1059, doi:10.1093/gji/ggv495.

Soule, S.A., and Cashman, K. V., 2005, Shear rate dependence of the pāhoehoe-to-'a 'ā transition: Analog experiments: Geology, v. 33, p. 361–364, doi:10.1130/G21269.1.

Sparks, R.S.J., 2013, Kimberlite Volcanism: Annual Review of Earth and Planetary Sciences, v. 41, p. 497–528, doi:10.1146/annurev-earth-042711-105252.

Sparks, R.S.J., and Cashman, K. V., 2017, Dynamic magma systems: Implications for forecasting volcanic activity: Elements, v. 13, p. 35–40, doi:10.2113/gselements.13.1.35.

Spender, M.R., Coey, J.M.D., and Morrish, A.H., 1972, The Magnetic Properties and Mössbauer Spectra of Synthetic Samples of Fe_3S_4: Canadian Journal of Physics, v. 50, p. 2313–2326, doi:10.1139/p72-306.

Spry, A., 1962, The origin of columnar jointing, particularly in basalt flows: Journal of the Geological Society of Australia, v. 8, p. 191–216, doi:10.1080/14400956208527873.

Stasiuk, M. V, Jaupart, C., and Sparks, R.S.J., 1993, Influence of cooling on lava-flow dynamics: Geology, v. 21, p. 335–338, doi:10.1130/0091-7613(1993)021<0335:IOCOLF>2.3.CO.

Staudigel, H., Gee, J., Tauxe, L., and Varga, R., 1992, Shallow intrusive directions of sheeted dikes in the Troodos ophiolite: Anisotropy of magnetic susceptibility and structural data: Geology, v. 20, p. 841–844.

Stephens, T.L., Walker, R.J., Healy, D., Bubeck, A., England, R.W., and McCaffrey, K.J.W., 2017, Igneous sills record far-field and near-field stress interactions during volcano construction: Isle of Mull, Scotland: Earth and Planetary Science Letters, v. 478, p. 159–174, doi:10.1016/j.epsl.2017.09.003.

Stephenson, A., 1994, Distribution anisotropy: two simple models for magnetic lineation and foliation: Physics of the Earth and Planetary Interiors, v. 82, p. 49–53, doi:10.1016/0031-9201(94)90101-5.

Stimac, J., Goff, F., and Goff, C.J., 2015, Intrusion-Related Geothermal Systems, *in* The Encyclopedia of Volcanoes, p. 799–822, doi:10.1016/b978-0-12-385938-9.00046-8.

Sumita, I., and Ota, Y., 2011, Experiments on buoyancy-driven crack around the brittle–ductile transition: Earth and Planetary Science Letters, v. 304, p. 337–346, doi:10.1016/j.epsl.2011.01.032.

Sun, W.D. et al., 2013, The link between reduced porphyry copper deposits and oxidized magmas: Geochimica et Cosmochimica Acta, v. 103, p. 263–275, doi:10.1016/j.gca.2012.10.054.

Taisne, B., and Jaupart, C., 2009, Dike propagation through layered rocks: Journal of Geophysical Research, v. 114, p. B09203, doi:10.1029/2008JB006228.

Taisne, B., and Tait, S., 2011, Effect of solidification on a propagating dike: Journal of Geophysical Research: Solid Earth, v. 116, p. 1–14, doi:10.1029/2009JB007058.

Taisne, B., and Tait, S., 2009, Eruption versus intrusion? arrest of propagation of constant volume, buoyant, liquid-filled cracks in an elastic, brittle host: Journal of Geophysical Research: Solid Earth, v. 114, p. 1–7, doi:10.1029/2009JB006297.

Taisne, B., Tait, S., and Jaupart, C., 2011, Conditions for the arrest of a vertical propagating dyke: Bulletin of Volcanology, v. 73, p. 191–204, doi:10.1007/s00445-010-0440-1.

Tauxe, L., 2010, Essentials of Paleomagnetism: Los Angeles, University of California Press, 488 p.

Tauxe, L., Bertram, H.N., and Seberino, C., 2002, Physical interpretation of hysteresis loops: Micromagnetic modeling of fine particle magnetite: Geochemistry, Geophysics, Geosystems, v. 3, p. 1–22, doi:10.1029/2001GC000241.

Tauxe, L., Gee, J.S., and Staudigel, H., 1998, Flow directions in dikes from anisotropy of magnetic susceptibility data: The bootstrap way: Journal of Geophysical Research, v. 103, p. 17775, doi:10.1029/98JB01077.

Thomson, K., 2007, Determining magma flow in sills, dykes and laccoliths and their implications for sill emplacement mechanisms: Bulletin of Volcanology, v. 70, p. 183–201, doi:10.1007/s00445-007-0131-8.

Thomson, K., and Hutton, D., 2004, Geometry and growth of sill complexes: insights using 3D seismic from the North Rockall Trough: Bulletin of Volcanology, v. 66, p. 364–375, doi:10.1007/s00445-003-0320-z.

Tibaldi, A., Bonali, F.L., and Corazzato, C., 2014, The diverging volcanic rift system: Tectonophysics, v. 611, p. 94–113, doi:10.1016/j.tecto.2013.11.023.

Tortini, R., Bonali, F.L., Corazzato, C., Carn, S. a., and Tibaldi, A., 2014, An innovative application of

the kinect in earth sciences: Quantifying deformation in analogue modelling of volcanoes: Terra Nova, v. 26, p. 273–281, doi:10.1111/ter.12096.

Townsend, M.R., Pollard, D.D., and Smith, R.P., 2017, Mechanical models for dikes: A third school of thought: Tectonophysics, v. 703–704, p. 98–118, doi:10.1016/j.tecto.2017.03.008.

Trindade, R.I.F., Bouchez, J.L., Bolle, O., Nédélec, A., Peschler, A., and Poitrasson, F., 2001, Secondary fabrics revealed by remanence anisotropy: Methodological study and examples from plutonic rocks: Geophysical Journal International, v. 147, p. 310–318, doi:10.1046/j.0956-540X.2001.01529.x.

Truby, J.M., Mueller, S.P., Llewellin, E.W., and Mader, H.M., 2015, The rheology of three-phase suspensions at low bubble capillary number.: Proceedings of the Royal Society A, v. 471, p. 20140557, doi:10.1098/rspa.2014.0557.

Urbani, S., Acocella, V., and Rivalta, E., 2018, What Drives the Lateral Versus Vertical Propagation of Dikes? Insights From Analogue Models: Journal of Geophysical Research: Solid Earth, v. 123, p. 3680–3697, doi:10.1029/2017JB015376.

Vachon, R., and Hieronymus, C.F., 2017, Effect of host-rock rheology on dyke shape, thickness and magma overpressure: Geophysical Journal International, v. 208, p. 1414–1429, doi:10.1093/gji/ggw448.

Varga, R.J., Gee, J.S., Staudigel, H., and Tauxe, L., 1998, Dike surface lineations as magma flow indicators within the sheeted dike complex of the Troodos Ophiolite, Cyprus: Journal of Geophysical Research, v. 103, p. 5241, doi:10.1029/97JB02717.

Walker, G.P.L., 1973, Lengths of lava flows: Philosophical Transactions of the Royal Society, London, v. 274, p. 107–118, https://about.jstor.org/terms (accessed September 2020).

Walker, G.P.L., 1993, Re-evaluation of inclined intrusive sheets and dykes in the Cuillins volcano, Isle of Skye: Geological Society, London, Special Publications, v. 76, p. 489–497.

Wallace, P.J., and Anderson, A.T., 1998, Effects of eruption and lava drainback on the H 2 O contents of basaltic magmas at Kilauea Volcano: Springer-Verlag.

Walter, T.R., and Troll, V.R., 2003, Experiments on rift zone evolution in unstable volcanic edifices: Journal of Volcanology and Geothermal Research, v. 127, p. 107–120, doi:10.1016/S0377-0273(03)00181-1.

Walter, T.R., and Troll, V.R., 2001, Formation of caldera periphery faults: An experimental study: Bulletin of Volcanology, v. 63, p. 191–203, doi:10.1007/s004450100135.

Wartho, J.-A., Kelley, S., and Blake, S., 2001, Magma flow regimes in sills deduced from Ar isotope systematics of host rocks: Journal of Geophysical Research, v. 106, p. 4017–4035,

doi:10.1029/2000JB900327.

Watanabe, T., Masuyama, T., Nagaoka, K., and Tahara, T., 2002, Analog experiments on magma-filled cracks: Competition between external stresses and internal pressure: Earth Planets and …, v. 54, p. 1247–1261.

Weijermars, R., 1986, Flow behaviour and physical chemistry of bouncing putties and related polymers in view of tectonic laboratory applications: Tectonophysics, v. 124, p. 325–358, doi:10.1016/0040-1951(86)90208-8.

Weinberg, R.F., and Leitch, A.M., 1998, Mingling in mafic magma chambers replenished by light felsic inputs: fluid dynamical experiments.:

Wilson, L., and Head, J.W., 1983, A comparison of volcanic eruption processes on Earth, Moon, Mars, Io and Venus: Nature, v. 302, p. 663–669, doi:10.1038/302663a0.

Witham, F., Woods, A.W., and Gladstone, C., 2006, An analogue experimental model of depth fluctuations in lava lakes: Bulletin of Volcanology, v. 69, p. 51–56, doi:10.1007/s00445-006-0055-8.

Woods, A.W., and Bursik, M.I., 1994, A laboratory study of ash flows: Journal of Geophysical Research: Solid Earth, v. 99, p. 4375–4394, doi:10.1029/93JB02224.

Woods, A.W., and Caulfield, C.-C.P., 1992, A laboratory study of explosive volcanic eruptions: Journal of Geophysical Research, v. 97, p. 6699, doi:10.1029/92JB00176.

Worm, H.-U., Clark, D., and Dekkers, M.J., 1993, Magnetic Susceptibility of Pyrrhotite: Grain Size, Field and Frequency Dependence: Geophysical Journal International, v. 114, p. 127–137, doi:10.1111/j.1365-246X.1993.tb01472.x.

Wyrick, D.Y., Morris, A.P., Todt, M.K., and Watson-morris, M.J., 2015, Physical analogue modelling of Martian dyke-induced deformation: Volcanism and Tectonism Across the Inner Solar System, Geological Society, London, Special Publications, v. 401, p. 395–403, doi:10.1144/SP401.15.

Yamato, P., Tartèse, R., Duretz, T., and May, D. a., 2012, Numerical modelling of magma transport in dykes: Tectonophysics, v. 526–529, p. 97–109, doi:10.1016/j.tecto.2011.05.015.

Závada, P., Calassou, T., Schulmann, K., Hrouda, F., Štípská, P., Hasalová, P., Míková, J., Magna, T., and Mixa, P., 2017, Magnetic fabric transposition in folded granite sills in Variscan orogenic wedge: Journal of Structural Geology, v. 94, p. 166–183, doi:10.1016/j.jsg.2016.11.007.

Závada, P., Dědeček, P., Mach, K., Lexa, O., and Potužák, M., 2011, Emplacement dynamics of phonolite magma into maar-diatreme structures - Correlation of field, thermal modeling and AMS analogue modeling data: Journal of Volcanology and Geothermal Research, v. 201, p. 210–226, doi:10.1016/j.jvolgeores.2010.07.012.

Závada, P., Kratinová, Z., Kusbach, V., and Schulmann, K., 2009, Internal fabric development in complex lava domes: Tectonophysics, v. 466, p. 101–113, doi:10.1016/j.tecto.2008.07.005.

Appendix A

Published copy of:

Kavanagh, J.L., Engwell, S. and **Martin, S.A.** (2018) A review of laboratory and numerical modelling in volcanology. *Solid Earth,* **9** (2). doi: 10.5194/se-9-531-2018.

Solid Earth, 9, 531–571, 2018
https://doi.org/10.5194/se-9-531-2018

A review of laboratory and numerical modelling in volcanology

Janine L. Kavanagh[1], Samantha L. Engwell[2], and Simon A. Martin[1]

[1]Department of Earth, Ocean and Ecological Sciences, University of Liverpool, Liverpool L69 3GP, UK
[2]British Geological Survey, The Lyell Centre, Research Avenue South, Edinburgh EH14 4AP, UK

Correspondence: Janine L. Kavanagh (janine.kavanagh@liverpool.ac.uk)

Received: 18 April 2017 – Discussion started: 15 May 2017
Revised: 23 February 2018 – Accepted: 6 March 2018 – Published: 27 April 2018

Abstract. Modelling has been used in the study of volcanic systems for more than 100 years, building upon the approach first applied by Sir James Hall in 1815. Informed by observations of volcanological phenomena in nature, including eyewitness accounts of eruptions, geophysical or geodetic monitoring of active volcanoes, and geological analysis of ancient deposits, laboratory and numerical models have been used to describe and quantify volcanic and magmatic processes that span orders of magnitudes of time and space. We review the use of laboratory and numerical modelling in volcanological research, focussing on sub-surface and eruptive processes including the accretion and evolution of magma chambers, the propagation of sheet intrusions, the development of volcanic flows (lava flows, pyroclastic density currents, and lahars), volcanic plume formation, and ash dispersal.

When first introduced into volcanology, laboratory experiments and numerical simulations marked a transition in approach from broadly qualitative to increasingly quantitative research. These methods are now widely used in volcanology to describe the physical and chemical behaviours that govern volcanic and magmatic systems. Creating simplified models of highly dynamical systems enables volcanologists to simulate and potentially predict the nature and impact of future eruptions. These tools have provided significant insights into many aspects of the volcanic plumbing system and eruptive processes. The largest scientific advances in volcanology have come from a multidisciplinary approach, applying developments in diverse fields such as engineering and computer science to study magmatic and volcanic phenomena. A global effort in the integration of laboratory and numerical volcano modelling is now required to tackle key problems in volcanology and points towards the importance of benchmarking exercises and the need for protocols to be developed so that models are routinely tested against "real world" data.

1 Introduction

Many people have a profound fascination with volcanoes: from the beautiful landscapes they produce and art they inspire (Sigurdsson, 2015b) to the impact their eruptions have on individuals, societies, and civilisations (e.g. Sheets, 2015). However, this fascination is often met with fear as the destruction volcanoes can cause may have far-reaching effects. Volcanic activity is often unpredictable and occurs in an environment that is highly changeable and forbidding; however, there is a compelling need to improve our understanding of these complex systems. Approximately 800 million people around the world live close enough to a volcano to be directly affected by an eruption (Loughlin et al., 2015), and many more are at risk of social or economic impact as the consequences of volcanism extend from regional to potentially global reaches (e.g. Svensen et al., 2004). The huge range of style and intensity of volcanic activity means that societies living nearby do so with high risk; there are however many benefits too: volcanoes produce habitable environments on a local scale through production of fertile soil, and magmatic activity is associated with economic deposits such as copper porphyry. On a planetary scale, the gases volcanoes emit lead to the creation of our oceans and the atmosphere. Life on Earth and the physical processes that govern volcanic activity are thus intimately connected.

The effects of volcanic eruptions can be felt long after surface activity has ceased, with the potential for both physical environments and societies to be impacted many decades after the event (e.g. the occurrence of lahars decades after the 1991 Mt Pinatubo eruption). The challenges of working in volcanic terrains and gathering useful data mean that laboratory and numerical models have gained significant importance in studying the dynamics of volcano growth and erup-

Published by Copernicus Publications on behalf of the European Geosciences Union.

Appendix B

Published copy of:

Martin, S.A., Kavanagh, J.L., Biggin, A.J. and Utley, J.E. (2019) The origin and evolution of magnetic fabrics in mafic sills. *Frontiers in Earth Science,* **7**, 1-23, doi:10.3389/feart.2019.00064.

frontiers in Earth Science

ORIGINAL RESEARCH
published: 18 April 2019
doi: 10.3389/feart.2019.00064

The Origin and Evolution of Magnetic Fabrics in Mafic Sills

Simon A. Martin, Janine L. Kavanagh*, Andrew J. Biggin and James E. P. Utley*

Department of Earth, Ocean and Ecological Sciences, University of Liverpool, Liverpool, United Kingdom

Studying extinct volcanoes where erosion has exposed dykes and sills provides direct access to the fossil remnants of magma movement, however, linking crystallized magma to emplacement dynamics is challenging. This study investigates how magma flow varies across the thickness of a thin (6 m thick) mafic sill. We use a high-resolution sampling regime to measure micro-scale variations in magnetic anisotropy, which is associated with the orientation of the magnetic particles present within the crystalline rock. Fieldwork was conducted on exposed sills of the British and Irish Palaeogene Igneous Province, Isle of Skye, Scotland. Here Jurassic sedimentary rocks have been intruded by a series of sills, of picrite to crinanite composition, from the Little Minch Sill Complex (c.60 Ma). Anisotropy of magnetic susceptibility (AMS) and anisotropy of anhysteretic remanent magnetization (AARM) signals have been used to separate a crinanite sill into distinct magnetic groupings. We identified two AMS groups (the upper and lower sill margins, and the central region) and four AARM groups (the lower margin, the middle region, a region just below the upper margin, and the upper margin). Both AMS and AARM signals originate from titanomagnetite of multi-domain or vortex-state to single-domain sized grains, respectively. The AMS and AARM fabrics are aligned with each other in the margin regions preserving a history of magma flow toward the North during initial emplacement. However, in the sill interior the magnetic fabrics are oblique to each other, thus reflecting multiple origins. We suggest the AMS fabrics have recorded magma flow during sill growth, and AARM fabrics have recorded melt percolation flow as the interstitial melt migrated upward through a solidifying crystal mush. We demonstrate that when AMS and AARM are used in combination they enable a detailed understanding of magma flow and solidification dynamics to be obtained, from initial emplacement to solidification. Overall, our detailed sampling and analysis indicates that magnetic fabrics can be highly variable over small distances, supporting the suggestion of horizontal flow restriction and propagation path migration within growing sills, and that previous reports of magma flow and solidification dynamics based on under-sampled bodies may require reconsideration.

Keywords: sill emplacement, AMS, AARM, magma flow, British and Irish Palaeogene Igneous Province

OPEN ACCESS

Edited by:
Julian Lauthold,
ETH Zürich, Switzerland

Reviewed by:
Gautier Nicoll,
University of Cambridge, United Kingdom
Craig Magee,
University of Leeds, United Kingdom
Ben Hayes,
University of the Witwatersrand, South Africa

****Correspondence:***
Simon A. Martin
smartin@liverpool.ac.uk
Janine L. Kavanagh
janine.kavanagh@liverpool.ac.uk

Specialty section:
This article was submitted to Petrology, a section of the journal Frontiers in Earth Science

Received: *06 December 2018*
Accepted: *14 March 2019*
Published: *18 April 2019*

Citation:
Martin SA, Kavanagh JL, Biggin AJ and Utley JEP (2019) The Origin and Evolution of Magnetic Fabrics in Mafic Sills. Front. Earth Sci. 7:64. doi: 10.3389/feart.2019.00064

INTRODUCTION

Determining the physical, chemical and thermal processes that occur during the propagation, transport and emplacement of magma within magmatic intrusions is necessary for understanding how volcanic systems develop (e.g., Magee et al., 2018b). Magma is transported through the crust in a series of sheet intrusions called dykes, inclined sheets, and sills (e.g., Mathieu et al., 2008). These

Appendix C

Expanded version of Figure 4.8: Thermomagnetic data for all locations of the basaltic dyke.

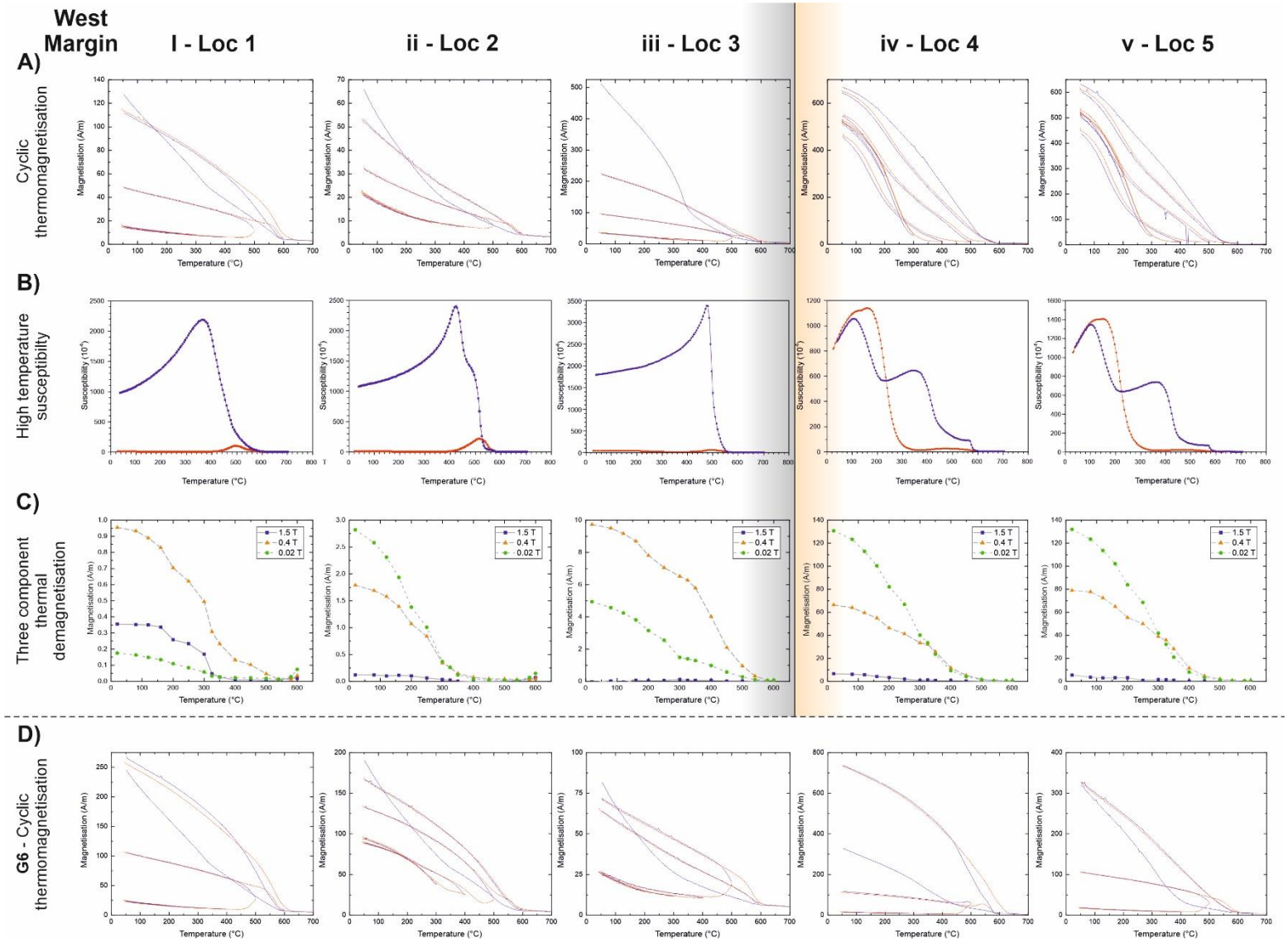
West Margin
I - Loc 1
ii - Loc 2
iii - Loc 3
iv - Loc 4
v - Loc 5
A)
Cyclic thermomagnetisation
B)
High temperature susceptibilty
C)
Three component thermal demagnetisation
D)
G6 - Cyclic thermomagnetisation
Magnetisation (A/m)
Susceptibility (10⁻⁸)
Temperature (°C)
1.5 T
0.4 T
0.02 T

East Margin
vi - Loc 6
vii - Loc 7
viii - Loc 8
ix - Loc 9
A) Cyclic thermomagnetisation
B) High temperature susceptibility
C) Three component thermal demagnetisation
D) G6 - Cyclic thermomagnetisation
Magnetisation (A/m)
Susceptibility (10⁻⁶)
Temperature (°C)
1.5 T
0.4 T
0.02 T